UNIVERSITY OF CALIFORNIA
Los Angeles

Plasma Inter-Particle and Particle-Wall Interactions

A dissertation submitted in partial satisfaction
of the requirements for the degree
Doctor of Philosophy in Aerospace Engineering

by

Marlene Idy Patino

2017

ABSTRACT OF THE DISSERTATION

Plasma Inter-Particle and Particle-Wall Interactions

by

Marlene Idy Patino
Doctor of Philosophy in Aerospace Engineering
University of California, Los Angeles, 2017
Professor Richard E. Wirz, Chair

An improved understanding of plasma inter-particle and particle-wall interactions is critical to the advancement of plasma devices used for space electric propulsion, fusion, high-power communications, and next-generation energy systems. Two interactions of particular importance are (1) ion-atom collisions in the plasma bulk and (2) secondary electron emission from plasma-facing materials.

For ion-atom collisions, interactions between fast ions and slow atoms are commonly dominated by charge-exchange and momentum-exchange collisions that are important to understanding the performance and behavior of many plasma devices. To investigate this behavior, this work developed a simple, well-characterized experiment that accurately measures the effects of high energy xenon ions incident on a background of xenon neutral atoms. By comparing these results to both analytical and computational models of ion-atom interactions, we discovered the importance of (1) accurately treating the differential cross-sections for momentum-exchange and charge-exchange collisions over all neutral background pressures, and (2) commonly overlooked interactions, including ion-induced electron emission and neutral-neutral ionization collisions, at high pressures. Data provide vital information on the angular scattering distributions of charge-exchange and momentum-exchange ions at 1.5 keV relevant for ion thrusters, and serve as canonical data for validation of plasma models.

This work also investigates electron-induced secondary electron emission behavior relevant to materials commonly considered for plasma thrusters, fusion systems, and many other plasma devices. For such applications, secondary electron emission can alter the sheath potential, which can significantly affect device performance and life. Secondary electron emission properties were measured for materials that are critical to the efficient operation of many plasma devices, including: graphite (for tokamaks, ion thrusters, and traveling wave tubes), lithium (for tokamak walls), tungsten (the most promising material for future tokamaks such as ITER), and nickel (for plasma-enhanced chemistry). Measurements were made for incident electron energies up to 1.5 keV and angles between 0 and 78°.

The most significant results from these measurements are as follows: (1) first-ever measurements of naturally-forming tungsten fuzz show a more than 40% reduction in secondary electron emission and an independence on incidence angle; (2) original measurements of lithium oxide show a 2× and 6× increase in secondary electron emission for 17% and 100% oxidation; and (3) unique measurements of Ni(110) single crystal show extrema in secondary electron emission when incidence angle is varied and an up to 36% increase at 0° over polycrystalline nickel. Each of these results are important discoveries for improving plasma devices. For example, from (1), the growth of tungsten fuzz in tokamaks is desirable for minimizing adverse secondary electron emission effects. From (2), the opposite is true for tokamaks with lithium coatings which are oxidized by typical residual gases. From (3), secondary electron emission from Ni(110) catalysts in plasma-enhanced chemistry may facilitate further reactions.

The dissertation of Marlene Idy Patino is approved.

Nasr M. Ghoniem

Xiaolin Zhong

Walter N. Gekelman

Lee Johnson

Yevgeny Raitses

Richard E. Wirz, Committee Chair

University of California, Los Angeles
2017

Table of Contents

List of Figures

List of Tables

Acknowledgments

The author is thankful for the support and time of each of her committee members: Profs. Richard Wirz, Nasr Ghoniem, Xiaolin Zhong, and Walter Gekelman, and Drs. Lee Johnson and Yevgeny Raitses.

Thanks are due to Dr. Taylor Matlock and Lauren Chu of the UCLA Plasma and Space Propulsion Laboratory for education on experimental methods and for collaboration on ion-neutral collision experiments. Thanks are also due to Drs. Ben Dankongkakul and Samuel Araki of UCLA, and Drs. Paul Giuliano and Ian Boyd from the University of Michigan, for many insightful discussions on ion-neutral collisions and development of complementary computational collision models. The author would like to give their sincerest thanks to Ray Swindlehurst and Nowell Niblett of the Jet Propulsion Laboratory for invaluable assistance with maintenance of the ion beam facility and fabrication of critical components.

Similarly, thanks are due to Dr. Angela Capece of the Princeton Plasma Physics Laboratory (PPPL) for education on surface science diagnostics and for collaboration on secondary electron emission experiments of nickel and lithium. Thanks are also due to Prof. Bruce Koel, Drs. Xiaofang Yang and Luxherta Buzi, and Yuxin Yang and Michelle Hofman of PPPL and Princeton University for valuable discussions on surface chemistry. The author would also like to thank Drs. Philip Efthimion, Robert Kaita, and Igor Kaganovich of PPPL for fruitful discussions of secondary electron emission physics and effects in plasma. Thanks to Drs. Dennis Whyte and Graham Wright of the Massachusetts Institute of Technology for providing the tungsten fuzz sample, and Dr. Yao-Wen Yeh of Princeton University for characterizing the fuzz sample with scanning electron microscopes. Thanks to David Caron, Hadar Lazar, and Chenggang Jin for assistance in data collection, and Alex Merzhev and Gustav Smalley of PPPL for much technical assistance in the development of the facility for measuring graphite, fabrication of important components, and troubleshooting of all secondary electron emission facilities. The author is also grateful to Cesar Huerta of UCLA

for development of a complementary computational model to investigate secondary electron emission from textured surfaces such as tungsten fuzz.

The author gratefully acknowledges the financial support from the UCLA Dissertation Year Fellowship, UCLA Eugene V Cota-Robles Fellowship, UCLA School of Engineering and Applied Science, DOE Office of Science Graduate Student Fellowship, PPPL Off-Site University Research Support Program, Air Force Office of Scientific Research (Grants FA9550-11-1-0282, FA9550-09-1-0695, FA9550-14-1-0053, and FA9550-14-10317), University of Michigan/AFRL Center of Excellence in Electric Propulsion (Grant F9550-09-1-0695), and US Department of Energy (Contracts DE-AC02-09CH11466 and DE-SC0012890). Additional funding was provided by NASA CA Space Grant, HENAAC Graduate Student Leadership, and General James H Doolittle Fellowships.

Chapter 3 of this document is a version of a paper being prepared for publication [M.I. Patino and R.I. Wirz, "Experimental Characterization of Xe^+-Xe Collisions for Computational Model Validation," *Physics of Plasmas*] and previously presented [M.I. Patino, L.E. Chu, and R.E. Wirz, "Ion-Neutral Collision Analysis for a Well-Characterized Plasma Experiment," 48th Joint Propulsion Conference, 2012, AIAA-2012-4119, pp. 1-12]. Chapter 4 is a conglomerate of material previously published, submitted, and being prepared for submission [M.I. Patino, Y. Raitses, B.E. Koel, and R.E. Wirz, "Analysis of Secondary Electron Emission for Conducting Materials Using LEED Optics," *Journal of Physics D: Applied Physics*, 2015, Vol. 48, 195204; A.M. Capece, M.I. Patino, Y. Raitses, and B.E. Koel, "Secondary Electron Emission from Lithium and Lithium Compounds," *Applied Physics Letters*, 2016, Vol. 109, 011605; M.I. Patino, Y. Raitses, and R.E. Wirz, "Secondary Electron Emission from Plasma-Generated Nanostructured Tungsten Fuzz," *Applied Physics Letters*, 2016, Vol. 109, 201602; C. Huerta, M.I. Patino and R.E. Wirz, "Secondary Electron Emission from Textured Surfaces," *Journal of Physics D: Applied Physics*, submitted; and M.I. Patino, Y. Raitses, R.E. Wirz, and B.E. Koel., "Angular, Temperature, and Impurity Effects of Secondary Electron Emission from Ni(110)," *Journal of Applied Physics*, in preparation].

VITA

2009-2010	Undergraduate Student Researcher, Plasma and Space Propulsion Laboratory, UCLA
2010	B.S. (Aerospace Engineering), UCLA
2010-2014	Fellowship, Eugene V. Cota-Robles Fellowship Program, UCLA
2010-2017	Graduate Research Assistant, Mechanical and Aerospace Engineering Department, UCLA
2012	M.S. (Aerospace Engineering), UCLA
2013, 2015-2016	Visiting Graduate Student Researcher, Princeton Plasma Physics Laboratory, Princeton, New Jersey
2013-2015, 2017	Fellowship, NASA CA Space Grant Fellowship
2014-2015	Scholarship, General James H. Doolittle Scholarship
2014-2015	Scholarship, HENAAC Graduate Student Leadership Award
2015	Honor, Edward A. Bouchet Graduate Honor Society
2015-2016	Fellowship, Department of Energy Office of Science Graduate Student Research Program
2016	Fellowship, Dissertation Year Fellowship, UCLA
Spring 2017	Teaching Assistant, MAE C150R/C250R *Rocket Propulsion Systems*, Mechanical and Aerospace Engineering Department, UCLA

PUBLICATIONS

R. Majeski et al, *Compatibility of Lithium Plasma-Facing Surfaces with High Edge Temperatures in the Lithium Tokamak Experiment*, *Physics of Plasmas*, Vol. 24, 056110, 2017.

M.I. Patino, Y. Raitses, and R.E. Wirz, *Secondary Electron Emission from Plasma-Generated Nanostructured Tungsten Fuzz*, *Applied Physics Letters*, Vol. 109, 201602, 2016.

A.M. Capece, M.I. Patino, Y. Raitses, and B.E. Koel, *Secondary Electron Emission from Lithium and Lithium Compounds*, *Applied Physics Letters*, Vol. 109, 011605, 2016.

M.I. Patino, Y. Raitses, B.E. Koel, and R.E. Wirz, *Analysis of Secondary Electron Emission for Conducting Materials Using LEED Optics*, *Journal of Physics D: Applied Physics*, Vol. 48, 195204, 2015.

M.I. Patino, Y. Raitses, B.E. Koel, and R.E. Wirz, *Application of Auger Spectroscopy for Measurement of Secondary Electron Emission from Conducting Material for Electric Propulsion Devices*, in 33rd International Electric Propulsion Conference, Washington, D.C., 2013.

M.I. Patino, L.E. Chu, and R.E. Wirz, *Ion-Neutral Collision Analysis for a Well-Characterized Plasma Experiment*, in 48th Joint Propulsion Conference, Atlanta, GA, 2012.

R.E. Wirz, L.E. Chu, M.I. Patino, H.–S. Mao, and S.J. Araki, *Well-Characterized Plasma Experiments for Validation of Computational Models*, in 32nd International Electric Propulsion Conference, Wiesbaden, Germany, 2011.

CHAPTER 1

Introduction

1.1 Motivations

This effort aims to understand, predict, and ultimately control the interactions of plasma particles (i.e., ions, electrons, and neutral atoms) in the bulk and at the edge of many plasma devices, including electric propulsion and nuclear fusion devices. Such insights may lead to improvements in the performance and lifetime of such plasma devices, thereby enabling space propulsion technologies that extend the capabilities for solar-system exploration and the production of nuclear energy.

1.1.1 Electric Propulsion

Electric propulsion devices are in-space propulsion systems that utilize electric power to produce a high-speed exhaust. A major advantage of these devices over conventional chemical propulsion devices is the higher efficiency (or specific impulse I_{sp}). The propellant mass m_{prop} is related to the initial mass m_0 of a spacecraft and the total change in spacecraft velocity Δv via the rocket equation

$$m_{prop} = m_0[1 - \exp(-\frac{\Delta v}{I_{sp} g_0})] \tag{1.1}$$

where $g_0 = 9.8$ m/s^2. Therefore a spacecraft with electric propulsion requires much less propellant for a mission with given Δv, leading to significant cost savings or the ability for added payload mass (e.g., for science instrumentation). Alternatively, electric propulsion enables missions with larger mission Δv, leading to extended mission lifespans (e.g., for commercial satellites that provide cell-phone communication, broadband internet, and GPS, and for satellites studying the Earth's climate, agricultural resources, and renewable resources) or the ability to reach previously inaccessible targets. The thrust produced from electric propulsion devices is smaller than that produced by chemical systems, but is more accurate, a requirement for high-precision formation flying missions.

Two electric propulsion devices which have been employed for satellites and interplanetary missions include the ion thruster and Hall-effect thruster. In an ion thruster (see Figure 1.1(a)), electrons are produced by a hollow cathode inside the discharge chamber and accelerated to the anode (i.e., the walls of the discharge chamber). Neutral gas injected into the discharge chamber is ionized via electron-impact ionization; a magnetic field is employed to increase the time an electron spends in the chamber (not collected on the walls) and thus to increase ionization. Ions are then extracted and accelerated out of the thruster by a set of high voltage grids. To prevent charge buildup of the spacecraft, an additional source of electrons from a hollow cathode outside of the thruster is used to neutralize the exhausted ions. In a Hall thruster (see Figure 1.1(b)), electrons from an external hollow cathode are ejected and accelerated to the anode at the back face of the Hall thruster discharge channel. Neutral gas injected at the back face is ionized via electron-impact ionization; a radial magnetic field is employed to increase the time an electron spends in the discharge channel and thus to increase ionization. The magnetic field and electron population confined along the field lines, act to set up a voltage drop in the axial direction which accelerates the ions.

In addition to extracting and accelerating ions into the beam for thrust, the grids of an ion thruster must also keep neutrals in the discharge chamber for increased ionization, keep plasma electrons in the discharge, and prevent neutralizing electrons from streaming back into the thruster (see the bottom insert in Figure 1.1(a)). An accelerator grid with an aperture smaller than the aperture of the screen grid is used to keep neutrals in. An

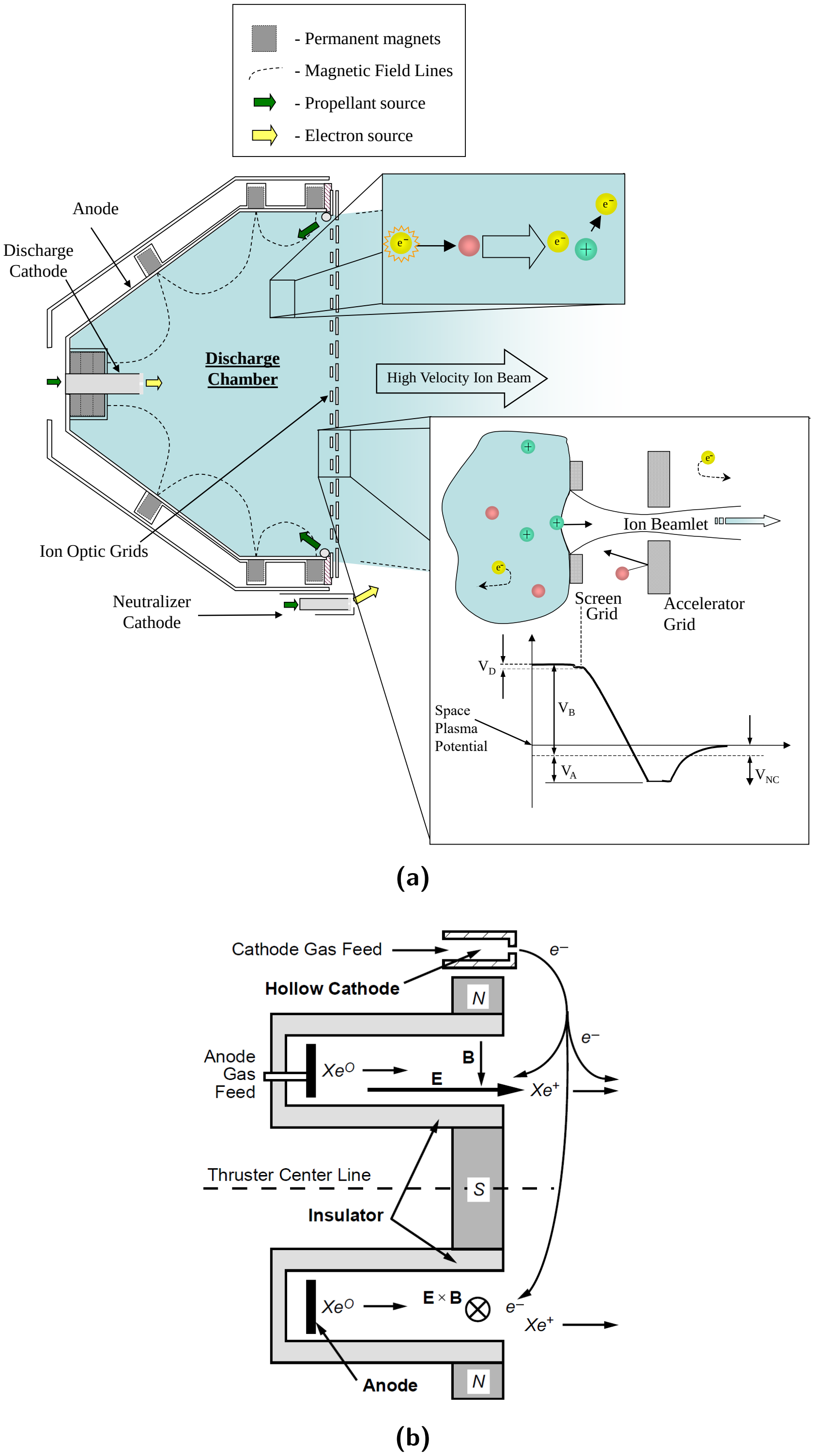

Figure 1.1: (a) Ion and (b) Hall-effect thrusters [1, 2]

accelerator grid with negative potential is used to keep plasma electrons in and neutralizing electrons out. Additionally, a negative potential on the accelerator grid results in larger beam current (and thus thrust), since the maximum current density extracted (due to space-charge effects) between two parallel plate electrodes as given by the Child-Langmuir equation is

$$J_{beam} = \frac{4\epsilon_0}{9}\left(\frac{2e}{m_i}\right)^{1/2}\frac{\Delta V^{3/2}}{l^2} \tag{1.2}$$

where ΔV is the difference in potential on the screen and accelerator grids, l is the gap between the grids, m_i is the ion mass, e is electron charge, and ϵ_0 is the permittivity of free space.

Ion thruster grids do not fully prevent the escape of neutrals. 10-15% of the neutral atoms injected into the discharge chamber escape through the grids unionized (the pressure inside an ion thruster is approximately 1×10^{-4} Torr, while the neutral density is 2.3×10^{17} m^{-3} or pressure is 7.1×10^{-6} Torr just outside of the thruster) [2]. 5% of the neutral atoms injected into an SPT (Hall) thruster leave unionized, and neutral particles densities up to 3×10^{18} m^{-3} from the thruster are calculated outside of the BPT-400 Hall thruster (neutral densities up to 4×10^{18} m^{-3} escaping from the hollow cathode were also calculated) [2, 40].

High-neutral densities outside of the thrusters are undesirable since collisions between the fast beam ions and the slow neutral atoms can lead to the production of charge-exchange ions (to be discussed in Section 2.1.3). The charge exchange ions, which have a small velocity and large scattering angle, are strongly affected by the electric fields established by the thruster grids (i.e., the negatively biased accelerator grid) and impact the downstream thruster grid with energies greater than 200 eV, leading to erosion of the grids (see Figures 1.2-1.3) [3, 4, 41]. Charge exchange ions from ion and Hall thrusters also contribute to unwanted sputtering/erosion of other spacecraft surfaces (e.g., solar arrays) [4]. The typical propellant used is xenon, while beam ions have an energy on the order of 1500 eV for ion thrusters and 300 eV for Hall thrusters [2].

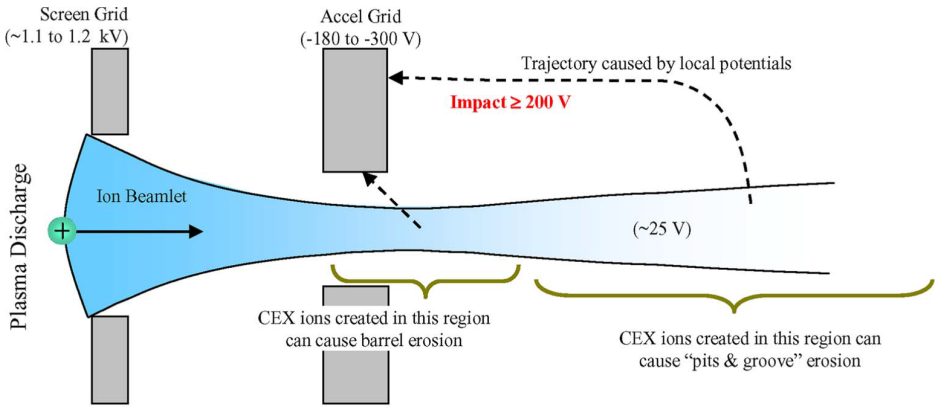

Figure 1.2: Barrel and pits and groove erosion of ion thrusters grids by CEX ions [3].

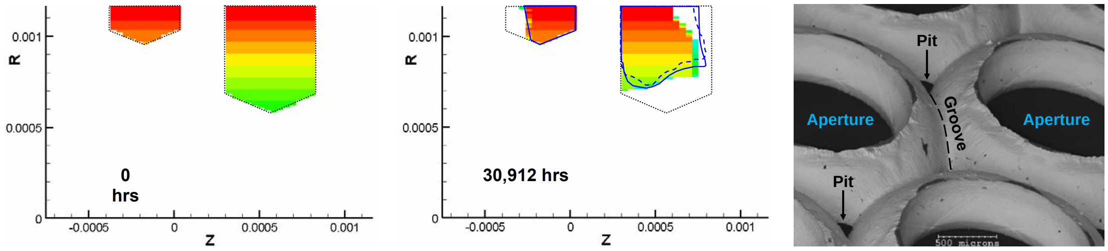

(a) (b) (c)

Figure 1.3: (a-b) Simulation of ion thruster grid erosion. Screen and accelerator grid (a) before thruster operation and (b) after approximately 31,000 hours of operation. (c) Accelerator grid after approximately 31,000 hrs of operation. [4, 5, 6]

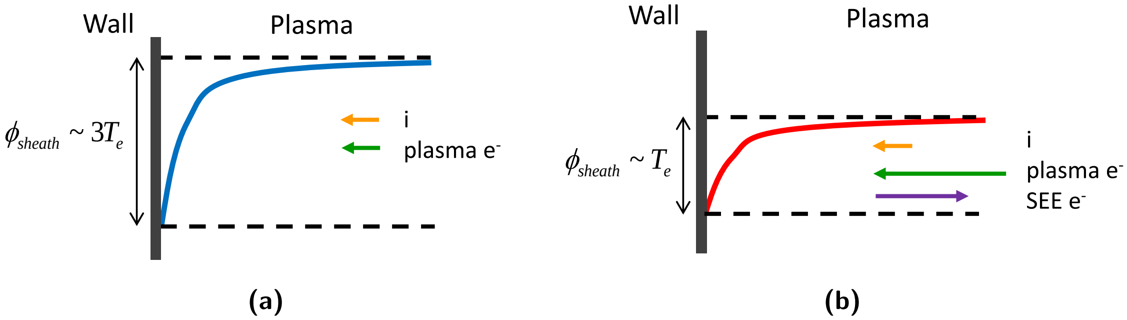

Figure 1.4: Potential structure of the plasma sheath at the plasma-wall interface (a) without secondary electron emission (b) with secondary electron emission.

Additionally, ions, neutrals, and electrons impacting materials can cause electrons to be emitted from the materials. This may cause the material to electrically build up charge and/or can have a significant impact on the sheath and overall behavior of plasmas. Plasma electrons with sufficient energy to overcome the near-wall negative-going sheath potential can impact the wall and produce secondary electrons. This secondary electron emission (SEE) can then reduce the sheath potential ϕ_{sheath} as given by

$$-e\phi_{sheath} = k_b T_e ln\left[\frac{1-\sigma}{\sqrt{2\pi m_e/mi}}\right] \tag{1.3}$$

where σ is the total SEE yield (i.e., flux of emitted electrons to incident electrons), T_e is the plasma electron temperature, m_e and m_i are the electron and ion masses, k_b is Boltzmann's constant, and e is the electron charge [42]. For example, a reduction in the sheath potential from $3T_e$ to T_e is possible (see Figure 1.4).

The reduced sheath potential can then lead to increased plasma electron energy lost to the walls (which are replaced with lower energy secondary electrons from the walls), increased heating of the wall and cooling of the bulk plasma, and significant power losses. From Equation 1.3, these effects become significantly large as the SEE yield approaches 1. Therefore, plasma-facing materials with low SEE are beneficial to maintain higher T_e in the bulk. For example, Ref. [43] found that the max T_e in a Hall thruster was higher when typically-used boron nitride walls were replaced with carbon velvet walls, which have smaller SEE [44, 45].

A similar reduction in sheath potential and increase in plasma cooling can occur due to ion-induced electron emission, although the yields are typically smaller for ion-induced emission than for electron-induced emission.

1.1.2 Fusion Devices

Magnetic fusion devices utilize magnetic fields to confine plasma for nuclear fusion energy. A common reaction utilizing deuterium-tritium plasmas to produce helium and energetic neutrons is

$$ {}_1^2D +_1^3 T \longrightarrow_2^4 He(3.5MeV) + n^0(14.1MeV) \tag{1.4} $$

.

For tokamaks in particular, the plasma is confined in a torus (see Figure 1.5). Plasma is surrounded by the first wall, which shields external components from high energy neutrons and harvests their energy. The divertor is located at the bottom of the tokamak and collects high particle and heat fluxes from energetic He and other impurities. As with the plasma-facing walls of electric propulsion devices, the divertor in a tokamak may also emit secondary electrons due to impact by energetic plasma electrons (electron energies are typically 1-100 eV in the divertor).

Materials typically utilized for the divertor and first wall of tokamaks include graphite, lithium, and tungsten. Lithium improves the plasma performance in tokamaks, including LTX (Lithium Tokamak Experiment) and NSTX (National Spherical Tokamak Experiment) at the Princeton Plasma Physics Laboratory [46], due to its ability to effectively getter hydrogen and impurities that may otherwise be recycled into the plasma. However, lithium oxidizes rapidly in the presence of oxygen or water vapor (i.e., in the vacuum chamber

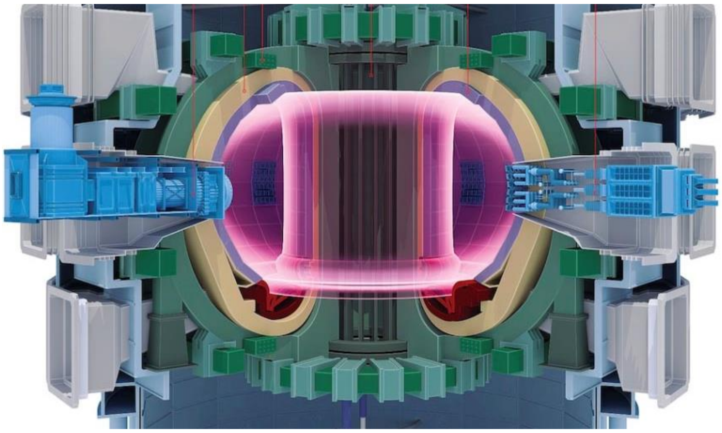

Figure 1.5: Cross-sectional view of a tokamak, including the divertor (shown in red) located at the bottom of the first wall. Plasma is shown in pink [7].

background). For example, a lithium film is 50% oxidized in 10 s when in a background of 1×10^{-6} of O_2 or H_2O [47]. Therefore, impure lithium films are typical in a tokamak [48, 49] where pressures are $10^{-6} - 10^{-5}$ Torr. Additionally, tungsten is the leading candidate for the divertor in ITER due to its high melting temperature and thermal conductivity, and low gas inventory and sputtering yield [50, 51]. However, studies have revealed the growth of nanostructures on the surface of tungsten exposed to helium plasma under conditions which may exists at the divertor [51, 52, 53, 54, 55]. For example, 50 eV, 10^{26} m^{-2} helium ions incident on W will form fuzz/fibers and voids/bubbles for W at 1000-2000 K and >2000 K, respectively. Therefore, SEE yields for oxidized lithium and nanostructured tungsten are required to accurately model the plasma-wall interface of tokamaks which use tungsten and lithium. However, little reliable SEE data exists for materials whose chemical, structural, or architectural properties are modified by exposure to plasma.

1.1.3 Other Applications

SEE is also important for plasma processing since a reduction in the sheath potential can affect ion acceleration in the sheath. Ion energy may be significantly reduced, which in turn may reduce sputtering/erosion/texturing of processed materials. In plasma chemistry, SEE can affect chemical reactions occurring at metallic surfaces. For example, in plasma-enhanced dry-methane reforming (i.e., $CO_2 + CH_4 \rightarrow 2H_2 + 2CO$), emitted secondary electrons can lead to fragmentation of $\mathrm{CO_2}$ and $\mathrm{CH_4}$ as well as charging of nanoparticles used as catalyst. Of particular importance is Ni(110) for its unique ability to chemisorb $\mathrm{CO_2}$ at room temperature.

In particle accelerators (e.g. with positron beams), particle impact and cyclotron radiation incident on the walls can produce electrons that themselves can interact with the wall and lead to SEE. This multipacting effect [56] can create a cloud of electrons that may lead to instabilities in the particle beams and overheating of facility components [57]. For these applications, copper, aluminum, and stainless steel are often used as the wall materials, yet carbon coatings may form on walls with carbon-containing contaminants due to electron irradiation [58].

1.2 Objectives

This objectives of this work are to use well-characterized canonical experiments to improve the understanding of (1) interactions between plasma particles in the plasma bulk, and (2) interactions between plasma particles and plasma-confining walls at the plasma edge. In particular, this work focuses on

- Collisions between ions and neutral atoms, such as those that occur in the exhaust of electric propulsion devices and lead to erosion and reduced lifetime of thruster components (e.g., ion optic grids) or other spacecraft surfaces (e.g., solar panels). The angular distribution of scattered charge-exchange ions are examined for $\mathrm{Xe^+}$-Xe collisions at 1500 eV, conditions characteristic of ion thrusters.
- Secondary electron emission from electric propulsion and fusion relevant materials that may lead to electric charging and significant power losses. Investigated materials include graphite, lithium and lithium oxide, smooth tungsten and nanostrocutured tung-

sten fuzz, and a nickel single crystal.

Such understanding is necessary for self-consistent modeling, and for furthering the development and use of electric propulsion, magnetic confinement fusion, high-power communication, and other plasma applications.

1.3 Overview of Dissertation

A review of the important plasma particle interactions in electric propulsion and magnetic confinement fusion devices is provided in Chapter 2. The dominant collisions between high-energy ions and neutrals in a partially-ionized plasma are discussed, with emphasis on momentum- and charge-exchange collisions. Additionally, electron emission from materials due to ion and electron impact is introduced.

Chapter 3 outlines the effort undertaken by the author to investigate ion-neutral collisions in a simplified, well-characterized experimental domain. The experimental setup is introduced. Results of 1500 eV Xe^+ impacting Xe gas are presented and compared to complementary semi-analytical and fully computational models of the experimental domain. The experimental effort serves to validate the computational models that simulate heavy species collisions, while the computational models served to guide improvements to the experiment.

Electron emission from the confining walls of the experimental domain due to impact by energetic ions and neutrals was found to be important in the measurements of ion-neutral collisions. Results of the ion-induced electron emission from 300-2000 eV Ar^+ and Xe^+ impacting tungsten (used for validation) and stainless steel (used for the walls in the initial collision experiment) are presented in Appendix G.

Chapter 4 summarizes the research effort conducted utilizing existing surface analysis instruments for measuring secondary electron emission properties of conducting materials. The experimental setup and approach are introduced. Measurements of the total SEE yield and of the energy of emitted electrons are presented for graphite, smooth tungsten, tungsten fuzz, oxidized lithium, and single crystal nickel due to electrons incident at 2-1500 eV and 0-78°. Experimental data are compared to values found in the literature and to empirical and computational models. Chapter 5 concludes with significant accomplishments from this study.

CHAPTER 2

Background: Plasma Particle Interactions

In order to understand the physics and predict the performance and lifetime of plasma devices, it is necessary to understand the interactions occurring between the plasma particles (i.e., between neutral atoms, charged ions and electrons) and between the plasma particles and plasma-confining walls. Section 2.1 discusses the dominant collisions occurring in the plasma bulk, while Section 2.2 discusses important physics occurring at the plasma edge. Previous theory and measurements for collisions between xenon ion and neutrals and for electron emission from plasma-facing materials are reviewed, and improvements and extensions of the theory and measurements by this work are discussed.

2.1 Dominant Inter-Particle Collisions in the Plasma Bulk

This section reviews types of collisions between ion and neutrals, which is one main thrust of research conducted by the author. However for completeness, different types of electron-neutral, electron-ion, and less prevailing neutral-neutral, ion-ion, and electron-electron collisions will first be briefly introduced.

2.1.1 Electron-Neutral and Electron-Ion Collisions

Significant collisions between electrons and neutral atoms occur for weakly ionized ($n_n \gg n_i$) and partially ionized ($0.1n_n \geq n_i$) plasmas, where n_n and n_i are neutral and ion densities, respectively. These include elastic collisions in which only kinetic energy is transferred [59].

Inelastic ionization collisions, where a high-energy electron causes the neutral atom to emit additional electrons (i.e., $\tilde{e}+A \longrightarrow 2e+A^+$), are used to create a plasma once initial energetic electrons are produced [59]. Inelastic excitation collisions, where a fast electron causes the atom to be in an excited state (i.e., $\tilde{e}+A \longrightarrow e+A^*$), and the reverse superinelastic collision (i.e., $e + A^* \longrightarrow \tilde{e} + A$) are also possible [59]. Lastly, a fast electron impacting a neutral atom may emit a photon (i.e., $\tilde{e} + A \longrightarrow e + A + h\nu$) in a radiative collision [59]. Here "˜" denotes an energetic particle and " * " denotes an excited particle.

For partially ionized and fully ionized ($n_n \leq n_i$) plasmas, collisions between electrons and ions dominate. These include ionization and excitation collisions as above, recombination (i.e., $e + A^+ \longrightarrow A + h\nu$), and electron scattering from ions due to long-range Coulomb collisions [59].

2.1.2 Neutral-Neutral, Ion-Ion, and Electron-Electron Collisions

Momentum is transferred in ion-ion and electron-electron elastic collisions [59]. Neutral atoms, often treated as hard spheres with variable cross-sections [32, 60, 61, 62, 63], interact with each other through weak intermolecular forces [59]. The following collisions between fast neutral atoms $\tilde{A}$ and slow neutrals are possible.

Momentum-exchange:

$$\tilde{A} + A \longrightarrow \tilde{A} + A \tag{2.1}$$

Ionization:

$$\tilde{A} + A \longrightarrow A + A^+ + e \tag{2.2}$$

Excitation:

$$\tilde{A} + A \longrightarrow A + A^* \tag{2.3}$$

Direct ionization via Equation 2.2 is small, and instead ionization is likely to occur via a two step process where the first step is given by Equation 2.3 and the second step is given by

$$\tilde{A} + A^* \longrightarrow A^+ + A + e \tag{2.4}$$

The fast neutrals are assumed to be ionized in the collision and scattered at small angle in the forward direction. Generated electrons are assumed to scatter isotropically.

Integral cross-sections for neutral-neutral collisions for xenon and other noble gases are discussed in Appendix A.1.

2.1.3 Ion-Neutral Collisions

Collisions between ions and neutral atoms in electric propulsion and plasma processing devices are predominately of two types. In elastic momentum-exchange (MEX) collisions, the energy and momentum are conserved between the incident and target particles (see Figure 2.1(a)):

$$\tilde{A}^+ + A \longrightarrow \tilde{A}^+ + A \tag{2.5}$$

In charge-exchange (CEX) collisions, one or more electrons are also exchanged (see Figure 2.1(b)). A symmetric CEX collision is a CEX collision in which the pre- and post-collision particles are identical, e.g.:

$$\tilde{A}^+ + A \longrightarrow \tilde{A} + A^+ \tag{2.6}$$

Inelastic excitation and ionization collisions between ions and neutral atoms (i.e., $\tilde{A}^+ + A \longrightarrow A^+ + A^+ + e$ and $\tilde{A}^+ + A \longrightarrow A^+ + A^*$, respectively) are possible to a lesser degree [59, 64].

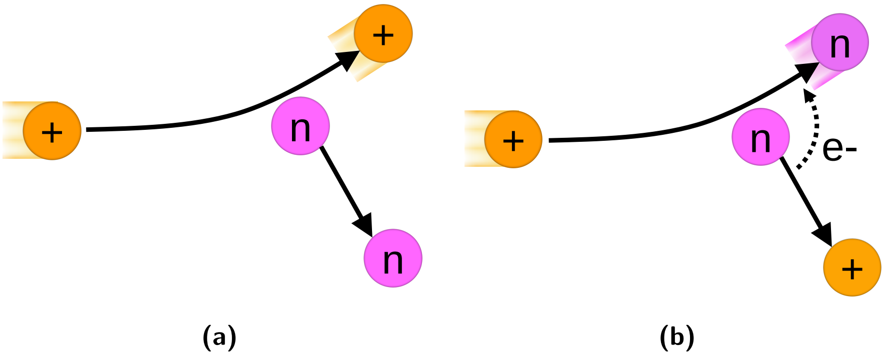

Figure 2.1: (a) Momentum-exchange and (b) charge-exchange collisions between fast ions and stationary neutral atoms. Fast particles are depicted with "comet-tails".

2.1.3.1 Differential Cross-Sections of Ion-Neutral Collisions of Xenon

The differential cross-section $d\sigma/d\Omega$ provides information on the probability of the incoming projectile scattering within a small solid angle $d\Omega$ about θ measured with respect to the initial projectile direction (see Figure 2.2). Therefore, the differential cross-section provides details of the collision dynamics not readily obtainable from the integral cross-section σ. Since the interaction between a particle pair is sensitive to (i) the electronic and nuclear structure of each particle, (ii) the interparticle separation, and (iii) the duration of the interaction, the differential cross-section may vary significantly between different ion and neutral species and for different incident energies. Yet, little previous work has been done on MEX or CEX angle-resolved differential cross-sections for xenon ion-neutral collisions. This contrasts with the integral cross-section which has been extensively investigated experimentally and theoretically for xenon and other noble gas ion-neutral pairs (see Appendix A.1 for a discussion of these integral cross-sections).

Chiu *et al* [41] measured the differential cross-sections for MEX and CEX collisions between Xe^+-Xe at 5 to 20 eV (and between Xe^{2+}-Xe at 10-40eV) in a guided ion beam experiment, whereby a pulsed xenon ion beam was directed to a collision cell filled with a background of xenon neutrals. The unscattered and scattered ions traveled through an octopole before reaching a detector (the octopole ensured complete collection of ions) [41,

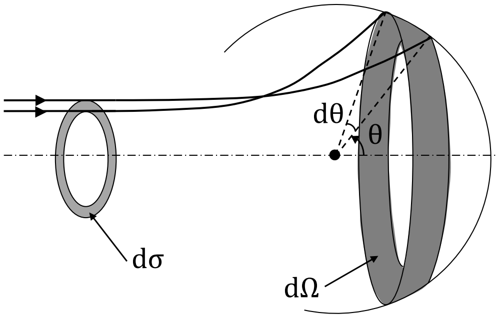

Figure 2.2: Scattering of a particle through a differential solid angle $d\Omega$ (outlined by a range of angles $d\theta$ about θ centered around the collision partner) in a collision with differential cross-section $d\sigma$.

65, 66, 67, 68]. The time of flight data provided information on the velocity of the collision products. From kinematic constraints on energy and momentum, scattering angles and differential cross-sections were obtained. Jones *et al* [69] utilized an energy analyzer with small collection angle and varied its angular position to measure the scattering angle of ions experiencing MEX collisions in a collision cell (the energy analyzer ensured only MEX ions were detected). Measurements were made of differential cross-sections for Xe^+-Xe at 20-340 eV, but only for scattering angles between 1 and 15°. Furthermore, Morris [70] measured the scattering angle of CEX neutrals on a position sensitive detector just downstream of a collision cell, and thus obtained the scattering angle and differential cross-section for CEX ions from conservation of energy and momentum. An incident ion energy of 1100 eV was used, which is characteristic of the energies in the plume of an ion thruster, yet measurements were only made for scattering of CEX ions between 86.4 and 90°.

Chiu *et al* [41] also calculated the MEX and CEX differential cross-sections at 5-30 eV and 270 eV, using the Xe^+-Xe interaction potential derived by Paidarova and Gadea [9] (see Figure 2.3). From the interaction potential, the center of mass deflection function χ may be calculated using Smiths method:

$$\chi(b, E_r) = \pi - 2b \int_{R_m(b,E_r)}^{\infty} \frac{dr}{r^2[1 - b^2/r^2 - V(r)/E_r]^{\frac{1}{2}}} \tag{2.7}$$

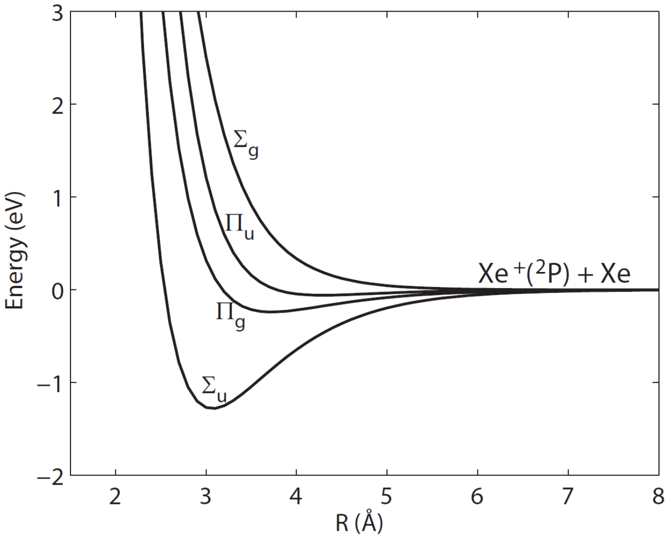

Figure 2.3: Xe^+-Xe spin-orbit free interaction potential [8, 9].

where b is the impact parameter, E_r is the initial kinetic energy in the center of mass frame, r is the interparticle separation, R_m is the distance of closest approach, and $V(r)$ is the sum of the four spin-orbit free potentials (whereby the potentials have been fit to Morse equations). The differential cross-section in the lab frame can then be calculated from

$$\frac{d\sigma}{d\Omega}\Big|_{LAB} = 4cos(\chi/2)\frac{d\sigma}{d\Omega}\Big|_{CM} = 4cos(\chi/2)\Big|\frac{b}{\sin(\chi)(d\chi/db)}\Big|. \tag{2.8}$$

Jones *et al* [69] used the opposite approach to estimate the xenon interaction potentials including spin-orbit from their measurements of MEX differential cross-section. See Ref. [71] for other methods of solving for differential cross-sections from general interaction potentials.

In order to reduce computational time in plasma simulations, Scharfe *et al* [38] developed a logarithmic curve fit of the MEX and CEX differential cross-sections calculated by Chiu *et al* for 300 eV Xe^+-Xe:

$$\frac{d\sigma_{MEX}}{d\Omega} = \begin{cases} (\theta_{MEX})^{A_{MEX}} 10^{B_{MEX}} & 0^\circ \le \theta \le \theta_{MEX} \\ (\theta)^{A_{MEX}} 10^{B_{MEX}} & \theta_{MEX} \le \theta \le 90^\circ \end{cases} \tag{2.9a}$$

$$\frac{d\sigma_{CEX}}{d\Omega} = \begin{cases} (90^\circ - \theta)^{A_{CEX}} 10^{B_{CEX}} & 0^\circ \leq \theta \leq \theta_{CEX} \\ (90^\circ - \theta_{CEX})^{A_{CEX}} 10^{B_{CEX}} & \theta_{CEX} \leq \theta \leq 90^\circ. \end{cases} \tag{2.9b}$$

Here θ is the deflection angle of the incident particle in degrees and θ_{MEX} and θ_{CEX} are cutoff angles established such that the differential cross-sections remain finite. θ_{MEX} and θ_{CEX} are determined such that $\sigma_{CEX} = \int_0^{90^\circ} \frac{d\sigma_{CEX}}{d\Omega} 2\pi \sin\theta d\theta = \sigma_{MEX} = \int_0^{90^\circ} \frac{d\sigma_{MEX}}{d\Omega} 2\pi \sin\theta d\theta$ matches the value of 53.6 Å^2 and 44.1 Å^2 for a 300 eV and 1500 eV ion beam, respectively, as determined experimentally by Miller *et al* [72]. Values for the coefficients in Equations 2.9a and 2.9b at 300 eV were corrected by Giuliano and Boyd [10]. Additionally, Giuliano and Boyd extended the expressions for differential cross-sections to 1500 eV in collaboration with the experimental work presented herein. Coefficients for 300 eV and 1500 eV are reproduced in Table 2.1.

The differential cross-sections for MEX and CEX ions produced in 1500 eV Xe^+-Xe collisions are plotted in Figure 2.4. Note that the differential cross-section for a CEX neutral is the same as for a MEX ion since CEX and MEX collisions are identical except that in the former case an electron is also transferred; therefore, both a slow ion and fast neutral are generated in a CEX collision. The probabilities that an ion will be scattered below a given angle θ in MEX and CEX collisions are given by

$$P_{\theta,MEX} = \frac{1}{\sigma_{MEX}} \int_0^{\theta} \frac{d\sigma_{MEX}}{d\Omega} 2\pi \sin\theta d\theta \tag{2.10a}$$

$$P_{\theta,CEX} = \frac{1}{\sigma_{CEX}} \int_0^{\theta} \frac{d\sigma_{CEX}}{d\Omega} 2\pi \sin\theta d\theta \tag{2.10b}$$

From Figure 2.4, ions experiencing MEX collisions have a large probability of small angle scattering and small probability of large angle scattering. The opposite is true for CEX ions. In fact, the most probable scattering angles are 2.3° for a MEX ion and 88.1° for a CEX ion.

Table 2.1: Coefficients for Differential Cross-Sections of Xe$^+$-Xe at 300 eV [38] and 1500 eV [10]

	300 eV	1500 eV
A_{MEX}	-2.02	-2.502
A_{CEX}	-1.098	-1.380
B_{MEX}	3.24	3.508
B_{CEX}	1.53	1.610
θ_{MEX}	3.53E-5°	0.114°
θ_{CEX}	(90-0.00137)°	(90-0.061)°

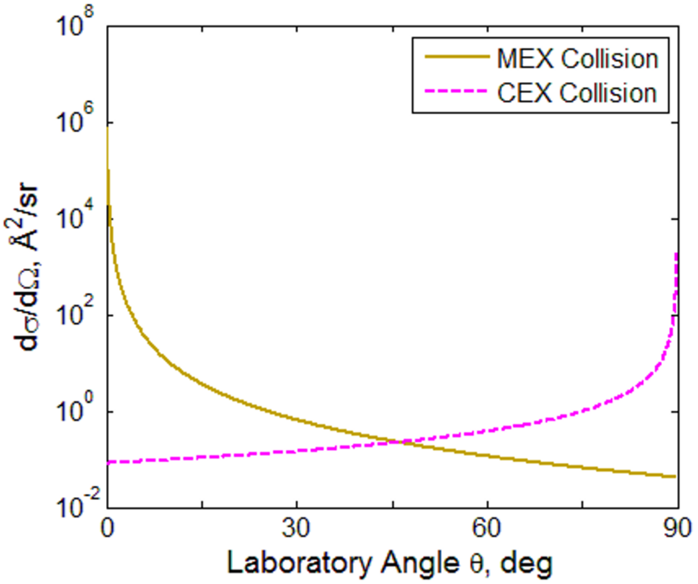

Figure 2.4: CEX and MEX differential cross-sections for Xe$^+$-Xe at 1500 eV [10].

Since there is a strong bias towards very small and very large angle scattering, it would be incorrect to assume an arbitrary scattering distribution, such as an isotropic distribution (especially for MEX ions). Therefore, to accurately include ion-neutral collisions in plasma models such as DC-ION [73] for ion thrusters and HPHall [74] for Hall thrusters, the differential cross-section must be measured or calculated under conditions of interest (e.g., for particular particle species and incident energy). Katz *et al* [75], Boyd and Dressler [76], and Mikellides *et al* [40] used Equations 2.7 and 2.8 with interaction potentials for the Xe^+-Xe differential cross-section at 300 eV in Hall thruster simulations. Yet as previously discussed, differential cross-section have only been measured or calculated for a full range of scattering angles for Xe^+ at incident energies below 340 eV. To analyze ion-neutral collisions at ion-thruster-relevant conditions, we developed a test cell to measure MEX and CEX collisions between 1500 eV xenon ions and neutrals. Analytical and computational models were coupled with experiment to inform theory (i.e., to extend Equations 2.9a and 2.9b of the differential cross-section to 1500 eV). Additionally, the precision measurements from the simple, well-characterized experiment serve as canonical data by which plasma models may be validated.

2.2 Interactions of Plasma Particles with the Plasma Confining Walls

Important ion-wall and electron-wall interactions, also investigated by the author, are discussed in Section 2.2.1 and 2.2.2, respectively.

2.2.1 Ion-Induced Electron Emission

Ions incident on a surface may cause the emission of electrons from the material (termed ion-induced electron emission, IIEE). For low energy ions (i.e., below approximately 105 m/s), the electrons are emitted by potential emission, where incident ions are Auger neutralized outside the material surface and the energy provided by the process releases a free electron in the material bulk [77]. Hence two electrons are emitted per ion in Auger neutralization, requiring an ion energy of twice the work function of the material and resulting in a maximum electron energy dependent on the ion neutralization energy and material work function (i.e., $E_{IIEE}^{max} = E_i - 2\phi_S$). Ions may also be resonance neutralized and deexcited by the Auger process.

For higher energy ions, kinetic emission dominates, where the transfer of kinetic energy leads to electrons being emitted. This can occur by excitation of the target atom (valence band and inner shell electrons), ionization of the target atom (valence band electrons), Auger decay of a target atom inner shell vacancy, excitation of surface and bulk plasmons and their decay with creation of an electron-hole pair, or cascade excitation and ionization events in the material bulk by generated electrons [77]. After diffusing to the surface and losing energy along the way by collisions, the electrons able to overcome the surface potential are emitted with a small energy (i.e., maximum of 15-20 eV) [78]. High energy neutral atoms impacting materials can also lead to kinetic emission (emission due to both ions and neutrals is termed particle-induced electron emission, PIEE).

Previous theoretical and experimental work has led to equations for the dependence of the potential and kinetic emission yields on incident energy [33, 77, 79, 80, 81] and angle, and the energy [82] and angular distribution of emitted electrons.

2.2.1.1 IIEE from Plasma Facing Materials due to Noble Gas Ions

In order to predict the effect of materials utilized in electric propulsion, plasma processing, and dusty plasma devices and to determine suitable materials for these plasma devices, it is necessary to better characterize their IIEE properties. For example, graphite, molybdenum, and tungsten are utilized in ion thrusters for grids and discharge cathodes; graphite is used for walls in Hall thrusters; and various materials are utilized in plasma processing [131]. Table 2.2 summarizes previous efforts to investigate IIEE from such conducting materials due

Table 2.2: Previous Investigations of IIEE from Conducting Materials by Nobel Gas Ions

Surface	Incident Energy, keV		
	Ar^+	Kr^+	Xe^+
C	0.1-5 [83] 0.5-13 [85] 1-20 [87] 10-30[88] 30 [89, 84] 52-835 [86]	25 [84]	0.1-5 [83] 80-100 [86]
Al	0.6-10 [90] 1-14 [92] 1.5-30 [77, 93] 3-20 [87] 3.5-62 [96] 10-50 [78, 94] 10-320 [97] 20-200 [99]		1-10 [91] 3-9.5 [93] 10-50 [94] 10-130 [95] 10-350 [97] 40-320 [98]
Fe	10-40 [100] 15-100 [101]	10-40 [100]	60 [101]
Stainless	0.125-0.37 [102] 1-5 [87] 15, 26 [103] 30 [104]		15-26 [103] 120 [95]
Ni	1-10 [90] 1-50 [106]	17-25 [105]	0.5-10 [91] 50 [107] 80 [78]
Cu	0.5-10 [90] 10-40 [100] 15-100 [101] 20 [109, 110] 25-30 [84, 111, 112] 25-400 [108] 40-430 [97] 50 [113] 52-200 [99]	0.5-10 [90] 10-40 [100] 15-100 [101] 25-30 [84] 25-400 [108] 40-380 [97]	0.5-10 [90] 15-100 [101] 25-400 [108] 40-430 [97] 80 [95]
Mo	<1 [114] 0.05-0.4 [115] 0.1-2.5 [116, 117] 0.5-10 [90, 91] 0.7-65 [118] 1-20 [87, 119] 10-40 [100] 20-120 [120] 30 [84]	<1 [114] 25 [84] 10-40 [100]	<1 [114] 0.5-10 [90, 91] 1-40 [118]
W	<1 [34] 0.01-0.3 [37] 0.3-4 [123] 0.4-18 [125] 0.8-6 [126] 2-20 [127] 10-40 [100] 20-900 [99] 30 [84] 30-140 [124]	0.4-20.4 [121] 10-40 [100] 18-65 [124] 25 [84]	<1 [34] 0.5-8 [122] 50 [107]
Au	0.1-15 [128] 1-30 [77] 52-200 [99]		0.1-13 [128, 122] 5-30 [118] 10-130 [95] 20-60 [129] 50 [107] 80 [130]

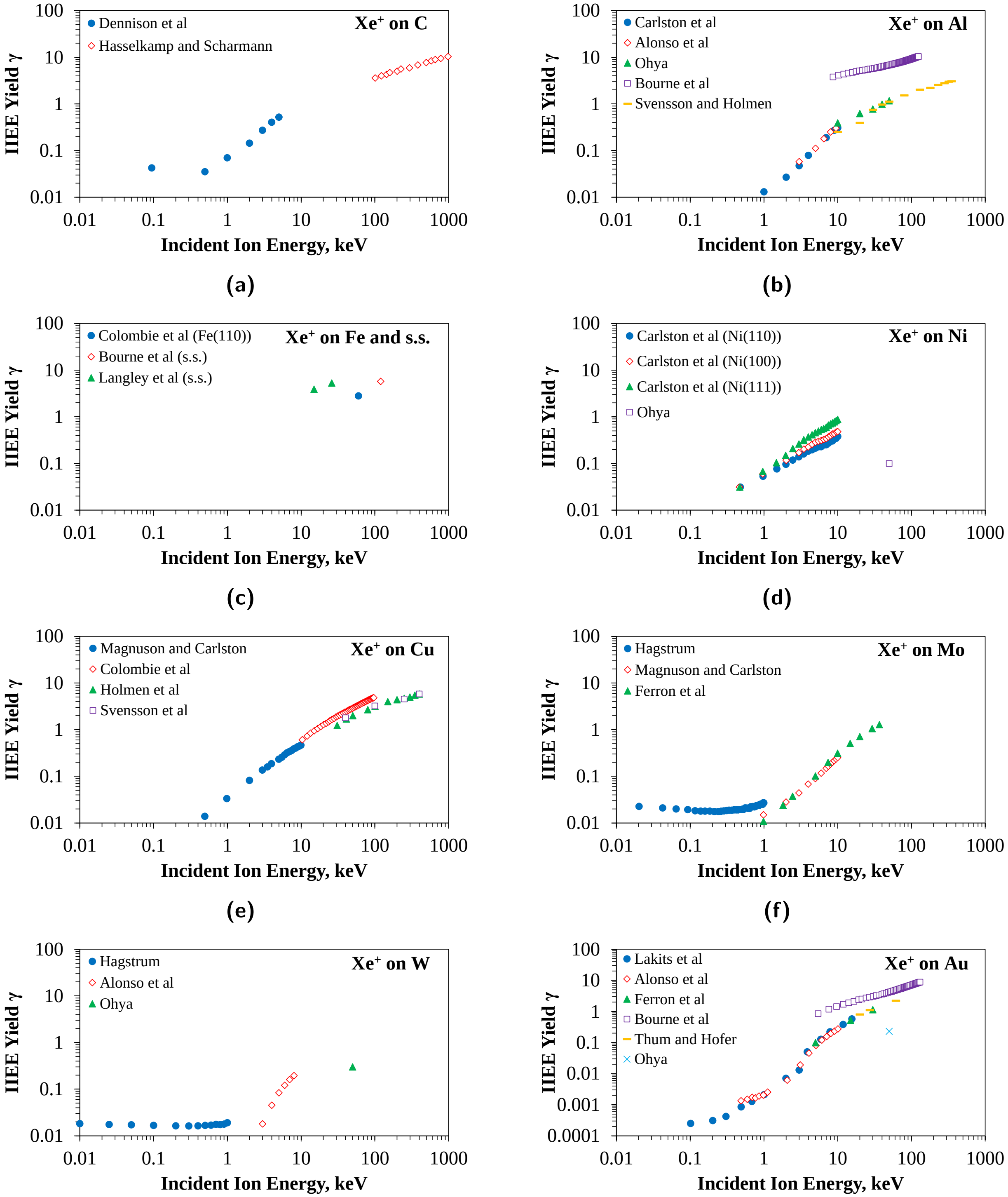

(a)

(b)

(c)

(d)

(e)

(f)

(g)

(h)

Figure 2.5: Ion-induced electron emission from various conducting materials due to incident xenon ions. Data is taken from references found in Table 2.2.

to noble gas ions utilized in these applications; note that the table is not fully comprehensive. Figure 2.5 shows the IIEE from these materials for Xe$^+$ impacting at a range of energies.

As can be seen in Figure 2.5, the IIEE yields are large at high incident energies (i.e., above approximately 1 keV) where kinetic emission dominates. However, yields are small and nearly constant at low energies where potential emission dominates. Yet, few measurements have been made at these low energies, particularly for stainless steel. Therefore, IIEE yields were measured by the author for Xe$^+$ incident on stainless steel; measurements of Xe$^+$ incident on tungsten were made for validation of the experimental setup and approach. Measurements of IIEE yields were made using approaches similar to SEE yields; monoenergetic ion beams are directed to the material under consideration and the incident ion and emitted electron currents are measured to calculate IIEE yield $\gamma = I_e/Ii$. Results of yields measured by the author are presented in Appendix G.

Additionally, materials from Figure 2.5 that are known to have low IIEE (i.e., gold and graphite) were utilized in all other ion experiments to minimize error.

2.2.2 Secondary Electron Emission

Secondary electrons are classified into three different groups based on their energy E_{SE} (see Figures 2.6-2.7) [15, 132, 133, 134, 135]. Elastically reflected electrons are primary electrons that are reflected by atoms at the surface of the material and leave the material with their initial incident energy E_{PE}. Inelastically reflected electrons with energies between 50 eV and E_{PE} are primary electrons that have undergone inelastic collisions and have lost energy due to collisions with core and continuous-band electrons and from phonon and plasmon generation [15, 133, 134, 135]. Note that Auger electrons, although a product of the Auger process, are often grouped with inelastically reflected electrons since they are in the 50 eV to E_{PE} energy range [135]. True secondary electrons are electrons originally from within the material that are ejected after ionization or excitation of atoms due to impact by primary or reflected electrons and after overcoming the material work function. Since there is no clear

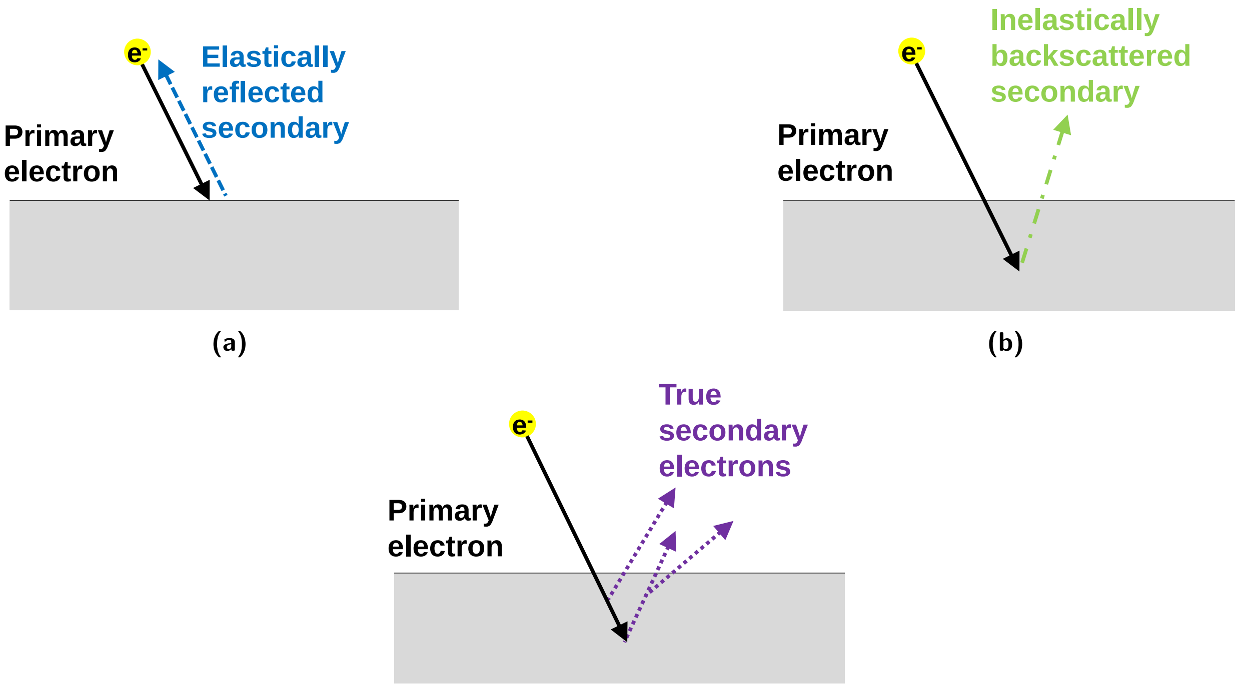

(a) (b) (c)

Figure 2.6: Types of secondary electrons emitted from materials (a) elastically reflected, (b) inelastically reflected, and (c) true secondary electrons [11].

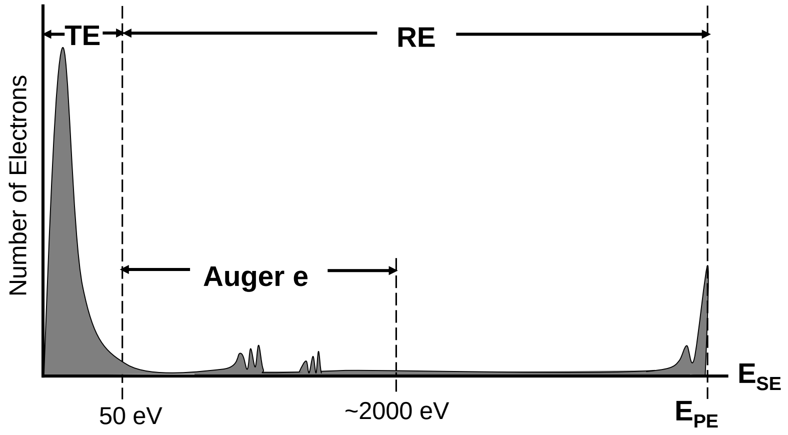

Figure 2.7: Representative energy distribution of secondary electrons emitted from materials. PE = primary electron, SE = secondary electron, TE = true secondary electron, RE = reflected electron

separation of inelastically reflected and true secondary electrons in the energy distribution, by convention all secondary electrons with energies below 50 eV that are not part of the discernible elastic peak are considered true secondaries [135].

2.2.2.1 SEE from Plasma Facing Materials

Previous investigations into SEE has led to many empirical equations for the dependence of the total SEE yield σ (i.e., ratio of the number of electrons emitted from the material to the number of incident electrons) with incident energy [12, 13, 17, 57, 135, 136, 137, 138, 139] and angle [136, 137] with respect to the surface, as well as semi-empirical equations for the energy, angular, and spatial distribution [136] of the emitted electrons. Particular attention was made to investigate materials that were clean, smooth, conducting, and polycrystalline. Measurements were made by exposing a sample of the material to a monoenergetic electron beam of known current I_{PE} and measuring (i) the sample current I_s [140, 141] or (ii) the current on a collecting electrode surrounding the sample I_{coll} [16, 139]. The total yield σ is then

$$\sigma = \frac{I_{SEE}}{I_{PE}} = \frac{I_{PE} - (I_{PE} - I_{SEE})}{I_{PE}} = \frac{I_{PE} - (I_s)}{I_{PE}} = 1 - \frac{I_s}{I_{PE}} \tag{2.11a}$$

$$\sigma = \frac{I_{SEE}}{I_{PE}} = \frac{I_{coll}}{I_{PE}} \tag{2.11b}$$

In addition, the contributions from the elastically reflected, inelastically reflected, and true secondary electrons were measured by inserting a hemispherical electrode in front of a hemispherical collector and applying a retarding potential to the electrode to separate out the true secondary electrons [12, 13, 142, 143]. Note that plasmas and magnetic fields complicate SEE measurements and are avoided whenever possible.

In particular, there have been many previous measurements of the SEE yield from graphite for electrons incident at 2-20,000 eV and 0° [12, 13, 14, 15, 16, 21, 26, 140, 141, 142, 143, 144, 145, 146, 147, 148, 149, 150]. In contrast, few measurements exist of the energy distribution of emitted secondary electrons; measurements have only been made for primary electrons at 262 eV [19] and 100 eV [18]. This work extends the measurements of the energy distribution for graphite to a larger range of incident energies from 50 to 500 eV.

SEE yields of Li were previously measured by Bruining and de Boer [22, 151] for pure and impure Li surfaces at electron energies ranging from 20 to 900 eV and inferred by Oyarzabal *et al* [152, 153] from I-V curves of a Li target immersed in He and Ar plasmas for energies up to 120 eV. The surface composition was not measured in either study, and no data exist on the impurity level of these surfaces. However,the yield results varied considerably between the "pure" and "impure" surfaces. For example, the maximum yields were measured as 0.56 and 4.2 for pure and impure Li, respectively [22]. These represent the lower and upper bounds of SEE coefficients for Li. However, no results of Li surfaces containing a mixture of Li metal and oxide, which may be more realistic of the surfaces in tokamaks, are available. In the work presented herein, first-ever measurements of the SEE yield of mixed Li surfaces are presented for primary electron energies of 25-600 eV. In order to measure the yield as a function of chemical composition, we perform *in-situ* measurements of surfaces exposed to controlled amounts of O_2 and H_2O.

Previous studies of SEE from smooth tungsten have determined SEE yields for electrons incident at 0° [21, 23, 24, 25, 26, 27, 153, 154, 155, 156, 157, 158] and 45° [27]. Takamura *et al* measured the floating potential of a W surface exposed to helium plasma [159]. They found a deepening of the floating potential as nanostructures formed on the W surface, and deduced that the reduction in floating potential was due to a reduction in SEE from a W surface with nanostructures. However, no prior attempts to directly measure SEE for W fuzz have been made to confirm this hypothesis. This work provides the first-ever direct measurements of the SEE yield from nanostructured tungsten fuzz at 5 to 1000 eV and 0 to 60°, important for fusion devices.

Additionally, SEE yields have been measured for nm to mm-sized soot particles [132]; silver with μm-sized pores [160, 161]; structured carbon and copper with μm-sized fibers/dendrites [44, 162, 163, 164]; copper, aluminum, and stainless steel triangular and rectangular grooves [165, 166]; and carbon and silver with μm-sized roughness [167]. Reductions in SEE yields were measured from these textured surfaces over their smooth counterparts. In contrast to these other textured surfaces which may be eroded away by ion sputtering when exposed to plasmas, tungsten fuzz is naturally generated when heated tungsten is exposed to helium plasma.

Many previous authors have also investigated SEE from clean polycrystalline Ni at room temperature [21, 22, 26, 154, 168]. These authors compared their results to as-received Ni, likely covered with C and O impurities. Additionally, Rao [169] investigated SEE from hydrogen exposed polycrystalline Ni, and found that the total SEE yield increased by more than 50%. In contrast, little previous work has investigated SEE from nickel single crystals; SEE yields from Ni(110) have only been measured by Ref. [28] for a clean surface at room temperature and primary electrons at 50° and 78°. This work provides unique measurements of the SEE yield from clean Ni(110) for up to 1.5 keV, 0 to 78°, and 300 to 600 K. Furthermore, SEE yields of Ni(110) exposed to deuterium ions and to carbon monoxide residual gas are presented and compared to clean Ni(110).

Previously measured SEE yields and energy distributions are plotted in Chapter 4 when comparing to this work.

2.3 Summary

Momentum-exchange (MEX) and charge-exchange (CEX) collisions which are the dominant type of ion-neutral collisions in electric propulsion devices were discussed. Particular attention was made for xenon ion-neutral collisions and its characterization with the differential cross-section. Additionally, ion-induced electron emission (IIEE) due to ions impacting materials was reviewed. For low energy incident ions, the process occurs via potential emission (PE), while kinetic emission (KE) is dominant for high energy ions. Particle-induced electron emission (PIEE) includes both ion-induced electron emission and electron emission due to energetic neutral atoms impacting materials. Finally, the three types of secondary electron emission (SEE) were discussed.

CHAPTER 3

Ion-Neutral Collisions

This chapter outlines the research performed to examine ion-neutral collisions, particular momentum-exchange and charge-exchange collisions between xenon ions and neutrals at 1500 eV, important for ion thrusters but for which there exists little data. Section 3.1 introduces the experimental facility, with full disclosure of all experimental details (e.g., facility dimensions and materials). Results from the collision experiment are presented in Section 3.2. Semi-analytical and fully computational models developed to couple with the experiment are described in Section 3.3, and results from these models are compared to experimental data to provide information on the collision dynamics. Main conclusions are summarized in Section 3.4.

3.1 Experimental Setup: Ion Beam Facility

Ion-neutral MEX and CEX collisions are investigated in a simple, well-characterized experiment in which a mono-energetic ion beam is attenuated through a collision cell (i.e., test cell) filled with a neutral target gas. The ion beam current entering the test cell is approximately 7 nA, such that 2x10^5 ions are in the experiment at a given time. Ionization from ion-neutral collisions is less than 10^{-5}% such that Coulomb collisions may be ignored (especially in the single collision regime) [8, 170]. Additionally, the electric potential due to beam ions is less than 0.01 eV such that space-charge effects are negligible [32, 171]. Important plasma parameters are calculated for conditions in the test cell in Table 3.1. Note from the ion Debye length that there is no collective plasma in the test cell.

Table 3.1: Plasma Parameters Inside the Test Cell

Min Neutral Density	$3\text{x}10^{17}$ m^{-3}
Max Neutral Density	$9\text{x}10^{19}$ m^{-3}
Ion Density	$7\text{x}10^{10}$ m^{-3}
Space Charge Potential	0.01 eV
Ion Debye Length	1.1 m

The facility used to produce, condition, and characterize the ion beam is described in Section 3.1.1. The test cell which makes up the experimental domain is described in Section 3.1.2.

3.1.1 Ion Beam Operation

The ion beam facility is located at the Jet Propulsion Laboratory (JPL). It is designed to examine a mono-energetic xenon ion beam accelerated into a xenon target gas [172, 173]. The facility is divided into three chambers - the source, filter, and test chambers (see Figure 3.1(a)). The ion beam is created in the source chamber, filtered in the filter chamber, and directed into the pressurized test cell in the test chamber. The three stainless steel chambers are separated by plates with 3.2 mm diameter apertures and are at 5° with respect to each other (see Figure 3.1(b)), which reduce the amount of neutrals from the source chamber that reach the test chamber. The filter and source chambers utilize CTI-8 cryogenic pumps to reach base pressures of $1\text{x}10^{-8}$ Torr and $2\text{x}10^{-8}$ Torr, respectively, while the source chamber utilizes a NRC diffusion pump to reach a base pressure of $5\text{x}10^{-8}$ Torr and working pressure of $5\text{x}10^{-6}$ Torr. The coordinate system of each chamber is taken to be such that the z-direction is along the chamber longitudinal axis (i.e., in the ion beam direction), the x-direction is in the horizontal direction, and the y-axis is in the vertical direction.

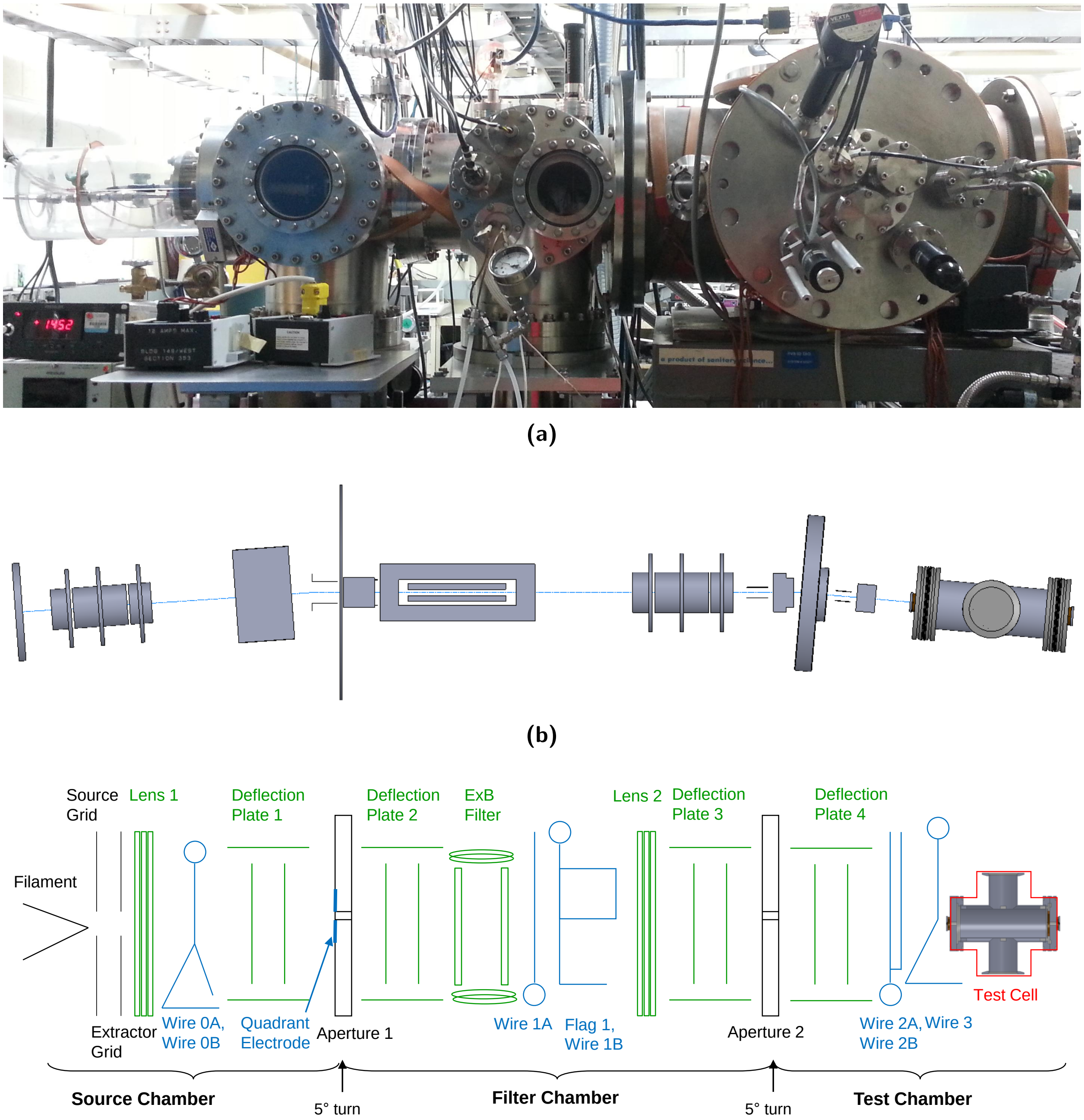
(a) (b) (c)

Figure 3.1: (a) Side view of the JPL ion beam facility with source, filter, and test chambers (from left to right). (b) The top view and (c) schematic showing beam conditioning devices (in green) and diagnostics (in blue). The blue line in (b) shows an optimal beam trajectory.

3.1.1.1 Plasma Source and Ion Optics

The ion beam is created in the source chamber by thermionic emission of a thoriated iridium filament to produce electrons (I_{fil} = 6A, V_{fil} = 3 V). The electrons are then accelerated to the positively biased anode held at 60 V with respect to the cathode. The high energy electrons ionize the neutral background gas via electron impact ionization to produce positive ions. Twelve stacks of samarium cobalt magnets are placed azimuthally around the plasma source to create a uniform magnetic field in the plasma source, which keeps electrons and ions confined in the axial direction.

A pair of differentially biased grids is used to extract and accelerate ions; note that the grids in this setup have a single hole through which ions are extracted. The source grid is set to the energy of the ions required, which is 1500 V for this work (a voltage typically used in ion thrusters). The extractor grid is set such that a beam of large current with small divergence is produced at the exit of the ion source. CEX2D, a computational model of ion optics developed by JPL, was used to determine initial settings for the extractor, but final settings were determined experimentally.

Lambda LK 350-FM and Hewlett-Packard 6205-C power supplies were used for the filament and anode, respectively, in conjunction with a in-house feedback control system. Fluke 412B high voltage power supplies were used for the source and extractor grids. An Apex 0.1 sccm range flow controller was used to leak in 0.020-0.035 sccm of 99.999% pure Xe into the plasma source.

3.1.1.2 Beam Conditioning Devices

Devices located throughout the three chambers are used to condition the ion beam prior to entrance into the test cell (see Figure 3.1(c) and Figure B.1). Values for electrostatic settings are found in Table C.1.

Two Einzel electrostatic lenses (i.e., lens 1 and lens 2) are located upstream of each chamber aperture and are used to focus the ion beam. Each Einzel lens consists of three biasable cylindrical electrodes. Ions are focused by the electric field structure generated by the potential difference on the closely-spaced cylinders. During operation, the two outer cylinders are kept grounded and only the center cylinder is biased such that the energy of the beam ions at the exit of the lens is the same as at the entrance of the lens. Computational models of the electrostatic fields and charged particle tracking developed using COMSOL Multiphysics and Field Precision software were used to determine initial settings for the lenses. However, lenses were ultimately set such that a large fraction of the beam passed through each aperture, while avoiding beam cross-over. Fluke 415B and Bertan 205A-205R power supplies were used for the lenses.

Four sets of biased vertical and horizontal plates (i.e. deflection plates 1-4) powered by a Lambda LQD-425 are found on each side of each chamber aperture to steer the beam through the apertures and into the test cell. The plates are differentially biased to $\pm V_{plate}$ such that an electric field is generated transverse to the ion beam (to deflect the beam left/right and up/down), but no electric field component exists in the longitudinal direction at the center of the deflection plates (to add/remove energy to the beam ions). Estimates of $\pm V_{plate}$ required can be determined analytically. For ions of mass m_i, charge Ze, and produced at V_{source} initially traveling in the axial direction,

$$\frac{1}{2} m_i v_{i,\parallel}^2 = ZeV_{source} \tag{3.1}$$

Hence the time it takes for ions to traverse the length of the deflection plates l_{plate} is

$$t = \frac{l_{plate}}{v_{i,\parallel}} = l_{plate}\sqrt{\frac{m_i}{2ZeV_{source}}} \tag{3.2}$$

The acceleration in the transverse direction due to the electric field established by the de-

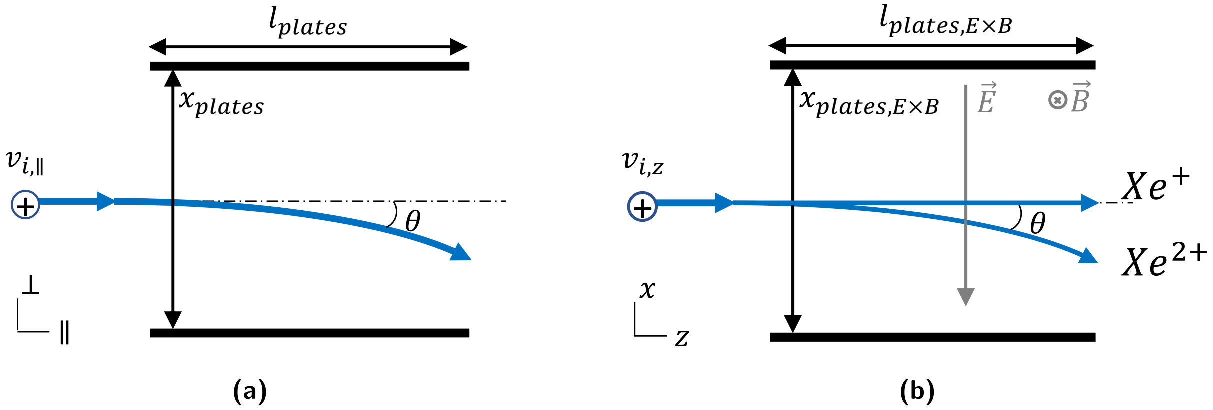

Figure 3.2: Ion deflection in the (a) deflection plates and (b) E×B filter.

flection plates separated by x_{plate} is given by

$$a_\perp = \frac{F_\perp}{m_i} = \frac{ZeE_\perp}{m_i} = \frac{ZeV_{plate}/x_{plate}}{m_i} \tag{3.3}$$

Therefore the angle at which the beam ions are deflected is

$$\theta = \tan^{-1}\left(\frac{v_{i,\perp}}{v_{i,\parallel}}\right) = \tan^{-1}\left(\frac{a_\perp t}{v_{i,\parallel}}\right) = \tan^{-1}\left(\frac{l_{plate}V_{plate}}{2x_{plate}V_{source}}\right) \tag{3.4}$$

From Equation 3.4, the turning angle is independent of charge Z, and other means are required to separate singly-charged and doubly-charged ions within the beam and created at the source.

A Colutron 600B E×B filter is used to select particles of the desired velocity and charge-to-mass ratio. Electromagnets powered by a Lambda LK 351-FM power supply are used to generate a magnetic field in the y-direction B_y, and deflect ions in the x-direction.

$$\vec{F}_B = Ze(\vec{v}_i \times \vec{B}) \rightarrow F_{B,x} = Zev_{i,z}B_y \tag{3.5}$$

Vertical differentially-biased plates powered by a Lambda LLS-4300 power supply is used to establish an electric field in the x-direction E_x, and deflect ions back.

$$F_{E,x} = ZeE_x = Ze\frac{V_{plates,E\times B}}{x_{plates,E\times B}} \tag{3.6}$$

where $V_{plates,E\times B}$ and $x_{plates,E\times B}$ are the potential difference and separation between the plates in the E×B filter. Only ions with a particular velocity (or charge-to-mass ratio) are deflected completely back along the original beam path such that they pass through the deflection plates and ultimately the chamber aperture into the test chamber:

$$F_{E,x} = F_{B,x} \rightarrow Zev_{i,z}B_y = ZeE_x \rightarrow v_{i,z} = \frac{E_x}{B_x} = \frac{V_{plates,E\times B}}{x_{plates,E\times B}B_y} \tag{3.7}$$

From Equation 3.1, this condition is given by

$$\frac{Z}{m_i} = \frac{v_{i,z}^2}{2eV_{source}} = \frac{1}{2eV_{source}}\left(\frac{V_{plates,E\times B}}{x_{plates,E\times B}B_y}\right)^2 \tag{3.8}$$

3.1.1.3 Beam Diagnostics

Various current diagnostics are located upstream of the test cell. These include a current collecting flag electrode, scanning wire electrodes, and a set of quadrature electrodes (see Figure 3.1(c)). The quadratures electrodes are located at the first aperture and measure how the beam current is split between four adjacent electrodes (i.e., top, bottom, left, and right) that surround the aperture. The flag (i.e., flag 1) is located in the filter chamber and measures total beam current. The scanning wires measure the current density across the beam to produce a beam profile. They are located in the source chamber downstream of lens 1 (i.e., wires 0A and 0B), in the filter chamber downstream of the E×B filter (i.e, wires 1A and 1B), and in the test chamber approximately 40 and 50 mm upstream of the test cell (i.e., wires 2A, 2B, and 3). Wires 0A, 0B, 1B, and 3 scan the beam vertically, whiles wires 1A, 2A, and 2B scan the beam horizontally; all use Rapidsyn DMA-64 stepper motors.

Wire 0A is 0.635 mm in diameter, while the remaining wires are 0.5 mm in diameter; all are made of tungsten. Keithley 485 picoammeters are used to measure the current on the flag and scanning wires, while a Keithley 2400 source meter and Keithley 7001 switch system are used to measure the current on the quadrature electrodes. Labview programs are written to control all stages and record all currents.

The beam profiles are used to ensure a centered, narrow beam with maximum current throughout the facility. Of particular importance is the beam profile and position at the entrance to the E×B filter since Equation 3.8 is only valid for a particular $v_{i,z}$, which must be kept constant for constant $B_y, V_{plates,E\times B}$, and $x_{plates,E\times B}$. Hence no acceleration or deceleration of the ions should occur within the E×B filter, a condition which is only met at the center of the filter. Additionally important is the beam profile at the entrance to the test cell, which is used as an input for model validation efforts. Example current profiles characterizing the ion beam throughout the facility are provided in Appendix C.

3.1.2 Collision Test Cell

The test cell was designed to provide a simple computational domain consisting of cylindrical electrodes (i.e, the inner cylinders) and end plate electrodes (i.e., the exit plate and front plate; see Figure 3.3). The ion beam is collimated and beam ions enter the test cell through the front aperture, collimator plate, and front plate. When the test cell is not pressurized, the beam ions traverse the length of the test cell, exit the test cell through a hole in the exit plate (i.e., the exit orifice), and are collected on the back aperture or collector plate electrodes placed approximately 20 cm downstream. When the test cell is pressurized with neutral gas, the beam ions may experience MEX and CEX collisions with slow neutral atoms and scatter to the walls of the test cell (i.e., the exit plate, inner cylinders, and front plate). Beam ions that do not experience a collision or are scattered at very small angles still reach the back aperture and collector plate. To examine heavy species interactions, the ion beam is held at constant conditions while the neutral pressure inside the test cell is incrementally

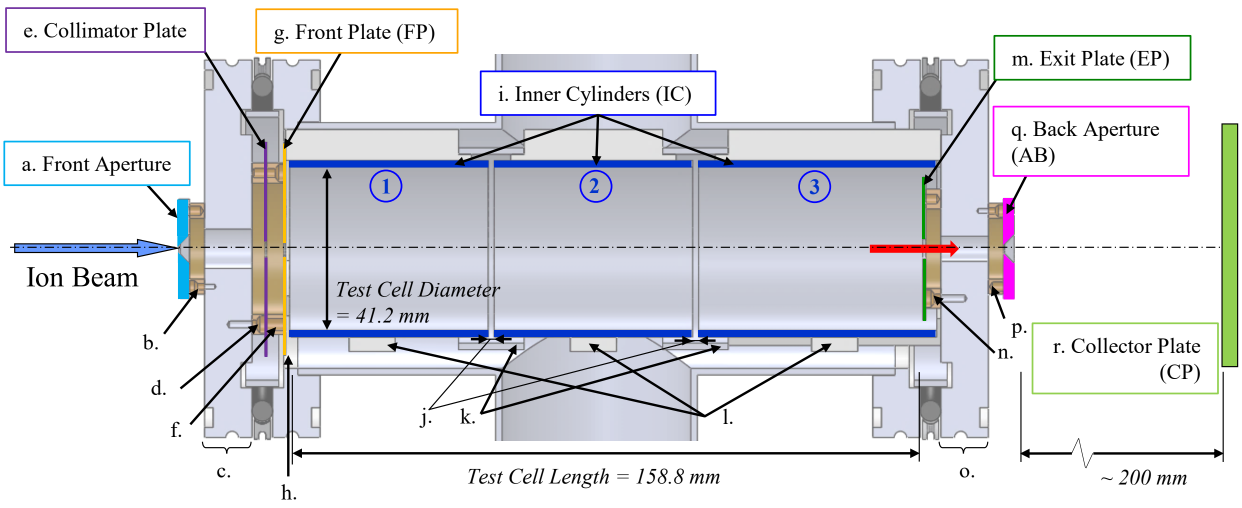

Figure 3.3: Test cell geometry with important electrodes highlighted. Further details can be found in Table 3.2 and Figure D.1.

increased from a base pressure of about 7x10^{-3} mTorr to several mTorr. A variable leak valve was used to leak in 99.999% pure Xe into the test cell, while a 1-Torr head baratron was used to measure test cell pressure.

As shown in Figure 3.3 and Table 3.2, test cell dimensions and materials are well-defined, a requirement for model validation [173]. All electrodes are insulated from each other and from the test cell housing (which is electrically grounded) with Ultem or Nylon spacers. Materials with low ion-induced electron emission (IIEE) were used for surfaces that collect energetic ions and neutrals. Pocographite and graphite were used for the front aperture, back aperture, and collector plate since the IIEE yield for 1.5 keV Xe^+ impacting graphite is 0.1 [83]. Similarly, gold was used for the exit plate and collimator plate since the IIEE yield for 1.5 keV Xe^+ on gold is 0.004 [122, 128]. Nickel and nickel-coated stainless steel were used for the front plate and inner cylinders, respectively, since both the ion-induced and electron-induced yields are low (i.e., the ion-induced yield for 1.5 keV Xe^+ on nickel is 0.05 [91] and the electron-induced yield for 50 eV electrons on nickel is 0.23-0.47 [29]). As will be discussed in the following sections, experimental data shows that electron emission from the test cell electrodes may still be non-negligible.

Table 3.2: Dimensions and Materials of Test Cell Components (from upstream to downstream).

Detail	Name	Dimensions, mm				Material	Comment
		ID	OD	t	L		
a	Front Aperture	2.6	-	2.5	-	Poco carbon	45° chamber
b	spacer	15.2	-	3.8	-	Ultem resin	
c	flange pass thru	9.1	-	-	11.9	-	
d	spacer	33.0	-	3.8	-	Ultem resin	
e	Collimator Plate	3.0	-	0.4	-	Gold	
f	spacer	33.0	-	3.8	-	Ultem resin	
g	Front Plate (FP)	3.2	-	0.4	-	Nickel	
h	gap	-	-	-	1.0	-	
i	Inner Cylinder 1 (IC1)	41.2	44.5	-	50.0	Nickel	
	Inner Cylinder 2 (IC2)	41.2	44.5	-	50.0	Nickel	
	Inner Cylinder 3 (IC3)	41.2	44.5	-	60.0	Nickel	
j	gap	-	-	-	1.5	-	
k	Outer Cylinders	47.5	50.8	-	14.5	Stainless Steel	
l	spacer	44.5	60.0	-	-	Teflon	
m	Exit Plate (EP)	5.0	36.0	0.25	-	Gold	
n	spacer	20.0	-	3.8	-	Ultem resin	
o	flange pass thru	6.4	-	-	11.9	-	
p	spacer	15.2	-	3.8	-	Ultem resin	
q	Front Aperture	2.6	-	2.5	-	Poco carbon	45° chamber
r	Collector Plate (CP)	-	-	-	∼90	Graphite	

Significant electron current was measured on the test cell walls at high test cell pressures, as will be shown below. The electrons are likely created in ionization collisions between ions and neutrals, and by electron emission from the wall materials. A set of Helmholtz coils were installed around the test cell to generate an axial magnetic field and prevent electrons generated near the centerline from reaching the inner cylinders and vice versa. The coils were operated at 26 G (calculated and measured with a magnetic field probe) to confine 2 eV electrons to a 2 mm gyroradius (or approximately $1/10^{th}$ of the test cell radius), without confining the fast 1500 eV beam or MEX ions or slow $\sim$0.04 eV CEX ions. Additionally, an electric field was applied to change the transport of low energy species, and hence to distinguish MEX and CEX ions collected on the test cell electrodes (results of which are presented in the appendix). Voltages of 0 to ±100 V were individually applied to the inner cylinders, exit plate, and front plate while all other electrodes were grounded. Keithley 236, 237, and 2400 source meters were used to apply voltage and read current from all test cell electrodes, along with Keithley 485 picometers and a Keithley 7001 switch system. Measurement error was less than 0.1%.

Note that while the ion beam facility was previously configured by Lee Johnson and others, many aspects of the experiment were worked on by the author. In particular, the test cell was designed and fabricated to provide measurements with better spatial resolution and minimize error from particle-induced electron emission (the previous version of the test cell is discussed in Appendix D). New ion optics and new flow systems were fabricated for a more collimated and steady ion beam at the exit of the ion source. Many of the flag and wire diagnostics for characterizing the ion beam were also fabricated. All labview programs for recording test cell currents, commanding scanning wire diagnostics, and monitoring chamber pressures were written by the author.

3.2 Experimental Results

Collisions between 1500 eV Xe^+ and Xe are measured by directing a xenon ion beam into a cell filled with xenon gas. Currents were measured on the test cell electrodes from scattered and unscattered ions, as the neutral gas pressure is increased [173]. The varied parameters are therefore (i) test cell pressure, (ii) electrode voltage (for affecting the transport of slow charged particles), and (iii) magnetic field strength (to affect electron transport). Experimental results are presented in Section 3.2.1 for the case in which no electric field is applied and in Section 3.2.2 when an electric field is established by applied voltages on the test cell electrodes.

3.2.1 Without Applied Electric Field

Currents measured on the front plate, inner cylinders, and exit plate are plotted in Figure 3.4 at a range of test cell pressures that includes the single collision regime (i.e., below 0.4 mTorr where Kn >1) and the multi-collision regime where other more complex collisions are significant. Also plotted is the current through the exit orifice, which is the sum of the currents measured on the back aperture and collector plate. All currents are normalized by the sum entering the test cell (i.e., for given electrode $j, \overline{I}_j = I_j/(I_{FP} + I_{IC} + I_{EP} + I_{EO})$) to account for any drifts in ion beam input conditions (e.g., changes in the filament cathode or in the xenon feed rate into the ion source). Measurements without magnetic field and with an axial magnetic field of 26 G are presented.

Figure 3.4 shows an increase in current scattered to the test cell walls and a decrease in current passing through the exit orifice as the test cell pressure and neutral density increases, and thus as more ions undergo collisions with background neutrals. From Figure 3.4, the current through the exit orifice decreases exponentially with pressure. Assuming ion beam attenuation along the length L of the test cell, the cross-section σ_{tot} for collisions that scatter

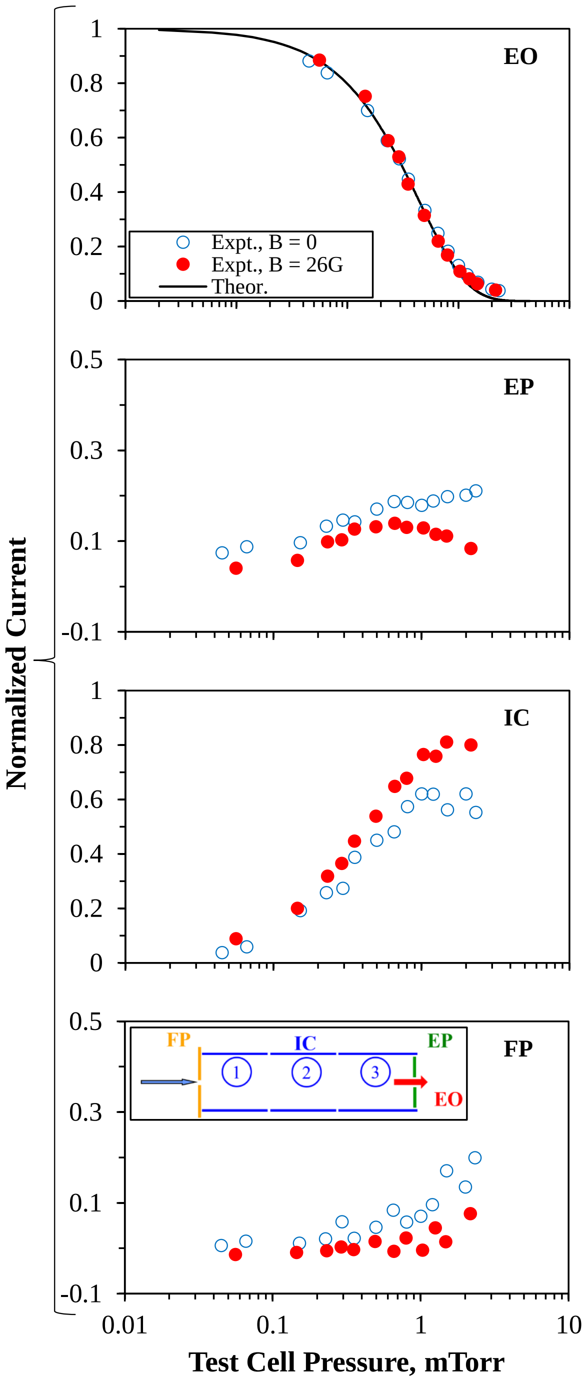

Figure 3.4: Current measured on the exit orifice (EO), exit plate (EP), inner cylinders (IC), and front plate (FP) as a function of test cell pressure without and with an axial magnetic field of 26 G; no electric fields are applied. Current calculated from Equation 3.9 with $\sigma_{tot} = \sigma_{CEX}$ is compared to exit orifice current and labeled as "Theor".

ions at large angles can be determined from the exit orifice current I_{EO}:

$$I_{EO} = I_{beam,0} e^{-n_n \sigma_{tot} L} \tag{3.9}$$

where $I_{beam,0}$ is the ion beam current at the entrance of the test cell, n_n is the neutral gas density, and σ_{tot} is the integral cross-section for Xe$^+$-Xe collisions. For 1500 eV Xe$^+$-Xe, MEX and CEX collisions are dominant. However, as was discussed in Section 2.1.3.1, the majority of ions experiencing MEX collisions are scattered at very small angle to the exit orifice. Hence, σ_{tot} can be assumed to be equal to σ_{CEX}. From Figure 3.4, there is excellent agreement between Equation Equation 3.9 with $\sigma_{tot} = \sigma_{CEX} = 44.1$ Å^2 (labeled as "Theor.") and current measured through the exit orifice. Results are independent of magnetic field since fast beam and MEX ions are already confined to the centerline.

Figure 3.4 shows corresponding increases in current to the exit plate, inner cylinders, and front plate from the increasing number of ions that are scattered from the beam centerline in the single collision regime and when no magnetic field is applied. At the very high pressures where multiple collisions are occurring, it is expected that few ions will reach the exit plate since nearly all beam ions undergo collisions (i.e., I_{EO} <3% at 2.4 mTorr), and since MEX and CEX collisions occur near the upstream end of the test cell away from the exit plate. Ions are instead expected to collect on the inner cylinders. However, from Figure 3.4, the current to the exit plate continuously increases and is significant at a pressure corresponding to six times the ion mean free path when no magnetic field is applied. That is, 20% of the current entering the test cell is collected on the exit plate at 2.4 mTorr where an ion will experience on average six collisions.

The continual increase in current measured on the exit plate is almost certainly not from beam ions, MEX ions, or CEX ions, but instead is likely due to ionization collisions in the bulk and particle-induced electron emission from the walls. Fast 1500 eV neutrals created in CEX collisions may experience ionization collisions with slow background neutrals to produce forward scattered ions and isotropically scattered electrons (i.e., $\tilde{X}e + Xe \longrightarrow \tilde{X}e^{+} + Xe + e$) [64, 174]. Additionally, while PIEE from the gold exit plate was expected to be negligible, the exit plate may emit electrons when bombarded with fast heavy particles (i.e., beam ions, MEX ions, or CEX neutrals); these emitted electrons are expected to collect on the inner cylinders. Both events lead to positive current on the exit plate and negative current to the inner cylinders without applied magnetic field. Neutral-neutral ionization and electron emission were explored in the analytical and computational models described below.

When a magnetic field is applied, ions may still be scattered towards the exit plate in MEX, CEX, or ionization collisions since ions are unmagnetized at 26 G. Similarly, electrons emitted from the exit plate are independent of axial magnetic field since electrons may stream along magnetic field lines. In contrast, ionization electrons scattered isotropically (mostly to the inner cylinders) without magnetic field, will be funneled to the exit plate and front plate in an axial magnetic field. This will lead to a decrease in exit plate and front plate current when a magnetic field is applied, as is observed in Figure 3.4.

As discussed above, the inner cylinders are expected to collect ions scattered from the centerline at large angle (particularly CEX ions), ionization electrons generated along the beam axis and scattered isotropically, and electrons emitted from the exit plate when no magnetic field is applied. From Figure 3.5, the current on the inner cylinder segments are approximately equal at test cell pressures below 0.4 mTorr, where beam ions experience on average less than one collision within the test cell and where ionization collisions and electron emission are negligible. At high pressures, a large percentage of the ion current was found to be collected on inner cylinder 1 since multiple collisions are likely to occur at the upstream end of the test cell. Inner cylinder 3 was measured to have the smallest current, and to collect significant electron current at high test cell pressures when no magnetic field is applied. Since neutral-neutral ionization is predominantly a two-step process and since fast neutrals must first be created in a CEX collision, a particle must undergo at least three collisions before an ionization collision event occurs. Therefore, ionization collisions are expected to occur at high test cell pressures and at the downstream end of the test cell near inner cylinder 3. Additionally, at high pressures, a significant fraction of the beam ions experience collisions, which produce fast MEX ions and neutrals that are scattered at small angles towards the exit plate. From view factor relations, 88% of electrons emitted from the exit plate with a cosine angular distribution are expected to collect on inner cylinder 3.

Figure 3.5 shows a large increase (to positive values) in current on inner cylinder 3 when an axial magnetic field is applied since the magnetic field prevents electrons generated near the centerline (from ionization in the bulk or electron emission from the exit plate) to be collected on the inner cylinders. A small increase was observed on inner cylinder 2, which was estimated from view factor relations to collect 8% of the electrons emitted from the exit plate. The current on inner cylinder 1 is independent of magnetic field since slow CEX ions are unmagnetized and since ionization electrons or emitted electrons are unlikely to collect on inner cylinder 1.

From Figure 3.4, there is a small decrease in current on the front plate with magnetic field. The decrease is likely due to ionization electrons generated at the centerline, some of which are funneled to the front plate with magnetic field (instead of being isotropically scattered to the inner cylinders without magnetic field). The decrease may also be due to electrons emitted from the exit plate that are funneled to the front plate with axial magnetic field, but which are negligible from view factor relations without magnetic field.

To summarize, ions are scattered from the centerline to the test cell walls after experiencing MEX and CEX collisions, ions and electrons are generated via neutral-neutral ionization collisions, and electrons are emitted from the walls due to incident ions and neutrals (i.e., PIEE). These processes are depicted in Figure 3.6. From semi-analytical and computational models discussed in Sections 3.3.1-3.3.3, CEX ions are scattered at large angle and may be collected at any of the test cell electrodes, although predominantly on the inner cylinders. MEX ions and fast neutrals are scattered at small angle and are predominantly collected on the exit plate in the single collision regime, but may experience further CEX and ionization

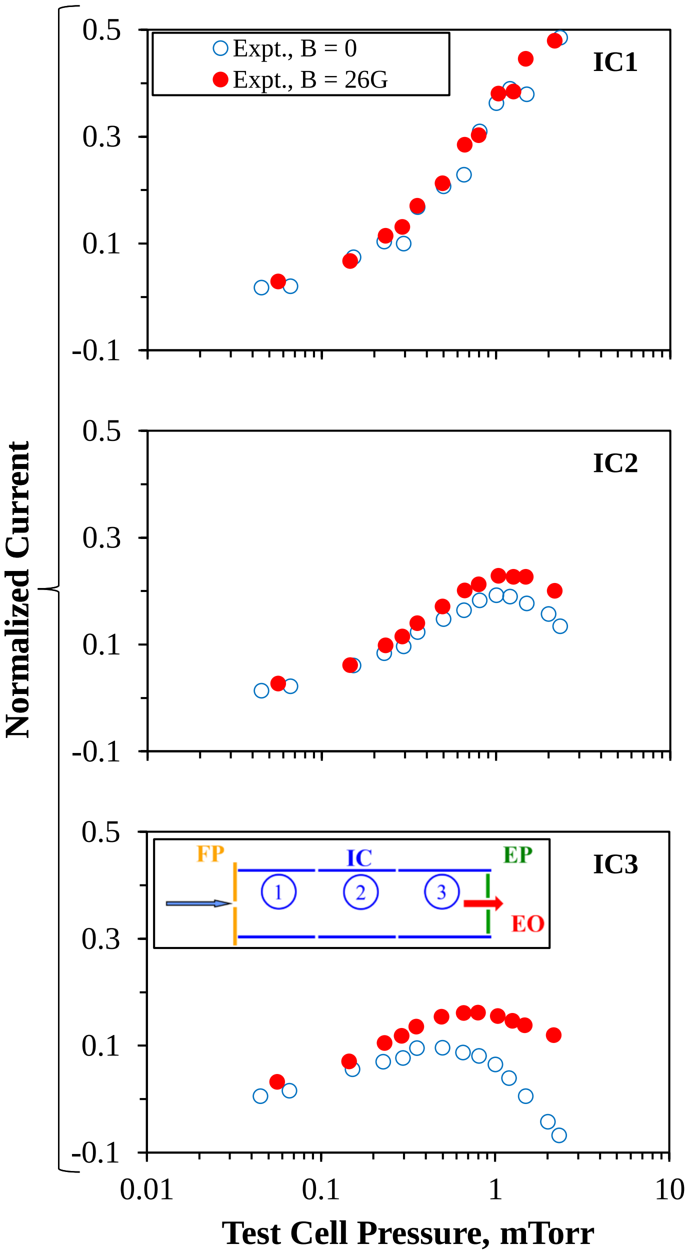

Figure 3.5: Current measured on inner cylinder 1 (IC1), inner cylinder 2 (IC2), and inner cylinder 3 (IC3) as a function of test cell pressure without and with an axial magnetic field of 26 G; no electric fields are applied.

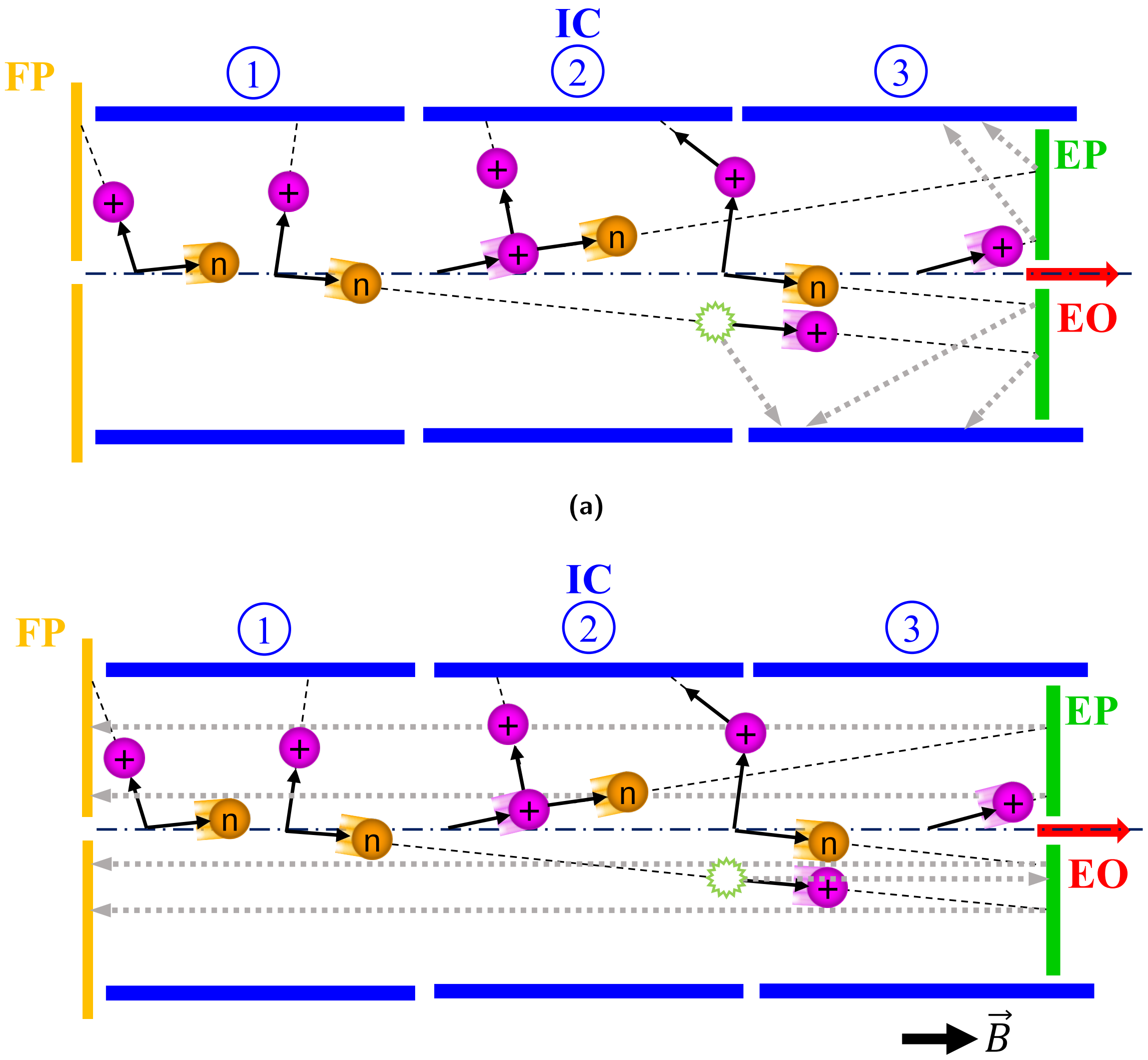

(a)

(b)

Figure 3.6: Scattering of MEX and CEX ions and fast neutrals to the test cell walls, generation of ionization ions and electrons, and electron emission from the walls due to incident fast ions and neutrals. Ions are depicted in pink, while neutral atoms are depicted in yellow; fast particles are shown with "comet tails". Ionization events are depicted as starbursts. Gray arrows depict electrons generated in ionization and electron emission events. Trajectories are shown for cases in which (a) no magnetic field is applied and (b) when an axial magnetic field of 26 G is applied.

collisions, respectively, that affect trajectories. Ionization ions are generated in the forward direction to the exit plate, while ionization electrons are generated isotropically near inner cylinder 3 and the exit plate. The fast MEX ions and fast neutrals on the exit plate lead to electron emission from the exit plate. Only electron trajectories are affected by an axial magnetic field, with ionization electrons reaching the exit plate and PIEE emission reaching the front plate.

3.2.2 With Applied Electric Field

Currents collected on the test cell electrodes are plotted in Figures 3.7-3.9 as a function of test cell pressure for the case in which the exit plate, inner cylinder, and front plate, respectively, are biased individually. Results without magnetic field are shown as symbols and with magnetic field are shown as lines. Current through the exit orifice is not shown since it is independent of electric potential (i.e., current is the same as in Figure 3.4). All currents are normalized by the total current entering the test cell when all electrodes are grounded (i.e., for given electrode $j, \overline{I}_j(V) = I_j(V)/[I_{FP}(0V) + I_{IC}(0V) + I_{EP}(0V) + I_{EO}(0V)]$).

Exit plate current decreases with positive exit plate voltage in Figure 3.7 as the exit plate collects more ionization and/or emitted electrons that would otherwise go to the inner cylinders, and repels any slow CEX and ionization ions. The opposite is true for negative exit plate voltage, and for current on the inner cylinders. Current on the front plate is independent of exit plate voltage when no magnetic field is applied since there is a small view factor between the exit plate and front plate. However, the dependence on front plate voltage is larger than on exit plate voltage at high test cell pressures, since more collisions (e.g., CEX) are occurring at the upstream end of the test cell near the front plate.

The above discussion also applies to the front plate when it is biased, as is shown in Figure 3.9. However, the effect of front plate voltage is larger than on exit plate voltage at high test cell pressures, since more collisions (e.g., CEX and ionization) are occurring at the upstream end of the test cell near the front plate.

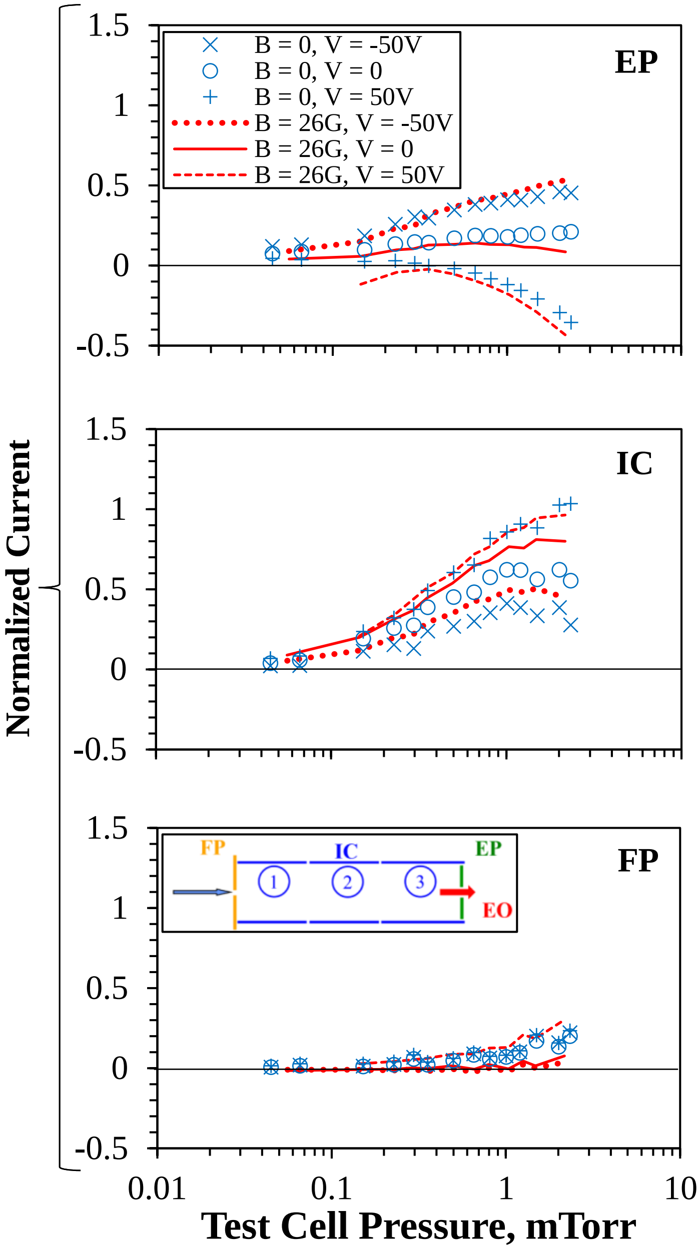

Figure 3.7: Current measured on the exit plate (EP), inner cylinders (IC), and front plate (FP) as a function of test cell pressure without (symbols) and with (lines) applied magnetic field for varied electric potential on the exit plate.

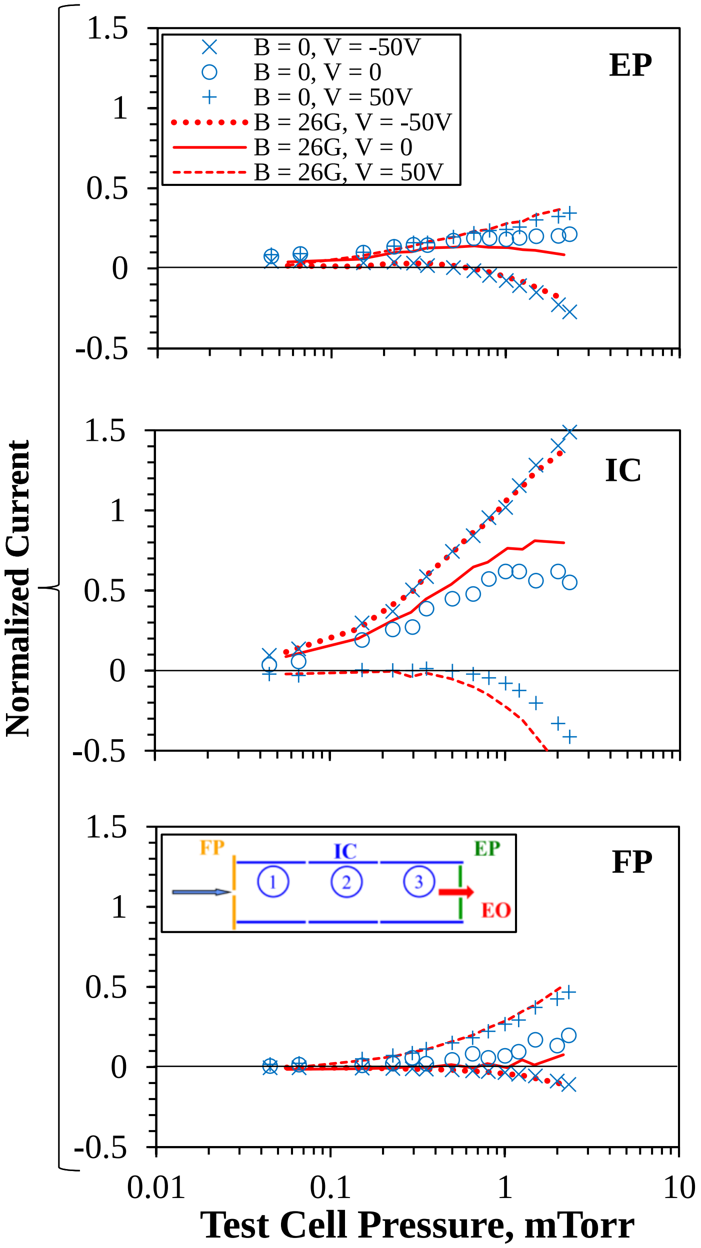

Figure 3.8: Current measured on the exit plate (EP), inner cylinders (IC), and front plate (FP) as a function of test cell pressure without (symbols) and with (lines) applied magnetic field for varied electric potential on the inner cylinders.

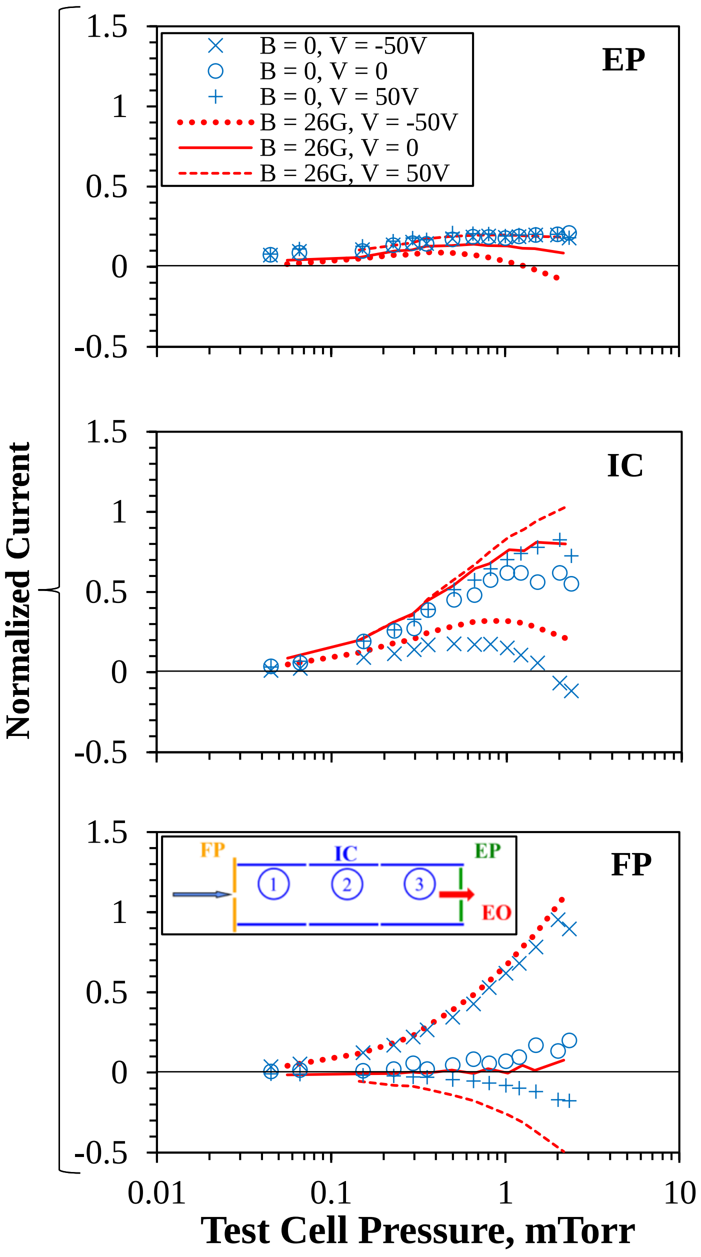

Figure 3.9: Current measured on the exit plate (EP), inner cylinders (IC), and front plate (FP) as a function of test cell pressure without (symbols) and with (lines) applied magnetic field for varied electric potential on the front plate.

Current on the inner cylinders decreases with positive inner cylinder voltage in Figure 3.8 as the inner cylinders collect more ionization and/or emitted electrons, and repel all slow CEX and ionization ions. The opposite is true for negative inner cylinder voltage, and for currents on the exit plate and front plate. The dependence on inner cylinder voltage is larger than the dependence on the exit plate seen in Figure 3.7 or the front plate voltage seen in Figure 3.9, since biasing of the inner cylinders creates electric fields at both ends of the test cell and affects the transport of low energy particles at both ends. All currents are independent of magnetic field at negative inner cylinder voltage since electrons are repelled from the inner cylinders in either cases.

Further discussion of electrode currents measured in the test cell with an electric field are found in Section F.1. Note that a system of equations may not be developed to determine the contributions from MEX ions, CEX ions, electrons from ionization, and emitted electrons to each electrode using the biased electrode data, since electrons are accelerated above the xenon ionization potential when electric fields are applied such that electron-impact ionization of neutral gas must also be considered.

3.3 Comparison with Ion-Neutral Collision Theory and Models

Treatments of the differential cross-sections previously discussed in Section 2.1.3.1 were utilized in semi-analytical and computational models that were developed complementary to the experimental effort presented herein. To quickly analyze the data collected and provide insight into the dominant mechanisms in the experiment, a semi-analytical collisionality model was developed. The semi-analytical model is sufficiently fast with runtimes that are a fraction of a second for a single pressure condition. Fully computational models of ion-neutral collisions in the test cell were developed by Araki and Wirz [173, 170, 8, 171, 175] at UCLA, and Giuliano and Boyd [10, 32, 62, 176, 63] at the University of Michigan, to explore more complex conditions not readily attainable with the semi-analytical model. These require runtimes of approximately 6-10 hours for Giuliano and Boyds model and 0.5-4 hours for Araki and Wirzs model for a single experimental condition (i.e., test cell pressure). All models are discussed below.

3.3.1 Semi-Analytical Model

For the case of no applied electric field, a model may be employed that uses empirical values for the collision cross-sections to rapidly determine current from ions that experience MEX and CEX collisions and are scattered to the front plate, inner cylinder, exit plate, and exit orifice (per the deflection angles defined in Figure 3.10). Assuming a one-dimensional beam centered along the test cell axis, the model treats the scattered MEX and CEX ions as discrete point sources located on the axis, where the magnitude of the source is attenuated due to scattering collisions. An angular distribution for the sources is calculated from the differential cross-sections given by Equations 2.9a and 2.9b and shown in Figure 2.4, to determine the MEX and CEX ion currents to each test cell electrode. Ions are assumed to follow a straight-line trajectory from the point of collision on the centerline to the test cell walls. The assumption is valid for $Kn > 1$, where the Knudsen number Kn is defined as $Kn = \lambda/L, \lambda$ is the mean free path of the ion, and L is the test cell length. For the test cell design in Figure 3.3, $Kn = 1$ corresponds to a pressure of approximately 0.4 mTorr. To extend the validity of the model to higher test cell pressures, multiple collisions were considered for fast particles as described below. Note that the semi-analytical model is an extension of the model discussed in Ref. [172].

For a given test cell pressure, the beam current at each discrete location along the test cell axis is calculated using from attenuation theory,

$$I_{beam,k} = I_{beam,k-1} e^{-n_n \sigma_{tot} \Delta x}, k = 1, 2, ..., m \tag{3.10}$$

where $I_{beam,k}$ is the beam current at position $x_k, I_{beam,k-1}$ is the beam current at position

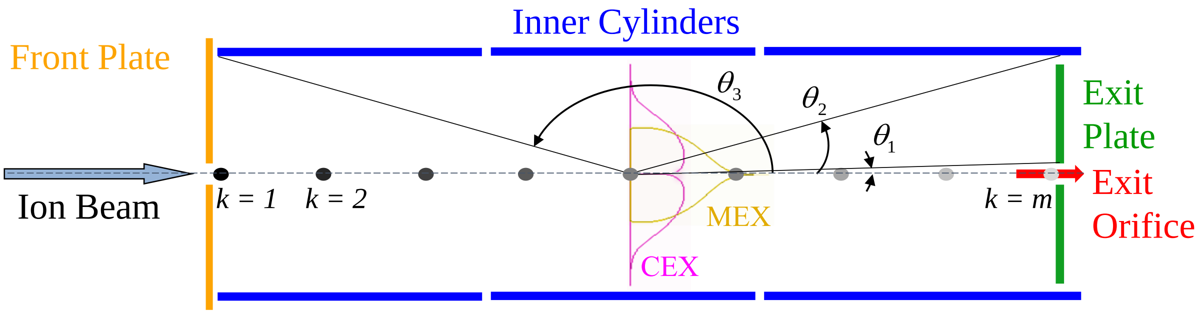

Figure 3.10: Test cell with attenuated MEX and CEX sources, MEX and CEX scattering angular distributions, and electrodes with bounding angles.

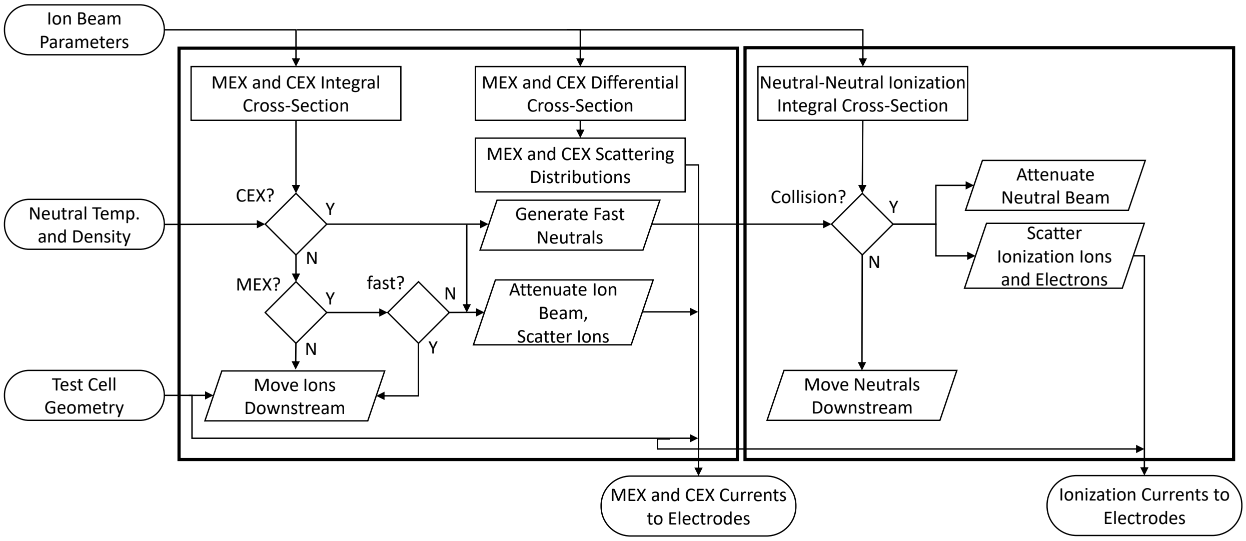

Figure 3.11: Flow chart for the semi-analytical model.

x_{k-1}, $\Delta x = x_k - x_{k-1}$, n_n is the neutral particle density in the test cell, $\sigma_{tot} = \sigma_{MEX} + \sigma_{CEX}$, and σ_{MEX} and σ_{CEX} are the MEX and CEX cross-sections calculated by integrating over the empirically-derived differential cross-sections in Equations 2.9a and 2.9b. The current scattered between x_k and x_{k-1} is then

$$\Delta I_{beam,k} = I_{beam,k-1}(1 - e^{-n_n \sigma_{tot} \Delta x}, k = 1, 2, ..., m). \tag{3.11}$$

Assuming $\sigma_{MEX} \approx \sigma_{CEX}$, half of the scattered current is from MEX collisions and half from CEX collisions. As was discussed in Section 2.1.3.1, a large portion of the MEX ions are scattered at very small angles, with a small change in energy. MEX ions that maintain a significant fraction of their pre-collision energy are effectively unscattered, and added back to the beam current $I_{beam,k}$ in the model to undergo further collisions, yet their scattering direction to the exit orifice or exit plate is retained. This allows for multiple collisions to be considered for MEX ions, and extends the range at which the analysis is valid to higher test cell pressures.

From conservation of energy and momentum, the post-collision MEX and CEX ion and neutral speeds assuming stationary target neutrals are

$$v'_{ion} = v_{ion} \cos\theta \tag{3.12a}$$

$$v'_n = v_{ion} \sin\theta \tag{3.12b}$$

where v_{ion} is the pre-collision ion speed and θ is the scattering angle of the MEX or CEX ion. Post-collision ion speeds are plotted in Figure 3.12 along with the probabilities of scattering below angle θ (from Equation 2.10). The average post collision speeds for MEX and CEX ions are approximately 46,500 m/s and 1,510 m/s, respectively, for collisions between 1500 eV Xe$^+$ and stationary Xe. In comparison, the mean thermal speed of the target neutrals is

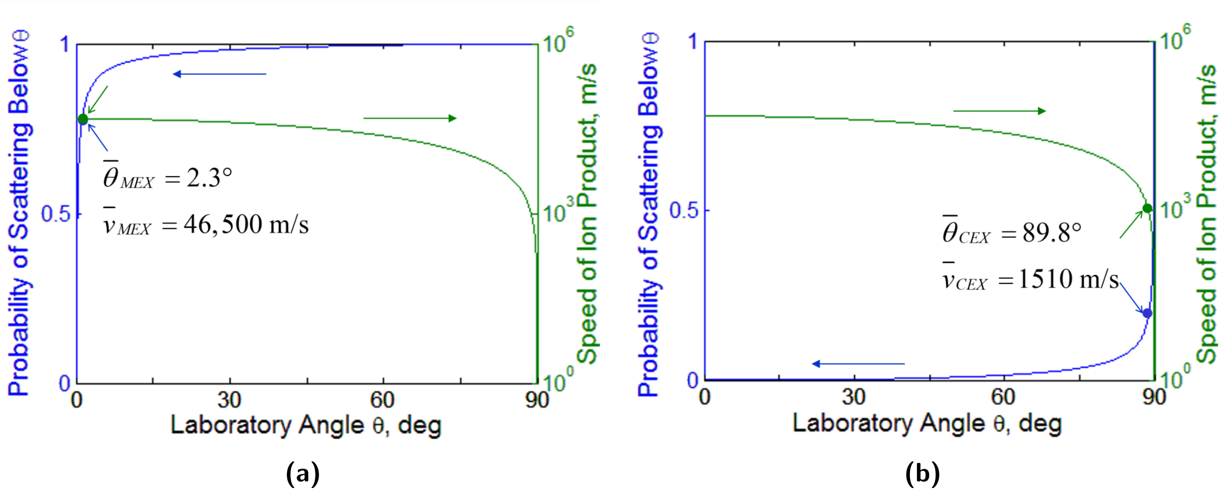

Figure 3.12: Cumulative probability of scattering below angle θ, speed of an ion scattered at angle θ, and average values of each for (a) MEX and (b) CEX ions; Xe$^+$-Xe at 1500 eV.

given by

$$v_{therm} = \sqrt{\frac{8k_bT_n}{\pi m_{Xe}}} \tag{3.13}$$

where k_b is the Boltzmann constant, T_n is the temperature of the target xenon neutrals, and m_{Xe} is the mass of a xenon atom; the mean thermal speed is approximately 200 m/s at 300 K. Thus, for ions resulting from MEX collisions, the random thermal speed of the neutral particles can be ignored and stationary target neutrals are assumed for MEX collisions. On the other hand, the post-collision speeds for most of the ions resulting from CEX collisions are comparable to the mean thermal speed of neutrals. Therefore, the post-collision velocity of ions resulting from CEX collisions is determined from the vector sum of the post-collision velocity distribution and an isotropic thermal velocity distribution such that

$$\vec{v'}_{tot} = \vec{v'}_{ion} + \vec{v'}_{therm}. \tag{3.14}$$

To calculate the MEX current to the exit plate, at each test cell location, the scattered

MEX current is multiplied by the probability of MEX scattering between θ_1 and θ_2 separating the exit plate from the exit orifice and inner cylinders, respectively, and then summed over all axial locations k. CEX current to the exit plate is analogous, i.e.,

$$I_{MEX,EP} = \sum_{k=1}^{m} \frac{\Delta I_{beam,k}}{2} (P_{\theta_2,MEX} - P_{\theta_1,MEX})_k \tag{3.15a}$$

$$I_{CEX,EP} = \sum_{k=1}^{m} \frac{\Delta I_{beam,k}}{2} (P_{\theta_2,CEX} - P_{\theta_1,CEX})_k \tag{3.15b}$$

Here P_θ is given by Equation 2.10 using the empirically-derived differential cross-sections in Equations 2.9a and 2.9b. The probability of scattering between θ_2 and θ_3 is used in the calculation for the inner cylinders, and above θ_3 for the front plate.

At higher test cell pressures where Kn <1, the scattered ions and neutrals are likely to experience multiple collisions. Since CEX ions are largely scattered isotropically, their scattering distribution is expected to be unchanged if they experience further MEX or CEX collisions. In contrast, MEX ions and fast neutrals may be scattered from their initial direction by further collisions. Thus, the model considers multiple collisions for these fast particles by adding them back into the beam if they experience MEX collisions. As mentioned previously, incident ions retain a large fraction of their energy in a MEX collision. The average energy for a 1500 eV ion that has experienced six consecutive MEX collisions is 1345 eV, or approximately 90% of its initial energy. Additionally, the integral collision cross-section was measured by Miller *et al* [72] to have little dependence of incidence energy. Therefore, the integral and differential cross-sections given by Equations 2.9a and 2.9b are assumed unchanged for the entire range of pressures examined (i.e., up to 2.6 mTorr or $Kn \sim 1/6$).

More complex collisions become non-negligible and must be considered in the multiple-collision regime. This includes ionization collisions between fast neutrals generated in CEX collisions and slow background neutrals (i.e., $\tilde{X}e + Xe \longrightarrow \tilde{Xe^{+}} + Xe + e$) [64, 174]. Since fast neutrals have small scattering angles from the test cell axis, the model treats the fast neutrals as a beam similar to the ion beam, i.e.,

$$J_{beam,k} = J_{beam,k-1} e^{-n_n \sigma_{ionz} \Delta x} + \Delta I^{CEX}_{beam,k-1}, k = 1, 2, ..., m. \tag{3.16}$$

Here $J_{beam,k}$ is the neutral beam current at position x_k, $J_{beam,k-1}$ is the neutral beam current at position x_{k-1}, n_n is the background neutral density, σ_{ionz} is the integral cross-section for neutral-neutral ionization, and $\Delta I^{CEX}_{beam,k-1}$ accounts for fast neutrals generated at position x_{k-1} (which is equal to beam ions that have undergone CEX collisions at position x_{k-1}).

An expression for the ionization cross-section was given by Drawin and Emard [64], and is calculated to be 21.4 Å^2 at 1500 eV for xenon-xenon collisions. However, a value of 5.0 Å^2 was used instead since Ref. [177] determined that this expression can overpredict the cross-section by up to an order of magnitude for rare gases. The fast neutrals are assumed to be ionized in the collision and scattered at small angle in the forward direction. Generated electrons are assumed to scatter isotropically. Note that since the energy of MEX ions decreases slightly from 1500 eV with each collision, the energy of a fast neutral generated in a collision between a MEX ion and background neutral may be smaller than the energy of a fast neutral generated in a collision between a beam ion and a background neutral. However, as discussed previously, MEX ions retain more than 90% of their initial energy, even after experiencing six collisions. Additionally, from Drawin and Emard [64], the integral cross-section for neutral-neutral ionization only decreases by 10% between 1500 eV and 1350 eV. Therefore, it is valid to assume a constant collision cross-section.

3.3.2 Monte Carlo Collision Model

Araki and Wirz [4, 170, 8, 171, 175] developed a Monte Carlo collision (MCC), particle-in-cell model for preliminary computational analysis during the development phase of the experiment. The MCC model utilizes classical scattering with spin-orbit-free potential [9] for collisions between high energy ions and neutrals, the variable hard sphere model [178] for collisions between low energy ions and neutrals, and the semi-analytical HFD-B2 potential [179] for collisions between high and low energy neutrals. The probability for a collision and the angular distribution of scattered beam and MEX ions are calculated from the interaction potentials in Figure 2.3, while the variable hard sphere model assumes isotropic scattering. Particle induced electron emission (PIEE) from the exit plate due to fast ions and neutrals is considered and assumed to produce 4 eV electrons emitted with a cosine angular distribution. The yield due to incident ions is varied from 0 to 0.4; the yield due to incident neutrals is assumed to be 0.8 times the value for incident ions. Primary ions, MEX ions, CEX ions, fast neutral atoms, and electrons are tracked individually, and the electric potential is solved iteratively until convergence. Further details on the model are found in Refs. [171, 175].

3.3.3 Direct Simulation Monte Carlo Model

Giuliano and Boyd [10, 32, 62, 176, 63] used the results from the experiment to extend the theory of Xe^+-Xe collisions to higher incident ion energies. Their model employs direct-simulation Monte Carlo (DSMC) and particle-in-cell techniques. Similar to the semi-analytical model, the DSMC model utilizes the semi-empirical differential cross-section for MEX and CEX collisions between xenon ions and neutrals at 1500 eV (i.e., Equations 2.9a and 2.9b). The variable hard sphere model [61] and an isotropic distribution are utilized for neutral-neutral collisions. Electron emission from the walls due to impact from fast ions and neutrals are considered; a yield of 0.016 is used for the inner cylinder and of 3×10^{-6} is used for the exit plate. Both ions and neutrals are tracked in a non-quasineutral manner. Additionally, the DSMC model allows for applied potentials at the test cell walls, however, the reader is referred to Refs. [32, 62, 176, 63] for these results and results considering electron emission.

3.3.4 Model Results and Comparison to Experimental Data

Models results of a 1-D beam of 1500 eV Xe^+ beam impacting a uniformly distributed Xe gas in the test cell domain, are compared to experimental data measured without applied magnetic field in Figure 3.13. Simulations were run considering only MEX ions incident on the walls (i.e., "MEX") and considering both MEX and CEX ions on the walls (i.e., "MEX + CEX"); for the exit orifice, current from unscattered beam ions is also considered. Also included are simulation results from the semi-analytical and MCC models when considering electrons from neutral-neutral ionization (i.e., "MEX + CEX + ionz") and particle-induced electron emission (i.e., "MEX + CEX + PIEE"), respectively.

From Figure 3.13, the semi-analytical and computational models are able to reproduce the exponential decrease in current measured through the exit orifice with increasing test cell pressure. Results considering beam, MEX, and CEX ions and electrons all lie on a single curve, thus demonstrating that all current reaching the exit orifice is due to beam ions that have experienced no collisions and MEX ions that are deflected at very small angle. This once again confirms the use of Equation 3.9 with $\sigma_{tot} = \sigma_{CEX}$.

Model results of current to the exit plate in Figure 3.13 follow the initial increase with test cell pressure seen experimentally, the majority of which is predicted to be from MEX ions scattered at small angle. However, all models fail to predict the continual increase seen experimentally at high test cell pressures when considering only ions. The continual increase is observed in the MCC model only when PIEE from the exit plate is included with ion-induced yield = 0.4 (which is much larger than the yield reported in the literature). Similarly, the semi-analytical model is able to reproduce the continual increase when considering neutral-neutral ionization, since this leads to forwardly scattered ions. Therefore, both PIEE and neutral-neutral ionization collisions can separately explain the trend in exit plate current seen in the experiment, yet each underpredicts the magnitude of the measured current. Since the MCC model used relatively large yields to explain the behavior, there is likely a combination of effects from both PIEE and neutral-neutral ionization.

The semi-analytical and computational models give the same results for ion current to the exit plate. Thus, the different implementation of ion-neutral collisions used in the models are synonymous. The empirical differential cross-sections shown in Figure 2.4 correctly capture the physics of the theoretically-derived interaction potentials shown in Figure 2.3, and may be used in plasma models instead of the more computationally expensive interaction potentials. Additionally, the fact that the ion-only results from the semi-analytical model match those of the DSMC and MCC models, gives confidence in the validity of the semi-analytical model for the entire pressure range, including for $Kn < 1$.

Figure 3.13 shows that the models match the increased current observed on the inner cylinders and front plate at low test cell pressure, and the decreased current on the inner cylinder above 1 mTorr. The semi-analytical model predicts that the majority of the current is from CEX ions that are scattered at large angles. At high test cell pressures, the ion-only model results overpredict the current on the inner cylinders. The MCC and semi-analytical models better match experimental data when PIEE (from the exit plate to the inner cylinders) and neutral-neutral ionization collisions (leading to isotropically scattered electrons) are included. As expected from view factor relations, the MCC model predicts no electrons emitted from the exit plate reach the front plate. Additionally, since neutral-neutral ionization is likely to occur at the downstream end of the test cell (since requires multiple collisions), its effect on the front plate is negligible.

Figure 3.14 compares results from the semi-analytical model with experimental data taken without and with applied magnetic field. For the case of applied magnetic field, the semi-analytical model assumes that no electrons generated in neutral-neutral ionization collisions in the near-centerline region reach the inner cylinders. Instead, electrons are assumed to be predominately funneled to the exit plate (i.e., 90% to the exit plate and 10% to the front plate). Therefore, current through the exit orifice is independent of magnetic field as shown Figure 3.14. Current on the inner cylinders increases with magnetic field and agrees well with experimental data in the entire pressure range. Current on the front plate decreases

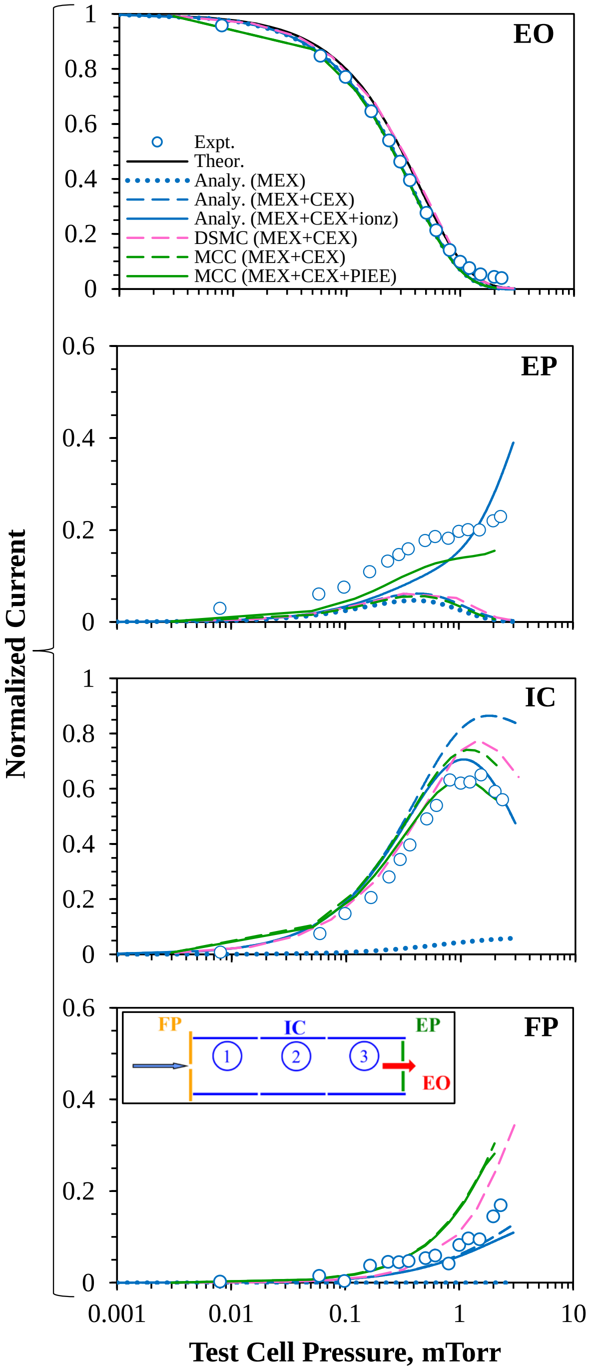

Figure 3.13: Results from the semi-analytical and computational models of current to the exit orifice (EO), exit plate (EP), inner cylinders (IC), and front plate (FP) as a function of test cell pressure. Contributions from MEX ions (dotted lines), from MEX and CEX ions (dashed lines), and from ions and electrons (solid lines) are shown. Electrons from neutral-neutral ionization collisions are considered in the semi-analytical model, while particle-induced electron emission is considered in the MCC model.

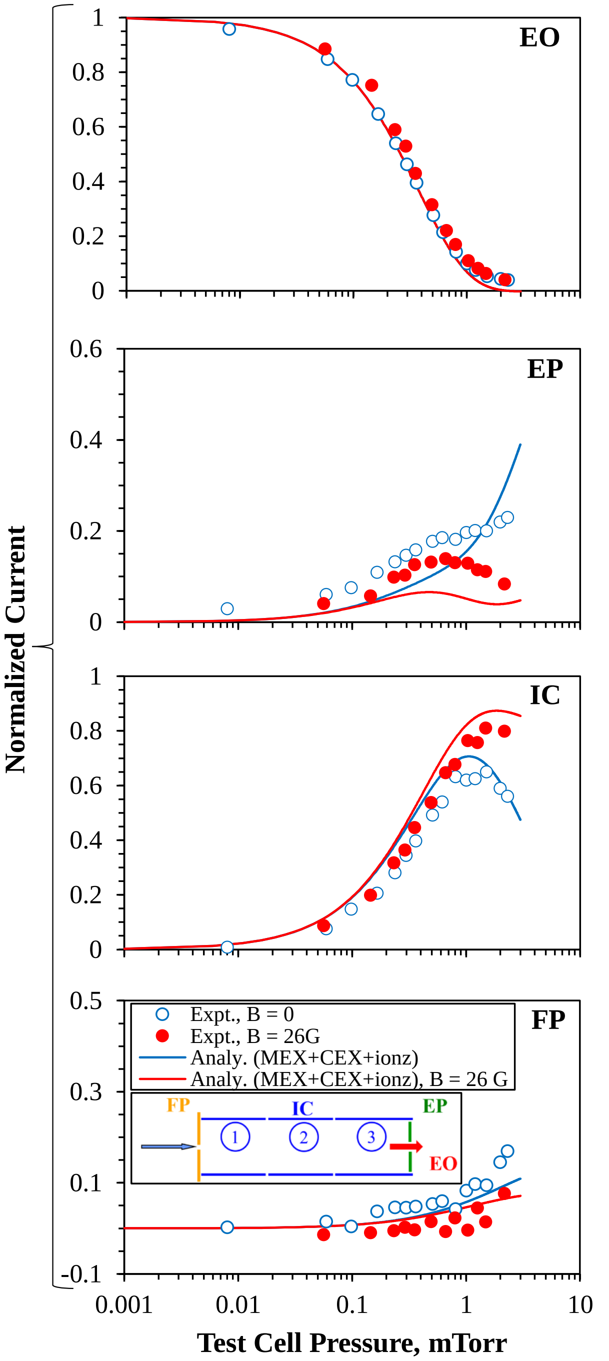

Figure 3.14: Results from the semi-analytical model of current to the exit orifice (EO), exit plate (EP), inner cylinders (IC), and front plate (FP) as a function of test cell pressure when no magnetic field is applied and when an axial magnetic field of 26 G is applied. Contributions from MEX ions (dotted lines), from MEX and CEX (dashed lines), and from ions and electrons (solid lines) are shown. Neutral-neutral ionization collisions are considered in the generation of electrons.

with magnetic field as in the experiment. Similarly, current on the exit plate decreases with magnetic field. The model captures the trends seen experimentally (i.e., a continual increase in exit plate current without magnetic field, and a decrease at test cell pressures above 0.5 mTorr with magnetic field), yet underpredicts the measured current. The overall general agreement between the model results and experimental data with applied magnetic field further validates the physics included in the model: ion-neutral collisions are correctly captured by Equation 3 and the contribution from neutral-neutral ionization collisions is non-negligible.

Further supplementary results from the semi-analytical and MCC models are discussed in Appendix F.2.

3.4 Summary

Ion-neutral collisions are important for accurate modeling of partially ionized plasmas in electric propulsion devices, and of the interactions between these devices and other spacecraft surfaces. For example, grid erosion due to charge-exchange ions is currently the life-limiting factor of ion thrusters, yet there is a lack of information on ion neutral collisions ions at ion-thruster-relevant energies. Using a precision experiment of a xenon ion beam directed to a collision test cell pressurized with xenon neutrals up to several mTorr, momentum-exchange and charge-exchange collisions were investigated for 1500 eV Xe^+-Xe. Current collected on the walls of the test cell (i.e., front plate, inner cylinders, and exit plate) and downstream of the test cell (i.e., exit orifice) were measured.

At low neutral pressures, where each ion experiences one or less collision, experimental data agrees well with results from a semi-analytical model and with results from more complex Monte Carlo computational models developed by collaborators. Measurements therefore provide information on the angular scattering distributions of charge-exchange and momentum-exchange ions at the high energies relevant for ion thrusters, and serve as canonical data for basic validation of plume-spacecraft integration models. For accurate interpretation of results at higher test cell pressures where more collisions are occurring, neutral-neutral ionization collisions and/or particle-induced electron emission from the walls must be considered.

CHAPTER 4

Secondary Electron Emission

This chapter presents research to measure SEE properties from conducting materials using existing surface analysis instruments in vacuum, including original measurements of graphite, lithium and lithium oxide, nanostructured tungsten, and nickel single crystal. Sections 4.1 discusses the facilities and approach used herein for material preparation, characterization, and SEE measurements. Results of SEE yield and energy distributions of emitted electrons are provided in Section 4.2 and compared to values found in the literature, when available. A semi-analytical emission model developed by the author and two Monte Carlo models developed by collaborators of SEE are discussed in Section 4.3, and their results compared with measurements. Section 4.4 provides concluding remarks and implications of the experimental results for plasma and particle devices. Note that the work on lithium was a joint effort with Dr. Angela Capece of the Princeton Plasma Physics Laboratory and published as [180].

4.1 Experimental Setup

Three different facilities were used to measure the SEE properties of graphite, tungsten, lithium oxide and nickel. Since graphite is such a chemically inert material, a facility with a background pressure at 10^{-8} Torr was sufficient to avoid formation of adsorbate layers, which can significantly change SEE properties. On the contrary, tungsten and lithium can easily oxidize. Thus facilities with lower base pressure (i.e., $10^{-10} - 10^{-9}$), *in-situ* ion cleaning, and *in-situ* surface characterization was required to provide information on the state of the surface at the time of SEE measurement. In particular, a facility was required for depositing lithium films. The three facilities were each was calibrated with comparison to SEE values found in the literature, whenever possible. The facilities are discussed in detail below.

4.1.1 Facility for Measuring SEE from Graphite

A facility in the Surface Science and Technology Laboratory (SSTL) at the Princeton Plasma Physics Laboratory was established to measure SEE from graphite. A PHI model 15-120 LEED/AES optics was used, consisting of an electron gun capable of producing a steady monoenergetic electron beam with an energy between 3 and 1600 eV, four hemispherical semitransparent grids (the first with 120° solid angle), and a final hemispherical solid screen. The optics was connected to a PHI model 11-120 LEED electronics control unit, and is commonly used for Low Energy Electron Diffraction (LEED) and Auger Electron Spectroscopy (AES) to study the structure and composition of material surfaces. An unconditioned sample of Highly Ordered Pyrolytic Graphite (HOPG, see Figure 4.1) was placed at a working distance of 20 mm in front of the edge of the LEED/AES optics, as shown in Figure 4.2. The collection angle of the LEED/AES optics could not be increased to 180° (e.g. by moving the sample closer to the LEED/AES optics) since the sample was placed onto the sample holder then rotated in front of the LEED/AES optics, which required ample clearance between the sample holder and the edge of the LEED/AES optics.

The pressure in the vacuum chamber near the sample was measured by an ionization gauge not far from the sample to be 5x10^{-8} Torr. To determine that this background pressure of residual gases in the chamber had no effect on the SEE measurements we considered: (i) scattering of primary and secondary electrons by the residual gases in front of the sample, and (ii) inelastic scattering of primary and secondary electrons within the sample material. The mean free path for scattering of both primary and true secondary electrons (i.e., greater than 50 eV and $\sim$ 2 eV, respectively) by the residual gases at this pressure is calculated to be many orders of magnitude larger than the sample-gun and sample-collector separation (λ/L

(a)

Figure 4.1: 20 mm diameter graphite sample.

$\sim 10^3$, see Appendix H), thus this has no effect on our results. In addition, while the chamber pressure is much higher than for typical surface science experiments, this also has no effect on our SEE results on graphite since this is such a chemically inert surface and no adsorbate layers can form at these pressures. Since no cleaning of the sample surface was done in-situ, there may be impurities or contamination from surface reactions during exposure of the graphite to atmospheric pressure before during mounting of the sample that can lead to differences in SEE properties of this as-is sample compared to clean graphite (since the inelastic mean free path is only about two monolayers at 50 eV)[181]. Spectra from Energy Dispersive Spectroscopy performed on the graphite sample before SEE measurement, showed that the sample is 99.4% C and 0.6% O.

The LEED/AES system was used for SEE measurements of primary electron beams between 50 and 500 eV impacting graphite at normal incidence. As was done by Pedgley *et al* [12] in conjunction with Farhang *et al* [13], and by Cimino and Collins [182] the total SEE yield σ was calculated using two methods for improved accuracy: (i) measuring the sample current

$$\sigma = \frac{I_{SEE}}{I_{PE}} = \frac{I_{PE} - (I_{PE} - I_{SEE})}{I_{PE}} = \frac{I_{PE} - (I_s)}{I_{PE}} = 1 - \frac{I_s}{I_{PE}}, \tag{4.1}$$

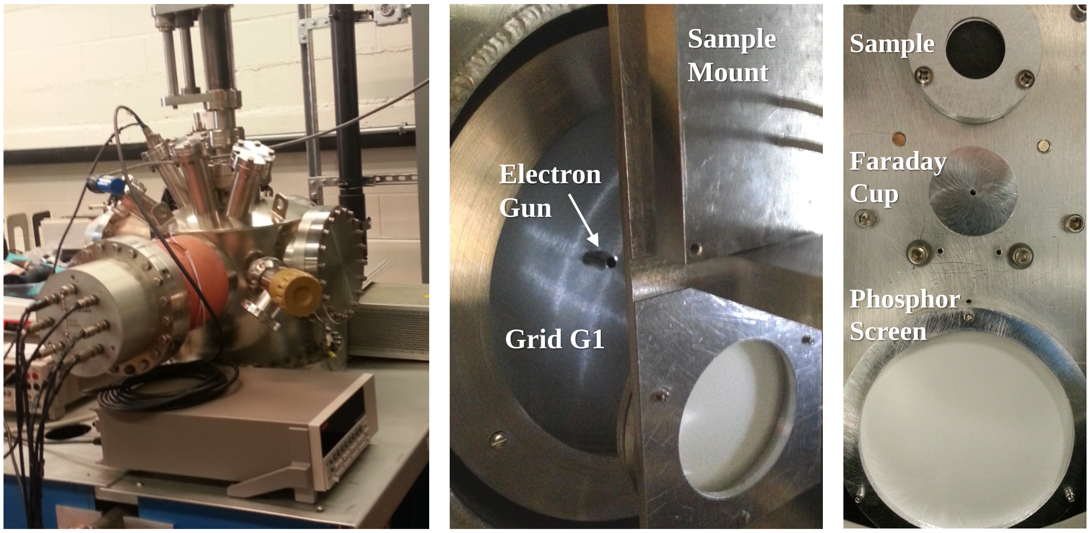

(a) (b) (c)

Figure 4.2: Facility for measuring secondary electron emission from graphite, including (a) chamber, (b) LEED/AES electron optics, and (c) sample mount.

and (ii) measuring the collector current

$$\sigma = \frac{I_{SEE}}{I_{PE}} = \frac{I_{coll}}{I_{PE}} \tag{4.2}$$

Here Equations 4.1 and 4.2 are repeated from Equations 2.11a and 2.11b, and I_{PE}, I_{SE}, and I_s are primary electron, secondary electron, and sample currents, respectively. The incident current on the sample was measured by applying an increasingly positive voltage on the sample to keep secondary electrons on the sample, while the grids of the LEED/AES optics were kept at ground potential, as shown in Figure 4.3(a). Secondary electron current was measured using the LEED/AES optics by applying a positive voltage on the first grid G1, which has a 120° solid angle, to improve collection efficiency while grounding the other grids (see Figure 4.3(b)). Note that measuring the current on all grids of the LEED/AES optics and biasing the first grid G1 minimizes error in the secondary electron current due to the emission of tertiary electrons from the grids of the LEED/AES optics. A Keithley 2410 was used to apply voltage and measure current on the sample for primary electron current, and on the LEED/AES optics for secondary electron current.

The secondary electron energy distribution was measured at each primary electron energy by applying a negative retarding potential on grids G2 and G3 of the LEED/AES optics and measuring the current on the final hemispherical screen from secondary electrons with sufficient energy to overcome the applied retarding electric field (see Figure 4.3(c)). The retarding voltage was increased after the steady-state current on the hemispherical screen was measured. The LEED/AES optics thus served as a high pass filter and the secondary electron energy distribution (i.e., number of secondary electrons emitted at a given energy) was calculated by taking the derivative of the measured curve. The secondary electron energy distributions were corrected for difference in contact potential (i.e., difference in work function between the graphite sample and stainless steel retarding grids) to obtain the secondary electron energy with respect to the sample vacuum level (i.e., $E_{SE} = V_{G2,3} - \Phi_S - \Phi_{G2,3}$) where $\Phi_S = 4.6$ eV [183] and $\Phi_{G2,3} = 4.4$ eV, see Figure 4.4). Note that for energy distribution measurements, the final hemispherical screen of the LEED/AES optics was biased positive to minimize the emission of tertiary electron from this screen, and less than 6% error was calculated for any tertiary electrons emitted by grids G1-G3 (see Appendix I.2). The retarding voltage on grids G2 and G3 was applied with a 0-10 V signal that was multiplied by an Ortec 556 high voltage power supply, while the the current on the final hemispherical screen was measured with a Keithley 6485 picoammeter. Further details on the experimental facility and technique for measuring secondary electron emission are discussed in Refs. [184, 185].

4.1.2 Facility for Measuring SEE from Nickel and Lithium

The ultra-high vacuum ($<5 \times 10^{-10}$ Torr) facility at PPPL in Figure 4.5 was used for SEE measurements of Ni and Li. Electron guns integral to LEED/AES optics and the AES system were used to produce primary electrons with energy up to 1500 eV and 3000 eV,

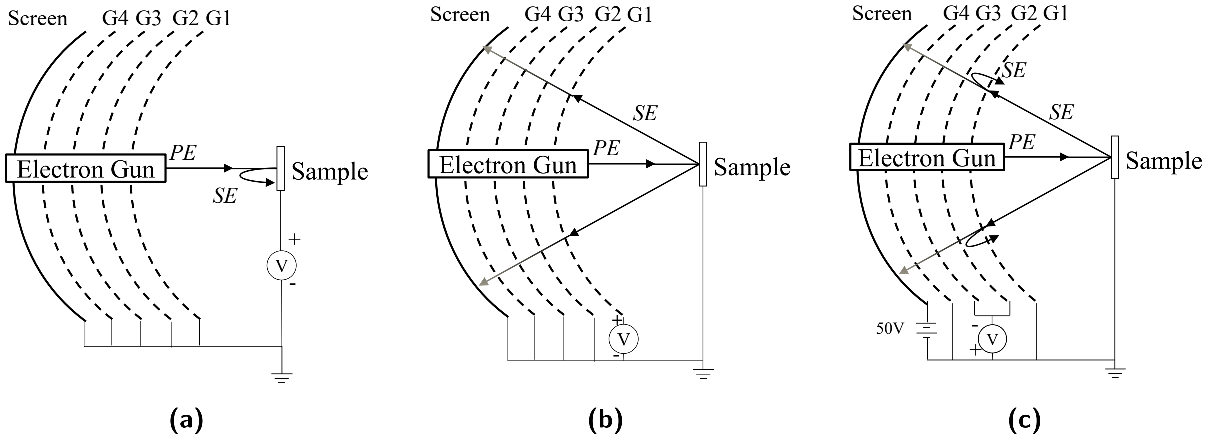

Figure 4.3: Configuration of the 4-grid LEED/AES optics for measuring: (a) primary electron current, (b) secondary electron current, and (c) secondary electron energy distribution function. PE = Primary Electron, SE = Secondary Electron

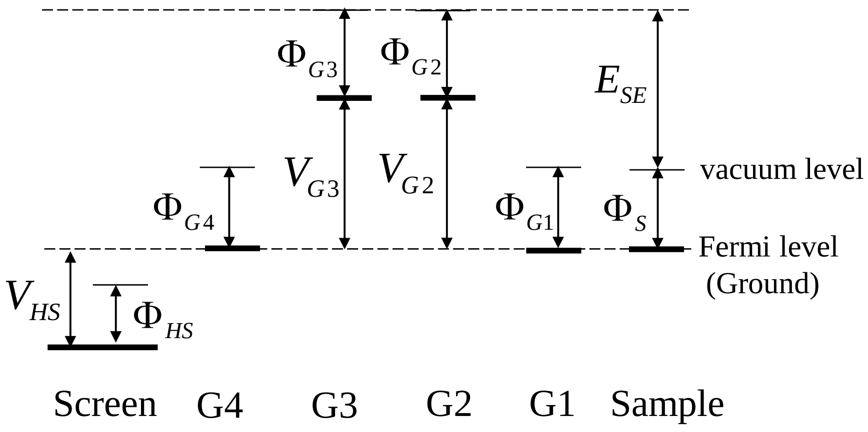

Figure 4.4: Energy level diagram for LEED/AES optics, where E_{SE} is secondary electron energy, V is applied electrode voltage, and Φ is electrode work function. S = sample, $G1-4$ = Grids 1 through 4, and HS = hemispherical screen.

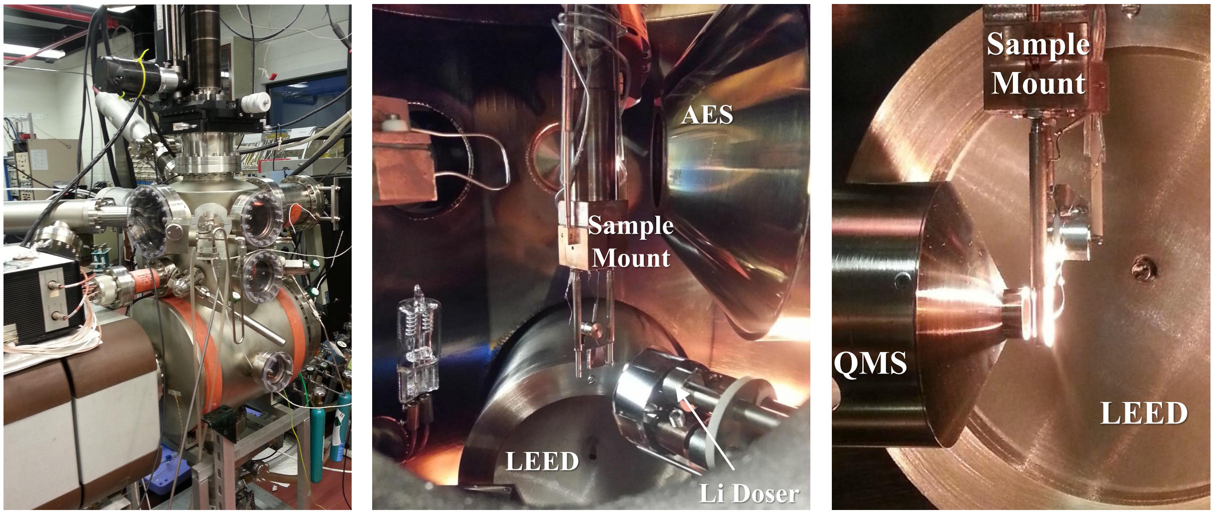

(a) (b) (c)

Figure 4.5: (a) External and (b-c) internal views of facility for measuring secondary electron emission from Ni and Li, and for preparing and characterizing the samples *in-situ*.

respectively, for SEE measurements. The sample method to measure total SEE yield was employed when using the electron gun from the LEED/AES and AES systems. The collector method was only employed when using the electron gun from LEED/AES optics, since the AES has a small collection solid angle. SEE yields from samples at elevated temperatures were only measured using the collector method since the sample was heated by running current through the sample from an external power supply. A Keithley 2410 source meter was used to apply voltage to and measure current from the sample; up to +150 V was applied to measure primary electron current, and -20 V to measure secondary electron current. A Keithley 6485 picoammeter in parallel with a +36 V battery was used to measure current on the LEED/AES optics. Measurements were performed repeatedly, and error bars due to measurement repeatability, systematic error due to unsaturated primary/secondary currents when suppressing/inciting SEE, and instrumentation error from the Keithley electrometers are included in the plots below.

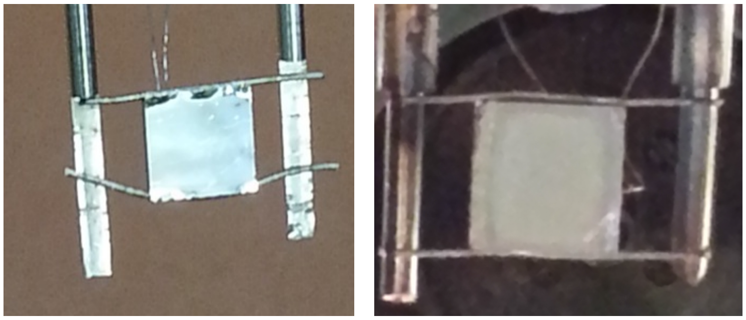
(a) (b)

Figure 4.6: (a) Ni(110) single crystal and (b) thick Li film on Ni.

4.1.2.1 Surface Preparation and Characterization of Ni(110)

A Ni(110) single crystal polished to a surface roughness of less than 0.01 μm, was mounted between two tantalum posts by spotwelding to 0.015-in diameter tantalum wire (see Figure 4.6(a)). The sample was cleaned of sulfur impurities by sputtering with 1 keV argon ions from a tectra GenII electron cyclotron resonance (ECR) plasma source. The sample was then flashed to 1100 K by running current through the tantalum wires to remove any adsorbed oxygen and carbon, and to anneal the sample. LEED was performed using the LEED/AES optics to obtain a diffraction pattern of the sample on the final phosphor-coated hemispherical screen, and thus to ensure that the sample was successfully annealed. A PHI 255G cylindrical mirror analyzer for AES was used to monitor the surface chemical composition before and after SEE measurements.

The SEE from Ni(110) under a number of conditions was investigated. The sample mount was attached to a rotary stage that allowed SEE to be measured at a range of primary electron incident angles from 0° to ±78°. By continuously running current through the tantalum wires spotwelded to the sample, the sample may be kept at elevated temperatures during SEE measurements. The current was set with a Eurotherm 3508 PID controller, and the temperature was monitored using a type C thermocouple spot-welded to the back of the sample. Ni with subsurface hydrogen was prepared by exposing Ni(110) to 700 eV deuterium ions from a PHI 04-303A ion gun at 2×10^{-8} Torr for 150 s, while the sample was at 250-280 K. After SEE measurements, the amount of adsorbed hydrogen was determined by using Temperature Programmed Desorption (TPD). During TPD, the sample was heated with a 10 K/s linear temperature ramp up to 650 K while monitoring the D (2 amu), HD (3 amu), and D_2 (4 amu) signals with a UTI 100C Quandrupole Mass Spectrometer (QMS); the Eurotherm 3508 PID controller was again used for TPD measurements. By comparing the total area under the D_2 desorption curve after the D_2^+ SEE measurements, to the total area under the H_2 desorption curve after H_2 exposure leading to H_2 saturation, it was calculated that the sample had 55% of the hydrogen saturation, which is 1.5 monolayers (ML) for Ni(110) [186].

The AES spectra of clean and as-received Ni(110) after SEE measurements are plotted in Figure 4.7. The AES spectra of clean Ni has large peaks at 61, 716, 782, and 848 eV, and smaller peaks at 102, 663, 676, and 865 eV corresponding to Ni [187]. The as-is Ni sample has additional peaks at 273, 381, and 510 eV, corresponding to C, N, and O, respectively. From the peak-to-peak heights of the C, N, O, and Ni peaks at 273, 381, 510, and 848 eV [187], respectively, and the AES sensitivity factors [188], the as-is sample was determined to be 78% Ni, 14% C, 5% N, and 3% O. No AES spectrum was recorded for the D_2^+ exposed sample since AES cannot detect hydrogen. H_2, HD, and D_2, desorbed from Ni(110) exposed to D_2^+ during TPD and after SEE measurements is plotted in Figure 4.8.

4.1.2.2 Surface Preparation and Characterization of Lithium Films

Lithium was deposited onto the Ni(110) substrate by thermal evaporation from a SAES Getters alkali metal dispenser [189] while the sample was held at room temperature (see Figure 4.6(b)). The dispensers are typically used for preparing thin Li films, but the Li films used here were made sufficiently thick such that there were no contributions to the SEE yield from the Ni substrate. The maximum penetration depths of 600 eV primary electrons in Li and Li_2O were determined from CASINO v2.48 [190] to be 56 nm and 17 nm; for mixed

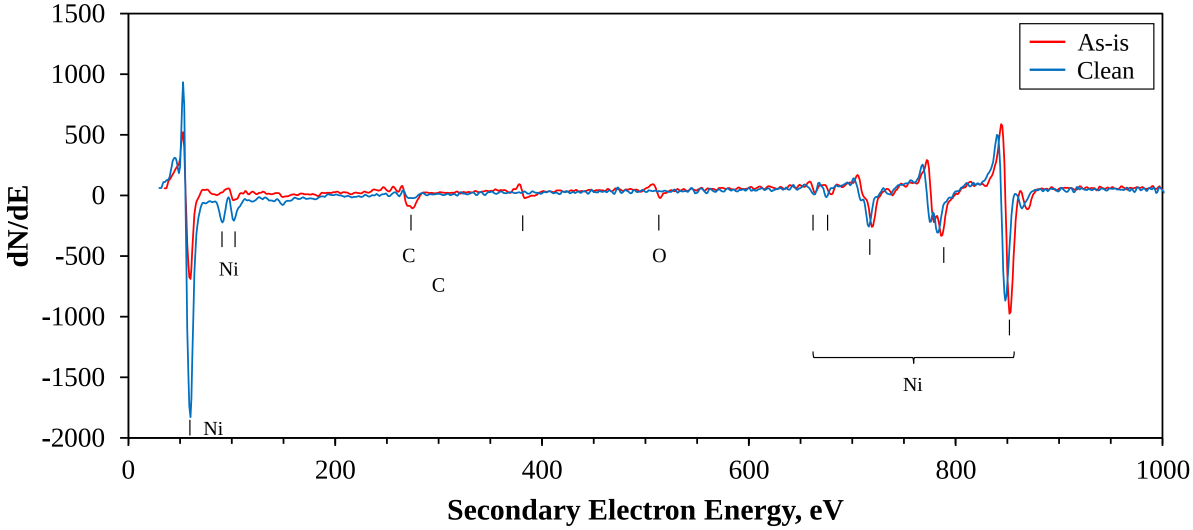

Figure 4.7: AES spectra of clean (blue) and as-received (red) Ni(110).

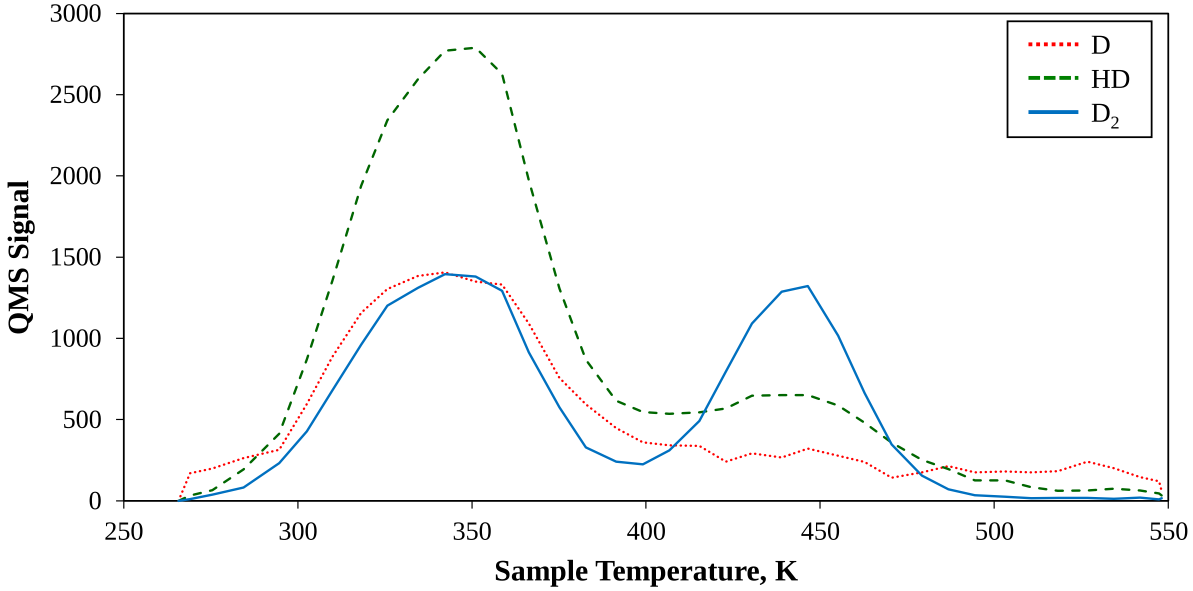

Figure 4.8: TPD Spectra of D (red dotted line), HD (green dashed line), and D_2 (blue solid line) desorbed from the D_2^+ exposed sample at a heating rate of 10 K/s.

films, assuming a 5-nm film of Li_2O on Li, maximum penetration depth is 40 nm. The film thicknesses used in this work are close to these calculated penetrations depths. However, the region of interest in this work is where the yield approaches a value of 1 and where it reaches a maximum, which occur at lower energies (less than 200 eV and 350 eV, respectively). The maximum penetration depth for 350 eV primary electrons in Li is only 22 nm, and therefore, the films generated in this work are thick enough to provide reliable data at these lower energies.

The Li film thickness was measured using TPD, which was conducted by resistively heating the sample with a 7-10 K/s linear temperature ramp up to 1300 K and monitoring the desorbed species with a QMS while the sample was in direct line of sight of the QMS ionizer. Temperature control was implemented using a Eurotherm 3508 PID controller, and the temperature was monitored using a type C thermocouple spot-welded to the back of the Ni sample. The amount of Li deposited on the surface was determined by comparing the total area under the Li desorption curve to the integral of the Li monolayer desorption curve. Figure 4.9(a) shows desorption curves of Li films of various thicknesses from Ni(110). For submonolayer Li coverages, only peaks at 770 and 910 K are observed [191]. For larger coverages, a multilayer peak starting at 500 k is also observed [191, 192]. The assignment of the one-monolayer Li TPD is shown by the shaded purple region [193]. Peaks at 990 and 1200 K (not seen in Figure 4.9(a)) correspond to the decomposition and desorption of Li oxide [192]. The amount of Li measured was converted to a film thickness assuming the metallic radius of Li is 1.52 Å[194] and the lattice parameter of Li_2O is 4.62 Å[195].

Li films with different levels of oxidation were created using two different approaches. In the first approach, a film of lithium oxide was created by evaporating Li onto the Ni sample for 15 minutes and then exposing the Li film to O_2 gas (99.999%, Specialty Gases of America) at a partial pressure of 1×10^{-7} Torr for 100 s (i.e., 10 L O_2 exposure). In the second approach, more of the Li film was oxidized by evaporating Li onto the Ni sample in a background of O_2 gas at a partial pressure of 1×10^{-7} Torr for 15 minutes (i.e., 90 L O_2 exposure).

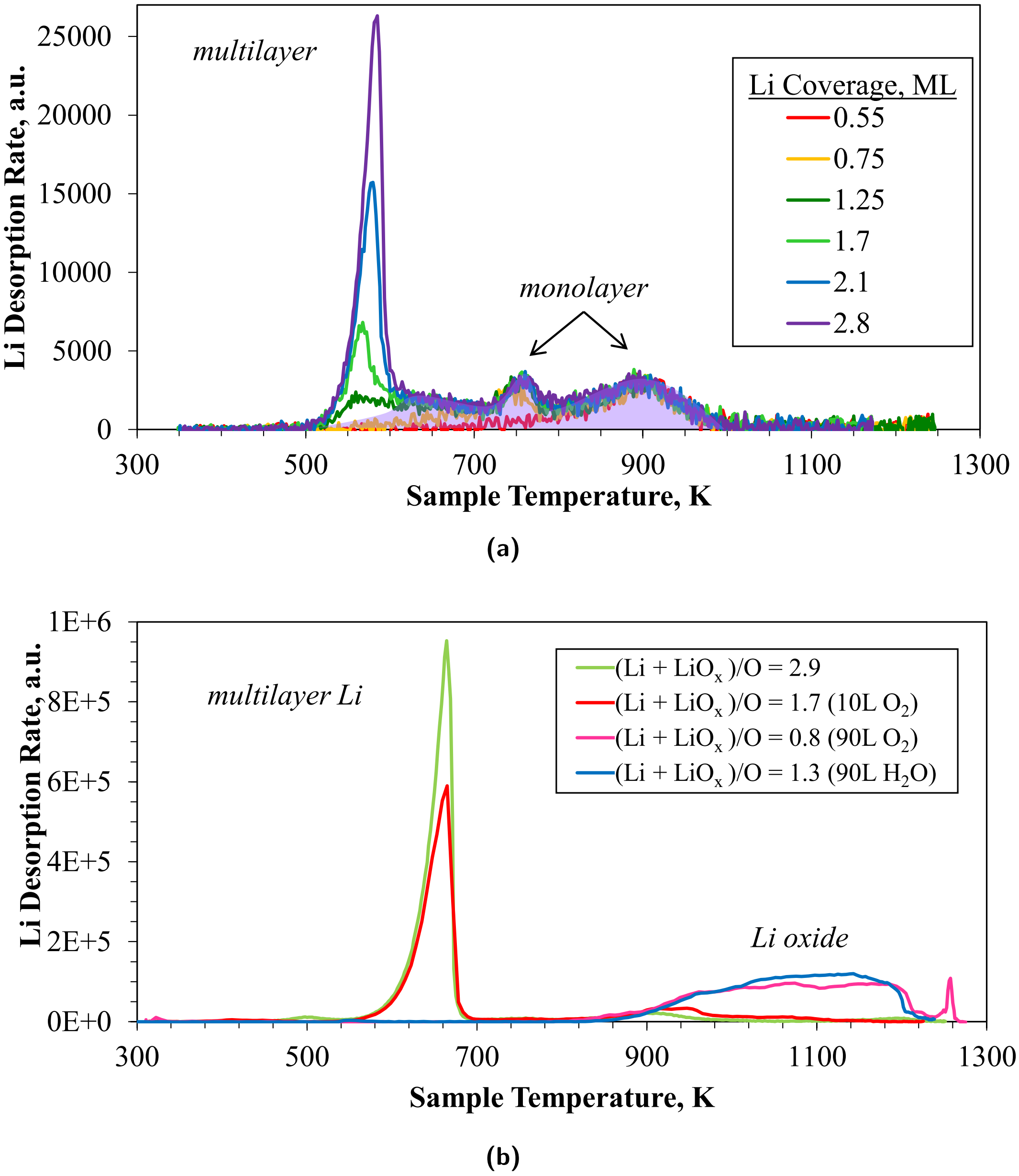

Figure 4.9: (a) TPD curves for Li films of various thicknesses on Ni(110). Desorption of the multilayer starts at 500 K, and monolayer peaks exist at 770 and 900 K. The shaded purple region is equal to one monolayer. (b) TPD curves for thick Li and Li oxide films of various compositions. Desorption of the multilayer starts at 500 K, and decomposition and desorption of Li oxide occurs at higher temperatures.

Table 4.1: Properties of Li Films with Different Oxygen and Water Exposures

	Film Thickness, ML	Chemical Composition						
		Ni	Li	LiO_x	O	C	F	$(Li + LiO_x)/O$
Li		48	9	6	0	12	23	3.8
Li	33	29	10	35	16	7	2	2.8
Li + 10 L O_2	20	37	2	35	21	3	1	1.7
Li + 90 L O_2	22	5	2	32	46	7	7	0.8
Li + 90 L H_2O	22	2	7	46	42	1	1	1.3

Contaminated Li samples were also created by evaporating Li while simultaneously exposing the sample to a background of water vapor (prepared using a freeze-pump-thaw degasification procedure in a Schlenk flask) at a partial pressure of 1×10^{-7} Torr for 15 minutes (i.e., 90 L H_2O exposure); the Li deposition and H_2O exposure were performed with the sample held at a temperature between 180 and 200 K. The latter approach ensured complete oxidation of the Li film.

TPD and AES were used to determine the chemical state of each film following SEE measurements. From Figures 4.9(b) and 4.10, 20-24 ML thick lithium oxide films were produced with $Li/LiO_x = 0.152$, 0.057, and 0.063 by exposure to 10 L O_2, 90 L O_2, and 90 L H_2O, respectively. Additionally, a 33 ML (i.e., 9-11 nm) thick Li film was produced with some oxidation ($Li/LiO_x = 0.30$) due to an outgassing event. Properties of all films are summarized in Table 4.1. The concentrations reported were determined from the peak-to-peak heights of LiO_x, Li, C, O, and Ni at 40, 51, 273, 510, and 848 eV, respectively, and applying the AES sensitivity factors listed in Refs. [196, 197]; the sensitivity factor for the Li oxide peak at 42 eV was assumed to be the same as for the metallic Li peak at 52 eV. Note that Ni peaks are visible in Figure 4.10 since the AES spectra were taken with 3 keV incident primary electrons, and the electron penetration depth in Li and Li_2O at 3 keV is much larger than at 350 eV or 600 eV (the energy range in which SEE was investigated).

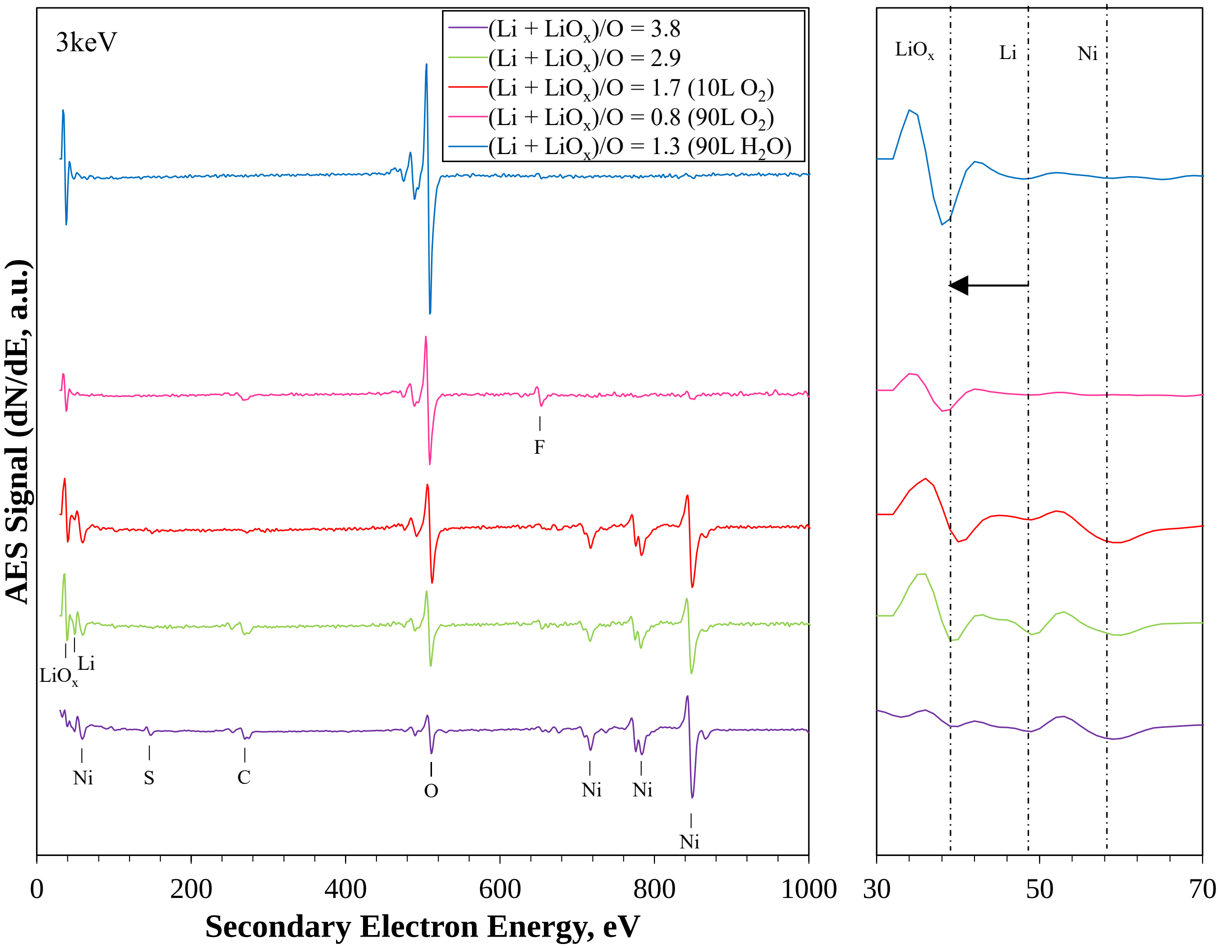

Figure 4.10: AES spectra of Li on Ni(110) with different oxygen and water exposures, and zoomed-in view at low energy. Important peaks are labeled.

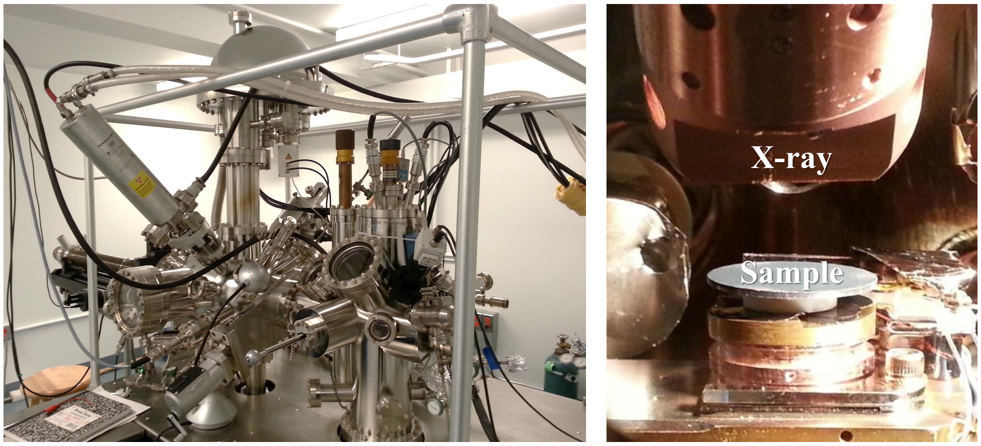

(a) **(b)**

Figure 4.11: (a) Facility for measuring secondary electron emission and characterizing the composition in-situ. (b) W fuzz sample positioned under the X-ray source for XPS.

4.1.3 Facility for Measuring SEE from Tungsten

Total SEE yields for smooth W and W fuzz were measured in an ultra-high vacuum chamber facility (with base pressure at 1 to 5×10^{-9} Torr) at Princeton University. A Kimball Physics 2×1 3310 electron gun produced primary electrons with energies up to 1 keV. The primary electron beam was characterized with a Faraday cup to ensure the beam is focused (diameter <3 mm) and centered on the sample. Primary electron current was measured on the sample when biased to +100 V or +150 V to collect all true secondary electrons and minimize elastically reflected electrons [185]; note that primary current was also measured on a Faraday cup and the primary currents using both approaches are within the total instrumentation error. Total SEE yields were measured using the sample method, and secondary electron current was measured on the sample when biased slightly negative (i.e., 0 to -20 V) to prevent collection of tertiary electrons from the chamber walls. Primary electron energies were corrected for sample bias. A Keithley 2410 source meter was used to apply voltage and read current from the sample. Less than 13% error in total yield was calculated from instrumentation error in the Keithley 2410 and systematic error due to non-saturated sample currents when suppressing/inciting SEE.

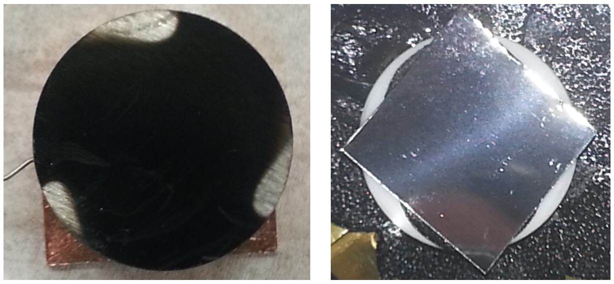

(a) (b)

Figure 4.12: (a) 1 in. diameter W fuzz sample. The black region is where W fuzz has formed due to He$^+$ exposure. (b) 15 mm x 15 mm smooth W sample.

Table 4.2: Tungsten fuzz fiber dimensions

Fiber diameter	25-50 nm
Fiber length	100-200 nm
Fiber separation	125-250 nm

4.1.3.1 Surface Preparation and Characterization

The W fuzz sample (see Figure 4.12(a)) was prepared at the MIT Plasma Science and Fusion Center by exposing bulk W at 1270 K to 60 eV He$^+$ (flux = 3.7×10^{21} m^{-2} s^{-1}, fluence = 1.3×10^{25} m^{-2}) [54]. A Scanning Electron Microscope (SEM) in a separate facility imaged the top surface of the W fuzz sample to determine fiber diameter and packing density. To estimate fiber length, a slit was cut in the W fuzz sample with a Focused Ion Beam (FIB) and the cross-section was imaged with SEM. Figure 4.13 shows that the W fibers are 25-50 nm in diameter, 5-10 fiber diameters apart, and 100-200 nm long. From Figure 4.13(c), the nanofeatures at the cut edge are distorted by cutting of the sample with FIB. Therefore, the fiber length measured is an estimate, but close to the lengths measured by Ref. [51] using other cutting techniques.

A smooth W sample (see Figure 4.12(b)) was cleaned with alcohol prior to insertion into the vacuum chamber. It was further cleaned *in-situ* by light sputtering with 500 eV Ar$^+$

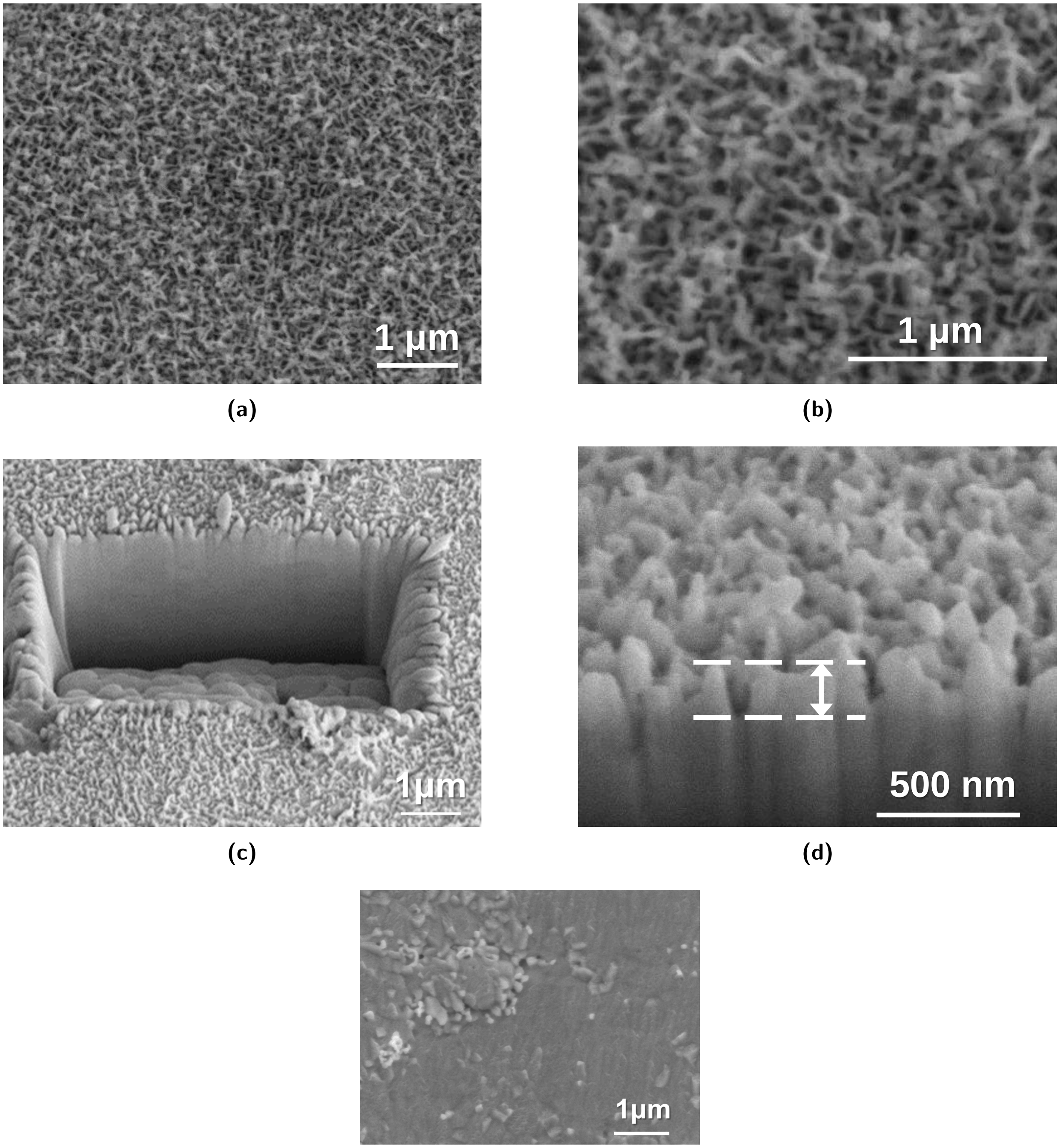

Figure 4.13: SEM images of the (a) top view and (c) cross-sectional view of the W fuzz sample. (b) and (d) are zoomed-in views of (a) and (c), respectively. A SEM image of a region on the sample that was not exposed to He$^+$ plasma (since covered by mounting clamps) and hence did not form fuzz is shown in (e) for comparison.

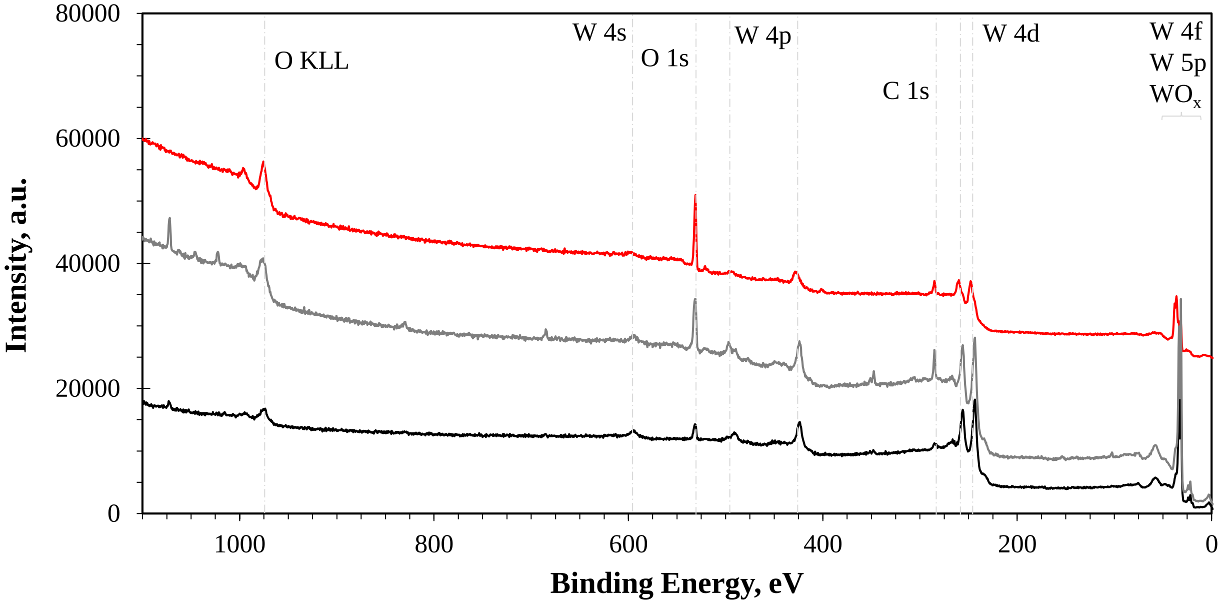

(a)

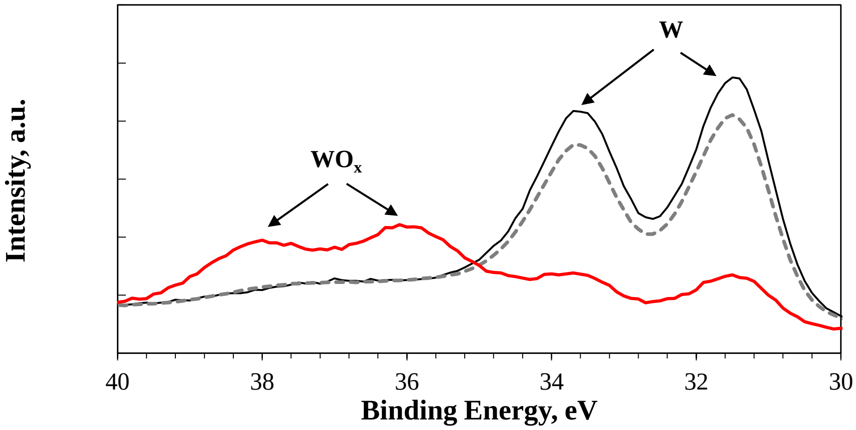

(b)

Figure 4.14: (a) Full XPS spectra of pre-sputtered smooth W (gray), Ar-sputtered smooth W (black), and W fuzz (red). Labels of the positions for W, O, and C are included. (b) Zoom in of W 4f and WO$_x$ peaks.

Table 4.3: Chemical Composition of Smooth W and W fuzz

	% W	% O	%C	WO_x/W
Smooth W, pre-sputtered	35	27	29	0
Smooth W, post-sputtered	63	14	22	0
W fuzz	31	41	27	1.5

to remove impurities for better comparison with previous SEE investigations of cleaned W. X-ray Photoelectron Spectroscopy(XPS) was used to characterize the sample surface *in-situ* before SEE measurements; a PHI 40-458 x-ray source with Al anode and SPECS PHOIBOS 100 hemispherical energy analyzer were used to obtain XPS spectra. Figure 4.14(b) shows the XPS spectra of W fuzz and smooth W between 30 and 40 eV binding energy. The smooth W spectra show large W peaks at 31 and 33 eV. The W fuzz spectra show smaller W peaks, and the appearance of large W oxide peaks between 35 and 38 eV ($WO_x/W = 1.53$); from Ref. [198], the oxide produced is WO_3. Additionally, there is a large oxygen signal at 531 eV in the full XPS scan for the W fuzz sample (see Figure 4.14(a)); this oxygen peak is significantly smaller for sputtered smooth W. From the full XPS scans, the surface compositions were 35.3% W, 27.4% O, and 28.6% C for pre-sputtered smooth W, 62.9% W, 13.8% O, and 22.3% C for post-sputtered smooth W, and 30.6% W, 40.9% O, and 26.8% C for W fuzz. Hence the light sputtering of the smooth W sample was effective in removing some, but not all, of the O and C impurities; the O was not in the form of WO_x as there was no WO_x peak in the XPS spectra of the smooth W sample in Figure 4.14(b). The W fuzz sample could not be cleaned by Ar sputtering to remove oxides since sputtering would almost certainly erode the W fibers.

4.2 Results of Secondary Electron Emission Properties

4.2.1 Graphite

Measurement of the SEE total yield and energy distribution were made for 50-500 eV monoenergetic primary electron beams impacting HOPG graphite at normal incidence. HOPG was investigated since it is the material used for plasma-facing components in many applications such as plasma thrusters, and divertors and limiters of magnetic fusion devices.

4.2.1.1 Total SEE Yield

The current from the sample to ground at each of several primary electron beam energies E_{PE} and sample voltages V_S are plotted in Figure 4.15(a). For all curves, the sample electron current increases to an asymptote as V_S increases. This is due to the increasing number of low energy true secondary electrons that are redirected back to the sample by the applied electric field. Note that while the positive sample voltage increases the primary electron impact energy at the sample, and hence changes the number of secondary electrons emitted, all true secondary electrons are recollected on the sample. Additionally the increased impact energy changes the number and/or energy of elastically and inelastically reflected electrons, but their contribution is negligible and decreases with primary electron energy. Hence the current on the sample at 50 V is primarily from incident primary electrons. As illustrated by Figure 4.15(a), the SEE current I_{SEE} can also be measured from the sample current: $I_S = I_{PE} - I_{SEE}$ where I_S is the sample current with no bias and I_{PE} is the primary electron current (i.e., the sample current at 50 V).

Figure 4.16 shows the current measured on the collector assembly of the LEED/AES optics for each primary electron beam energy E_{PE} and for various G1 grid voltages V_{G1} (Figure 4.3(b)). The secondary electron current to the LEED/AES optics initially increases substantially with increasing G1 voltage as more secondary electrons with emission angles greater than 60° from the surface normal are redirected to the LEED/AES system by the

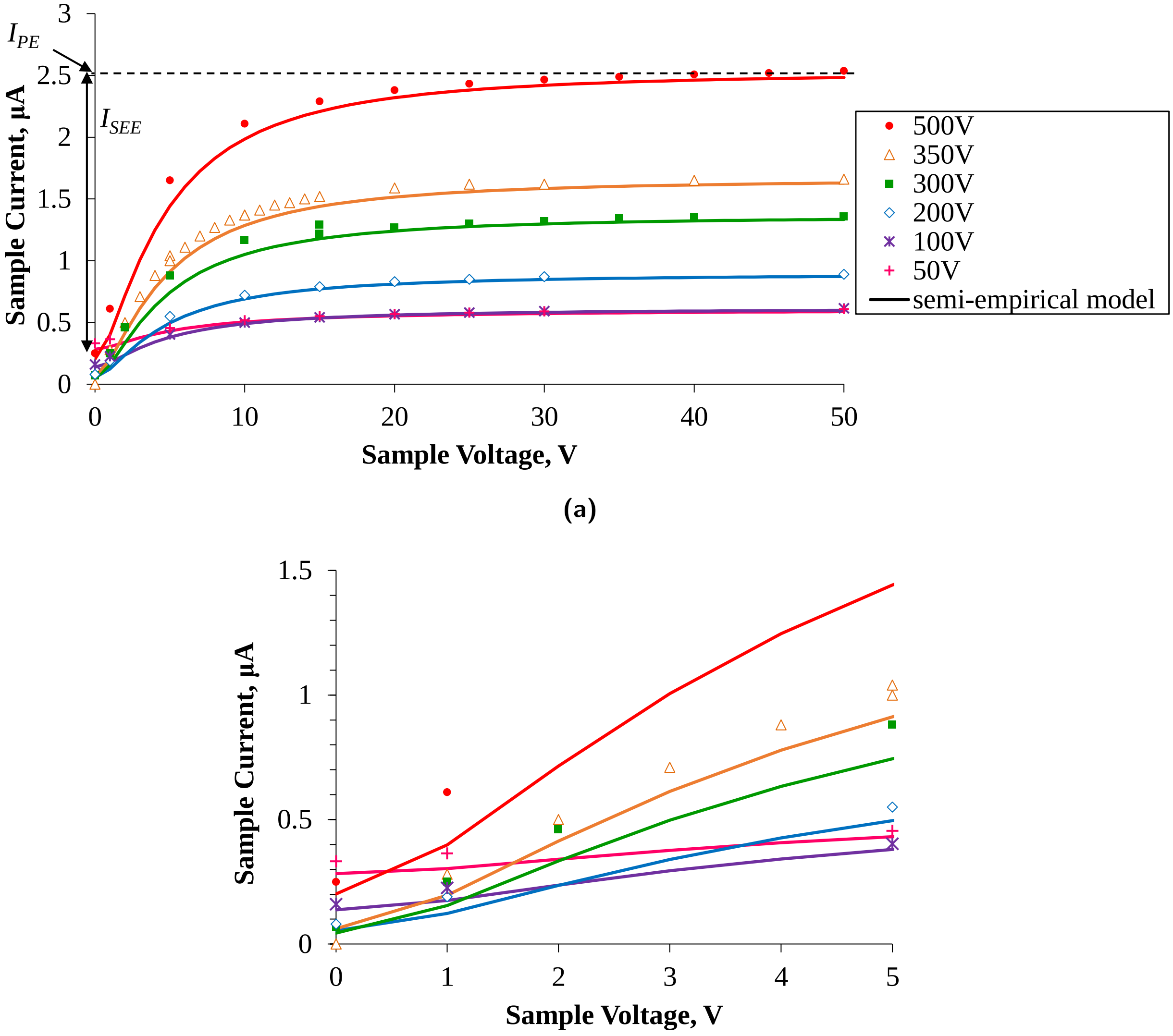

(a)

(b)

Figure 4.15: Current measured (symbols) from sample to ground for different primary electron energies and sample voltages. At each primary electron energy, the primary electron current is the sample current when the sample is at 50 V (e.g., see the dashed line for $E_{PE} = 500$ eV). The secondary electron current is the difference between the primary electron current and the sample current at zero sample voltage (e.g., see magnitude encompassed by the vertical arrow for $E_{PE} = 500$ eV). Also plotted are sample currents calculated from semi-empirical equations of SEE (solid lines; see section 4.3.1). A zoomed in view at low sample voltages in provided in (b).

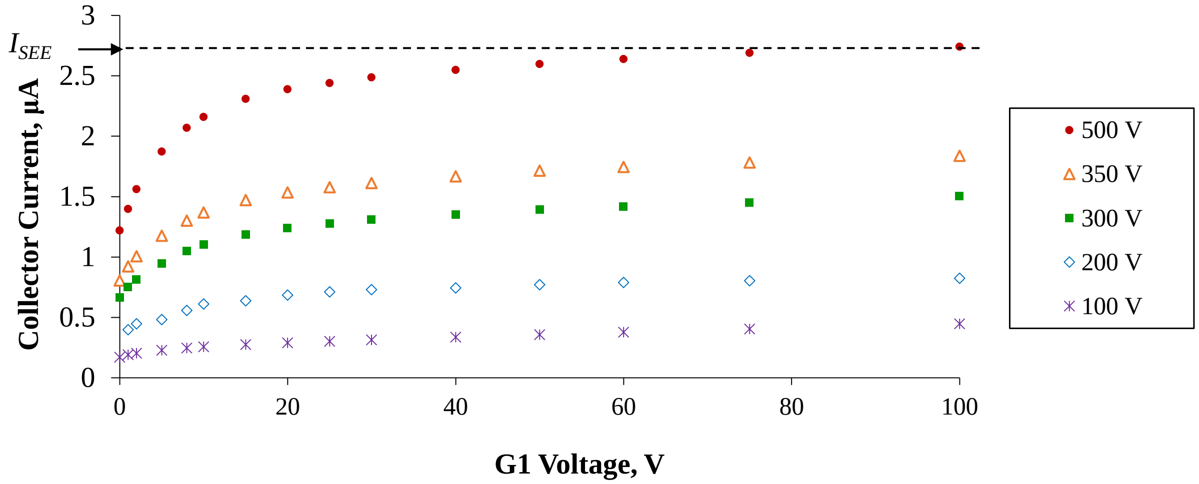

Figure 4.16: Collector current at different primary electron energies and G1 voltages. For each energy, the secondary electron current is found by taking the collector current when G1 is at 50 V (dashed line).

applied electric field, and then asymptotes. The SEE current for primary electron energies above 100 eV was set to be equal to the current measured when G1 is at 50 V (see the dashed line for $E_{PE} = 500$ V in Figure 4.16). Note that by measuring the SEE current on the entire collector assembly instead of the final collector (as is usually done13), negated the need to consider the effective transparency of the grids (which may be different than the optical transparency), thereby improving the accuracy of the measurements. For example, of the SEE current collected on the LEED/AES assembly in Figure 4.16, 85-87% was collected on G1, 12.5-13.5% on G2 and G3, and less than 1.5% on the hemispherical screen when G1 was biased to 50 V. This differs from the suggested 17% optical opacity of each of the grids. Also note that by biasing G1, an applied electric field is created in front of the sample that may have possible effects on the measurements (e.g., G1 attracting primary electrons and/or reducing the primary electron energy at the sample). However as is seen below, the effects caused by biasing G1 to 50 V do not seem to be significant since the SEE current calculated with the collector method compares well to the SEE current from the sample method.

The total SEE yield was calculated using both Equations 4.1 and 4.1, where the SEE current was measured from the sample current and the LEED/AES optics, respectively, and

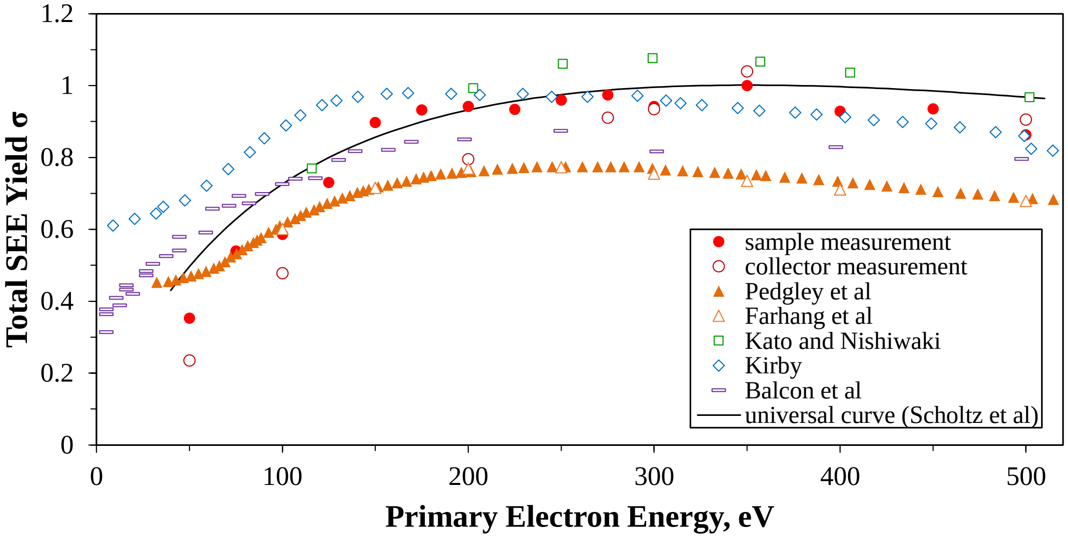

Figure 4.17: Total secondary electron yield for graphite from secondary electron current measurements using the sample current and LEED/AES collector assembly current. Comparison is made to measurements by Refs. [12, 13, 14, 15, 16] and a universal curve given by Ref. [17].

is shown in Figure 4.17. These measurements are compared to an empirical equation for the energy dependence of the total yield found by fitting a Gaussian function of $ln(E_{PE}/(E_{PE}^{max}))$ with variance $\alpha = 1.6$ to the experimental data [17]:

$$\sigma(E_{PE}) = \sigma_{max} \exp\left\{ -\frac{[ln(\frac{E_{PE}}{E_{PE}^{max}})]^2}{2\alpha^2} \right\} \tag{4.3}$$

where σ_{max} and E_{PE}^{max} are the peak total SEE yield and the primary electron energy at which the peak yield occurs, respectively, both of which are material specific. From Figure 4.17, the total yields measured compare well with the empirical equation. Note that for semiconductors, values for σ_{max} and E_{PE}^{max} are similar to values for conductors since the energy bands near the Fermi level are thermally populated with electrons. However for insulators, the maximum yield is larger since the mean free path for secondary electrons en route to the surface is much larger in insulators than the mean free path in metals (due to a lack of free electrons and hence a reduction in electron-electron interactions) [132, 133].

In Figure 4.17 we also plot the total yield measurements by Pedgley *et al* [12], Farhang *et al* [13], Kato and Nishiwaki [14], Kirby [15], and Balcon *et al* [16]. We postulate that the large variation in experimental measurements is due to the dependence of the yield on the condition of the graphite surface when measurements were taken (e.g., if the sample was processed to remove oxidation and the level of vacuum in the testing chamber). Farhang *et al* [13] and Pedgley *et al* [12] operated in vacuum chambers at 10^{-9} Torr and heated the samples by electron bombardment. The data from Kato and Nishiwaki [14] are for as-received graphite samples, as are the present measurements. In Figure 4.17, the present measurements lie close to the measurements from Kato and Nishiwaki, thereby validating the development of this facility for SEE measurements.

4.2.1.2 Emitted Secondary Electron Energy Distribution

The measured secondary electron energy distributions for 75 to 500 eV primary electrons incident on graphite are shown in Figure 4.18, along with previously measured secondary electron energy distributions for 100 eV[18] and 425 eV[19] primary electrons incident on graphite. There are two main peaks of E_{SE} in Figure 4.18(a). The first peak at lower energies (i.e., below 50 eV) is due to true secondary electrons generated within the material, while the second peak at higher energy (i.e., $E_{SE} = E_{PE}$) is due to elastically reflected electrons that have lost little to no energy in collisions with surface atoms. The latter peak confirms the energy of the primary electron beam. Additional smaller peaks within a few eV of E_{PE} are due to specific inelastic losses suffered by the elastically reflected electrons.

Figure 4.18(b) shows the secondary electron distribution curves normalized by the primary electron current I_{PE} for each primary energy:

$$N(E_{SE}) = -\frac{1}{I_{PE}} \frac{I_{HS}(V_{G2,3}^{2}) - I_{HS}(V_{G2,3}^{1})}{V_{G2,3}^{2} - V_{G2,3}^{1}} \tag{4.4}$$

where E_{SE} is the energy of the secondary electrons with respect to the sample vacuum level and $I_{HS}(V^i_{G2,3})$ is the current measured on the hemispherical screen of the LEED/AES optics when retarding voltage $V^i_{G2,3}$ is applied on grids G2 and G3. Focusing on the peak of true secondary electrons ($E_{SE} < 50$ eV), the distributions are compared to a theoretical result that treats SEE as a three-step process: (i) ionization/excitation of secondary electrons by primary electrons, (ii) transport of secondary electrons to the material surface, and (iii) escape of secondary electrons from the material work function [20]. The energy distribution derived by Chung and Everhart [20] for conducting and non-conducting material, assuming charge accumulation has negligible effect on the beam (e.g., sufficiently short beam exposure times for non-conducting material) [135, 199], is given by

$$N(E_{SE}) = C\frac{E_{SEE}}{(E_{SEE} + \Phi_S)^4} \tag{4.5}$$

where C is a material constant, Φ_S is the work function of the material, and E_{SE} is the energy of the secondary electron with respect to the sample vacuum level (i.e., $E_{SE} = V_{G2,3} - (\Phi_S - \Phi_{G2,3})$, see Figure 4.4). From Figure 4.18(b), at higher secondary electron energies (i.e., above 10 eV) the measured energy distributions agree well with the theoretical distribution for the range of primary electron energies examined. Below 10 eV, there is a large scatter in the measured distributions due to the low resolution of $V_{G2,3}$ applied. However, the distributions are seen to follow the trend of the theoretical curve with a maximum between 1.3 and 3 eV.

The contributions to the secondary electron yield from elastically reflected, inelastically reflected, and true secondary electrons can be separated from the energy distributions in Figure 4.18(a). In Figure 4.19 we plot the yields of elastically reflected electrons, the sum of elastically and inelastically reflected electrons, and true secondary electrons for graphite between 50 and 500 eV, along with an empirical curve for the elastically reflected yield [17]:

$$\eta(E_{PE}) = \sigma(E_{PE}) \exp[1.59 + 3.75 \ln E_{PE} - 1.37(\ln E_{PE})^2 + 0.12(\ln E_{PE})^3] \tag{4.6}$$

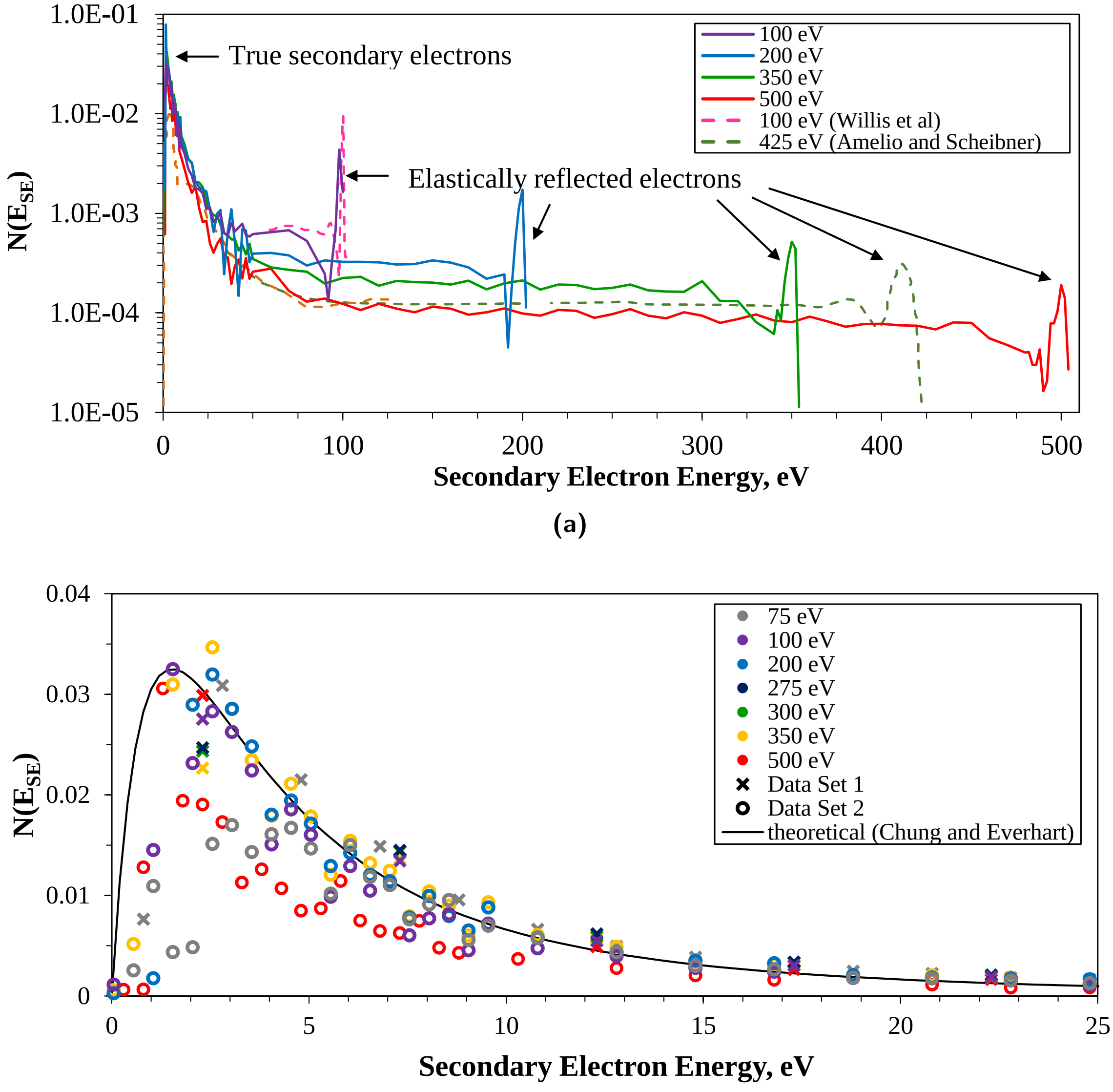

(a)

(b)

Figure 4.18: Secondary electron energy distributions (with respect to the sample vacuum level) for 75 eV through 500 eV primary electrons impacting graphite. Previous measurements by Willis *et al* [18] and Amelio and Scheibner [19] are included in (a). A zoomed in view at low secondary electron energy is provided in (b), as well as comparison to the theoretical distribution given by Chung and Everhart [20].

where η is the yield of elastically reflected electrons and E_{PE} is between 5 and 100 eV. In deriving Eq. 4.6, Scholtz *et al* [17] fit a single curve to data from various materials. From Figure 4.19 the experimentally measured yield for graphite follows a similar curve. The yield of elastically reflected electrons increases as the primary electron energy decreases. This agrees with theory that as the primary electron energy is reduced, elastically reflected electrons become increasingly important. However, the exact behavior at very low primary electron energy (below approximately 30 eV) is still uncertain since previous measurements at low primary energies were difficult due to the limitation of electron guns to produce beams of ample primary electrons at low energies (where the current is space charge limited) and/or due to the presence of stray electric and magnetic fields (including the Earths magnetic field) that can affect low energy primary electron beams. For example, Balcon *et al* [16] warned that the absence of a magnetic shield in their measurements (where the distance from the electron gun to the sample was larger than the primary electron gyroradius) could have possibly prevented beam primary electrons from reaching the sample surface.

Also plotted in Figure 4.19 are curves for the true secondary yield and the elastically and inelastically reflected yield measured by Pedgley *et al* [12] and El Gomati *et al* [21] for graphite. Our results for the elastically and inelastically yield follow the trend of these two prior reports, i.e., the yield increases with primary electron energy at low energies (below 125 eV) and is relatively insensitive to energy at higher primary energies. Our measured elastically and inelastically yields are consistent with Pedgley *et al* [12] at low primary electron energies, but are larger than values measured by Pedgley *et al* [12] and El Gomati *et al* [21] at higher energies. The true secondary yield determined herein also follows the trend of Pedgley *et al* [12] with values comparable with their measured values. Quantitative differences with the results of Pedgley *et al* [12] could be due to differences in sample preparation and cleanliness.

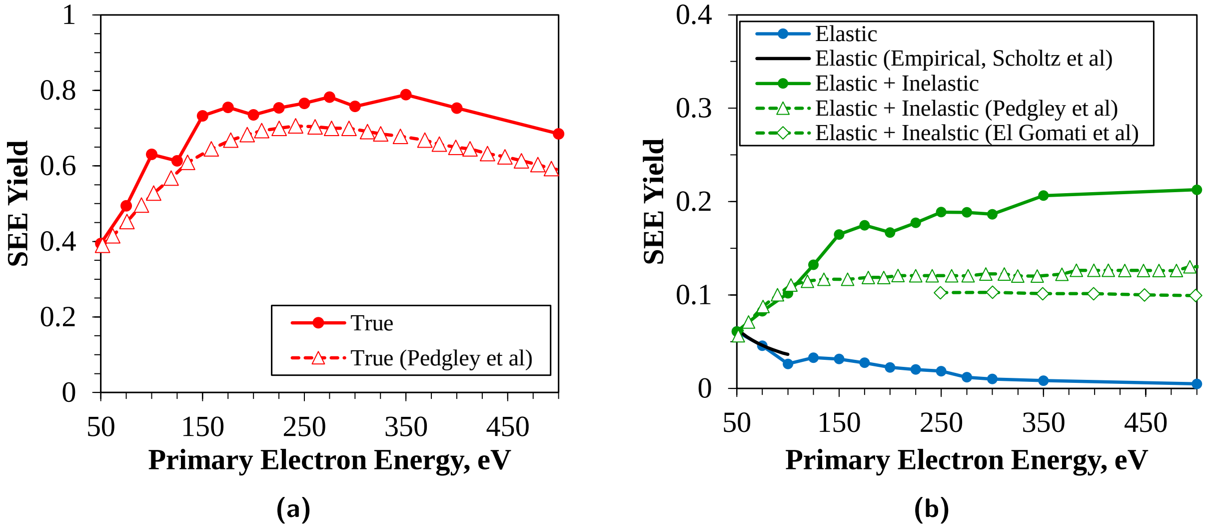

Figure 4.19: Yields of elastically reflected, inelastically reflected, and true secondary electrons versus primary electron energy for graphite. Comparison are made to previous measurements by Pedgley *et al* [12] and El Gomati *et al* [21] and to values calculated using Equation 4.6 [17].

4.2.2 Lithium and Lithium Oxide

Figure 4.20 shows the total SEE yield as a function of primary electron energy for lithium films of different oxygen and water exposures. Measurements using the sample (filled symbols) and collector (unfilled curves) methods are within 10% of each other. For the oxidized 20-22 ML (i.e., 9-11 nm) thick films, two datasets were collected for each film over a 1-h time period and no change was observed, indicating that charging does not occur for these films. This may be the result of electron tunneling, which can occur in lithium oxide films 5-10 nm thick [200, 201]. The relative error in yield measurements is 5-10% for O_2 films and up to 20% for the H_2O film; this includes instrumentation error of the Keithley 2410 source meter and Keithley 6485 picoammeter in addition to the systematic error due to non-saturation of currents when attempting of fully collect or repel secondary electrons. Previous results from Bruining and de Boer [22] are also plotted for comparison as the black curve (for pure Li) and gray curve (for contaminated Li).

From Figure 4.20, the yield for Li films with $(\mathrm{Li} + \mathrm{LiO}_x)/\mathrm{O} = 3.8$ and 2.9 have maximums

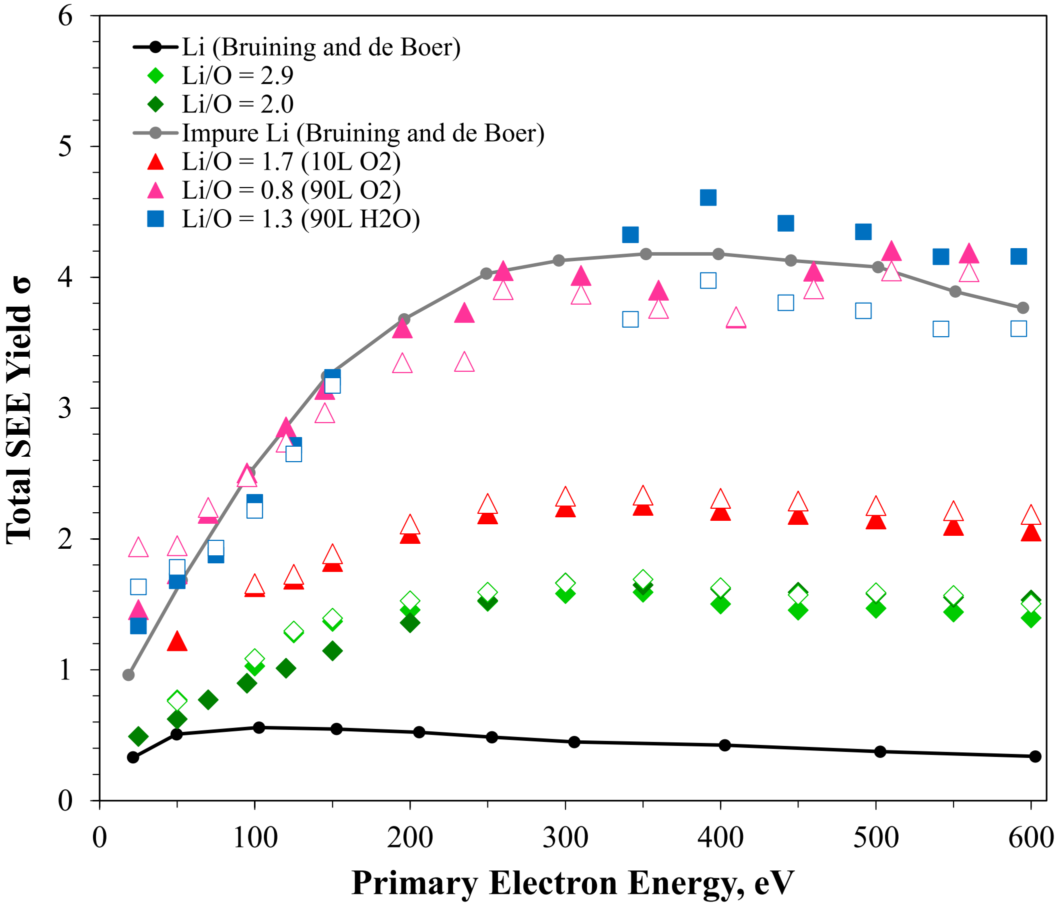

Figure 4.20: Total secondary electron yield for lithium films with different oxygen and water exposures. Measurements used the sample current (filled symbols) and LEED collector current (unfilled symbols). Comparisons are made to a measurements by Ref. [22].

at 350 eV of 1.2 and 1.7, respectively. These are higher than the yield measured by Bruining and de Boer for "‘pure" Li, which has a maximum yield of 0.6. The discrepancy is due to the fact that the metallic Li films were exposed to approximately 5 L of CO_2 when a vacuum component outgassed just prior to SEE measurements. This resulted in some oxygen contamination as indicted by the oxygen and lithium oxide peaks in the AES and TPD spectra (see Figures 4.10 and 4.9(a)).

Figure 4.20 shows the yield is 40% higher when Li is exposed to 10 L of oxygen, resulting in further oxidation and (Li + LiO_x)/O = 1.7. The yield reaches a value of 1 at primary electron energies less than 70 eV, and has a maximum of 2.3. Also shown in Figure 4.20 are results from a Li film that was deposited in an oxygen background at pressures high enough to ensure complete oxidation of the film. AES in Figures 4.10 indicated that a (Li + LiO_x)/O ratio of 0.8 was reached, and the post-experiment TPD in 4.9(a) indicated full conversion to Li oxide (i.e., no metallic Li peak at low temperature). The yield for the fully oxided Li film is shifted further upward and matches the yield from Bruining and de Boer for contaminated Li, particularly at low primary electron energies (less than 150 eV).

Results indicate that the maximum SEE yield increases with oxygen content. The increase is likely due to the fact that lithium oxide is insulating. Insulators have no conduction electrons, and secondary electrons generated in the material bulk are less likely to experience e-e collisions en route to the material surface [135]. Thus, secondary electrons are more likely to arrive at the surface with enough energy to overcome the surface potential barrier and be emitted. Additionally, the increase in SEE with oxygen content may be due to to a change in work function. Parker and Rhead observed an initial decrease in work function, and thus, an increase in SEE with increasing O_2 exposure of Li films on a Ag(111) substrate [202]. For a 1 ML thick Li film, the work function reached a minimum at approximately 1 L of O_2. For thicker Li films, the work function is thought to decrease with further O_2 exposure. Hence, for the 33 ML thick Li films studied here, the work function may decrease for O_2 exposures up to 90 L, which may also explain the increase in the SEE yield.

The increase in SEE with Li oxidation observed here contradicts conclusions made by Oyarzabal *et al* [152], which were based on sputter times of oxidized Li immersed in a He plasma. No direct measurements of oxygen contamination in the Li were reported by Oyarzabal, and it is not clear if the He plasma was effective at sputtering the oxygen or if it introduced more impurities due to the high gas pressure. Furthermore, it is uncertain if sputtering lead to surface roughnening, which can also affect SEE.

Figure 4.20 shows the total SEE yield for a Li film that was completely oxidized by depositing Li in a background of H_2O. The yield values are very similar to those for a Li film that was completely oxidized in O_2 (i.e., 90 L O_2) and also match the yields measured by Bruining and de Boer [22]. The yield reaches a value of 1 at primary electron energies less than 25 eV and has a maximum of between 3.9 and 4.6.

Hoenigman and Keil determined through XPS that a 1 ML Li film exposed to between 5 and 100 L of O_2 resulted in the formation of Li_2O [203]. They also suggested that for H_2O exposures between 1 and 100 L, Li_2O is predominant over LiOH at room temperature. Hence, for 1 ML of Li and for O_2 and H_2O coverages less than 100 L, O_2 and H_2O are dissociated on Li to form Li_2O. Assuming this to also be true for Li films thicker than 1 ML, the similarity in the SEE yield curves between the samples of Li exposed to 90 L of O_2 and 90 L of H_2O can be explained by the formation of Li_2O in both samples.

4.2.3 Tungsten

4.2.3.1 As-Received and Sputter Cleaned Smooth Tungsten

Figure 4.21(a) shows the total SEE yield measured from sputtered smooth W at 0° [204]. The maximum σ is 1.6 at 700 eV and the critical value of $\sigma = 1$ occurs at 140 eV. Results are compared to previously published results for SEE from polycrystalline W cleaned by heating the sample to 1300 K [23] or 2700 K [24, 25], and by ion sputtering [21, 26]. From Figure 4.21(a), the total SEE yield matches with previous values for the range of primary electron energies considered. Some deviations from these previous studies are likely due to differences in surface composition, which was not previously monitored with XPS or any other technique. Therefore, this work also provides the first SEE measurements of smooth W with *in-situ* characterization of the surface at these laboratory plasma relevant energies. Yields from El Gomati and Walker [21, 26] are significantly lower and be underestimated since yields were measured using a collector method with LEED/AES-like optics, and may not have considered the grid transparency.

Also plotted in Figure 4.21(a) is the total SEE yield for smooth W at 0° prior to sputter cleaning. The yield for the pre-sputtered W is up to 48% higher than for post-sputtered W since O and C contamination [205] and many oxides [206, 207] increase SEE (due to an increased secondary electron mean free path within the material). Refs. [23], [26], and [21] also saw a higher total yield (up to 35% higher) for ungassed W than for sputter cleaned W at primary energies <500 eV.

Additionally, the total SEE yield measured from smooth, sputtered W at 45° is compared in Figure 4.21(b) to the yield calculated for 45° assuming SEE yield from the sample follows a $1/\cos(\theta)$ dependence (i.e., $\sigma_{calc}(45°) = \sigma_{exp}(0°)/\cos(45°)$). From Figure 4.21(b), there is a large increase in measured yield with angle: the maximum σ increases from 1.6 to 2.3 and the energy at which $\sigma = 1$ decreases from 149 to 75 eV. Furthermore, the measured and calculated yields at 45° agree well, confirming that smooth W follows a $1/\cos(\theta)$ dependence typical for smooth polycrystalline samples. This dependence is due to the increased generation of secondary electrons within the material escape depth at grazing angles [135, 132]. Since the yield for the smooth, sputtered W is within the range of published values, increases with O and C contamination, and follows a $1/\cos(\theta)$ dependence as expected, the measurements in Figure 4.21 of smooth W validate the use of the facility for SEE investigations. Yields measured by Chaudhri and Khan [27] are lower than measured in this work, and may be due to differences in chemical composition and/or use of the collector method for measuring secondary electron current.

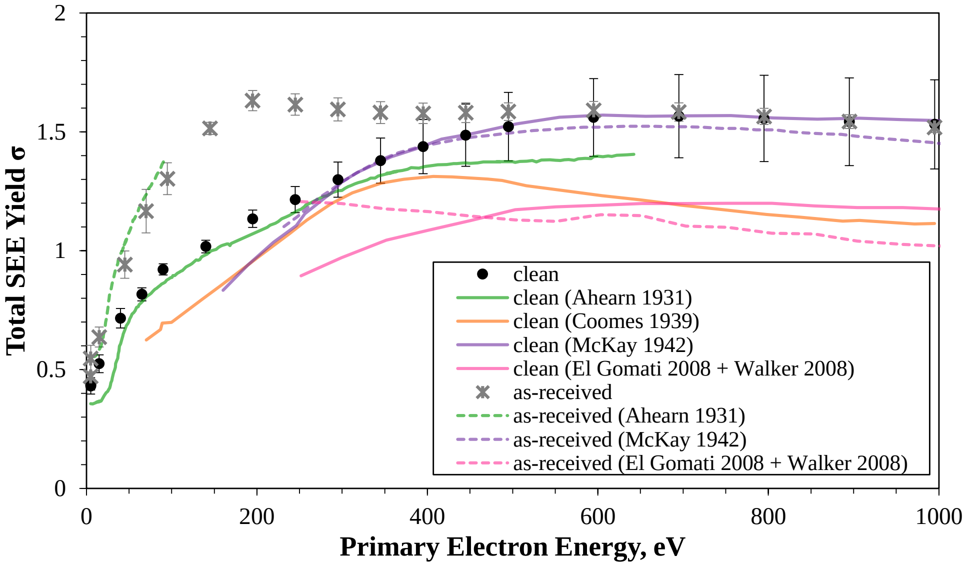

(a)

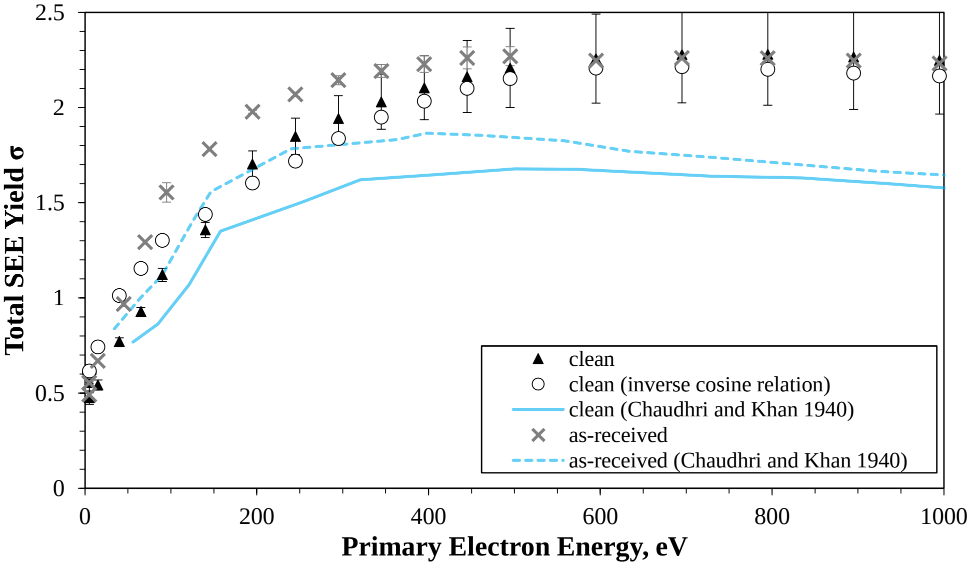

(b)

Figure 4.21: The total SEE yield from smooth, sputtered-cleaned W as a function of primary electron energy, for primary electrons incident at (a) 0° (black filled circles) and (b) 45° (black filled triangles). Measurements at 45° are compared to values calculated considering a $1/\cos(\theta)$ dependence (black open circles). Also shown are SEE yields of the as-received W sample prior to sputtering cleaning (gray asterisks and crosses). Comparison is made to previous measurements by Ahearn [23], Coomes [24], McKay [25], El Gomati *et al* [21], Walker *et al* [26], and Chaudhri and Khan [27] (solid and dashed lines).

4.2.3.2 Tungsten Fuzz

The total SEE yield from W fuzz at 0° and 45° are compared to smooth W in Figure 4.22(a) [204]. Data show two important trends: (1) W fuzz significantly reduces SEE yield compared to smooth W and (2) W fuzz SEE is largely independent of primary electron incident angle. Both of these trends can be explained by a discussion of the secondary electron behavior in the presence of the W fuzz structure.

Assuming W fuzz has a cage-like geometry comprised of vertical and horizontal fibers, primary electrons at normal incidence impact either the flat substrate, the top of vertical fibers, or the curved sides of horizontal fibers. The penetration depth for 1 keV primary electrons is $\sim$5 nm in W (from CASINO v2.48 [190]), and smaller for lower energy incident electrons. Therefore, over 97% of the primary electrons impacting the 25-50 nm fibers can be assumed to not pass through an individual fiber. Primary electrons impacting the flat top of vertical fibers or the smooth substrate should not change the SEE, while the curved fiber sides should increase secondary electrons generation and enhance local emission since SEE yield increases with local incident angle. Thus the net reduction in SEE observed for W fuzz at 0° incidence can be attributed to trapping of secondary electrons within the complex fuzz structure, and not from a reduction in secondary electrons generated within the fibers.

Similar reductions in SEE yields at normal incident have been measured for conducting surfaces with nm to mm-sized soot particles [132], triangular and rectangular grooves [208, 165, 166], pores [161], dendrites/fibers [44, 164, 163], and surface roughness [167]. Complementary computational modeling for the porous, grooved, and fiberous surfaces by Refs. [160], [165], and [11], respectively, show a reduction in SEE for these featured surfaces, particularly for features with large aspect ratio. An important aspect of the SEE behavior of these naturally-occurring W-fuzz structures is that, unlike the artificially structured surfaces mentioned above which may be eroded by ion sputtering when exposed to plasma, W fuzz is self-produced in a He plasma and therefore builds a natural suppression against SEE.

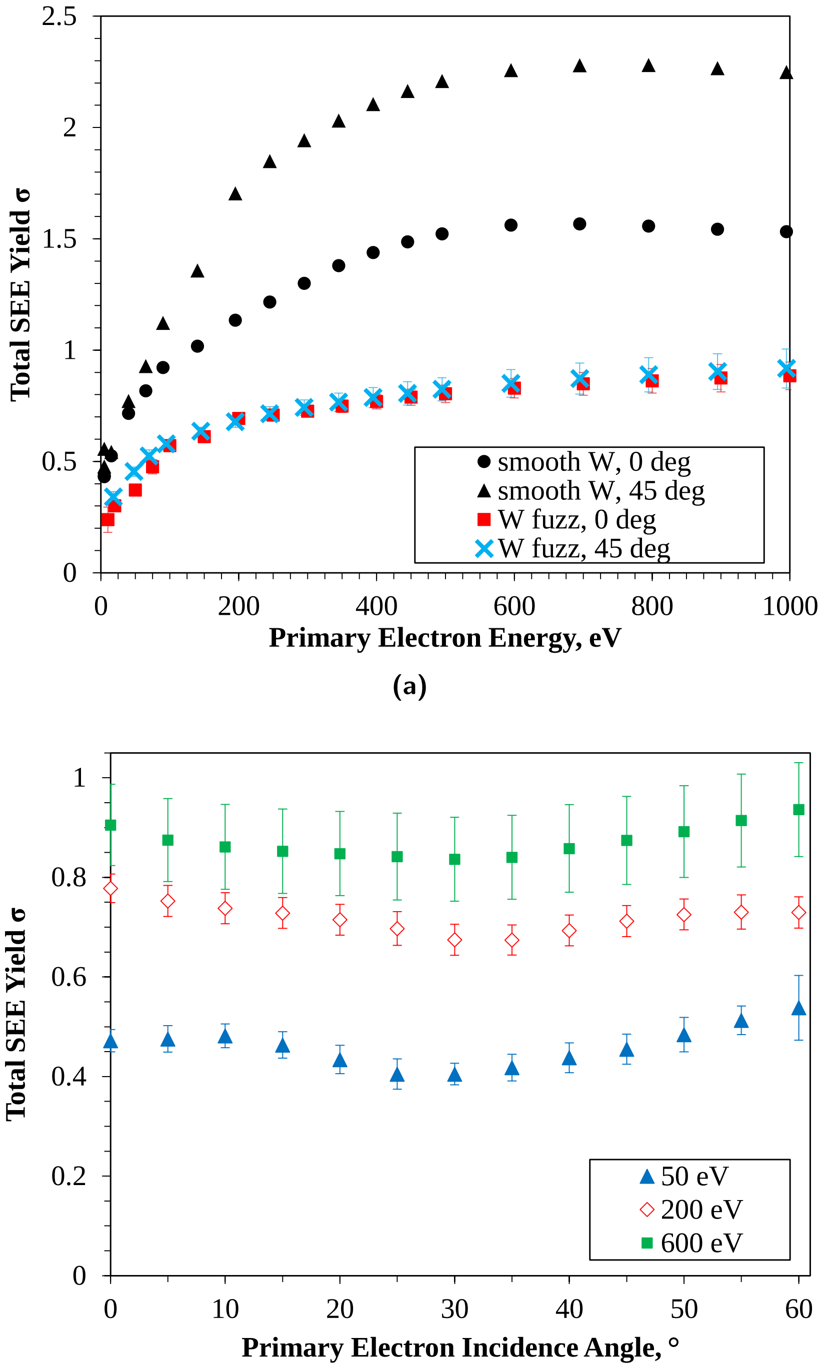

(a)

(b)

Figure 4.22: (a) Total SEE yield from W fuzz as a function of primary electron energy, for primary electrons incident at 0° and 45°. Total SEE yields from smooth W at 0° and 45° are reproduced. (b) Total SEE yield from W fuzz as a function of primary electron incidence angle for primary electrons at 50 eV, 200 eV, and 600 eV.

Note that the reduction in SEE from W fuzz is not due to the large amount of WO_x, O, and C on the surface, since this study and previous studies on contaminated W surfaces show that adsorbed O and C and many oxides increases SEE, especially at low primary electron energies [23, 26, 21, 27, 205, 206, 207]]. Hence the reduction in SEE for W fuzz is in fact due to the nanostructuring of the surface.

Figures 4.22(a) and 4.22(b) show that the total SEE yield from W fuzz is nearly independent of incident angle (within experimental error). While the fundamental $1/\cos(\theta)$ dependence of SEE on local incident angle is preserved, the orientation of the fibers within the complex fuzz structure leads to a wide distribution of local incident angles that is independent of the global primary electron beam angle. Additionally, recapturing of secondary electrons reduces the influence on global incidence angle.

A lack of angular dependence is direct quantitative evidence that the SEE measured is entirely from the complex W fuzz structure and not from the underlying smooth substrate. SEE from smooth polycrystalline surfaces follows a $1/\cos(\theta)$ dependence, and angular dependence is expected if primary electrons that were able to reach the substrate create secondary electrons that are able to reach the fuzz surface. Therefore, SEE from the substrate has a negligible effect on our measurements

A similar weakening of the dependence of true/total SEE yield on incident angle was also measured for structured carbon and copper with μm-sized dendrites [162, 163], silver with μm-sized pores [161], and carbon and silver with μm-sized roughness [167]. Modeling of the dendritic [11] and porous surfaces [161] captured this weakening on angle (e.g., 30% simulated increase for dendritic surfaces versus 40% increase for smooth surfaces between 0° and 45°). As mentioned above, unlike previous experimental and modeling efforts on artificially structured surfaces, the W fuzz materials considered herein are self-generated in He plasma. Additionally, whereas previous efforts have shown an angular dependence for artificially structured surfaces, the total SEE yield for W fuzz is independent of angle between 0° and 60°.

An important trend from the W fuzz data is the very large reduction in SEE at high incident electron angles. At oblique angles there is a larger reduction of SEE for W fuzz over smooth W. For example, near 500 eV there is a 47% reduction in SEE for primary electrons incident at 0° but a 63% reduction in SEE at 45°. Since the retarding potential of the plasma sheath reduces the normal component of the incident electron velocity, high angle incident electrons will dominate in plasma devices. Therefore these results can be important for plasma applications.

4.2.4 Nickel Single Crystal

Total SEE yields for clean Ni(110) at 0° and a range of primary electron energies are presented in Figure 4.23(a) as a function of time after cleaning. Figure 4.23(a) (and the insert of yield at 580 eV) shows that the total SEE yield decreases as a function of time (the rate itself decreasing with time) before approaching a steady state value. This follows trends in the AES data which show decreasing Ni concentration and increasing C and O concentrations (see Figure 4.23(b)), and suggests that the change in SEE is due to adsorption of CO. CO is known to stick strongly to Ni at coverages up to 1 ML for temperatures below 420 K, with the sticking coefficient being initially linear then leveling off. Therefore, the largest change in SEE is expected to occur early when the sticking coefficient is largest and the surface composition is most rapidly changing, as is observed in Figure 4.23. The 0 min data in Figure 4.23(a) was determined at each primary energy by linearly extrapolating the first few data points in time.

Note that the concentrations of C and O in Figure 4.23(b) are small. However, concentrations were calculated from AES spectra assuming uniform distributions in the bulk in the top 10-20 nm probed by AES, not considering that CO lies only on the surface (since a CO molecule is much bigger than a Ni atom). Additionally, peak-to-peak heights were used in the calculation, but the carbon AES signal may have different lineshapes that may change the magnitude of the peak-to-peak height. Therefore, the concentrations in Figure 4.23(b)

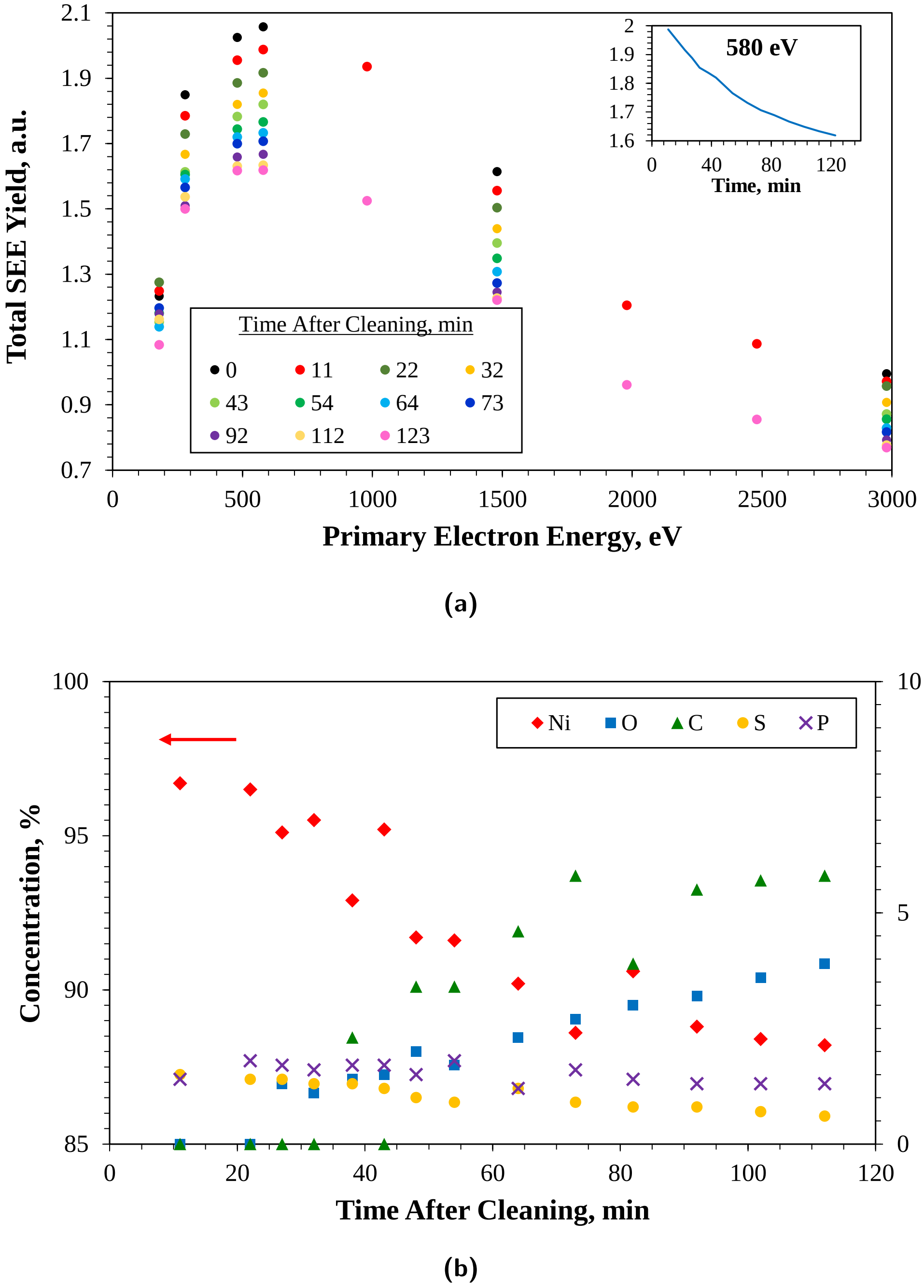

Figure 4.23: (a) Total SEE yield from from Ni(110) as a function of primary electron energy and time after cleaning; yields are in arbitrary units. The insert shows the decrease in yield as a function of time after cleaning for primary electrons at 580 eV. (b) Chemical composition of Ni(110) as a function of time after cleaning.

are taken to be qualitative, not quantitative.

Both CO and hydrogen are the largest residual gases observed in the chamber by the QMS. Although hydrogen cannot be detected by AES, the author is confident that there is no hydrogen on the surface since it desorbs from Ni(110) at temperatures below 210 K [209]. Additionally, the decrease in SEE in Figure 4.23(a) is not due to sample temperature (recall that samples were cleaned and annealed by heating to temperatures up to 1100 K), since a 10% reduction in total SEE yield was observed when the sample was at 327-350 K. Furthermore, recrystallization processes and primary electron dose from the LEED/AES optics were determined to also not be the cause of the decrease in Figure 4.23(a). Therefore, the high sensitivity of SEE from Ni(110) on physisorbed CO was confirmed. Similar sensitivity was measured by Ref. [210] for CO on Cu.

Total SEE yields for clean Ni(110) due to primary electrons at 0°, 50°, and 78° (with respect to the surface normal) are presented in Figure 4.24(a). Measurements are compared in Figure 4.24(b) to previously measured yields for primary electrons impacting Ni(110) at 50° and 78° from Ref. [28]. The agreement between our results and those in Ref. [28] gives confidence in the experimental setup and procedure. Also plotted in Figure 4.24(b) is the yield measured by Ref. [29] of SEE from clean polycrystalline Ni; these match other measurements of clean polycrystalline Ni by Refs. [22, 21, 26]. As can be seen from the figure, SEE from Ni(110) is significantly larger (i.e., by up to 36%) than from polycrystalline Ni. In plasma chemistry applications that utilize Ni(110), such as dry-methane reforming of CO_2 and CH_4, these larger yields may be beneficial since emitted secondary electrons may lead to further fragmentation of CO_2 and CH_4.

The total SEE yields in Figure 4.24 increase with incident angle (i.e., the maximum yield is 1.6, 1.9, and above 2.3 at 0°, 50°, and 78°), as is the general trend. However, as Figure 4.25 shows, the SEE for single crystals has a more complex dependence on primary electron incidence angle. The total SEE yields for 100-990 eV primary electrons incident on as-is Ni(110) as a function of incident angle are plotted in Figure 4.25(a). Data show a

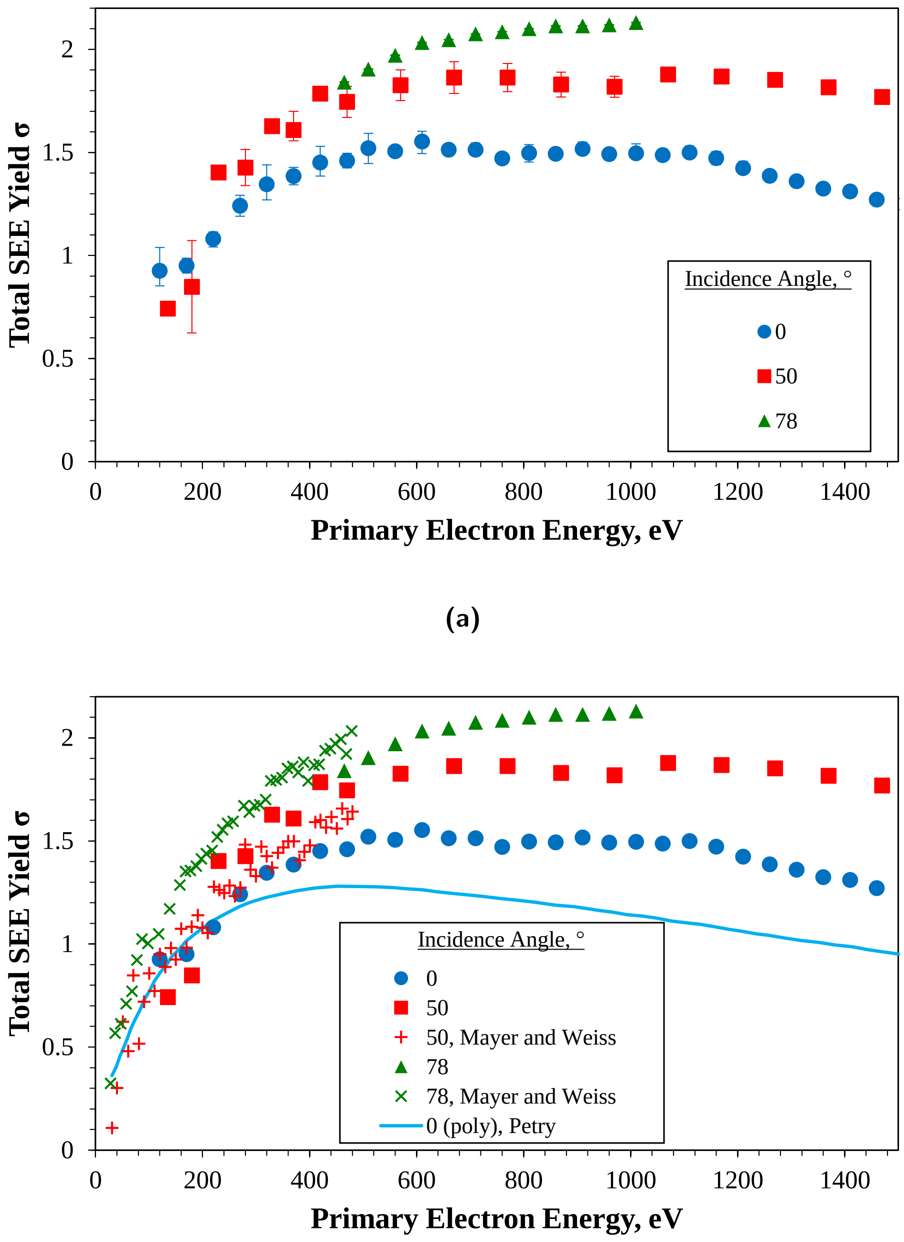

(a)

(b)

Figure 4.24: (a) Total SEE yield measured for up to 1500 eV primary electrons impacting clean Ni(110) at 0, 50, and 78° with respect to the surface normal. (b) Measurements are compared to data of Ni(110) from Ref. [28] and of polycrystalline Ni from Ref. [29].

maximum at 0°, minima at approximately ±12°, and increased yields at larger angles. Similar maxima and minima have been observed for other single crystals [211, 212, 213, 214, 215], including W(110) whose SEE yield at 2 keV is plotted in Figure 4.25(b) (in arbitrary units) [30] with data of Ni(110) at 450 eV.

Yields are a superposition of the general $1/\cos(\theta)$ curve (plotted in Figure 4.25(b)) expected for polycrystalline materials, and maxima that correspond to the crystal low-index axes. The maxima are due to an increase in SEE when the incident primary electrons are directed along the low-index axes, since primary electrons will experience increased scattering with atoms as they penetrate the crystal along close-packed directions. Hence the position of the maxima are independent of primary electron energy, as is shown in Figure 4.25(a), and are instead dependent on the angle at which the low-index axes make with respect to the sample normal, which is dependent on the crystal lattice parameters. For the W(110) sample which is rotated azimuthally, the maximum at 0° corresponds to the [110] direction and the maxima at ±34° correspond to the [111] direction. By fitting $1/\cos(\theta)$ curves to the data at different primary energies, the yields for polycrystalline Ni may be estimated. At 450 eV, a yield of 1.35 is estimated for polycrystalline Ni from Figure 4.25(b), which compares well with the value of 1.28 measured by Petry [29] and plotted in Figure 4.24(b).

The total SEE yields from clean Ni(110) at 300 and 600 K are plotted in Figure 4.26 as a function of primary electron energy for primary electrons at normal incidence. The yields are nearly identical (and so also for yields at 50°), which suggests that SEE from clean Ni(110) is independent of temperature within this temperature range. Refs. [22] and [23] found the total SEE yield to be independent of sample temperature for clean polycrystalline metals (i.e., silver [22] and Ni [23] between 725-1300 K) since there is negligible effect on the diffusion of secondary electrons (i.e., secondary electron kinetic energy is larger than sample thermal energy, and there are few secondary electron-phonon interactions) [132]. However for single crystals, SEE dependence on temperature may be more complicated. Ref. [216] found that the maxima in the angular SEE curves decrease slightly with temperature due to

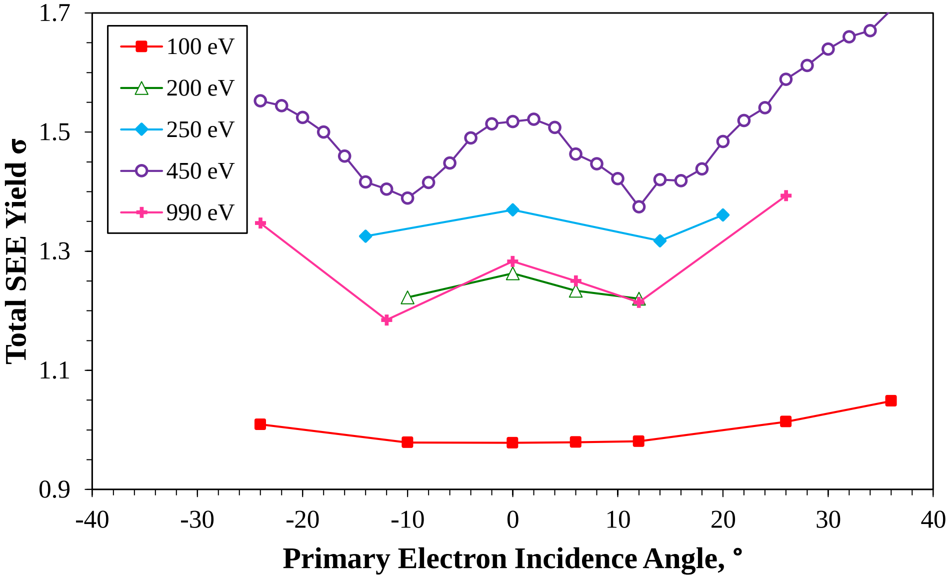

(a)

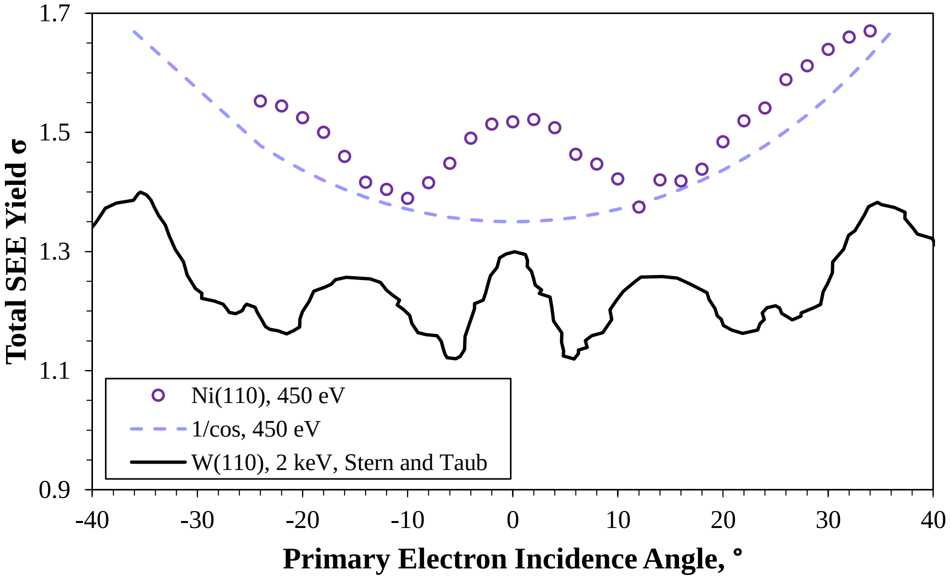

(b)

Figure 4.25: (a) Total SEE yield for 100-990 eV primary electrons impacting as-is Ni(110) at 300 K and 0-35° incidence angle. Lines are added to aid in visualization. (b) Total SEE yield for 450 eV primary electrons. Data from Ref. [30] of 2 keV primary electrons impacting clean W(110) is plotted in arbitrary units for comparison. Additionally, a $1/\cos(\theta)$ curve expected for polycrystalline materials is fit to the Ni(110) data.

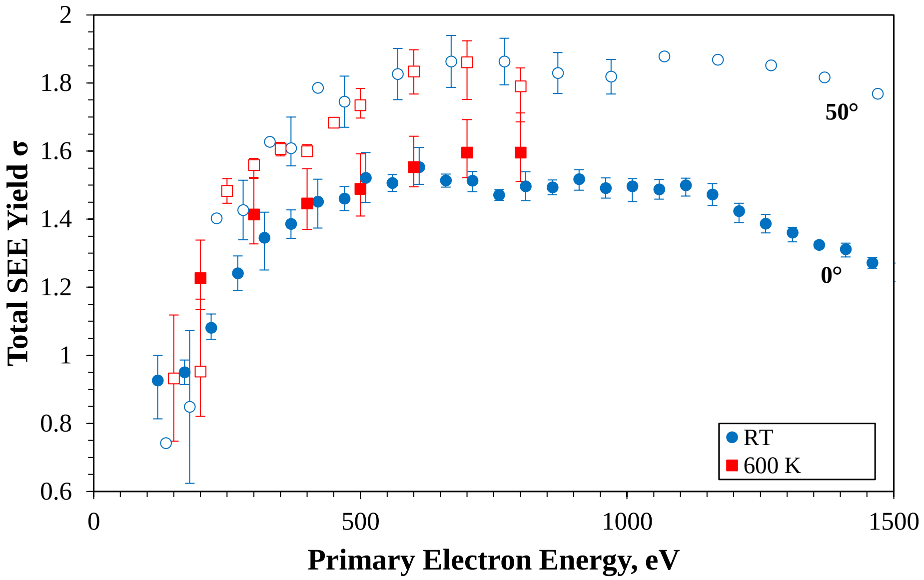

Figure 4.26: Total SEE yield for clean Ni(110) at 300 and 600 K, and 0 and 50° incidence angles.

a reduction in diffraction effects. However, the decrease is less than 5% between 100-600 K.

Figure 4.27 shows the total SEE yield measured from Ni(110) at 0° that has been pre-exposed to D_2 ions (leading to 55% D_2 saturation) and measured at 250-265 K. The yield is identical to that of clean Ni(110). This is because subsurface hydrogen (as opposed to physisorbed surface hydrogen) was likely formed by the deuterium ions. Rao [169] also measured a very small increase in SEE from polycrystalline Ni which he attributed to subsurface H, but observed a large increase in SEE when hydrogen was absorbed on the surface by exposure to a large background of hydrogen gas.

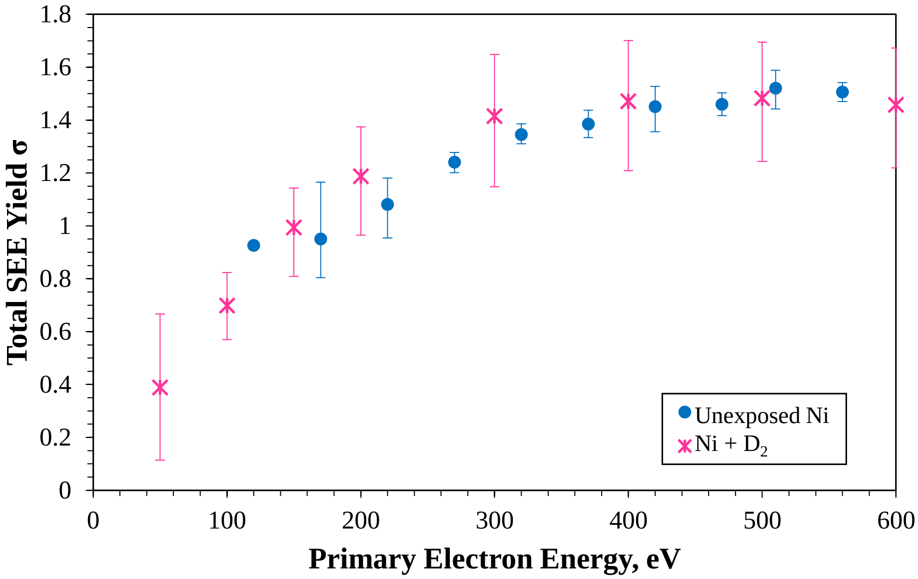

Figure 4.27: Total SEE yield measured for 50-600 eV, 0° primary electrons impacting clean Ni(110) and Ni(110) exposed to D_2^+.

4.3 Comparison with Secondary Electron Emission Theory and Models

4.3.1 Semi-Empirical Model

To further validate the sample method for determining primary electron current and SEE current, universal empirical and theoretical equations were used to reproduce the curves in Figure 4.15. Assuming the change in sample current I_S with sample bias voltage V_S is due to true secondary electrons that are recollected and to increased primary electron impact energies,

$$I_S(V_S) = I_{PE} - [I_{RE} + I_{TE}] = I_{PE}\left\{1 - \eta(E_{PE} + V_S) + \delta(E_{PE} + V_S)[1 - f(V_S)]\right\} \qquad (4.7)$$

where I_{PE}, I_{RE}, and I_{TE} are the currents from primary, elastically reflected, and true secondary electrons, respectively. The yield for true secondary electrons is

$$\delta(E_{PE}) = \sigma(E_{PE}) - \eta(E_{PE}), \tag{4.8}$$

where σ and η are given by Eq. 4.3 and Eq. 4.6, respectively. The fraction f of true secondary electrons with energy below $E_{SE} = V_S$ (i.e., recollected by the sample) is calculated from Eq. 4.5,

$$f(V_S) = \frac{N(E_{TE} < V_S)}{N_{tot}} = \frac{\int_0^{V_S} \frac{dN}{dE_{TE}} dE_{TE}}{\int_0^{50eV} \frac{dN}{dE_{TE} dE_{TE}}} = \frac{\frac{1}{\Phi_S} - \frac{\Phi_S + 3V_S}{(\Phi_{sS} + V_S)^3}}{\frac{1}{\Phi_S} - \frac{\Phi_S + 150eV}{(\Phi_S + 50eV)^3}} \tag{4.9}$$

The calculated curves are plotted with the measured curves in Figure 4.15. The fair agreement over the full range of sample bias voltages for the range of primary electron energies examined serves to validate the experimental setup and approach, as well as the equations for total SEE yield and energy distribution.

4.3.2 Monte Carlo Model of Structured Surfaces

Measurements of the total secondary electron yield from tungsten fuzz were compared with data from a computational model of SEE from complex structured surfaces developed by Huerta *et al* [31]. The Monte Carlo model tracks primary and secondary electrons between collisions with surface features (not within the material) through multiple collisions/generations until electrons escape the computational domain. It assumes electrons travel is straight line trajectories between surfaces (i.e., electron-electron collision mean free paths are much larger than the inter-fiber spacing), secondary electrons are emitted from the point on impact on the surface (i.e., primary electron penetration within the material is much smaller than the fiber diameters), and inelastically reflected electrons do not generate true secondary electrons. Empirical fits of $\varepsilon(E_{PE}, \theta_{PE})$ and $\eta(E_{PE}, \theta_{PE})$ from de Lara *et al* [217] and Tolias [157] (see Appendix J) are used to determine the probability for elastic and

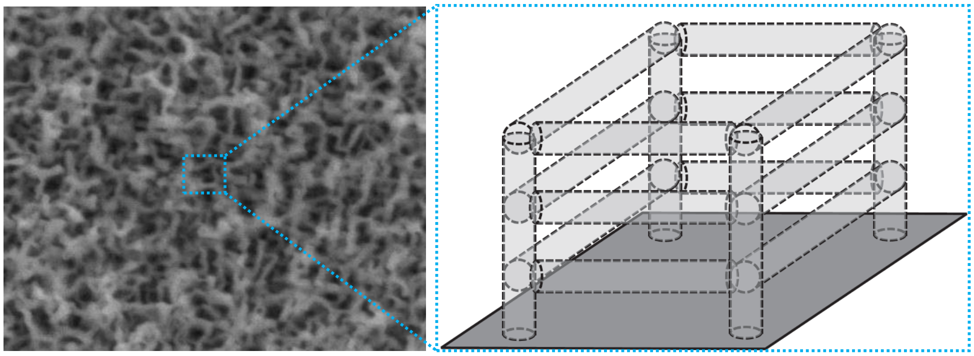

Figure 4.28: Cage-like geometry used to model SEE from W fuzz [31].

inelastic reflection at a surface. Elastically reflected electrons are emitted from the surface with their initial energy and through their original trajectory. Inelastically reflected electrons are emitted with a cosine angular distribution and with equal probability of emitted energy between 50 eV and E_{PE}. If it is determined that an incident primary electron generates true secondaries from the surface, a Poisson distribution is used to calculate the number of true secondaries generated. The true secondaries are emitted with a cosine angular distribution and an energy distribution as given by Equation 4.5 [20]. Since this is not a solid state model of electron interactions within the material, material dependent parameters in $\varepsilon(E_{PE}, \theta_{PE})$, $\eta(E_{PE}, \theta_{PE})$, and $\delta(E_{PE}, \theta_{PE})$ are determined by fitting to the experimental yield data from smooth, clean W at 0°. Additional details on the model can be found in Refs. [11, 31].

The model treats the inter-twined fibers of W fuzz as crossed vertical and horizontal cylindrical fibers in a cage-like geometry with lie on a flat substrate (see Figure 4.28; fiber radius = 12.5 nm, fiber length = 200 nm, fiber separation = 200 nm, 5 horizontal fibers per side). This geometry is more complex than the grooves, porous arrays, and parallel horizontal fibers considered in Monte Carlo models by Pivi *et al* [165], Ye *et al* [160, 161], and Swanson and Kaganovich [218], respectively.

Figure 4.29 shows the total SEE yields calculated from the model for W fuzz and compares the values to those measured. From Figure 4.29(a), the results of yield versus primary electron energy at 0° incidence agree very well with measurements. However, the model

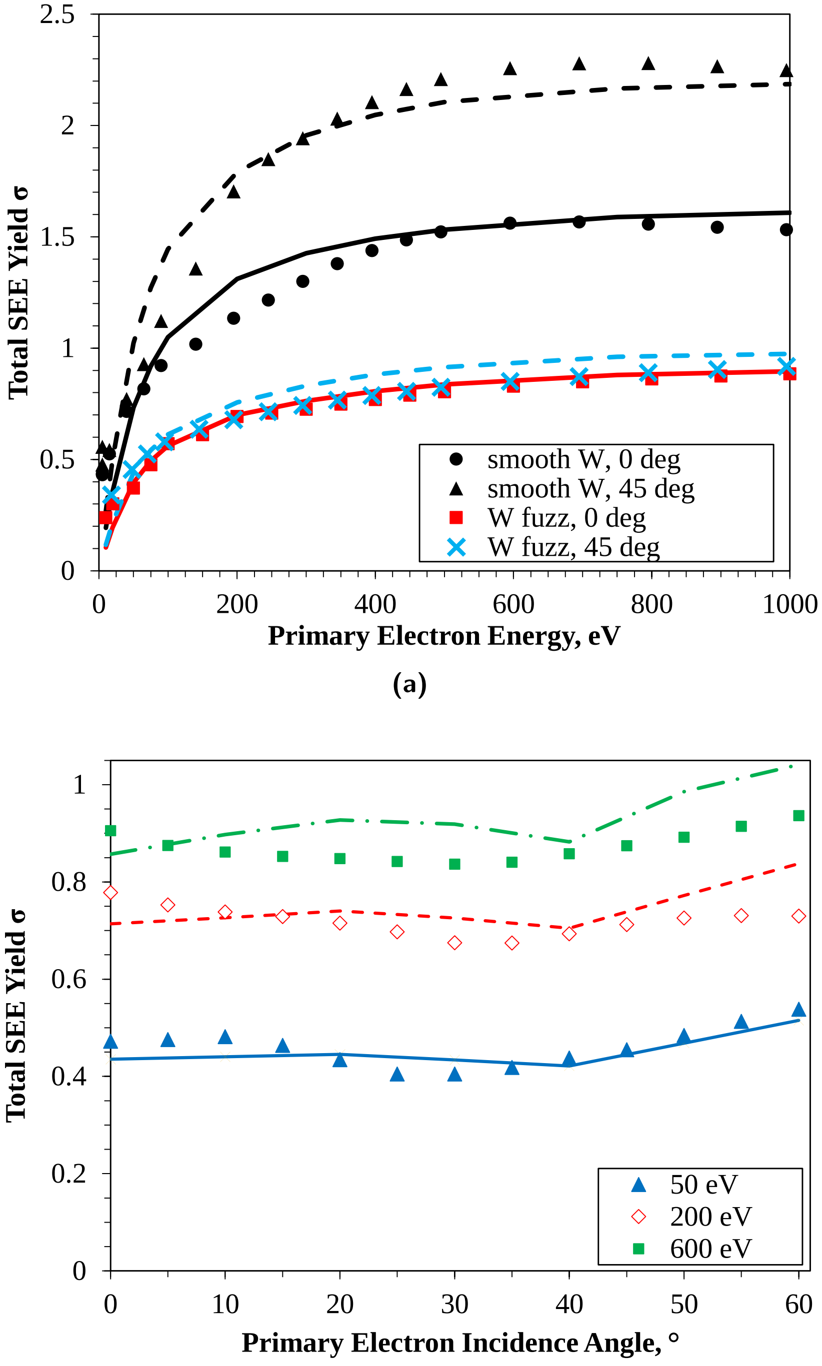

(a)

(b)

Figure 4.29: Computational results (shown as lines) of total SEE yield dependence on (a) incidence energy and (b) incidence angle for W fuzz. Experimental data is reproduced.

slightly overestimates the yield at 45° incidence. From Figure 4.29(b), the results of yield versus primary electron incidence angle are found to agree well with measurements at 50 eV, 200 eV, and 600 eV. Although a small minimum in total SEE yield is found in the experimental measures and model results at 25-40°, this minimum is within the error bars.

The agreement between experiment and model validates the use of the empirical fits for structured surfaces when treating the surface as locally flat, and indicates that the reduction in SEE from W fuzz is due solely to secondary electron trapping. The model will be used to predict the angular distribution of emitted secondary electrons, which will be different than the cosine emission observed for smooth surfaces and which requires specialized equipment to measure experimentally.

4.4 Summary

SEE properties were presented for graphite and tungsten fuzz, typical materials used in or expected to be generated in plasma thrusters, traveling wave tubes, and magnetic confinement fusion. The use of 4-grid LEED/AES optics for fully characterizing the secondary electron emission (yield and energy distribution of emitted secondary electrons) of conducting materials was validated with measurements of graphite for primary electron beam energies between 50 and 500 eV.Additionally, measurements of the energy distribution function of secondary electrons from graphite were provided for a wider range of incident electron energies, useful for modeling plasma-wall interactions in plasmas bounded by graphite walls, such as are found in plasma thrusters and divertors of magnetic fusion devices.

SEE from Li was measured as a function of oxygen exposure by introducing controlled amounts of O_2 and H_2O vapor, and by monitoring surface chemical composition *in-situ* (not previously done). The total SEE yield from Li was found to increase significantly with oxygen content. The lowest yield (with a maximum of 1.2) was measured for a Li film with $(\mathrm{Li} + \mathrm{LiO}_x)/\mathrm{O} = 3.8$. The highest yield (with maximum between 3.9 and 4.6) was measured for fully oxidized Li exposed to 90 L of H_2O or O_2 where (Li + LiO_x)/O = 1.3 and 0.8, respectively. The extreme sensitivity to oxygen content demonstrates the need to consider the higher SEE yield for oxidized Li when modeling the plasma-wall interactions in devices with Li walls, as this is more representative of the actual Li state in devices with realistic vacuum systems.

First-ever quantitative measurements were made of the total effective SEE from tungsten fuzz with nano-meter sized vertical and horizontal fibers. Such surfaces have been shown to grow on a hot tungsten surface under bombardment by energetic helium ions in different plasma discharges and applications, including magnetic fusion devices with plasma facing tungsten components.Two important results were found: (1) SEE values for tungsten fuzz are 40-63% lower than for smooth tungsten and (2) the SEE values for tungsten fuzz are independent of the angle of the incident electron. The reduction in SEE from tungsten fuzz is most pronounced at high incident angles, which has important implications for many plasma devices since in a negative-going sheath the potential structure leads to relatively high incident angles for the incident electrons at the plasma confining walls.Thus, the presence or self-generation in a plasma of a low SEE surface such as tungsten fuzz can be desirable for reducing plasma electron energy loss to the confining wall and improving performance of many plasma devices.

SEE from a temperature-controlled Ni(110) sample was examined for 50-1500 eV primary electrons impacting at 0-35°, 50°, and 78°. Measurements of secondary electron emission yield for Ni(110) showed a unique dependence on primary electron incidence angle characteristic of single crystal materials (i.e., a maximum at 0° and minima at ±12°). Yields were independent of sample temperature between 300 and 600 K, and of deuterium-exposure. Carbon monoxide adsorption was found to decrease emission yields by up to 20%. Results are important for dry-methane reforming (i.e., $CO_2 + CH_4 \rightarrow 2H_2 + 2CO$) where Ni(110) is proposed for use as a catalyst, and where low energy secondary electrons may influence the chemistry of surface-adsorbed species.

CHAPTER 5

Conclusions

This effort examined plasma inter-particle and particle-wall interactions important for the advancement of electric propulsion, fusion energy, high-power communications, and next-generation energy systems. Two interactions of particular importance, and which were the focus of this work, are (1) ion-atom collisions occurring within the plasma bulk and (b) secondary electron emission from plasma-facing materials.

5.1 Ion-Neutral Collisions

Collisions between fast ions and slow atoms produce slow charge-exchange ions that are important to understanding the performance and behavior of many plasma devices, including ion thrusters whose grids are eroded by charge-exchange ions. To investigate this behavior, this work developed a simple, well-characterized experiment that accurately measures the effects of high energy 1.5 keV xenon ions undergoing momentum-exchange and charge-exchange collisions with xenon neutral atoms. Measurements were made for pressures up to several mTorr, and with applied magnetic and electric fields to control the transport of low energy charge-exchange ions and any generated electrons.

By comparing results to both analytical and computational models of ion-atom interactions, we discovered the relative importance of using appropriate methods to treat momentum-exchange and charge-exchange collisions. In particular, measurements provided data on the angular scattering distributions of charge-exchange and momentum-exchange xenon ions at 1.5 keV relevant for ion thrusters, but for which little data exists. Additionally, the comparison revealed the importance of considering additional interactions, including ion-induced electron emission and neutral-neutral ionization collisions, at high pressures.

5.2 Secondary Electron Emission

This work also investigated the interaction of electrons incident on materials and the resulting secondary electron emission (SEE). For many plasma devices, including electric propulsion and fusion energy devices, SEE can alter the sheath potential and significantly affect device performance and life, making it imperative to maintain a low emitting surface. SEE properties were measured for materials pertinent for plasma applications, including graphite (used for ion thrusters, tokamaks, and traveling wave tubes), lithium (for tokamak walls), tungsten (the most promising material for future tokamaks such as ITER), and nickel (for plasma-enhanced chemistry). Measurements of the total SEE yield (defined as the ratio of emitted electron flux to incident electron flux) and of the energy distribution of emitted secondary electrons were made for incident electron energies up to 1.5 keV and angles between 0 and 78°.

First-ever measurements were made of SEE yields from nano-structured tungsten fuzz, which have been shown to grow on a hot tungsten surface under bombardment by energetic helium ions in different plasma discharges, including magnetic fusion devices with plasma facing tungsten components. A >40% reduction in SEE was observed at 2-1000 eV for tungsten fuzz when compared to smooth tungsten. More importantly, SEE from tungsten fuzz was independent of electron incidence angle between 0-60°. Comparison with computational models of SEE from textured surfaces, suggests trends are a result of horizontally-oriented fibers in the fuzz geometry. Thus, the growth of tungsten fuzz in tokamaks is desirable for minimizing adverse secondary electron emission effects, and may be more effective than artificially textured surfaces which can be eroded away by plasma exposure.

Original SEE measurements were made of lithium exposed to controlled amounts of O_2

and H_2O vapor for incident electron energies between 20 and 600 eV. SEE was found to be strongly dependent on oxidation: the maximum yield increased by 2×, 4×, and over 6× for lithium with $(\text{Li} + \text{LiO}_x)/\text{O} = 3.8$, exposed to 10 L of O_2, and fully oxidized with 90 L of H_2O or O_2, as compared to a "pure" lithium film (here $1\ \text{L} = 1\ \text{Langmuir} = 10^{-6}$ Torr s). *In-situ* analysis of the surface chemical state during SEE measurements (not provided by other authors) highlighted the difficulty in maintaining a clean lithium film, and allowed for quantification of SEE yield from mixed materials of metallic lithium and lithium oxide. Thus SEE is likely to be considerable in tokamaks with lithium coatings which are oxidized by typical residual gases.

Unique measurements of SEE from Ni(110) at 75-1500 eV showed a complex dependence on electron incidence angle (i.e., maxima at 0° and minima at ±12°), resulting in SEE that is 36% larger at 0° as compared to polycrystalline nickel. Additionally, yields were found to be highly sensitive to carbon monoxide adsorption from the chamber background, with up to a 20% decrease. Thus the higher SEE from Ni(110) catalysts in plasma-enhanced chemistry may facilitate further reactions of surface-adsorbed species, unless carbon monoxide is absorbed in which case the opposite is true.

Measurements of total SEE yield for graphite were found to compare well with measurements from other authors at incident electrons energies between 50 and 500 eV. Secondary electron energy distributions were measured for a larger range of primary electron energies than previously available. Comparison of sample currents measured to sample currents calculated from a simple semi-analytical model, allowed for validation of SEE models of yield and energy distribution, as well as validation of the setup and approach.

CHAPTER 6

Future Work

The following efforts may be undertaken to provide further insight into plasma interparticle and particle-material interactions in electric propulsion and fusion energy devices. They expand upon the work discussed in the preceding chapters, and are beyond the work of this dissertation.

6.1 Ion-Neutral Collisions

Experiments of ion-neutral collisions were conducted for singly-charged xenon ions impacting neutral xenon atoms at 1500 eV, and showed that scattering on ions is highly non-isotropic. Future measurements can be made at lower ion energies (i.e., 300 eV) which are relevant for Hall-effect thrusters. Collisions of doubly charged xenon ions with neutrals may be explored since doubly charged ions constitute approximately 10% and 20% of the ions in the plume of ion and Hall thrusters, respectively. Additionally, measurements of argon and krypton ions colliding with their parent gas is important for understanding the plasma performance of thrusters that use such propellant. Although the ion beam facility utilized for collision experiments is capable of producing ions at low energies and for filtering out only doubly-charged ions, the ion currents are small and lead to low signal-to-noise in the test cell.

The semi-analytical and computational models may also be improved. The semi-analytical model considered two-step ionization collisions between fast and slow neutrals, where the fast neutral atom is produced via charge-exchange of a fast ion and slow neutral. In contrast, the MCC and DSMC models considered electron emission from the test cell walls due to incident ion and neutral particles. Model results showed better comparison with measurements when neutral-neutral ionization and particle-induced electron emission were considered separately, yet still underpredicted currents observed in the experiment. Results are expected to match measurements when considering both neutral-neutral ionization and particle-induced emission.

Additionally, the MCC collision model considered only particle-induced electron emission from the exit plate, and assumed the yield was a constant across the entire electrode. The DSMC collision model considered electron emission from the exit plate and inner cylinder, but also assumed the yield to be constant and to be small. In reality, electrons are likely emitted from all test cell walls (i.e., exit plate, inner cylinder, and downstream front plate), and the yield is dependent on the energy, angle, and electronic state of the incident particle.

6.2 Secondary Electron Emission

The results in Section 4.2.3 revealed that secondary electron emission from tungsten decreases with cleaning and removal of oxygen and carbon impurities. Additionally, in was shown in Section 4.1.3.1 that the tungsten fuzz sample used in the experiments had significant impurities and oxidation. Therefore, it is expected that the secondary electron emission from clean tungsten fuzz is further reduced. Sputtering of tungsten fuzz would erode the nanostructures on the surface. Therefore, the secondary electron emission of cleaner tungsten fuzz may be investigated in a facility that generates the fuzz *in-situ*, such that the tungsten fuzz sample is not exposed to atmosphere. Alternatively, attempts may be made to heat the samples *in-situ* to temperatures above 2700 K to remove the impurities and oxide. However, it is uncertain whether such high temperatures would damage the nanostructures.

Modeling of secondary electron emission from tungsten fuzz have suggested that the angular distribution of true secondary electrons is not cosine, but instead shows features that may be associated with the fiber geometry. In order to measure the angular distribution of secondary electrons, a hemispherical collector with differential ring electrodes (difficult to construct) or a differential collector on a rotary stage, may be employed. Similar SEE is expected from other materials which form fuzz exposed to He^+ when at ∼0.3-0.5 times the melting temperature, including molybdenum [53, 219], tantalum [219], palladium [219], and copper [220, 219].

SEE measurements were made of lithium oxide Li_2O formed by exposure of a Li film to O_2 and H_2O. Yet in a tokamak utilizing the deuterium-tritium nuclear reaction, lithium may also form lithium deuteride LiD. The facility at PPPL used for the lithium investigation is capable of producing LiD films by exposing lithium to a background of D_2 or to D_2^+ ions.

6.3 Ion-Induced Electron Emission

Measurements were made of ion-induced electron emission yield for argon and xenon ions impacting tungsten and stainless steel (used in the initial test cell design) at a range of incident ion energies (see Section G). Future measurements may investigate the effect of yield on the charge of the incident ion.

APPENDIX A

Integral Cross-Sections for Ion-Neutral and Neutral-Neutral Collisions of Xenon and Other Rare Gases

A.1 Ion-Neutral Collisions of Xenon and Other Noble Gas Ions

Many previous investigations into ion-neutral collisions have focused on integral collision cross-sections σ, which provide information on the probability or frequency of a collision. Early collision experiments used ion beams to determine integral cross-sections of noble gas ions and their parent gas [221, 222]. Beam cell experiments were performed by Dillon *et al.* [223] and Ghosh and Sheridan [224] to measure symmetric CEX collisions of singly charged noble gas ions, and by Hasted and Hussein [225] to measure symmetric (i.e., $A^{2+} + A \longrightarrow A + A^{2+}$) and asymmetric (i.e., $A^{2+} + A \longrightarrow A^{+} + A^{+}$) CEX collisions of doubly charged noble gas ions. A drift tube experiment with a mass spectrometer as collector was used by Okuno *et al.* [226] to separate primary and CEX Xe^{2+} in symmetric CEX collisions, by Johnsen and Biondi [227] to investigate asymmetric CEX of doubly charged ions impacting neutrals, and by Koizumi *et al.* [228] for symmetric CEX collisions of Xe single and double ions. Other experiments to measure integral cross-sections utilized crossed beams, merged beams, and swarm methods [229].

Integral CEX cross-sections of Xe^{+} [256] were calculated by Johnson from *ab-initio* interaction potentials using an approach described below. Similarly, Rapp and Francis used interaction potentials derived from single-electron wave functions to calculate integral CEX

Table A.1: Previous Investigations of Noble Gas Ion-Neutral MEX and CEX Collisions.

Species	Energy of A^+, eV		Energy of A^{2+}, eV	
	MEX	CEX	MEX	CEX
He	1500 [230]	>0.02 [231]	-	-
		1.5-90 [232]		
		2-8 [233]		
		2-50 [234]		
		4-80 [235]		
		4-100 [236]		
		6-80 [237]		
		6.5-100 [238]		
		25-90 [239]		
		750-850 [223]		
		100-800 [224]		
		200-4000 [239]		
Ne		>0.11 [231]		75-180 [240]
		1-50 [234]		400-3600 [225]
		1.2 [241]		
		1.2-2.2 [242]		
		4-50 [243]		
		4-100 [244]		
		25-75 [245]		
		25-90 [240]		
		50-850 [223]		
		100-800 [224]		
		200-4000 [239]		
Ar	0.2-300 [246]	0.025 [247]		0.025 [247]
	20-340 [69]	>0.21 [231]		75-180 [240]
		1-4 [241]		400-3600 [248]
		1-15 [249]		
		1-85 [232]		
		1-100 [250]		
		2-40 [234]		
		4-100 [244]		
		5-60 [243]		
		10-60 [251]		
		50-850 [223]		
		100-800 [224]		
		200-4000 [239]		
		1000-2000 [252]		
Kr		0.01-2 [228]		0.01-5 [228]
		0.025 [247]		0.025 [247]
		0.4-2 [253]		0.04-20 [226]
		>0.44 [231]		75-180 [240]
		25-90 [240]		400-3600 [225]
		50-850 [223]		
		100-800 [225]		
		200-4000 [239]		
		400-1400 [248]		
		400-2000 [252]		
		3000-7000 [254]		
Xe	5-40 [41]	0.01-2 [228]	10-80 [41]	0.02-8 [228]
	20-340 [69]	0.025-9 [247, 255]		0.025 [247, 255]
		>0.69 [231]		0.04-20 [226]
		1-300 [72]		2-600 [72]
		25-90 [240]		75-180 [240]
		50-850 [223]		400-3600 [225]
		100-800 [224]		
		200-4000 [239]		
		300-2000 [252]		
		400-1400 [248]		

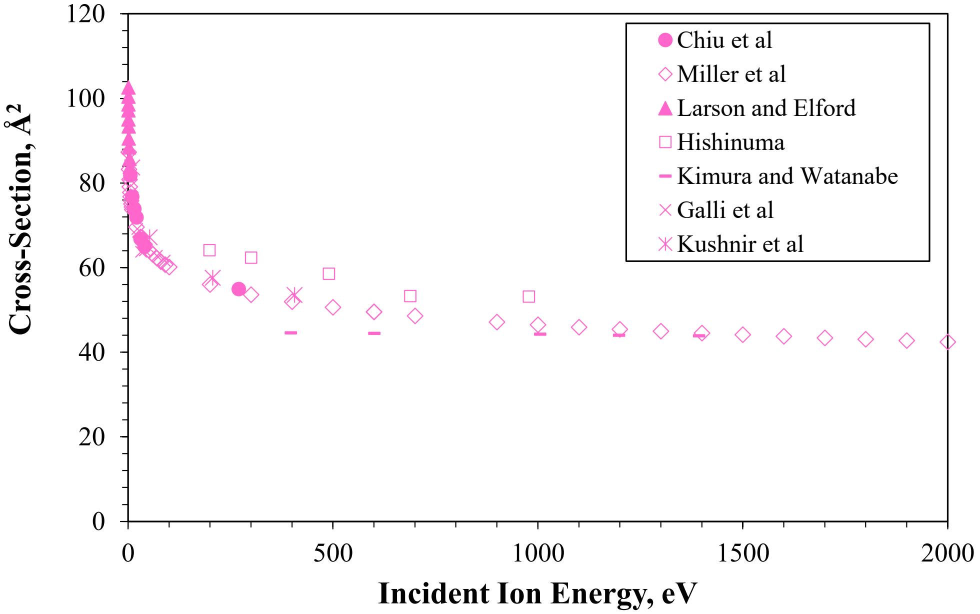

Figure A.1: CEX integral cross-section for Xe$^+$-Xe collisions at a range of incident ion energies. Data is taken from references found in Table A.1.

cross-sections for a large range of ion species. Other calculations have been made by Sakabe and Izawa [231], Firsov [257], and Fetisov and Firsov [258].

Experimental and theoretical investigations into Xe and other noble gas ion-neutral MEX and CEX collisions are summarized in Table A.1. Values of CEX integral cross-sections for Xe$^+$-Xe are plotted in Figure A.1 of a range of incident ion energies. In accordance with resonant charge-exchange collision theory, σ_{MEX} may be assumed to be equal to σ_{CEX} [76, 75]. From Refs. [259, 260], the integral cross-sections for excitation and ionization are more than an order of magnitude smaller for Xe$^+$-Xe at 1500 eV.

NIST tables [261] include CEX integral cross-sections for collisions between H and He ions and atoms with other species, but do not include Xe$^+$-Xe collisions investigated here.

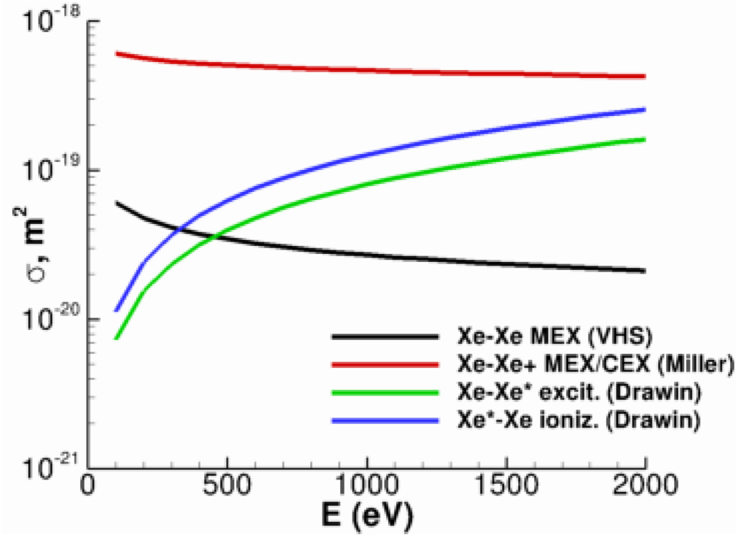

Figure A.2: Cross-section momentum-exchange, charge-exchange, excitation, and ionization collisions between xenon ions, atoms, and metastables [32].

A.2 Neutral-Neutral Collisions of Xenon and Other Noble Gases

The MEX integral collision cross-section for $Xe-Xe$ is plotted in Figure A.2 from Ref. [61]. An expression for the integral cross-section for the two-step ionization of noble gases was given by Drawin and Emard [64]:

$$\sigma_{ionz} = 4\pi a_0^2 (\frac{E_1^H}{E_0})^2 \frac{m_A}{m_H} \xi_0^2 \frac{2m_e}{m_e + m_A}(W_0 - 1)[1 + \frac{2m_e}{m_e + m_A}(W_0 - 1)]^{-2} \tag{A.1}$$

where m_A, E_0, ξ_0 are the mass, first ionization energy, and number of valence electrons of the neutral atom under consideration; m_e, E_1^H, and a_0 are the mass, first ionization energy, and Bohr radius of atomic hydrogen; m_e is electron mass; and $W_0 = E/E_0$ where E is the incident neutral energy. The ionization cross-section for $Xe - Xe$ from Equation A.1 is plotted in Figure A.2, and calculated to be 21.4Å^2 at 1500 eV. Since Ref. [177] determined that Equation A.1 can overpredict the cross-section by up to an order of magnitude for noble gases, the cross-section for 1500 eV $Xe - Xe$ may range from 2 to 22 Å^2.

APPENDIX B

Ion Beam Conditioning Devices

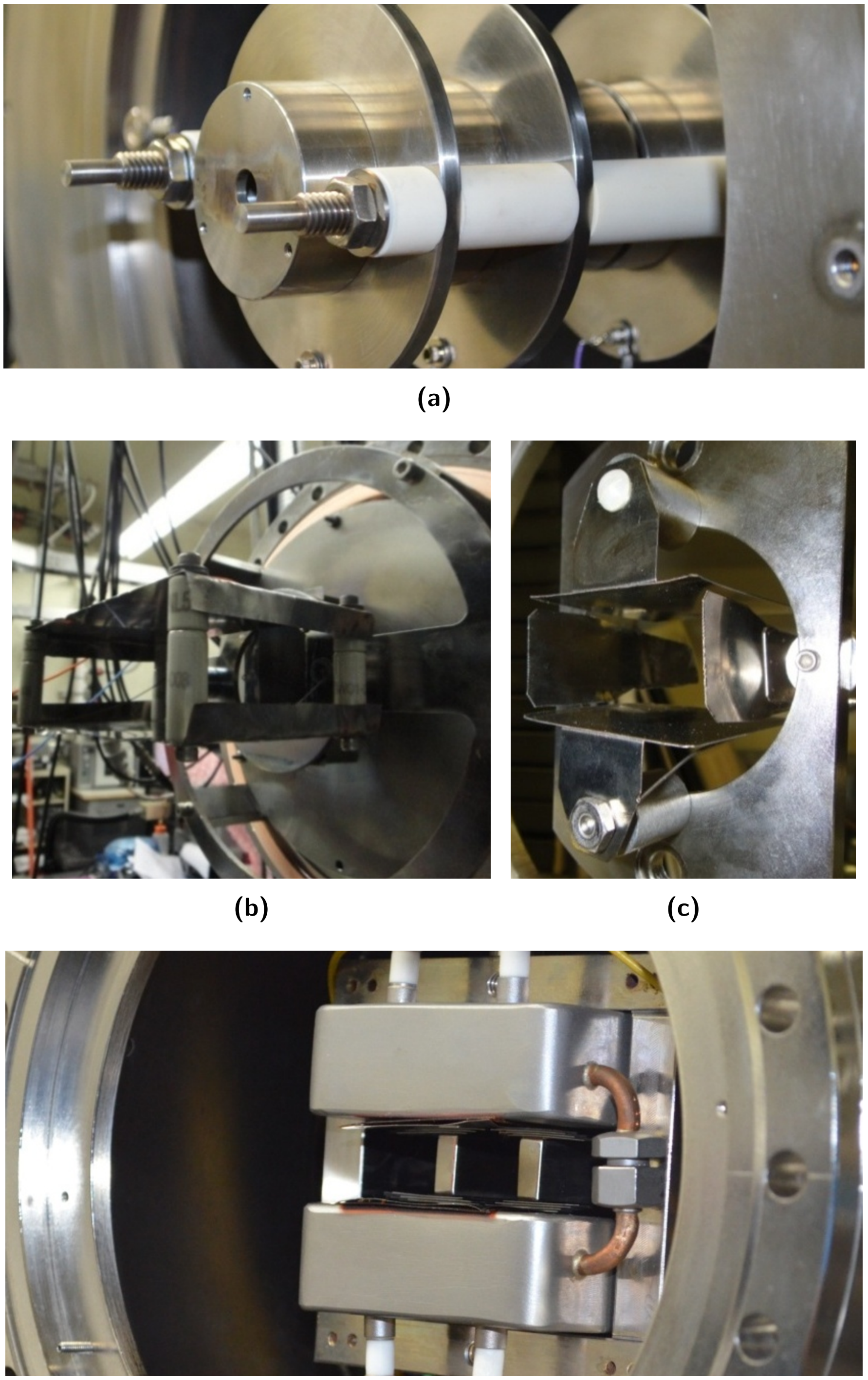

(a)

(b)

(c)

(d)

Figure B.1: Conditioning devices utilized in the ion beam facility: (a) electrostatic lens, (b-c) deflection plates, and (c) E×B filter.

APPENDIX C

Ion Beam Current Profiles

Various beam conditioning devices are located in the ion beam facility to steer the beam from the ion source to the test cell entrance. The experimental operating conditions of the first four data sets (i.e., data sets A-D) are provided in Table C.1. The source grid voltage determines the energy of the beam ions. The extractor grid, lens, and deflection plate voltages are adjusted to provide a well collimated beam of maximum current (as determined by ion beam profiles) at the entrance to the test cell.

Profiles of the beam are measured by scanning wires in each of the chambers. The profiles at wire 0 (located just of Lens 1 in the source chamber) are nearly identical for data set A-C data sets since the voltages on the extractor grid and lens 1 are the same (see Figure C.1(a)). Data set D has a slightly smaller peak current due to a smaller flow rate of xenon gas into the ion source.

The beam profile at wire 1 downstream of the E×B filter in the filter chamber is plotted in Figure C.1(b), and used to set the voltages on Deflection Plates 1 and 2 to get maximum current through Aperture 1 and to produce a centered and symmetric beam at the wire 1 location. From Figure C.1(b), a more symmetric beam was produced in data set D after deflection plates 1 and 2 were changed to allow for differential biasing of the horizontal plates (as opposed to absolutely biasing in which one plate is grounded). Also from comparison of the total integrated currents at wire 0 and wire 1 (found in the legend), less than 5% of the current in the source chamber passes through aperture 1 into the filter chamber. The full width at half maximum (FWHM) is reduced from approximately 15 mm to 2 mm for data

Table C.1: Ion Beam Operating Conditions

Voltage, V	Data Set			
	A	B	C	D
Source Grid	1500	1500	1500	1500
Extractor Grid	1140	1140	1140	1140
Lens 1	-3000	-3000	-3000	-3000
Lens 2	-500	-1900	-1900	-2000
Deflection Plate 1 (Top, Left, Right)	(85, 143, 0)	(86, 144, 0)	(86.3, 143.3, 0)	(57.3, 60.4 -47.8)
Deflection Plate 2 (Top, Left, Right)	(-113, 149, 0)	(-113, 152, 0)	(-116, 148.8, 0)	(-65.2, 75.4, -32)
Deflection Plate 3 (Top, Left, Right)	(51.4, 148, 0.6)	(12.5, 146, -18)	(34, 140.3, 28.6)	(-13, 153.7, -3.2)
Deflection Plate 4 (Top, Right)	(-35.3, 9.4)	(-9.5, 22)	(-36.1, -0.9)	(4.1, 27.4)

set D.

Before data at each test cell pressure is taken, the beam profile at wire 2 just upstream of the test cell is measured to supply as an input condition for model validation. Figure C.1(c) shows the average and envelope of the beam profiles, which accounts for the temporal drift due to changes in the ion source (i.e., filament cathode or xenon flow rate through the variable needle valve). From the total integrated currents in Figure C.1(c), less than 20% of the current at wire 1 reaches wire 2. For all data sets, the FWHW is approximately 2 mm.

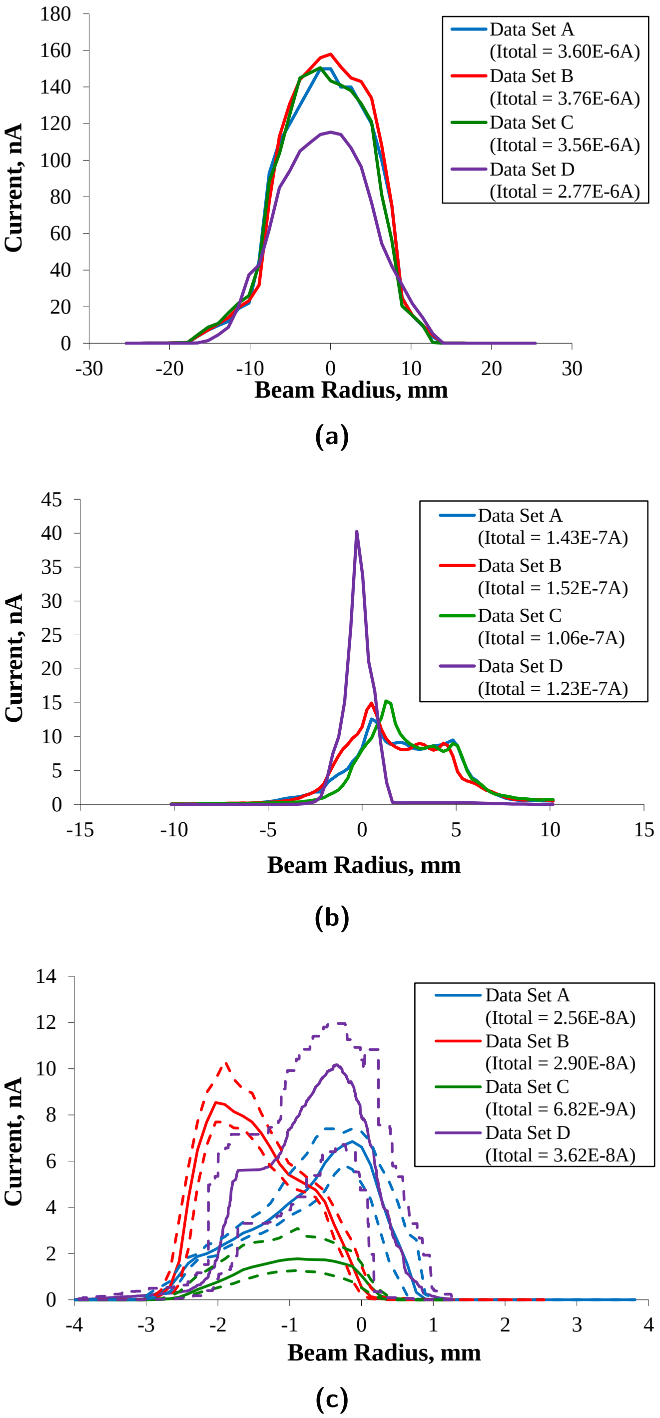

Figure C.1: Ion beam profile at (a) wire 1, (b) wire 2, and (c) wire 3. In (c), the average of beam profiles taken at various times is shown as solid lines, while the envelope of the beam profiles is shown as dashed lines.

APPENDIX D

Detailed Test Cell Geometry

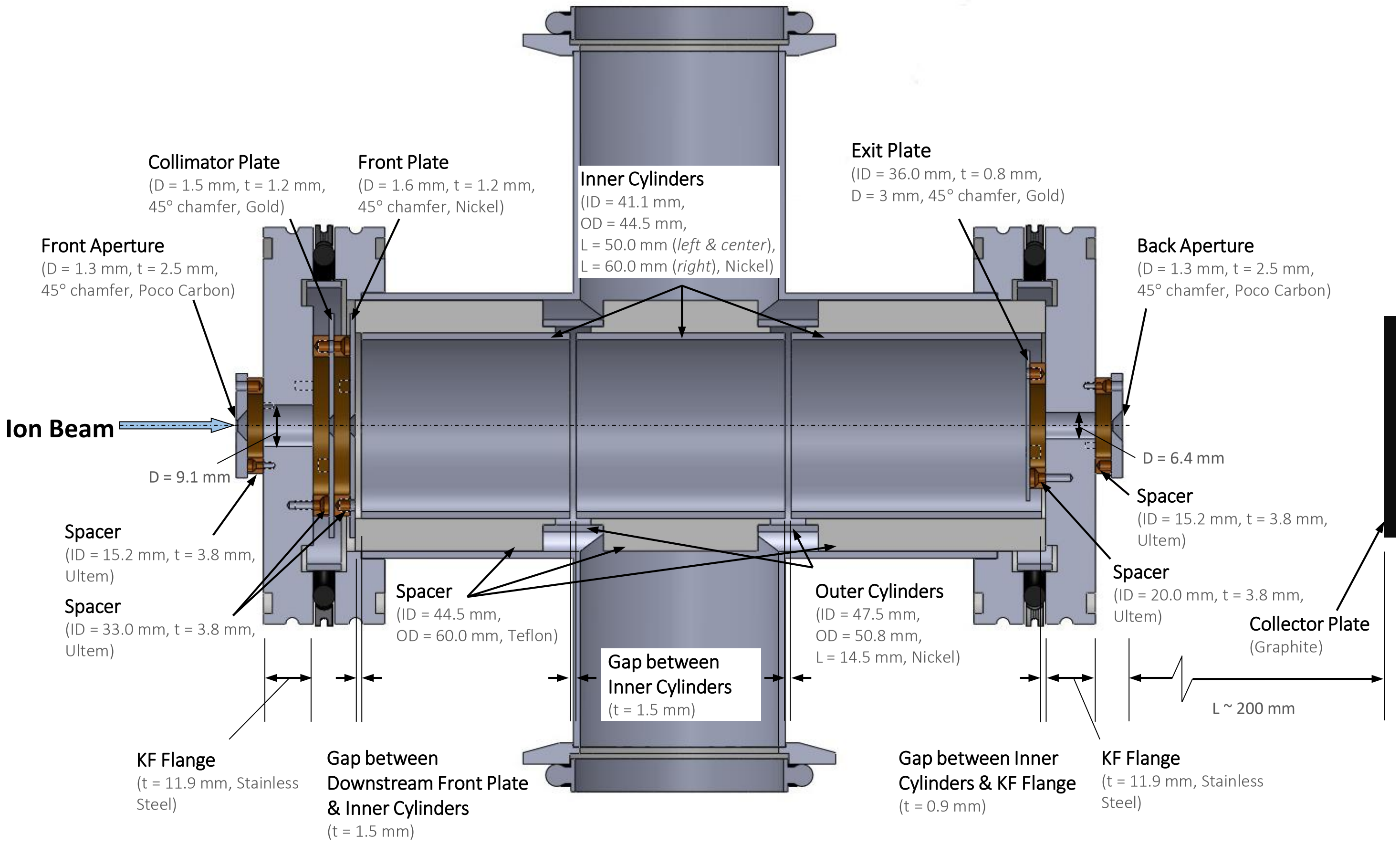

Figure D.1: Test cell geometry in the latest design with details on electrode dimensions and materials.

APPENDIX E

Initial Test Cell Geometry and Results

The initial version of the test cell was designed to examine the collisions occurring at low test cell pressures where collisions are localized near the exit plate. Therefore, it did not require an electrode on the upstream surface of the test cell. A front plate was later added to the improved test cell in order to investigate collisions at higher test cell pressures. Additionally, a single inner cylinder electrode was used in the initial test cell. To obtain spatial resolution of current along the inner cylinder, the single inner cylinder electrode was replaced with three cylindrical electrodes (i.e., inner cylinders 1-3) in the improved test cell. Lastly, both the exit plate and the inner cylinder were initially made from stainless steel. However, since the electron emission from 1.5 keV Xe^+ incident on stainless steel is unknown, these materials

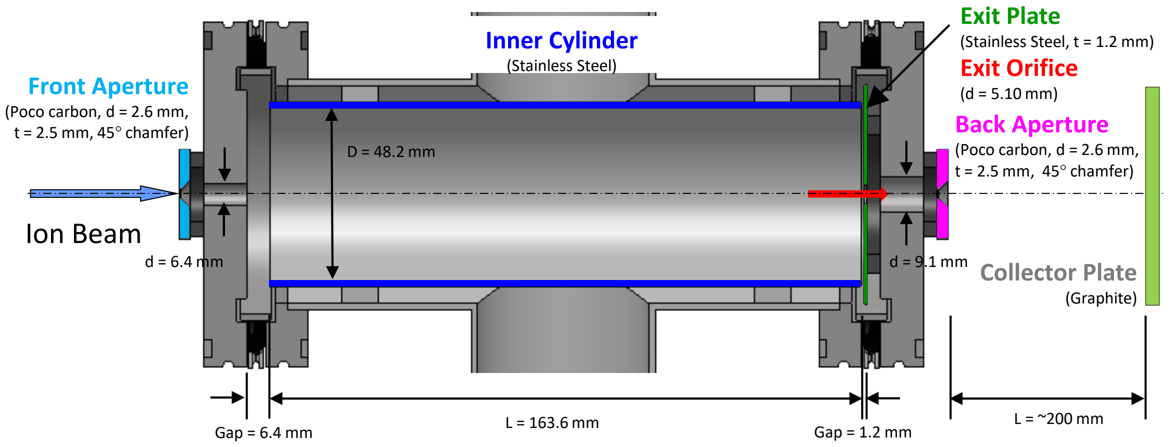

Figure E.1: Test cell geometry in the initial design with important electrodes highlighted. Important dimensions and materials are also included. Further details can be found in Figure E.2.

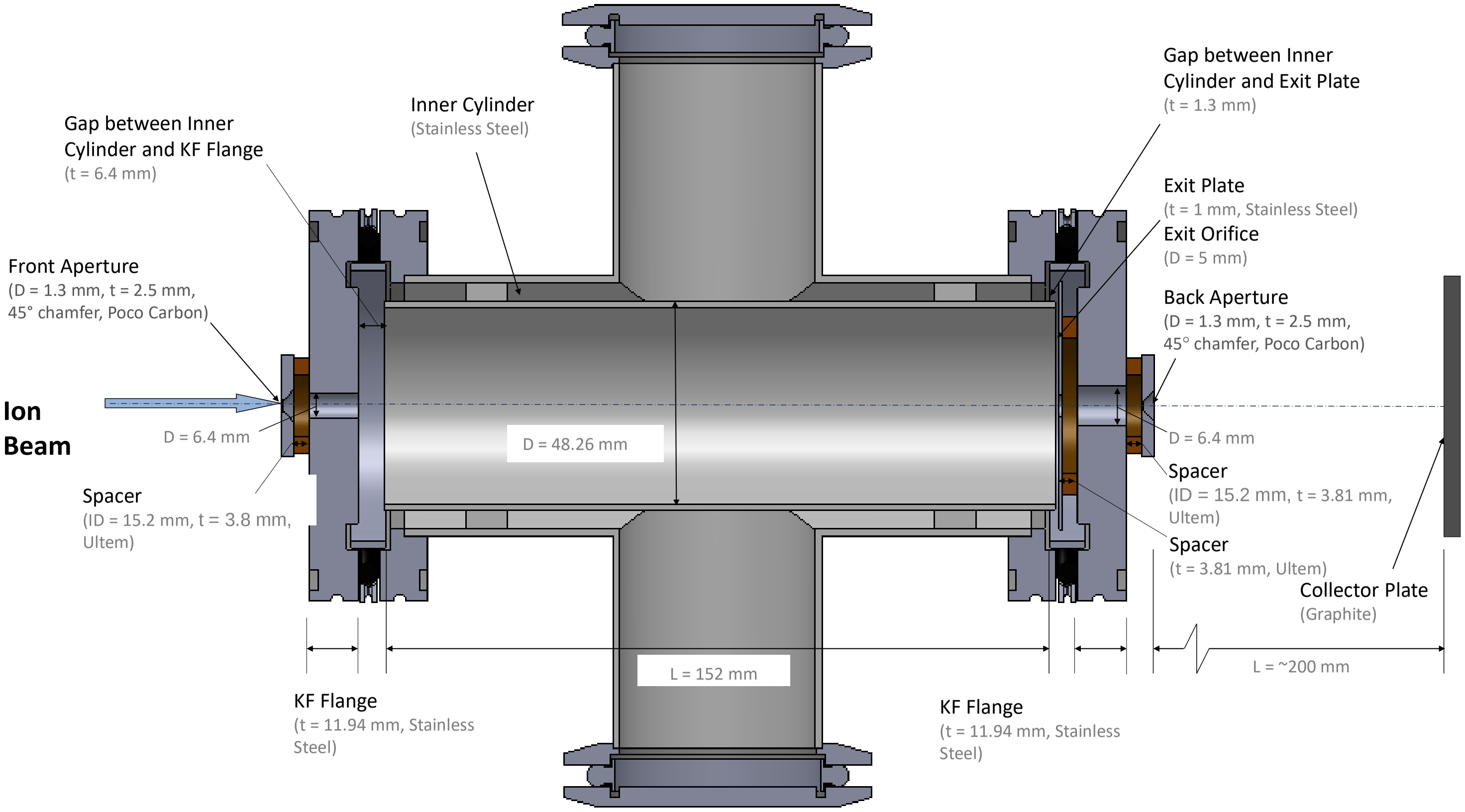

Figure E.2: Test cell geometry in the initial design with details on electrode dimensions and materials.

were later replaced with materials that are known to have low electron emission (i.e., gold and nickel). See Figure E.1 and E.2 for simplified and detailed drawings of the old test cell. These changes were made with insight gained from the semi-analytical and computational models of collisions in the test cell. They confirmed that the lack of an upstream electrode is in fact acceptable (<5% error) at low test cell pressures, but not above ∼0.4 mTorr. They also predicted a non-uniform spatial distribution of current along the inner cylinder at high test cell pressures.

Electrode currents measured with the old test cell as a function of pressure for the case of no applied electric and magnetic fields are plotted in Figure E.3(c) and compared to currents measured with the improved test cell; four data sets were taken with the initial test cell and are shown as unfilled symbols, while the four data sets taken with the improved test cell are shown as filled symbols. Note that since no current was measured on the front plate, all currents in Figure E.3(c) are normalized by $\tilde{I}_j = I_j/(I_{IC} + I_{EP} + I_{EO})$ for given electrode j. It show the excellent level of agreement between multiple data sets and between the data taken with the initial and improved test cells. Additionally, since the electron emission from gold and stainless steel are expected to be significantly different (i.e., stainless steel has a relatively low work function of 4.4 eV such that potential emission due to incident Xe^+ is possible), Figure E.3(c) shows that particle-induced electron emission from the exit plate to the inner cylinder is expected to be negligible for test cell pressures below 2 mTorr.

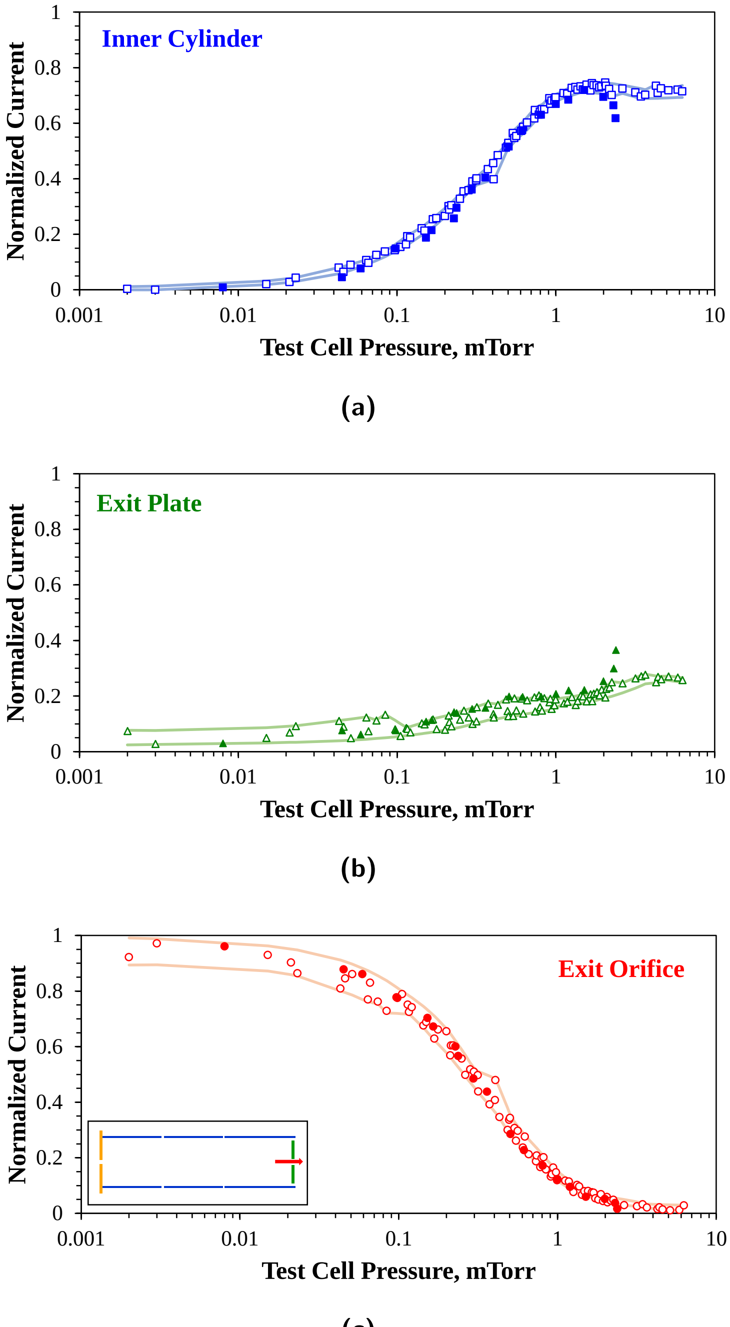

(a)

(b)

(c)

Figure E.3: Current measured on the (a) inner cylinder (blue squares), (b) exit plate (green triangles), and (c) exit orifice (red circles) as a function of test cell pressure. Data taken using the initial test cell design are shown as unfilled symbols and data taken using the improved test cell design are shown as filled symbols. Solid lines show the error bounds for the initial data sets. Currents are normalized by the sum of the inner cylinder, exit plate, and exit orifice currents.

APPENDIX F

Ion-Neutral Collisions Supplementary Data

F.1 Experimental Data

F.1.1 With Applied Electric Field, No Magnetic Field

In addition to MEX and CEX ions collected on each electrode, the electrodes may collect ions and electrons generated via neutral-neutral ionization and collect and emit electrons. To separate the current due to high energy MEX and ionization ions, low energy CEX ions, and low energy ionization and PIEE electrons, an electric field was applied by biasing the front plate, inner cylinder, and exit plate to modest voltages. The voltage on each electrode was swept from 0 to ±100 V, while all other electrodes were kept grounded. Thus as will be shown below, the curves of current versus voltage are similar to that observed during a Langmuir probe sweep.

The currents measured on the front plate, inner cylinder, exit plate, and exit orifice are plotted in Figure F.2 as a function of voltage on the front plate for a few selected test cell pressures. The current on the exit plate increases at negative voltages since the exit plate repels electrons and attracts slow CEX ions that may otherwise go to the inner cylinder. These effects are more pronounced at higher test cell pressures where more collisions occur. At positive voltage and low test cell pressures, the current decreases since the exit plate repels the few slow CEX ions that may otherwise go to it, reattracts emitted electrons, and attracts a large amount of electrons generated in neutral-neutral ionization collisions. The opposite trend is observed on the inner cylinder. However, there is still significant positive current measured on the inner cylinder at negative exit plate current. This is due to CEX ions that are created in the near-entrance region that are unaffected by the electric field is the near-exit region, and that still go to inner cylinder 1 and 2. The currents on the exit plate and exit orifice are nearly constant with voltage, which again suggests that few electrons emitted from the exit plate reach the front plate and no electrons or CEX ions pass through the exit orifice.

Figure F.1 shows the current measured on the test cell electrodes as a function of voltage on the exit plate for the same test cell pressures. When biased negative, there is an increase in current to the front plate, which is likely due to the front plate attracting slow CEX ions that may otherwise go to the inner cylinder and/or repelling ionization electrons. This increase is larger at higher test cell pressures, when more CEX ions are created and more electrons may be generated. At positive voltage and low test cell pressures, the current decreases to zero since the front plate repels slow CEX ions that may otherwise go to it and since there is no neutral-neutral ionization. At positive voltage and high test cell pressures where Kn >1, the current becomes negative since the front plate attracts ionization electrons. The opposite trend is observed on the inner cylinder. The currents on the exit plate and exit orifice are constant with voltage, which suggests that electrons emitted from the exit plate do not reach the front plate, and that few CEX ions created in the near-entrance region reach the exit plate or exit orifice.

The currents measured as a function of inner cylinder voltage are slightly more complicated as shown in Figure F.3 due to the fact that an electric field is established at both ends of the inner cylinder. At positive inner cylinder voltages and low test cell pressures (i.e., Kn >1), the current to the inner cylinder decreases from a non-zero value to zero, which suggests that ions collected on the inner cylinder are CEX ions. At positive voltages and high test cell pressures, negative currents are measured on the inner cylinder due to electrons emitted from the exit plate and generated via neutral-neutral ionization that collect on the inner cylinder. The repelled ions to and attracted electrons from the front plate and exit

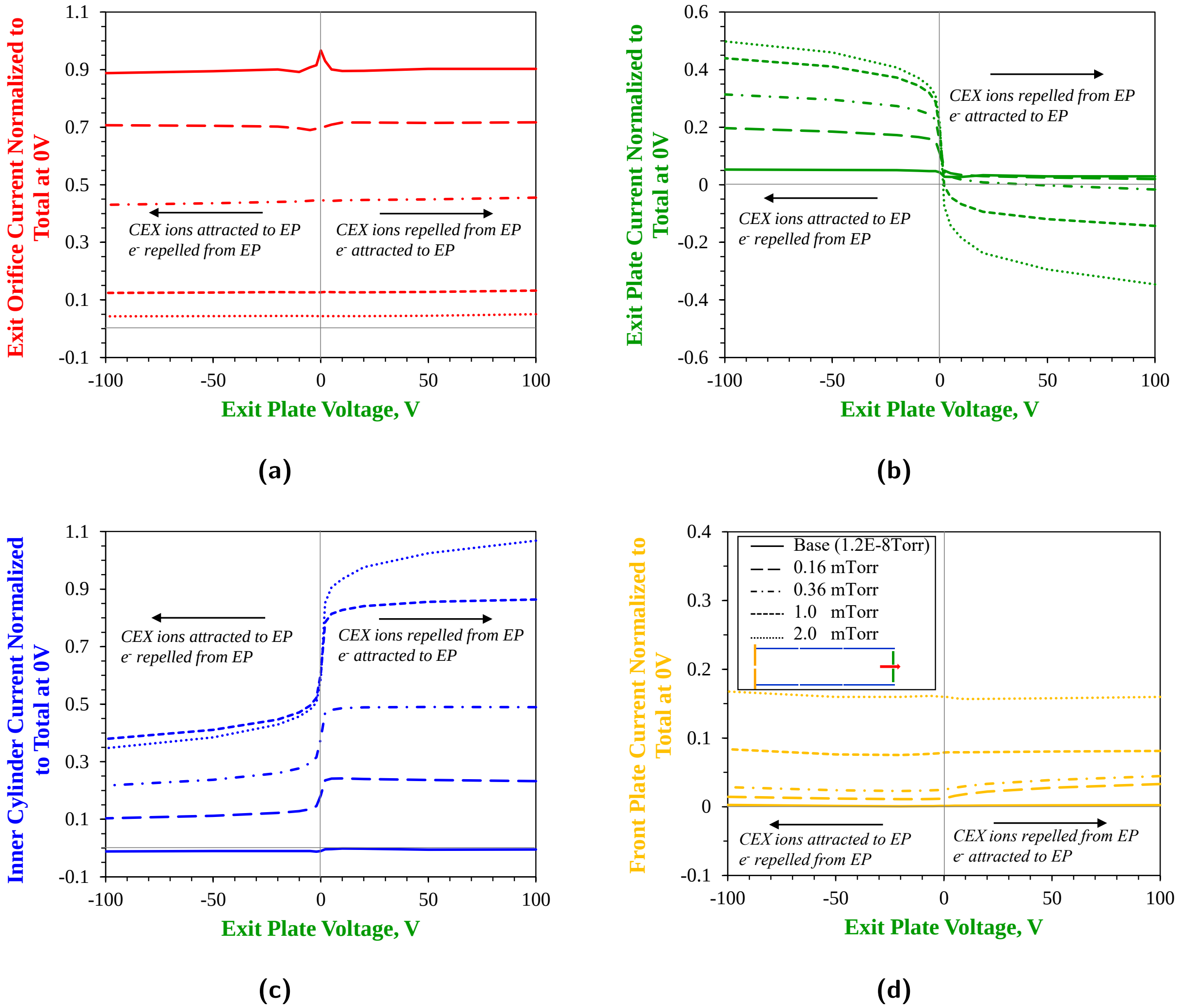

(a)

(b)

(c)

(d)

Figure F.1: Current measured on the (a) exit orifice (EO), (b) exit plate (EP), (c) inner cylinders (IC), and (d) front plate (FP) as a function of exit plate voltage at selected test cell pressures (the legend for all is shown in (d)).

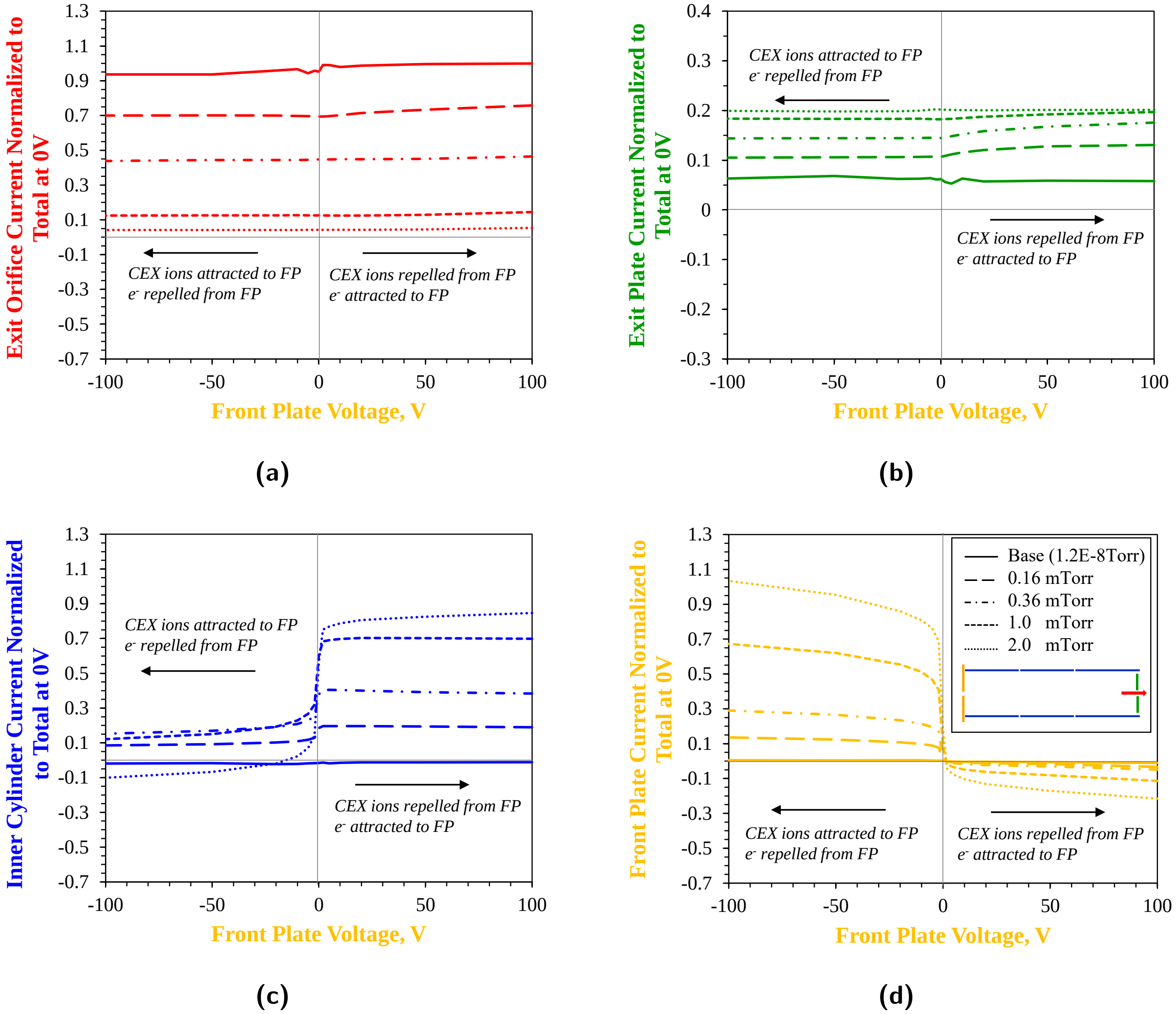

Figure F.2: Current measured on the (a) exit orifice (EO), (b) exit plate (EP), (c) inner cylinders (IC), and (d) front plate (FP) as a function of front plate voltage at selected test cell pressures (the legend for all is shown in (d)).

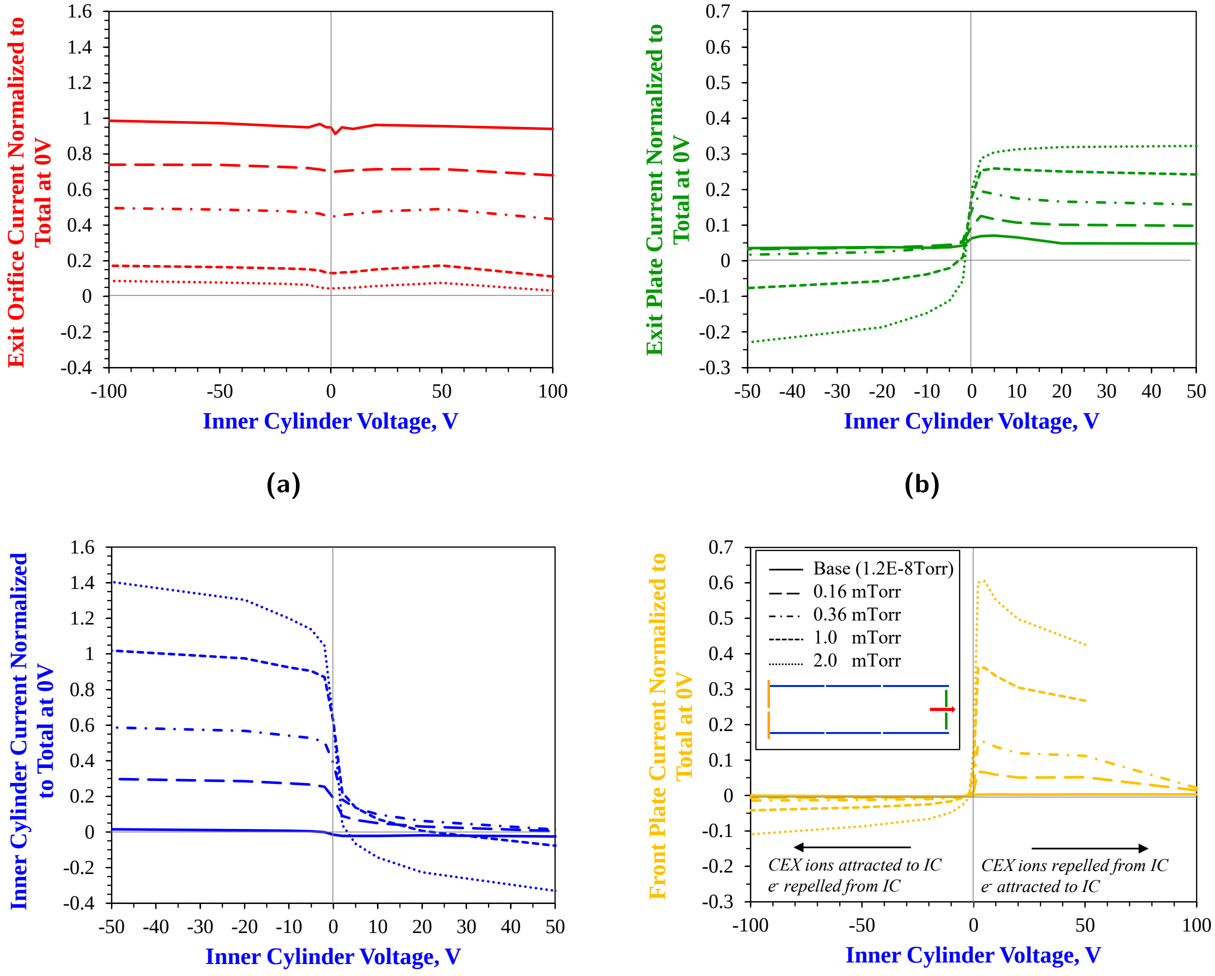

(a) (b)

(c) (d)

Figure F.3: Current measured on the (a) exit orifice (EO), (b) exit plate (EP), (c) inner cylinders (IC), and (d) front plate (FP) as a function of inner cylinder voltage at selected test cell pressures (the legend for all is shown in (d)).

plate are detected as an increase in current on these surfaces. The larger increase on the front plate than on the exit plate at high test cell pressures, suggests that more CEX ions are created at the near-entrance region (as expected). The current on the inner cylinder increases at negative voltages as more CEX ions are collected, and more electrons from the exit plate and ionization are repelled. This manifests as a decrease in current on the exit plate and front plate. Lastly, the constant current on the exit orifice suggests that no CEX ions (which scatter at large angle) and ionization electrons (which scatter isotropically) pass through the exit orifice.

To summarize, the biased data suggests the following for the the case where all test cell electrodes are grounded.

- Electrons emitted from the exit plate do not reach the front plate
- No CEX ions created in the near-entrance region of the test cell domain reach the exit plate
- No CEX ions, electrons emitted from any surface, and ionization electrons pass through the exit orifice
- Nearly all ions reaching the inner cylinder are CEX ions

F.1.2 With Applied Electric and Magnetic Fields

Finally, the transport of slow CEX ions was investigated without the complication of electron emission to and from the inner cylinder by biasing each of the test cell electrodes while an axial magnetic field was applied in the test cell domain. Figures F.4-F.6 show the currents measured on the test cell electrodes as a function of exit plate, front plate, and inner cylinder voltage. Electrode currents from Figures F.1-F.3 without magnetic field are included for comparison.

As discussed above, a difference in current on the exit plate with and without magnetic field is likely due to differences in electrons generated isotropically in neutral-neutral ionization collisions that may now be funneled to the the exit plate by the magnetic field. Electrons from the exit plate should be emitted at any front plate voltages above zero. Therefore, the increase in exit plate current (up to 20% of the total test cell current at 2 mTorr) observed at high test cell pressures in Figure F.5(b) as the front plate is increased from ground is due to ionization electrons. Decrease in exit plate current for negative front plate (up to 10% of the normalized current at 2 mTorr) is likely due to ionization electrons and electrons emitted from the exit plate that are repelled to the exit plate (also seen as an increase in front plate current). The same large increase in exit plate current (decrease in front plate current) is observed for negatively biased exit plate, and the same decrease in exit plate current (increase in front plate current) for positively biased exit plate.

The changes observed on the inner cylinder with varied electrode voltages when a magnetic field is applied should only be due to the transport of slow CEX ions. Therefore from the large variation in inner cylinder current observed in Figures F.5(b)-F.5(c), a significant fraction of CEX ions are collected on the inner cylinder. At positive inner cylinder voltages (where slow CEX are repelled) and low test cell pressures, the difference in inner cylinder current without and with magnetic field is due to PIEE, which is shown to be negligible (at these pressures). At positive inner cylinder voltages and high test cell pressured, the difference without and with magnetic field is due to ionization electrons, which are found to be significant.

The exit orifice current is found to be independent of voltages since no CEX ions and electrons are collected here.

To summarize, the data taken with applied electric and magnetic field suggests the following for the the case where all test cell electrodes are grounded.

- Significant CEX ions to the inner cylinder
- Significant ionization electrons to the exit plate, front plate, and inner cylinders

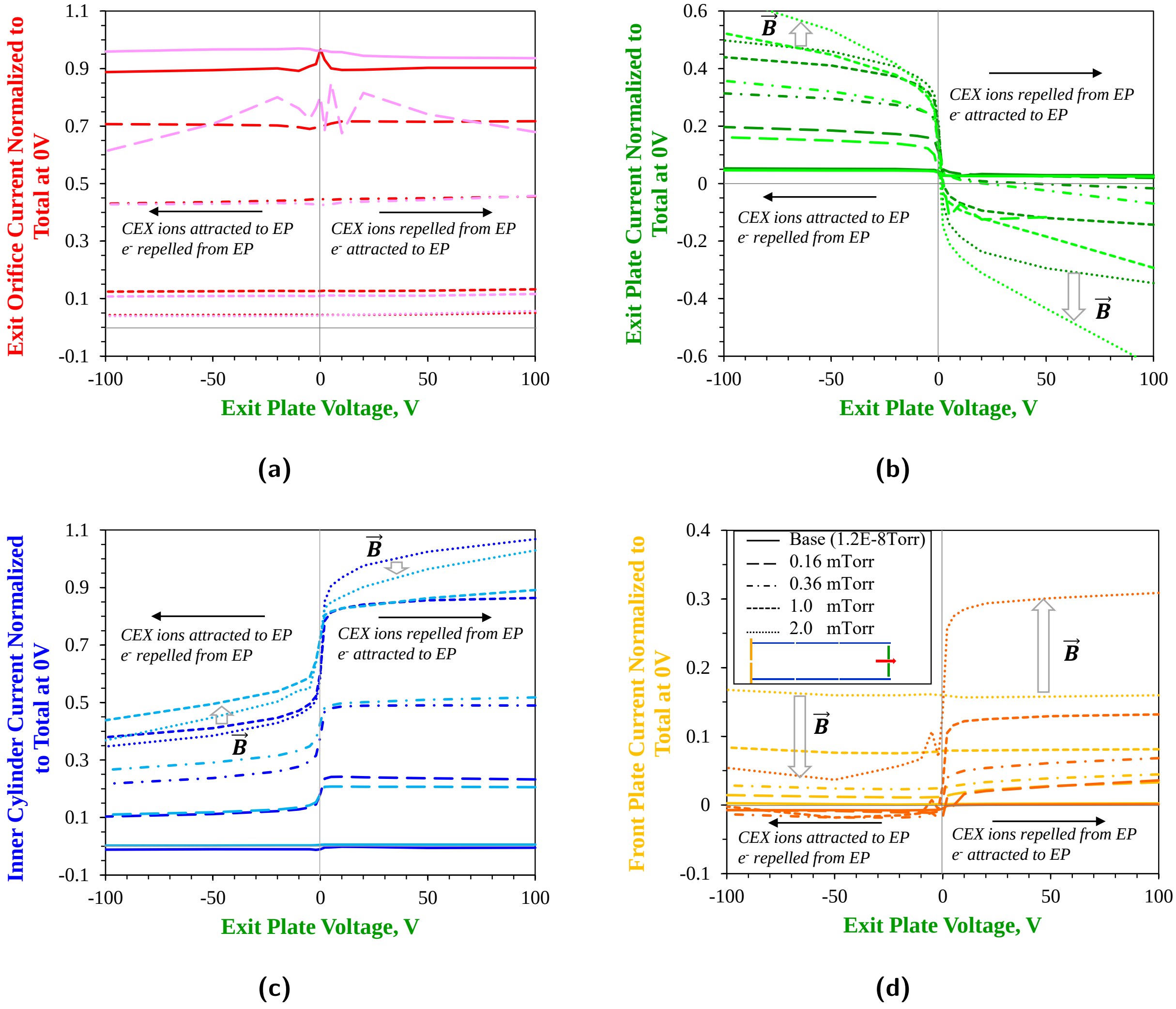

Figure F.4: Current measured on the (a) exit orifice (EO), (b) exit plate (EP), (c) inner cylinders (IC), and (d) front plate (FP) as a function of exit plate voltage at selected test cell pressures (the legend for all is shown in (d)). Data taken without magnetic field are reproduced from Figure F.2, while data taken with a magnetic field are shown in orange, turquoise, light green, and pink.

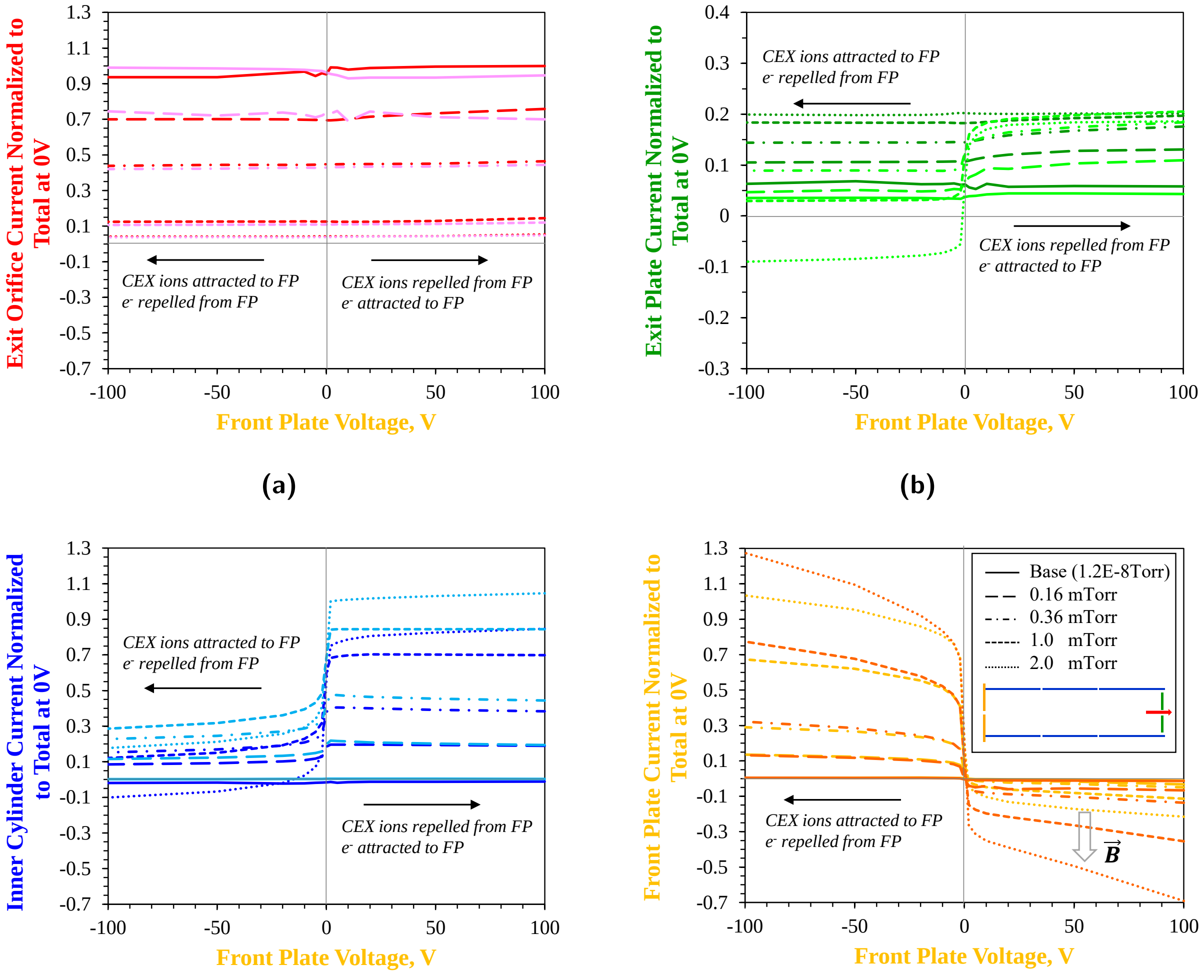

(a)

(b)

(c)

(d)

Figure F.5: Current measured on the (a) exit orifice (EO), (b) exit plate (EP), (c) inner cylinders (IC), and (d) front plate (FP) as a function of front plate voltage at selected test cell pressures (the legend for all is shown in (d)). Data taken without magnetic field are reproduced from Figure F.2, while data taken with a magnetic field are shown in orange, turquoise, light green, and pink.

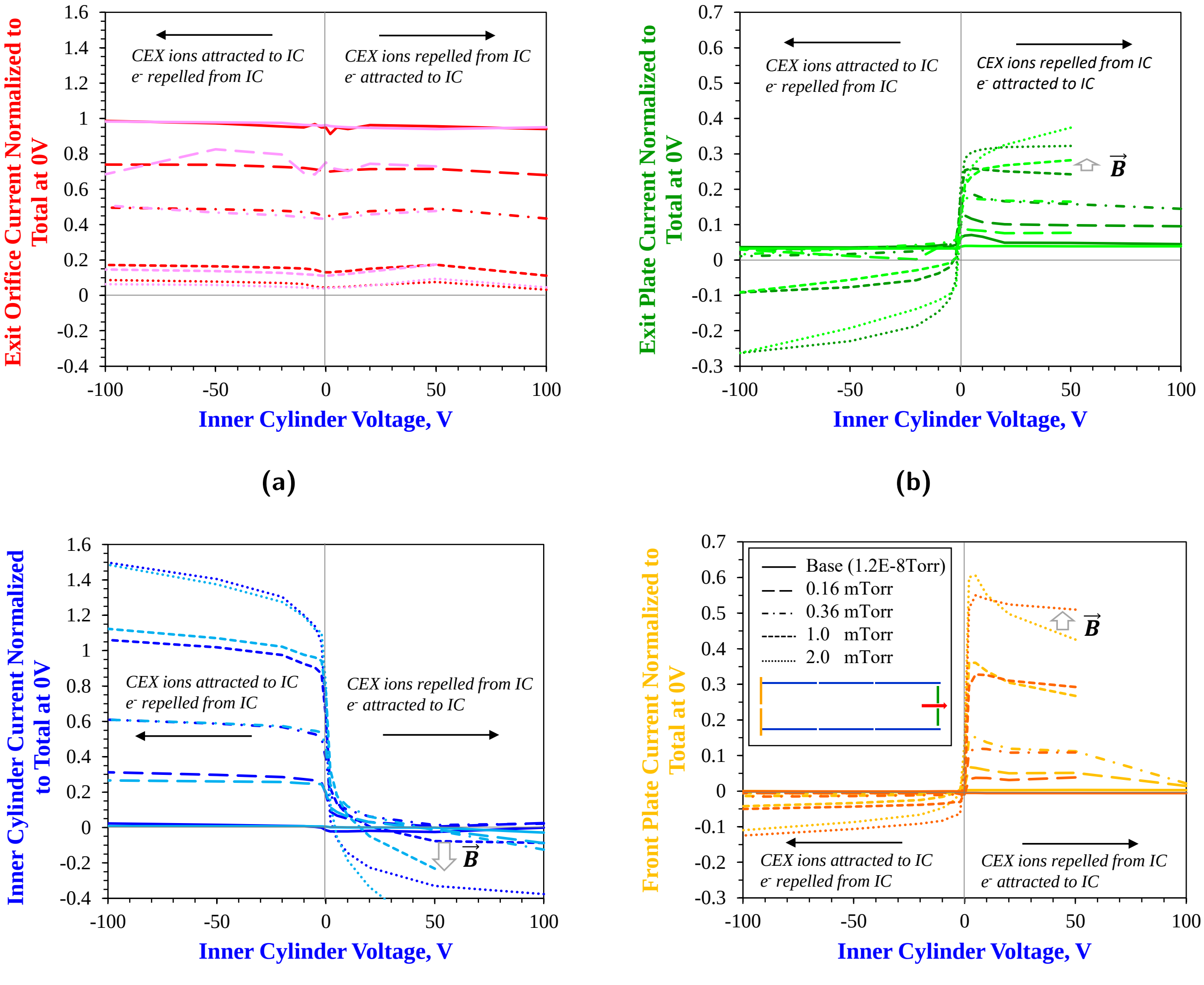

(a)

(b)

(c)

(d)

Figure F.6: Current measured on the (a) exit orifice (EO), (b) exit plate (EP), (c) inner cylinders (IC), and (d) front plate (FP) as a function of inner cylinder voltage at selected test cell pressures (the legend for all is shown in (d)). Data taken without magnetic field are reproduced from Figure F.2, while data taken with a magnetic field are shown in orange, turquoise, light green, and pink.

- No CEX ions, PIEE electrons, or ionization electrons pass through the exit orifice

Note that electric fields established in the test cell do change the velocity of charges particles, particularly CEX ions which have energies ~0.04 eV, PIEE electrons which are emitted with a peak energy of 2-4 eV, and low energy electrons generated via neutral-neutral ionization. However, the modest voltages applied here are not expected to significantly change the behavior of CEX ions, besides their trajectories. However, electric fields may increase electron energies such that electron-neutral collisions, particularly electron impact ionization, are considerable. The above discussion would still apply in such case since ions and electrons generated via electron-neutral ionization would follow similar trajectories to ions and electrons generated via neutral-neutral ionization.

F.2 Model Results

Model results of electrode currents at the walls of the test cell in the ion-neutral collision experiment are presented below. Figure 3.13 from Section 3.3.4 is reproduced here, but model results are added to plots in a step-wise fashion for clarity and to highlight results from the semi-analytical model developed by the author. Additionally, individual currents on the three inner cylinder segments are shown, as well as current distributions on the inner cylinders and exit plate.

F.2.1 Semi-Analytical Model

As discussed in Section 3.3.4, Figure F.7 shows the exit level of agreement between the semi-analytical model and experimental data for the exit orifice and front plate. Currents to the exit orifice and front plate are entirely from fast beam and MEX ions, and from large angle CEX ions, respectively. Substantial small-angle MEX ions and large-angle CEX ions reach the exit plate and inner cylinders, respectively. Qualitative agreement with measured currents on exit plate and inner cylinder is achieved when neutral-neutral ionization collisions are considered. This is also demonstrated in the result of current to each of the inner cylinder segments in Figure F.8.

F.2.2 Monte Carlo Collision Model

Results from the MCC-PIC model are shown in Figures F.9, F.10, and F.11. Currents considering only MEX ions, considering both MEX and CEX ions, and ions and electrons are shown, where particle-induced electron emission (PIEE) due to impact from ions and fast neutrals is considered assuming particle-induced yields of 0.2 and 0.4.

As discussed in Section 3.3.4, Figure F.7 shows excellent agreement with measured current on the exit orifice, and with ion-only results (i.e., ”MEX+CEX”) from the exit plate. Quantitative agreement with measurements of the exit plate and inner cylinders again is achieved when ion- and neutral-induced electron emission from the exit plate to the inner cylinders is considered, especially for higher yields. This is also observed in Figure F.10 for the inner cylinder segments. Since the model utilized high PIEE yields of 0.4 (i.e., Refs. [122, 128] suggest the yield for 1.5 keV Xe^+ impacting gold should be much lower), a combination of PIEE and neutral-neutral ionization collisions are likely to be at play.

The current distributions along the inner cylinder and exit plate are shown in Figure F.11. The current is uniform along the inner cylinder at low test cell pressures (i.e., Kn >1) since current to the inner cylinder is from CEX ions that are scattered at nearly 90° to the inner cylinder. Thus when Kn >1 and on average less than one collision occurs per beam ion, there is a uniform probability that the CEX ion is scattered at any position along the test cell domain. However at higher test cell pressures (when Kn <1), fast beam ions and MEX ions may experience multiple collisions that lead to a shift in current towards the entrance region of the test cell. The current along the exit plate exponentially increases towards the exit orifice due to the much larger number of MEX ions scattered at low angle. A smaller contribution on the exit plate due to CEX ions (difference between the dotted and dashed lines) is largest at large radii due to the large angle scattering of CEX ions. Electron

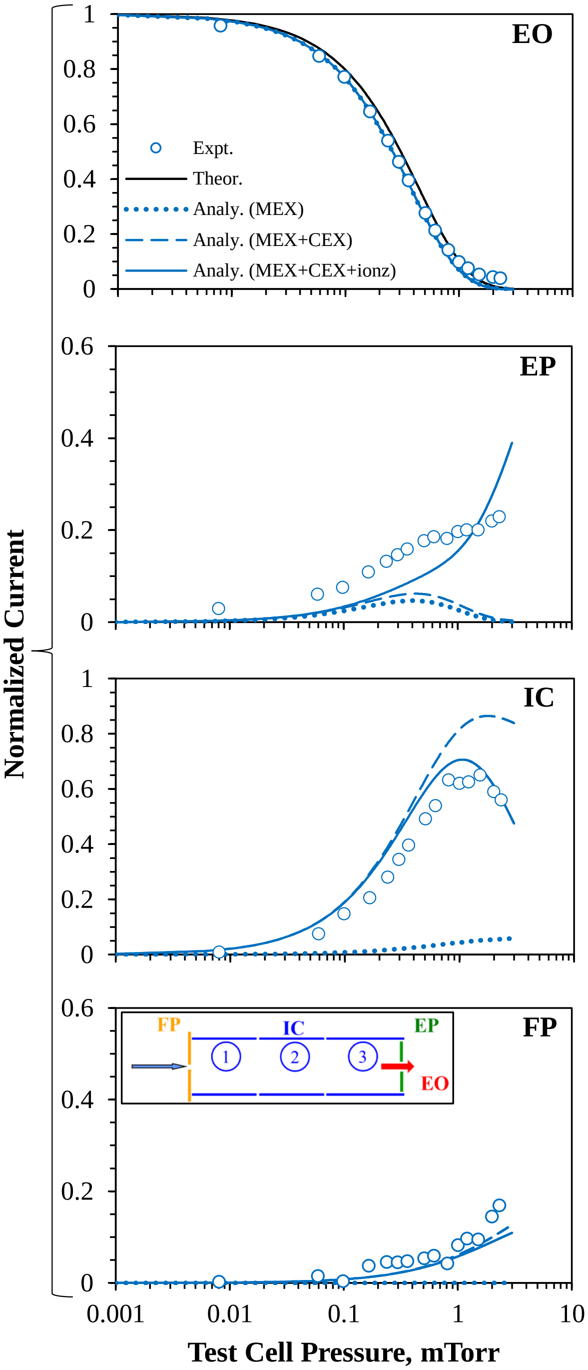

Figure F.7: Results from the semi-analytical model of current to the exit orifice (EO), exit plate (EP), inner cylinders (IC), and front plate (FP) as a function of test cell pressure. Contributions from MEX ions (dotted line), from MEX and CEX ions (dashed line), and from ions and electrons (solid lines) are shown, where electrons are assumed to be generated in neutral-neutral ionization collisions. Current calculated from Equation 3.9 with $\Delta x = L$ and $\sigma_{tot} = \sigma_{CEX}$ is compared to exit orifice current.

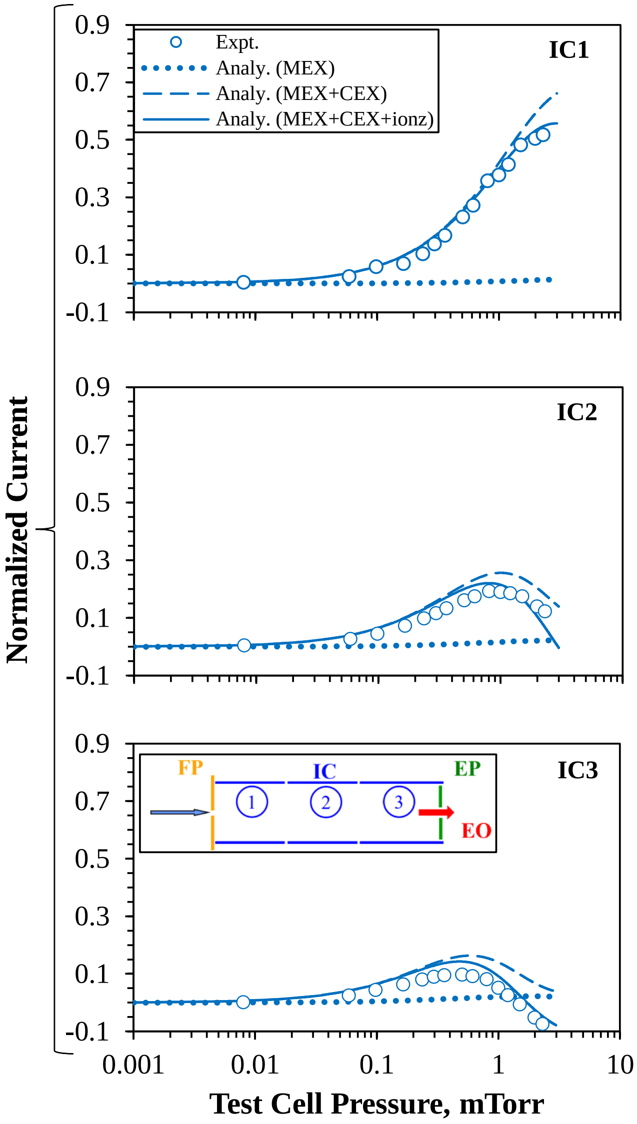

Figure F.8: Results from the semi-analytical model of current to inner cylinder 1 (IC1), inner cylinder 2 (IC2), and inner cylinder 3 (IC3) as a function of test cell pressure. Contributions from MEX ions (dotted line), from MEX and CEX ions (dashed line), and from ions and electrons (solid lines) are shown, where electrons are assumed to be generated in neutral-neutral ionization collisions.

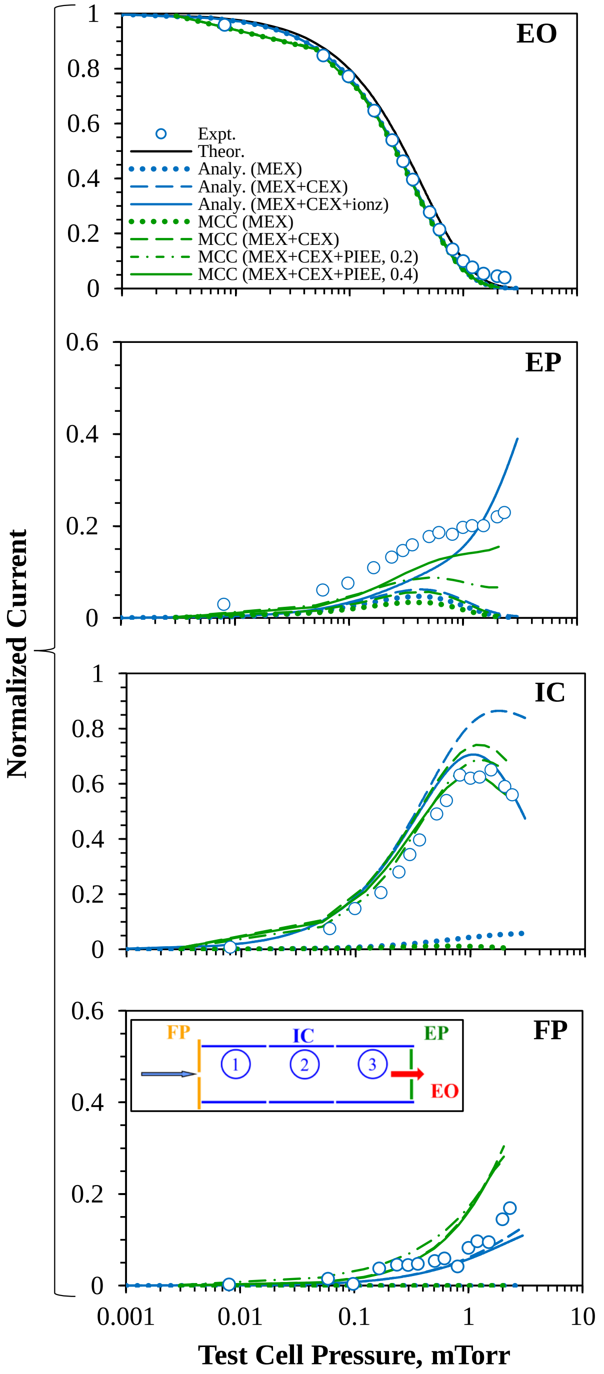

Figure F.9: Results from the MCC-PIC model of current to the exit orifice (EO), exit plate (EP), inner cylinders (IC), and front plate (FP) as a function of test cell pressure. Contributions from MEX ions (dotted line), from MEX and CEX ions (dashed line), and from ions and electrons (solid line) are shown, where electrons are assumed to be generated by particle-induced electron emission (PIEE) from the exit plate with yield equal to 0.2 or 0.4.

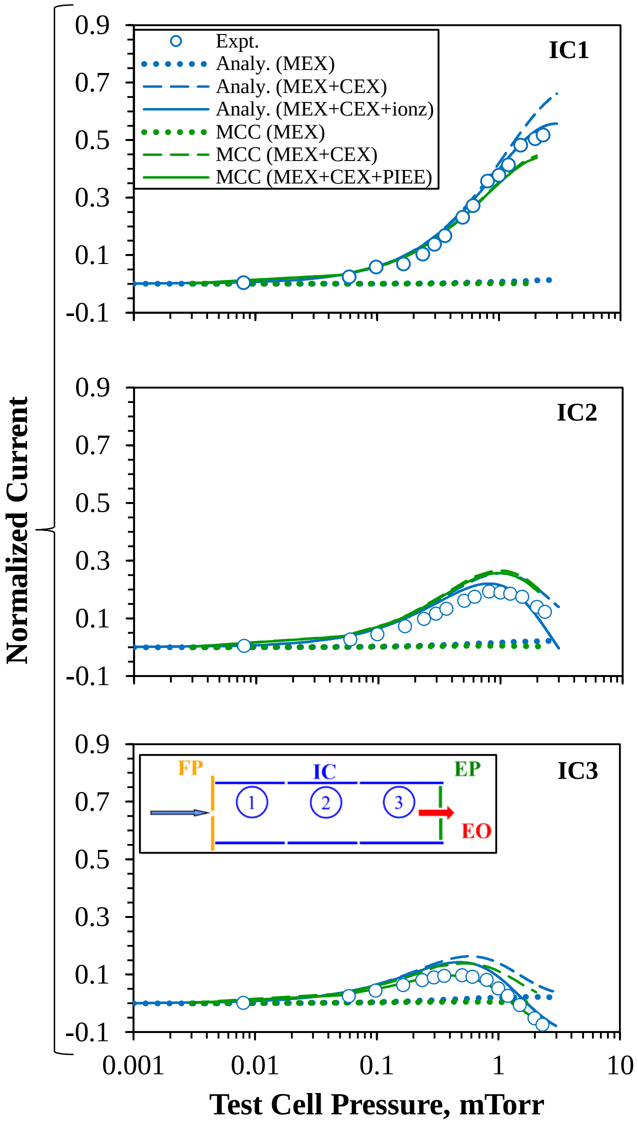

Figure F.10: Results from the MCC-PIC model of current to inner cylinder 1 (IC1), inner cylinder 2 (IC2), and inner cylinder 3 (IC3) as a function of test cell pressure. Contributions from MEX and CEX ions (dashed line), and from MEX and CEX ions plus PIEE electrons (solid line) are shown, where electrons are assumed to be generated by particle-induced electron emission (PIEE) from the exit plate with yield equal to 0.4.

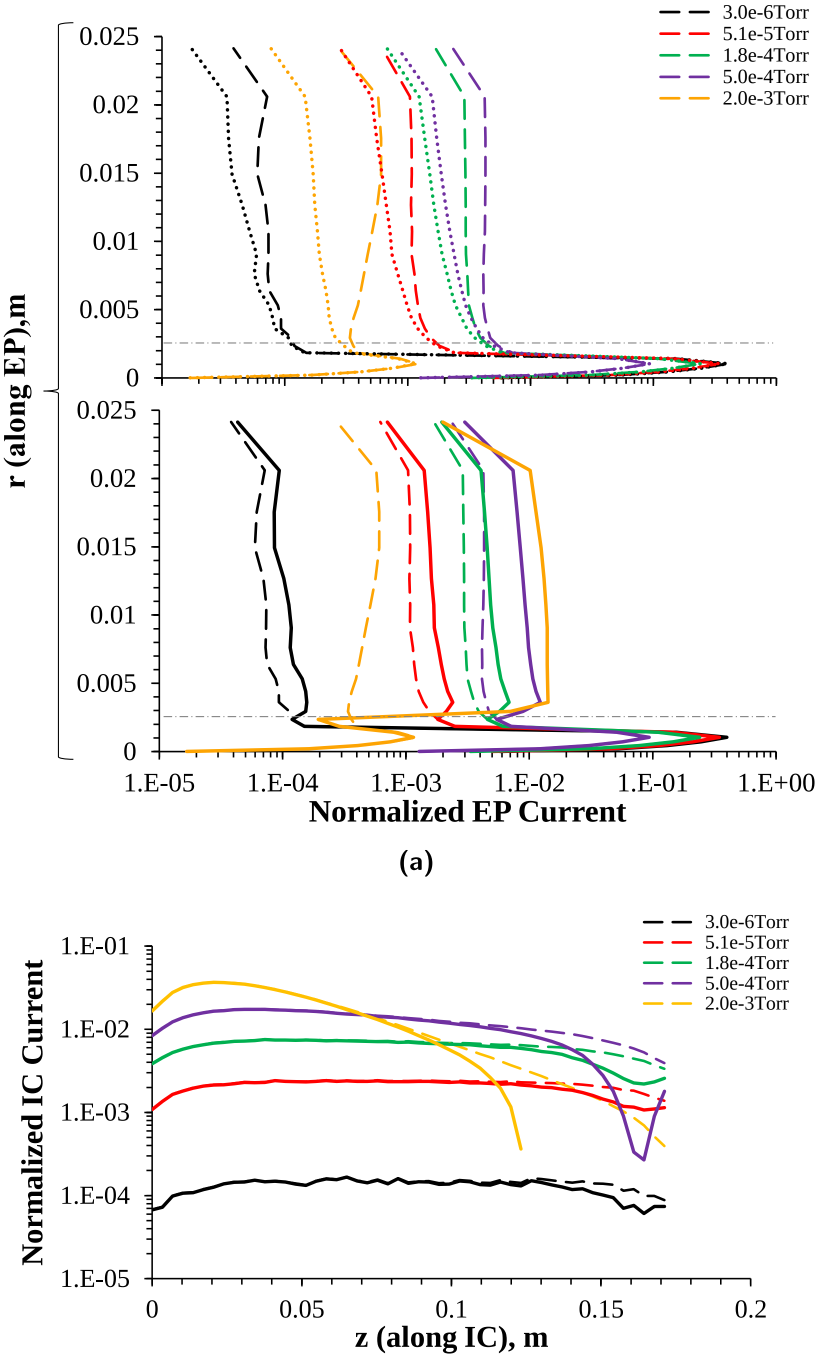

(a)

(b)

Figure F.11: Results from the MCC-PIC model of the MEX (dotted line), MEX and CEX (dashed line), and sum of ion and electron (solid line) current distribution along the (a) exit plate (EP) and (b) inner cylinder (IC) at select test cell pressures. Electrons are assumed to be generated by particle-induced electron emission (PIEE) from the exit plate with yield equal to 0.4.

emission from the exit plate (difference between the dashed and solid lines) is approximately uniform away from the exit orifice.

APPENDIX G

Measurements of IIEE from Ar^+ and Xe^+ Incident on Tungsten and Stainless Steel

This section introduces measurements of ion-induced electron emission (IIEE) properties of conducting materials. Section G.2 discusses utilization of the test cell for IIEE experiments. Distinct IIEE measurements of Xe^+ on stainless steel at incident energies below 2 keV are presented in Section G.3. IIEE measurements of Ar^+ and Xe^+ on tungsten are also presented, and compared to data obtained from previous researchers (shown in Figure 2.5(g)) for facility validation.

G.1 Techniques to Measure IIEE

Similar to previous effort, IIEE measurements are made by directing a mass analyzed and collimated beam of known current to a target material held in vacuum (10^{-8} Torr). The electrons emitted from the target I_{IIEE} can be measured from (i) a collector I_{coll} surrounding the target [77, 262, 77] or (ii) the target I_T. Hence the total IIEE yield γ (i.e., ratio of emitted electrons to incident ions) is then given by

$$\gamma = \frac{I_{IIEE}}{I_{beam}} = -\frac{I_{coll}}{I_{beam}} \tag{G.1a}$$

$$\gamma = \frac{I_{IIEE}}{I_{beam}} = \frac{(I_{IIEE} + I_{beam}) - I_{beam}}{I_{beam}} = \frac{I_T - I_{beam}}{I_{beam}} = \frac{I_T}{I_{beam}} - 1. \tag{G.1b}$$

The ion beam current I_{beam} can be measured on the target when biased positive to suppress IIEE from the target:

$$I_{beam} = I_T(V_T = +20V). \tag{G.2}$$

To ensure no tertiary electrons from the collector reach the target, the target should be biased negative when not suppressing electron emission from its surface:

$$I_{IIEE} = I_T(V_T = -20V) - I_{beam}. \tag{G.3}$$

G.2 Experimental Setup

The ion beam facility at the Jet Propulsion Laboratory described in Section 3.1 was adapted to examine IIEE. The ion beam energy was varied by the source grid voltage and E×B filter is used to allow only singly charged ions to pass into the test chamber. The ion beam was directed to a target of the conducting material under consideration, and the electron emitted from the target were measured on a surrounding collector. Modifications to the test cell, which holds the target and collector, are described in Section G.2.1. A calculation of the time required for residual gases inside the test cell to form a monolayer are provided in Section G.2.2 and compared to the time to sputter clean the target.

G.2.1 Modified Test Cell

The test cell was adapted to hold a sample of the material under consideration and the electron collector (see Figure G.1). The sample is mounted to the end of the test cell (i.e., where the exit plate was mounted in ion-neutral collision measurements). The downstream front plate and inner cylinder act as collector of the emitted electrons. Use of the front

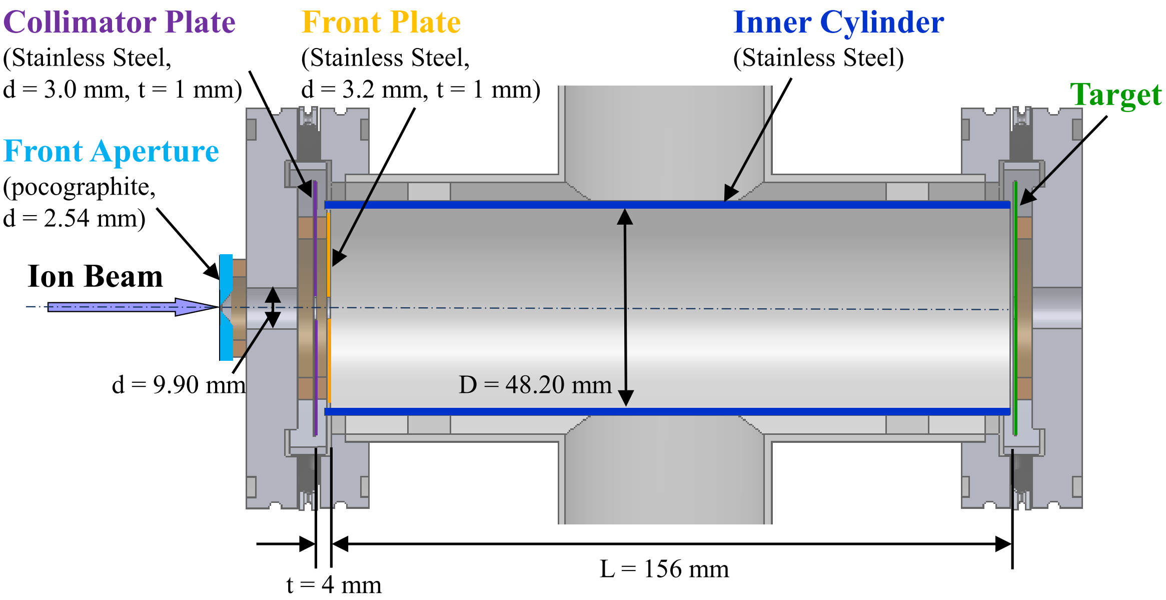

Figure G.1: Test cell electrodes for measuring ion-induced electron emission properties of conducting materials. Important materials and dimensions are included.

aperture and collimator plate result in an ion beam with less than 0.6° divergence, such that ions impact the target at normal incidence (since the IIEE yield is dependent on incidence angle) [262, 77]. The collimator plate is also biased positive during measurements to prevent any electrons created upstream of the test cell from entering the test cell. All electrodes are insulated from the test cell housing and each other with Ultem and Nylon spacers.

A Keithley 485 picoammeter is used to measure current on the front aperture electrode, and a Keithley 236 source meters to bias and measure the current on the collimator plate. A Keithley 237 source meter was used to bias and measure current on the front plate, inner cylinder, and target individually. When not biased, the inner cylinder current (calculated to be approximately 84% of the emitted electrons based on geometry and assuming cosine emission of electrons) was measured with a Keithley 617 electrometer (with highest resolution) and the front plate current with a Keithley 485 picoammeter.

G.2.2 Monolayer Formation Time

In order to characterize the surface of the materials, and ensure the target material is clean over the time of the measurement, the time for monolayer formation t_m is calculated by

$$t_m = \frac{N}{P_s \Gamma} \tag{G.4}$$

where N is the number density of atomic sites on the surface and P_s is the sticking probability. The flux of residual background gas Γ assuming ideal gas is given by

$$\Gamma = \frac{n_n v_{therm}}{4} \tag{G.5a}$$

$$p = n_n k_B T \tag{G.5b}$$

$$v_{therm} = \sqrt{\frac{8 k_B T}{\pi m_n}} \tag{G.5c}$$

For a surface density of 10^{19} m^{-2}, room temperature, and assuming a sticking probability of 1 for residual gases such as N_2, the monolayer time is given by

$$t_m \approx \frac{2.6 \times 10^{-6}}{p} \tag{G.6}$$

where p here is the pressure of the background gas in Torr. Hence for the 6.4×10^{-8} Torr vacuum facility, the target material develops a monolayer of adsorbed gas in about 40 s.

The time to form the monolayer is compared to the time required to remove the monolayer by sputtering with the Xe^+ or Ar^+ ion beam. The flux of sputtered ions from the target Γ_s

Table G.1: Sputter Yield of Xe^+ and Ar^+ Incident on N_2 (from Ref. [39]).

Projectile	300 eV	1500 eV
Xe^+	0.6	0.85
Ar^+	0.4	0.48

is calculated from the flux of ions to the target and the sputtering yield γ_{sputt}:

$$t_s = \frac{N}{\Gamma_s} = \frac{N}{\gamma_{sputt} I_{beam}/A_{beam} e}. \tag{G.7}$$

Sputter yield values for N_2 (for example) are provided in Table G.1.

For the ion beam currents produced by the facility, the time to sputter off a monolayer is 6 hours for a 500 eV, 7.7×10^{14} m^{-2} Xe^+ beam and 28 min for a 1 keV, 9.8×10^{15} m^{-2} Xe^+ beam. Hence there is some uncertainty in the IIEE yield measurements due to adsorbed residual gases. To account for this, the composition of the material surface is determined before and after IIEE measurement.

Prior to measurement, the tungsten target was also characterized by scanning electron microscopy (SEM) for surface structure and by electron diffraction spectroscopy (EDS) for surface composition. The composition was determined to be 96.2% tungsten, 3.3% carbon, and 0.5% oxygen. Hence the tungsten sample is not significantly oxidized by exposure to air before insertion into the vacuum chamber.

G.3 Experimental Results

Preliminary results are presented for 500-1000 eV Xe^+ and Ar^+ impacting tungsten. Tungsten was chosen to validate the experiment and approach since previous IIEE measurements exist for Xe^+ and Ar^+ at these energies. From Figure G.2, the yields follow the trend of increasing yield with increasing ion incident energy, but are more than five times higher than

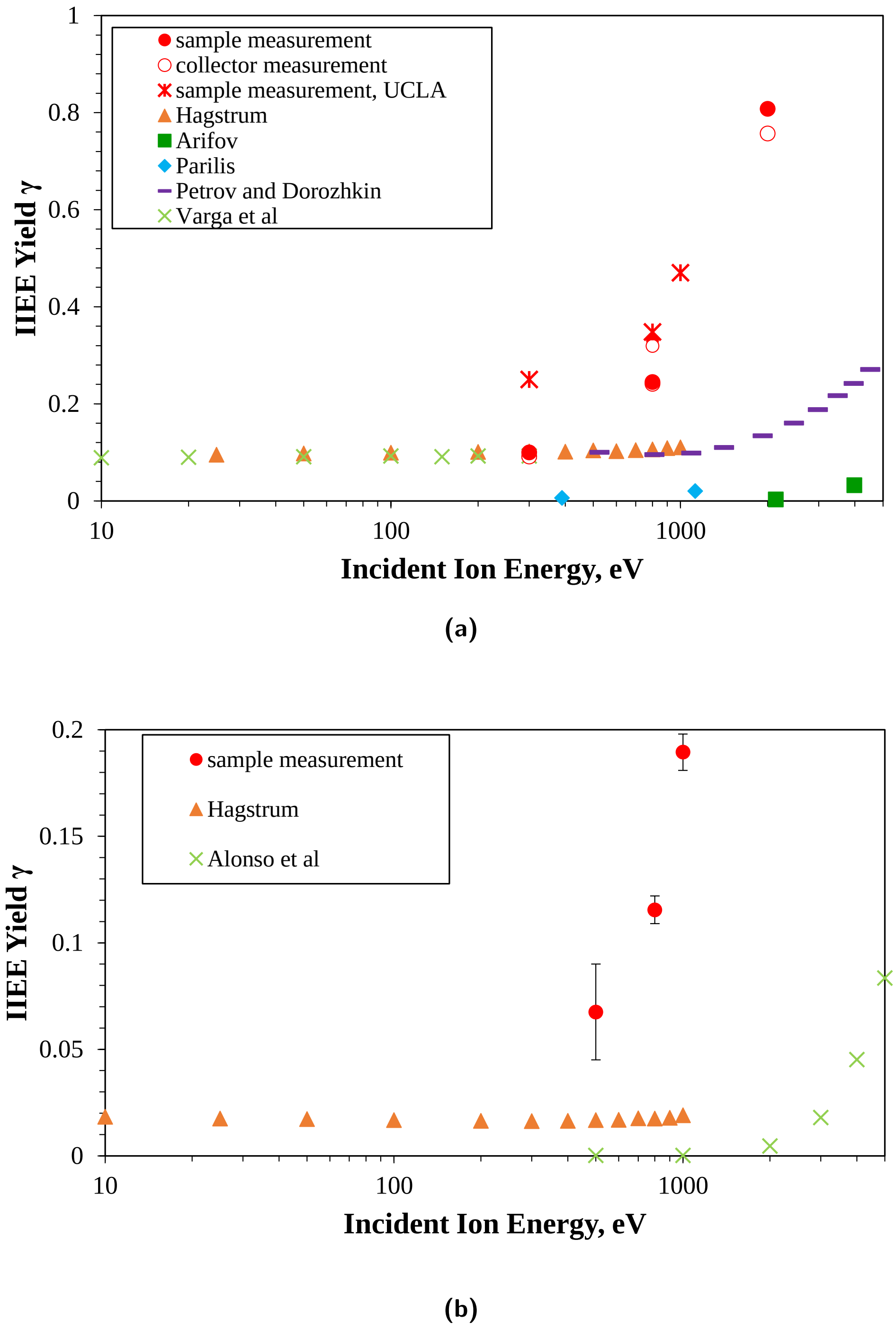

Figure G.2: Ion-induced electron emission yield for (a) Ar^+ and (b) Xe^+ incident on tungsten. Comparisons are made to previous measurements [33, 34, 35, 36, 37].

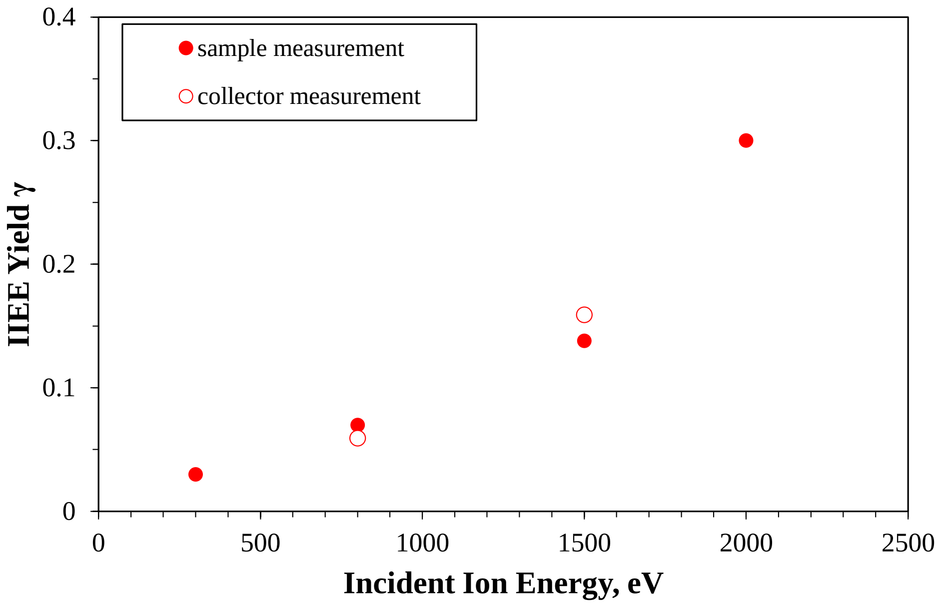

Figure G.3: Ion-induced electron emission yield for Xe^+ incident on stainless steel.

previous measurements. We believe the larger yield of the tungsten measured in our facility is likely due to surface condition (e.g., adsorption of residual gases and oxidation). The yield from Xe^+ incident on stainless steel is shown in Figure G.3. From this figure, it seen that the yield for 1.5 keV Xe^+ on stainless steel is approximately 0.15, which is smaller but the same order of magnitude as the values assumed in the MCC ion-collision models (i.e., $\gamma =$ 0.2 and 0.4).

APPENDIX H

Effects of Facility Background Pressure on SEE Measurements

The mean free path λ_{e-N_2} for electrons in N_2 gas (as an example) of given density $n_{N_2}$is given by

$$\lambda = \frac{1}{n_{N_2}\sigma_{e-N_2}} \tag{H.1}$$

where σ_{e-N_2} is the electron-nitrogen collision cross-section. For 2 eV true secondary electrons leaving the sample, σ_{e-N_2} is 3x10^{-19} m^2 [263] and the mean free path at 5x10^{-8} Torr is 2x10^3 m, which is four orders of magnitude larger than the distance between the sample and LEED/AES optics. A similar calculation can be done to show there is no effect due to scattering of primary electrons by the residual gases in front of the sample: for the lowest primary electron energy of 50 eV, σ_{e-N_2} is 8x10^-20 m^2 [263] and the mean free path at 5x10^{-8} Torr is 8x10^3 m, which is also large. We also note that at the electron energies and currents considered here, there is no thermal or electron-induced desorption, hence no local pressure increase near the sample.

APPENDIX I

Characterization of 4-Grid LEED/AES Optics

I.1 Secondary Electron Collection on Each Grid

Considering the geometry of the experiment, where the LEED/AES optics are 19 mm from the sample and the grids of the LEED/AES optics are 2.7 mm apart, the half-angle Θ from the sample center to the edge of each grid, as shown in Figure I.1, is calculated to have the values given in Table I.1. Assuming no obstruction between the sample and the respective grid, assuming zero grid transparency, and assuming a cosine distribution for emitted electrons, the fraction g of secondary electrons collected on each grid is

$$g = \int_0^{2\pi} \int_0^{\Theta} cos\theta sin\theta\theta d\theta d\phi = 1 - cos^2\Theta. \tag{I.1}$$

However, there are a number of grids of which each has the same transparency t (i.e., 83% not zero) and a number of grids N in front of the grid under consideration. Hence, the fraction of secondary electrons from the sample that are collected on each grid of the LEED/AES optics when each grid is grounded is calculated to be

$$\frac{I}{I_{SEE}} = gt^{N-1}(1-t) \tag{I.2}$$

Hence, theoretically only 56.4% of the current emitted from the sample is measured (not including G4 which cannot be measured) when grid G1 is kept at ground potential. This is close to the percentage of the measured current on the collection assembly when G1 is

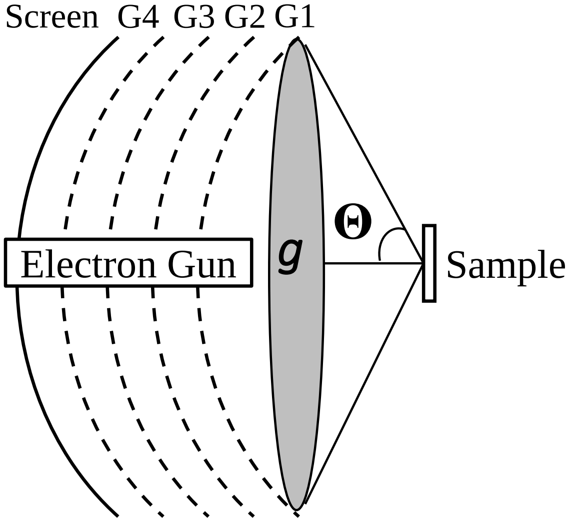

Figure I.1: Half-angles of LEED/AES grids.

Table I.1: Secondary Electron Collection on the LEED/AES Optics

Property	G1	G2	G3	G4	Screen
Θ	60°	56.6°	53.5°	50.8°	48°
g	0.75	0.70	0.65	0.60	0.55
$\frac{I}{I_{SEE}}$	12.8%	9.8%	7.6%	5.8%	26.2%

grounded versus when G1 is biased to 50 V (46.9-50.6% over the 50-500 eV range).

I.2 Tertiary Electron Collection on the Final Screen

Tertiary electrons from the grids may lead to error in energy distribution measurements, and must be quantified. Tertiary electrons from grids G1 and G2 are negligible since they are of low energy such that they are prevented from reaching the final hemispherical collector by the retarding potentials of grids G2 and G3. Considering the geometry of the LEED/AES optics, about 8% and 6% of secondary electrons emitted from the sample are calculated to impact grids G3 and G4, respectively, when the LEED/AES optics components are grounded (see I.1).

When calculating the number of tertiary electrons from G3 that are measured on the final hemispherical collector plate, it is assumed that (1-t) of tertiary electrons scattered backwards hit G2, t of those are scattered forward to pass through G3, and t of those pass through G4. Hence 12% of the tertiary electrons from G3 are measured on the final hemispherical collector.

Assuming a maximum possible yield of unity for low energy electrons impacting the stainless steel grids, assuming 12% of the tertiary electrons from G3 are measured on the final hemispherical collector (from above), and assuming all tertiary electrons from G4 are measured on the collector, a maximum of about 6% error (i.e., $8\% \times 12\% + 6\% \times 100\%$) is calculated for these effects on our energy distribution measurements.

APPENDIX J

Expressions for SEE Yields and Energy Distributions

J.1 Yield at Normal Incidence

J.1.1 True Secondary Yield

The empirical equation by Ref. [217] was used in the Monte Carlo model of nanostructured materials:

$$\delta(E_{PE}, 0) = \delta^{max} \frac{sE_{PE}/E_{PE}^{max}}{s - 1 + (\frac{E_{PE}}{E_{PE}^{max}})^s} \tag{J.1}$$

where δ^{max} is the maximum true SEE yield, E_{PE}^{max} is the corresponding energy at which the maximum yield occurs, and s is a material dependent parameter.

J.1.2 Inelastically Reflected Yield

The following empirical equation by Refs. [264, 217] was used in the Monte Carlo modeling of SEE from smooth and nanostructured surface:

$$\eta(E_{PE}, 0) = a(1 - bE_{PE})E_{PE}^{\gamma} \exp(-(\frac{E_{PE}}{E_b})^{\mu}), \tag{J.2}$$

where $E_b = c + dZ$, Z is the atomic number, a is a material dependent parameter (in the range of 7×10^{-3} to 10×10^{-3}), $b = 3 \times 10^{-5}, c = 300, d = 175, \gamma = 0.56, \mu = 0.70$, and $E_{PE} \leq 5000$ eV. Another empirical equation is provided by Refs. [265, 266].

J.1.3 Elastically Reflected Yield

The following empirical equation by Ref. [17] was used for comparison with data measured for graphite and in it's semi-empirical modeling:

$$\varepsilon(E_{PE}, 0) = f\sigma(E_{PE}, 0) \tag{J.3}$$

where $\ln f = 1.59 + 3.75 \ln E_{PE} - 1.37(\ln E_{PE})^2 + 0.12(\ln E_{PE})^3$ for E_{PE}=5-100eV and $f = 0$ for E_{PE} >100 eV, and σ is the total yield. For the Monte Carlo modeling of SEE from smooth and nanostructured surfaces, the following equation by Refs. [264, 217] was used:

$$\varepsilon(E_{PE}, 0) = \frac{\varepsilon_1}{1 + E_{PE}/E_{e1}} + \frac{\varepsilon_2}{1 + E_{PE}/E_{e2}}, \tag{J.4}$$

where $\varepsilon_1 = \varepsilon_0 - \varepsilon_2, \varepsilon_0$ is the elastic yield at $E_{PE} = 0, \varepsilon_2 = 0.07, E_{e1} = \frac{g}{\sqrt{Z}}, E_{e2} = hZ^2, g = 50, h = 0.25$, and Z is the atomic number. Anther empirical equations is provided by Refs. [265, 266]. Additionally Ref. [267] derived an expression using the Widdington velocity-distance relation and assuming single electron Rutherford scattering. Using simple quantum mechanics with a plane-wave electron wave function incident on a negative potential step of depth $\epsilon_0 = 150$ eV, Ref. [57] derived an expression.

J.1.4 Elastically and Inelastically Reflected Yield

The elastic and inelastic yields above can be summed to determine the reflected yield. Alternatively, empirical expressions were provided by Refs. [268, 157, 138, 269, 157]. Additionally, Ref. [270, 148, 13] derived an equation for low Z materials using the Widdington velocity-distance relation and assuming single electron Rutherford scattering.

J.1.5 Total Yield

The total SEE yield can be determined using the above equations for δ, η, and ε. However, for comparison of the total yield measured for graphite, the following expression by Ref. [17] was used:

$$\sigma(E_{PE}, 0) = \sigma^{max} \exp\left[-\frac{\left(\ln \frac{E_{PE}}{E_{PE}^{max}}\right)^2}{2\alpha^2}\right] \tag{J.5}$$

where $\alpha = 0.6$. An additionally empirical equation for the total yield includes that provided by Ref. [271].

J.2 Yield at Oblique Incidence

J.2.1 True Secondary Yield

The empirical equation by Ref. [217] was used in the Monte Carlo model of nanostructured materials:

$$\delta(E_{PE}, \theta_{PE}) = \delta(E_{PE}, 0)\frac{k+1}{k - \cos\theta_{PE}} \tag{J.6}$$

where $k = 0.0027Z + r, Z$ is the atomic number of the material, and r accounts for surface smoothness.

J.2.2 Inelastically Reflected Yield

The following empirical expression for the yield from inelastically reflected electrons given by Refs. [264, 217] was used in the Monte Carlo modeling of SEE from smooth and nanaostructured surfaces:

$$\eta(E_{PE}, \theta_{PE}) = \eta(E_{PE}, 0)^{\cos\theta_{PE}} C_1^{(1-\cos\theta_{PE})} \tag{J.7}$$

where $C_1 = \chi \frac{\eta(E_{PE},0)}{\eta(E_{PE},0)+\varepsilon(E_{PE},0)}$ and $\chi = 0.89$. Another empirical expression is provided by Ref. [266].

J.2.3 Elastically Reflected Yield

The empirical expression provided in [264, 217] was used in the Monte Carlo Model of SEE from smooth and nanostructured surfaces:

$$\varepsilon(E_{PE}, \theta_{PE}) = \varepsilon(E_{PE}, 0)^{\cos\theta_{PE}} C_2^{(1-\cos\theta_{PE})} \tag{J.8}$$

where $C_2 = \chi \frac{\varepsilon(E_{PE},0)}{\eta(E_{PE},0)+\varepsilon(E_{PE},0)}$ and $\chi = 0.89$. An additional empirical equation is provided by [266]. Using the Widdington velocity-distance relation and assuming single electron Rutherford scattering, Ref. [267] derived an expression for ε.

J.2.4 Elastically and Inelastically Reflected Yield

The elastic and inelastic yields above can be summed to determine the reflected yield. Alternatively, Refs. [272, 147, 273, 274, 275] provided empirical expressions.

J.3 Energy Distribution of Emitted Electrons

J.3.1 True Secondary Electrons

A theoretical derivation of the energy distribution of true secondary electrons was provided by Chung and Everhart [20]. A version of the distribution is provided in Equation 4.4.

J.3.2 Inelastically Reflected Electrons

The Monte Carlo modeling of smooth and nanostructured surfaces assumed that inelastically reflected electrons have an uniform probability of a energy between 50 eV and E_{PE}. However, empirical expressions for the energy distribution are provided by Refs. [265, 266, 264, 217].

J.3.3 Elastically Reflected Electrons

The Monte Carlo model of SEE from smooth and nanostructured surfaces assumed the energy of a elastically reflected electron is the same as the energy of the incident primary electron. In reality, there is a small spread around the primary electron energy. Refs. [265, 266] empirically determined this energy distribution.

J.3.4 Elastically and Inelastically Reflected Electrons

Ref. [267] stated that the mean energy for reflected electrons was about 2/3 of the incident energy for 10-100 keV incident electrons, while Refs. [276, 277, 158] found an an expression for the mean energy.

References

[1] Wirz, R. E., *Discharge plasma processes of ring-cusp ion thrusters*, Ph.D. thesis, California Institute of Technology, 2005.

[2] Goebel, D. M. and Katz, I., *Fundamentals of electric propulsion: ion and Hall thrusters*, Vol. 1, John Wiley & Sons, 2008.

[3] Wirz, R. E., Anderson, J. R., Goebel, D. M., and Katz, I., "Decel grid effects on ion thruster grid erosion," *IEEE Transactions on Plasma Science*, Vol. 36, No. 5, 2008, pp. 2122–2129.

[4] Wirz, R. E., Anderson, J. R., and Katz, I., "Time-Dependent Erosion of Ion Optics," *Journal of Propulsion and Power*, Vol. 27, No. 1, 2011, pp. 211–217.

[5] Wirz, R. and Katz, I., "XIPS ion thruster grid erosion predictions for deep space missions," *30th International Electric Propulsion Conference, Florence, Italy*, 2007.

[6] Wirz, E., Anderson, J. R., Goebel, D., and Katz, I., "XIPS Ion Thruster Grid Erosion Assessments for Deep Space Missions," AIAA-2008-4529, 44th Joint Propulsion Conference, Hartford, CT, 2008.

[7] www.popsci.com.

[8] Araki, S. J. and Wirz, R. E., "Ion-Neutral Collision Modeling using Classical Scattering with Spin-Orbit Free Interaction Potential," *IEEE Transactions on Plasma Science*, Vol. 41, No. 3, 2013, pp. 470–480.

[9] Paidarová, I. and Gadea, F. X., "Accurate ab initio calculation of potential energy curves and transition dipole moments of the Xe 2+ molecular ion," *Chemical Physics*, Vol. 274, No. 1, 2001, pp. 1–9.

[10] Giuliano, P. N. and Boyd, I. D., "Effects of detailed charge exchange interactions in DSMC-PIC simulation of a simplified plasma test cell," *32nd International Electric Propulsion Conference, Kurhaus, Wiesbaden, Germany*, 2011.

[11] Huerta, C. E. and Wirz, R. E., "Surface Geometry Effects on Secondary Electron Emission Via Monte Carlo Modeling," *52nd AIAA/ASME/SAE/ASEE Joint Propulsion Conference, Salt Lake City, Utah*, 2016, p. 4840.

[12] Pedgley, J., McCracken, G., Farhang, H., and Blott, B., "Measurements of secondary electron emission for fusion related materials," *Journal of nuclear materials*, Vol. 196, 1992, pp. 1053–1058.

[13] Farhang, H., Napchan, E., and Blott, B., “Electron backscattering and secondary electron emission from carbon targets: comparison of experimental results with Monte Carlo simulations,” *Journal of Physics D: Applied Physics*, Vol. 26, No. 12, 1993, pp. 2266.

[14] Kato, S., Nishiwaki, M., et al., “Secondary electron emission from metals and graphites,” *Accelerator Technical Design Report for J-PARC. JAERI, KEK. URL: http://hadron. kek. jp/˜ accelerator/TDA/tdr2003/chap2/2.3*, Vol. 8, 2003.

[15] Kirby, R., “Instrumental effects in secondary electron yield and energy distribution measurements,” Tech. rep., Stanford Linear Accelerator Center, Menlo Park, CA (US), 2004.

[16] Balcon, N., Payan, D., Belhaj, M., Tondu, T., and Inguimbert, V., “Secondary electron emission on space materials: evaluation of the total secondary electron yield from surface potential measurements,” *IEEE Transactions on Plasma Science*, Vol. 40, No. 2, 2012, pp. 282–290.

[17] Scholtz, J., Dijkkamp, D., and Schmitz, R., “Secondary electron emission properties,” *Philips journal of research*, Vol. 50, No. 3, 1996, pp. 375–389.

[18] Willis, R., Fitton, B., and Painter, G., “Secondary-electron emission spectroscopy and the observation of high-energy excited states in graphite: Theory and experiment,” *Physical Review B*, Vol. 9, No. 4, 1974, pp. 1926–1937.

[19] Amelio, G. and Scheibner, E., “Auger spectroscopy of graphite single crystals with low energy electrons,” *Surface Science*, Vol. 11, No. 2, 1968, pp. 242–254.

[20] Chung, M. and Everhart, T., “Simple calculation of energy distribution of low-energy secondary electrons emitted from metals under electron bombardment,” *Journal of Applied Physics*, Vol. 45, No. 2, 1974, pp. 707–709.

[21] El Gomati, M., Walker, C., Assa’d, A., and Zadražil, M., “Theory experiment comparison of the electron backscattering factor from solids at low electron energy (250–5,000 eV),” *Scanning*, Vol. 30, No. 1, 2008, pp. 2–15.

[22] Bruining, H. and De Boer, J., “Secondary electron emission: Part i. secondary electron emission of metals,” *Physica*, Vol. 5, No. 1, 1938, pp. 17–30.

[23] Ahearn, A. J., “The emission of secondary electrons from tungsten,” *Physical Review*, Vol. 38, No. 10, 1931, pp. 1858.

[24] Coomes, E. A., “Total Secondary Electron Emission from Tungsten and Thorium-Coated Tungsten,” *Physical Review*, Vol. 55, No. 6, 1939, pp. 519.

[25] McKay, K. G., “Total secondary electron emission from thin films of sodium on tungsten,” *Physical Review*, Vol. 61, No. 11-12, 1942, pp. 708.

[26] Walker, C., El-Gomati, M., Assa'd, A., and Zadražil, M., "The secondary electron emission yield for 24 solid elements excited by primary electrons in the range 250–5000 eV: a theory/experiment comparison," *Scanning*, Vol. 30, No. 5, 2008, pp. 365–380.

[27] Chaudhri, R. M., "Secondary electron emission from tungsten," *Proceedings of the National Institute of Sciences of India (National Institute of Sciences of India, 1941)*, Vol. 7, 1941, pp. 197.

[28] Mayer, R. and Weiss, A., "Comparative study of secondary-electron emission from positron and electron bombardment of Ni, Si, and MgO," *Physical Review B*, Vol. 38, No. 16, 1988, pp. 11927.

[29] Petry, R. L., "Critical potentials in secondary electron emission from iron, nickel, and molybdenum," *Physical Review*, Vol. 26, No. 3, 1925, pp. 346.

[30] Stern, R. and Taub, H., "Origin of the Angular Dependence of Secondary Emission of Electrons from Tungsten," *Physical Review Letters*, Vol. 20, No. 24, 1968, pp. 1340.

[31] Huerta, C. E., Wirz, R. E., and Patino, M. I., "Secondary electron emission from textured surfaces," *Journal of Applied Physics*, 2017, pp. submitted.

[32] Giuliano, P. and Boyd, I., "Analysis of a plasma test cell including non-neutrality and complex collision mechanisms," *48th AIAA/ASME/SAE/ASEE Joint Propulsion Conference & Exhibit, Atlanta, Georgia*, 2012, p. 3736.

[33] Parilis, E. and Kishinevskii, L., "Kinetic secondary electron ejection from molybdenum by cesium ions," *Sov Phys-Solid State*, Vol. 3, 1960, pp. 885.

[34] Hagstrum, H. D., "Auger ejection of electrons from tungsten by noble gas ions," *Physical Review*, Vol. 96, No. 2, 1954, pp. 325.

[35] Arifov, U., Kishinevskii, L., Mukhamadiev, E., and Parilis, E., "Auger neutralization of highly charged ions at the surface of a metal," *Soviet Physics Technical Physics*, Vol. 18, 1973, pp. 118.

[36] Petrov, N. and Dorozhkin, A., "Emission from tungsten induced by certain positive ions," *Soviet Physics, Solid State*, Vol. 3, 1961, pp. 38.

[37] Varga, P., Hofer, W., and Winter, H., "Auger neutralization of multiply charged noble gas ions at a tungsten surface," *Surface Science*, Vol. 117, No. 1, 1982, pp. 142–153.

[38] Scharfe, M. K., Azarnia, G., and Koo, J., "DSMC implementation of experimentally-based Xe++ Xe differential cross sections for electric propulsion modeling," Tech. rep., DTIC Document, 2010.

[39] Winters, H. F. and Sigmund, P., "Sputtering of chemisorbed gas (nitrogen on tungsten) by low-energy ions," *Journal of Applied Physics*, Vol. 45, No. 11, 1974, pp. 4760–4766.

[40] Mikellides, I. G., Katz, I., Kuharski, R. A., and Mandell, M. J., "Elastic scattering of ions in electrostatic thruster plumes," *Journal of propulsion and power*, Vol. 21, No. 1, 2005, pp. 111–118.

[41] Chiu, Y., Dressler, R., Levandier, D., Houchins, C., and Ng, C., "Large-angle xenon ion scattering in Xe-propelled electrostatic thrusters: differential cross sections," *Journal of Physics D: Applied Physics*, Vol. 41, No. 16, 2008, pp. 165503.

[42] Hobbs, G. and Wesson, J., "Heat flow through a Langmuir sheath in the presence of electron emission," *Plasma Physics*, Vol. 9, No. 1, 1967, pp. 85.

[43] Raitses, Y., Staack, D., Dunaevsky, A., and Fisch, N., "Operation of a segmented Hall thruster with low-sputtering carbon-velvet electrodes," *Journal of applied physics*, Vol. 99, No. 3, 2006, pp. 36103–36103.

[44] Raitses, Y., Kaganovich, I., and Sumant, A., "Electron emission from nano-and micro-engineered materials relevant to electric propulsion," *33rd International Electric Propulsion Conference, Washington DC, USA*, 2013.

[45] Dunaevsky, A., Raitses, Y., and Fisch, N., "Secondary electron emission from dielectric materials of a Hall thruster with segmented electrodes," *Physics of Plasmas (1994-present)*, Vol. 10, No. 6, 2003, pp. 2574–2577.

[46] Ono, M., Bell, M., Kaita, R., Kugel, H., Ahn, J.-W., Allain, J., Battaglia, D., Bell, R., Canik, J., Ding, S., et al., "Recent progress of NSTX lithium program and opportunities for magnetic fusion research," *Fusion Engineering and Design*, Vol. 87, No. 10, 2012, pp. 1770–1776.

[47] Skinner, C., Sullenberger, R., Koel, B., Jaworski, M., and Kugel, H., "Plasma facing surface composition during NSTX Li experiments," *Journal of Nuclear Materials*, Vol. 438, 2013, pp. S647–S650.

[48] Whyte, D., Evans, T., Wong, C., West, W., Bastasz, R., Allain, J., and Brooks, J., "Experimental observations of lithium as a plasma-facing surface in the DIII-D tokamak divertor," *Fusion Engineering and Design*, Vol. 72, No. 1, 2004, pp. 133–147.

[49] Abrams, T., Jaworski, M., Kallman, J., Kaita, R., Foley, E., Gray, T. K., Kugel, H., Levinton, F., McLean, A., and Skinner, C., "Response of NSTX liquid lithium divertor to high heat loads," *Journal of Nuclear Materials*, Vol. 438, 2013, pp. S313–S316.

[50] Pitts, R., Carpentier, S., Escourbiac, F., Hirai, T., Komarov, V., Lisgo, S., Kukushkin, A., Loarte, A., Merola, M., Naik, A. S., et al., "A full tungsten divertor for ITER: physics issues and design status," *Journal of Nuclear Materials*, Vol. 438, 2013, pp. S48–S56.

[51] Baldwin, M., Doerner, R., Nishijima, D., Tokunaga, K., and Ueda, Y., "The effects of high fluence mixed-species (deuterium, helium, beryllium) plasma interactions with tungsten," *Journal of Nuclear Materials*, Vol. 390, 2009, pp. 886–890.

[52] Kajita, S., Sakaguchi, W., Ohno, N., Yoshida, N., and Saeki, T., "Formation process of tungsten nanostructure by the exposure to helium plasma under fusion relevant plasma conditions," *Nuclear Fusion*, Vol. 49, No. 9, 2009, pp. 095005.

[53] De Temmerman, G., Bystrov, K., Zielinski, J. J., Balden, M., Matern, G., Arnas, C., and Marot, L., "Nanostructuring of molybdenum and tungsten surfaces by low-energy helium ions," *Journal of Vacuum Science & Technology A*, Vol. 30, No. 4, 2012, pp. 041306.

[54] Wright, G., Brunner, D., Baldwin, M., Doerner, R., Labombard, B., Lipschultz, B., Terry, J., and Whyte, D., "Tungsten nano-tendril growth in the Alcator C-Mod divertor," *Nuclear Fusion*, Vol. 52, No. 4, 2012, pp. 042003.

[55] Meyer, F. W., Hijazi, H., Bannister, M. E., Unocic, K. A., Garrison, L. M., and Parish, C. M., "Flux threshold measurements of He-ion beam induced nanofuzz formation on hot tungsten surfaces," *Physica Scripta*, Vol. 2016, No. T167, 2016, pp. 014019.

[56] Graves, T., Spektor, R., Stout, P., and Axley, A., "Transient-mode multipactor discharge," *Physics of Plasmas (1994-present)*, Vol. 16, No. 8, 2009, pp. 083502.

[57] Cimino, R., Collins, I., Furman, M., Pivi, M., Ruggiero, F., Rumolo, G., and Zimmermann, F., "Can low-energy electrons affect high-energy physics accelerators?" *Physical review letters*, Vol. 93, No. 1, 2004, pp. 014801.

[58] Cimino, R. and Demma, T., "Electron cloud in accelerators," *International Journal of Modern Physics A*, Vol. 29, No. 17, 2014, pp. 1430023.

[59] Jahn, R. G., *Physics of electric propulsion*, Courier Corporation, 2006.

[60] Bird, G., *Approach to translational equilibrium in a rigid sphere gas*, Vol. 6, AIP Publishing, 1963.

[61] Bird, G. A., *Molecular gas dynamics and the direct simulation of gas flows*, Clarendon, 1994.

[62] Giuliano, P. N. and Boyd, I. D., "Modeling particle-induced electron emission in a simplified plasma Test Cell," *Journal of Applied Physics*, Vol. 113, No. 11, 2013, pp. 113302.

[63] Giuliano, P. N., *Modeling fundamental plasma transport and particle-induced emission in a simplified Test Cell*, Ph.D. thesis, University of Michigan, 2013.

[64] Drawin, H. and Emard, F., "Atom-atom excitation and ionization in shock waves of the noble gases," *Physics Letters A*, Vol. 43, No. 4, 1973, pp. 333–335.

[65] Teloy, E. and Gerlich, D., "Integral cross sections for ionmolecule reactions. I. The guided beam technique," *Chemical Physics*, Vol. 4, No. 3, 1974, pp. 417–427.

[66] Dressler, R. A., Salter, R. H., and Murad, E., "Guided-ion beam measurements of the X++ H2O (D2O)(X= Ar, N2) collision systems," *The Journal of chemical physics*, Vol. 99, No. 2, 1993, pp. 1159–1171.

[67] Bastian, M. J., Dressler, R. A., Levandier, D. J., Murad, E., Muntean, F., and Armentrout, P. B., "Low energy collision-induced dissociation and photodissociation studies of the (N2O, H2O)+ cluster ion," *The Journal of chemical physics*, Vol. 106, No. 23, 1997, pp. 9570–9579.

[68] Williams, S., Chiu, Y.-H., Levandier, D., and Dressler, R., "Determination of photofragment ion translational energy and angular distributions in an octopole ion guide: A case study of the Ar2+ and (N2O? H2O)+ cluster ions," *The Journal of chemical physics*, Vol. 109, No. 17, 1998, pp. 7450–7461.

[69] Jones, P., Conklin, G., Lorents, D., and Olson, R., "Differential elastic-scattering measurements of Xe+ on Xe and Ar+ on Ar in the 20-340-eV range," *Physical Review A*, Vol. 10, No. 1, 1974, pp. 102.

[70] Morris, B., *Charge-exchange collision dynamics and ion engine grid geometry optimization*, Ph.D. thesis, California Institute of Technology, 2007.

[71] Blanchard, J., Ghoniem, N., and Chou, S., "An approximate solution to the scattering integral for general interatomic potentials," *Journal of applied physics*, Vol. 61, No. 8, 1987, pp. 3120–3123.

[72] Miller, J. S., Pullins, S. H., Levandier, D. J., Chiu, Y.-h., and Dressler, R. A., "Xenon charge exchange cross sections for electrostatic thruster models," *Journal of Applied Physics*, Vol. 91, No. 3, 2002, pp. 984–991.

[73] Goebel, D. M., Wirz, R. E., and Katz, I., "Analytical ion thruster discharge performance model," *Journal of Propulsion and Power*, Vol. 23, No. 5, 2007, pp. 1055–1067.

[74] Fife, J. M., *Hybrid-PIC modeling and electrostatic probe survey of Hall thrusters*, Ph.D. thesis, Massachusetts Institute of Technology, 1999.

[75] Katz, I., Jongeward, G., Davis, V., Mandell, M., Mikellides, I., Dressler, R., Boyd, I., Kannenberg, K., Pollard, J., and King, D., "A Hall effect thruster plume model including large-angle elastic scattering," *37th Joint Propulsion Conference and Exhibit*, 2001, p. 3355.

[76] Boyd, I. D. and Dressler, R. A., "Far field modeling of the plasma plume of a Hall thruster," *Journal of Applied Physics*, Vol. 92, No. 4, 2002, pp. 1764–1774.

[77] Baragiola, R., Alonso, E., and Florio, A. O., "Electron emission from clean metal surfaces induced by low-energy light ions," *Physical Review B*, Vol. 19, No. 1, 1979, pp. 121.

[78] Benazeth, N., "Review on Kinetic Ion-Electron Emission from Solid Metallic Targets," *Nuclear Instruments and Methods in Physics Research*, Vol. 194, No. 1-3, 1982, pp. 405–413.

[79] Kishinevsky, L., "Estimation of electron potential emission yield dependence on metal and ion parameters," *Radiation Effects*, Vol. 19, No. 1, 1973, pp. 23–27.

[80] Schou, J., "Transport theory for kinetic emission of secondary electrons from solids," *Physical Review B*, Vol. 22, No. 5, 1980, pp. 2141.

[81] Sternglass, E., "Theory of secondary electron emission by high-speed ions," *Physical Review*, Vol. 108, No. 1, 1957, pp. 1.

[82] Hagstrum, H. D., "Studies of adsorbate electronic structure using ion neutralization and photoemission spectroscopies," *Electron and Ion Spectroscopy of Solids*, Springer, 1978, pp. 273–323.

[83] Dennison, J., Thomson, C., Kite, J., Zavyalov, V., and Corbridge, J., "Materials characterization at Utah State University: Facilities and knowledgebase of electronic properties of materials applicable to spacecraft charging," Tech. rep., Utah State University, 2003.

[84] Evdokimov, I., Mashkova, E., Molchanov, V., and Odintsov, D., "Dependence of the Ion–Electron Emission Coefficient on the Angle of Incidence," *physica status solidi (b)*, Vol. 19, No. 1, 1967, pp. 407–415.

[85] Cernusca, S., Fürsatz, M., Winter, H., and Aumayr, F., "Ion-induced kinetic electron emission from HOPG with different surface orientation," *EPL (Europhysics Letters)*, Vol. 70, No. 6, 2005, pp. 768.

[86] Hasselkamp, D. and Scharmann, A., "Ion-Induced Electron Emission from Carbon," *physica status solidi (a)*, Vol. 79, No. 2, 1983.

[87] Szapiro, B. and Rocca, J. J., "Electron emission from glow-discharge cathode materials due to neon and argon ion bombardment," *Journal of applied physics*, Vol. 65, No. 9, 1989, pp. 3713–3716.

[88] Avilkina, V. S., Andrianova, N., Borisov, A., Mashkova, E., and Parilis, E., "Energy and temperature dependences of ion-induced electron emission from polycrystalline

graphite," *Nuclear Instruments and Methods in Physics Research Section B: Beam Interactions with Materials and Atoms*, Vol. 269, No. 9, 2011, pp. 995–998.

[89] Borisov, A. and Mashkova, E., "Ion beam-induced electron emission from carbon-based materials," *Nuclear Instruments and Methods in Physics Research Section B: Beam Interactions with Materials and Atoms*, Vol. 258, No. 1, 2007, pp. 109–115.

[90] Magnuson, G. and Carlston, C., "Electron ejection from metals due to 1-to 10-keV noble gas ion bombardment. I. Polycrystalline materials," *Physical review*, Vol. 129, No. 6, 1963, pp. 2403.

[91] Carlston, C., Magnuson, G., Mahadevan, P., and Harrison Jr, D., "Electron ejection from single crystals due to 1-to 10-keV noble-gas ion bombardment," *Physical Review*, Vol. 139, No. 3A, 1965, pp. A729.

[92] En, W. and Cheung, N. W., "A new method for determining the secondary electron yield dependence on ion energy for plasma exposed surfaces," *IEEE transactions on plasma science*, Vol. 24, No. 3, 1996, pp. 1184–1187.

[93] Alonso, E., Baragiola, R., Ferron, J., Jakas, M., and Oliva-Florio, A., "Z 1 dependence of ion-induced electron emission from aluminum," *Physical Review B*, Vol. 22, No. 1, 1980, pp. 80.

[94] Ohya, K., "Monte Carlo simulation of heavy ion induced kinetic electron emission from an Al surface," *Nuclear Instruments and Methods in Physics Research Section B: Beam Interactions with Materials and Atoms*, Vol. 195, No. 3, 2002, pp. 281–290.

[95] Bourne Jr, H., Cloud, R., and Trump, J., "Role of Positive Ions in High-Voltage Breakdown in Vacuum," *Journal of Applied Physics*, Vol. 26, No. 5, 1955, pp. 596–599.

[96] Baragiola, R., Alonso, E., and Raiti, H., "Ion-induced Auger-electron emission from aluminum," *Physical Review A*, Vol. 25, No. 4, 1982, pp. 1969.

[97] Svensson, B. and Holmen, G., "Electron emission from ion-bombarded aluminum," *Journal of Applied Physics*, Vol. 52, No. 11, 1981, pp. 6928–6933.

[98] Kawata, J., Ohya, K., and Mori, I., "Direct Monte Carlo simulation of incident-angle dependence of secondary electron emission from aluminum," *Japanese journal of applied physics*, Vol. 31, No. 5R, 1992, pp. 1453.

[99] Hasselkamp, D., Lang, K., Scharmann, A., and Stiller, N., "Ion induced electron emission from metal surfaces," *Nuclear Instruments and Methods*, Vol. 180, No. 2-3, 1981, pp. 349–356.

[100] Fogel, Y. M., Slabospitskii, R. P., and Rastrepin, A. B., “Emission of charged particles from metal surfaces under bombardment by positive ions,” *Soviet Physics - Technical Physics*, Vol. 5, 1960, pp. 58.

[101] Colombie, N., Fagot, B., and Fert, E. C., “Emission electronique cinetique de cibles monocristallines metalliques,” *Radiation Effects*, Vol. 2, No. 1, 1969, pp. 31–39.

[102] Böhm, C. and Perrin, J., “Retarding-field analyzer for measurements of ion energy distributions and secondary electron emission coefficients in low-pressure radio frequency discharges,” *Review of scientific instruments*, Vol. 64, No. 1, 1993, pp. 31–44.

[103] Langley, R. A., Bohdansky, J., Eckstein, W., Mioduszewski, P., Roth, J., Taglauer, E., Thomas, E., Verbeek, H., and Wilson, K., “Data compendium for plasma-surface interactions,” *Nuclear Fusion*, Vol. 24, No. S1, 1984, pp. S9.

[104] Brusilovsky, B., “Kinetic ion-induced electron emission from the surface of random solids,” *Applied Physics A: Materials Science & Processing*, Vol. 50, No. 1, 1990, pp. 111–129.

[105] Krebs, K. H., “Untersuchungen zum Isotopieeffekt bei der Sekundärelektronenauslösung an Metalloberflächen durch positive Ionen,” *Annalen der Physik*, Vol. 470, No. 1-2, 1965, pp. 111–112.

[106] Arifov, U. A., Rakhimov, R. R., and Khozinski, O. V., “Electron emission in the bombardment of certain metal ions of inert gases in the energy range up to 50 keV,” *Proc. of the Academy of Sciences of USSR, series: Physical*, Vol. 26, 1962, pp. 1398–1402.

[107] Ohya, K., “Comparative study of target atomic number dependence of ion induced and electron induced secondary electron emission,” *Nuclear Instruments and Methods in Physics Research Section B: Beam Interactions with Materials and Atoms*, Vol. 206, 2003, pp. 52–56.

[108] Holmén, G., Svensson, B., and Burén, A., “Ion induced electron emission from polycrystalline copper,” *Nuclear Instruments and Methods in Physics Research*, Vol. 185, No. 1-3, 1981, pp. 523–532.

[109] Mashkova, E., Odintsov, D., and Molchanov, V., “Anisotropy of ion-electron emission coefficient of single crystals,” *Doklady Akademii Nauk SSSR*, Vol. 151, No. 5, 1963, pp. 1074.

[110] Mashkova, E., Molchanov, V., and Fleurov, V., “Angular dependences of sputtering ratio, ion-electron emission coefficient and ion-induced photon emission yield at oblique ion incidence on crystalline targets,” *Radiation effects*, Vol. 89, No. 3-4, 1985, pp. 313–318.

[111] Brusilovsky, B. and Molchanov, V., “Some angular dependences of the ion-electron emission coefficient,” *Radiation Effects*, Vol. 23, No. 2, 1974, pp. 131–134.

[112] Borisov, A., Mashkova, E., Nemov, A., and Parilis, E., “Ion-induced electron emission – monitoring the structure transitions in graphite,” *Nuclear Instruments and Methods in Physics Research Section B: Beam Interactions with Materials and Atoms*, Vol. 230, No. 1, 2005, pp. 443–448.

[113] Drentje, S., “Remarks on the kinetic ejection of electrons from a copper monocrystal by argon ions with energy 20–80 keV,” *Physics Letters A*, Vol. 24, No. 1, 1967, pp. 12–14.

[114] Hagstrum, H. D., “Auger ejection of electrons from molybdenum by noble gas ions,” *Physical Review*, Vol. 104, No. 3, 1956, pp. 672.

[115] Vance, D. W., “Auger Electron Emission from Clean Mo Bombarded by Positive Ions. III. Effect of Electronically Excited Ions,” *Physical Review*, Vol. 169, No. 2, 1968, pp. 263.

[116] Mahadevan, P., Layton, J., and Medved, D., “Secondary electron emission from clean surface of molybdenum due to low-energy noble gas ions,” *Physical Review*, Vol. 129, No. 1, 1963, pp. 79.

[117] Arifov, U., Rakhimov, R., and Dzhurakulov, K., “Secondary Emission in the Bombardment of Molybdenum by Neutral Atoms and Argon Ions (Inst, of Nuclear Physics), Academy of Sciences,” *UZBEK (SSR) Dokladv Akatl. Nauk SSSR*, Vol. 143, 1962, pp. 309–311.

[118] Ferrón, J., Alonso, E., Baragiola, R., and Oliva-Florio, A., “Dependence of ion-electron emission from clean metals on the incidence angle of the projectile,” *Physical Review B*, Vol. 24, No. 8, 1981, pp. 4412.

[119] Gaworzewski, P. and Mai, M., *Untersuchungen zur Ionen-Elektronen-Emission an Festkörperoberflächen bei Beschuss mit positiven Edelgasionen im Energiebereich von 1, 5 bis 25 keV*, Ph.D. thesis, Humboldt University, 1971.

[120] Telkovsky, V., “Secondary Electron Emission of Metals Under the Action of Ions and Neutral Particles,” *Doklady Akademii Nauk SSSR*, Vol. 108, No. 3, 1956, pp. 444–446.

[121] Lachmann, J., Ph.D. thesis, Berlin, 1966.

[122] Alonso, E., Alurralde, M., and Baragiola, R., “Kinetic electron emission from solids induced by slow heavy ions,” *Surface Science Letters*, Vol. 166, No. 2-3, 1986, pp. L155–L160.

[123] Klein, H. J., “Ausbeuten und Winkelverteilungen der durch Edelgasionen an reinen Wolframoberflächen ausgelösten Sekundärelektronen,” *Zeitschrift für Physik A Hadrons and Nuclei*, Vol. 188, No. 1, 1965, pp. 78–92.

[124] Large, L., "Secondary electron emission from a clean tungsten surface bombarded by various positive ions," *Proceedings of the Physical Society*, Vol. 81, No. 6, 1963, pp. 1101.

[125] Parilis, J. S., "Kinetic Electron Emission and Fast Ion Bombardment," *A Survey of Phenomena in Ionized Gases. Invited Papers. A Collection of Invited Papers Presented at the Eighth International Conference on Phenomena in Ionized Gases*, 1968, pp. 309–351.

[126] Petrov, N., *Izvest. Akad Nauk S.S.S.R., Ser. Fiz.*, Vol. 26, 1962, pp. 1327.

[127] Arifov, U., Ayukhanov, A. K., and Starodubtsev, S., "Ion Scattering Coefficient as a Function of Colliding-Particle Mass Ratio," *Soviet Phys. JETP*, Vol. 6, 1958.

[128] Lakits, G., Aumayr, F., Heim, M., and Winter, H., "Threshold of ion-induced kinetic electron emission from a clean metal surface," *Physical Review A*, Vol. 42, No. 9, 1990, pp. 5780.

[129] Thum, F. and Hofer, W. O., "Z1-Oscillations in ion-induced kinetic electron emission," *Nuclear Instruments and Methods in Physics Research Section B: Beam Interactions with Materials and Atoms*, Vol. 2, No. 1-3, 1984, pp. 531–535.

[130] Veje, E., "Study of secondary electron emission from Be, B, Mg, and Au as a function of the projectile incidence angle," *Nuclear Instruments and Methods in Physics Research Section B: Beam Interactions with Materials and Atoms*, Vol. 2, No. 1-3, 1984, pp. 536–539.

[131] Goebel, D. M. et al., *High voltage breakdown limits of molybdenum and carbon-based grids for ion thrusters*, Pasadena, CA: Jet Propulsion Laboratory, National Aeronautics and Space Administration, 2005.

[132] Bruining, H., *Physics and Applications of Secondary Electron Emission*, McGraw-Hill, 1954.

[133] Dekker, A., "Secondary electron emission," *Solid State Physics*, Vol. 6, 1958, pp. 251–311.

[134] Wells, O. C., *Scanning electron microscopy*, McGraw-Hill, 1978.

[135] Seiler, H., "Secondary electron emission in the scanning electron microscope," *Journal of Applied Physics*, Vol. 54, No. 11, 1983, pp. R1–R18.

[136] Lye, R. G. and Dekker, A., "Theory of secondary emission," *Physical Review*, Vol. 107, No. 4, 1957, pp. 977.

[137] Vaughan, J. R. M., "A new formula for secondary emission yield," *IEEE Transactions on Electron Devices*, Vol. 36, No. 9, 1989, pp. 1963–1967.

[138] Thomas, E., "Particle-impact induced electron ejection from surfaces," *Int. Nuclear Data Committee Report*, 1995.

[139] Ordonez, C. and Peterkin Jr, R., "Secondary electron emission at anode, cathode, and floating plasma-facing surfaces," *Journal of applied physics*, Vol. 79, No. 5, 1996, pp. 2270–2274.

[140] Zameroski, N. D., Kumar, P., Watts, C., Svimonishvili, T., Gilmore, M., Schamiloglu, E., and Gaudet, J. A., "Secondary electron yield measurements from materials with application to collectors of high-power microwave devices," *IEEE Transactions on plasma science*, Vol. 34, No. 3, 2006, pp. 642–651.

[141] Belhaj, M., Roupie, J., Jbara, O., Puech, J., Balcon, N., and Payan, D., "Electron emission at very low electron impact energy: experimental and Monte-Carlo results," *arXiv preprint arXiv:1308.1301*, 2013.

[142] Woods, M., Hopkins, B., and McCracken, G., "Secondary electron yield measurements from limiter materials in the Joint European Torus," *Surface Science*, Vol. 162, No. 1-3, 1985, pp. 928–933.

[143] Woods, M., Hopkins, B., Matthews, G., McCracken, G., Sewell, P., and Fahrang, H., "An investigation of the secondary-electron emission of carbon samples exposed to a hydrogen plasma," *Journal of Physics D: Applied Physics*, Vol. 20, No. 9, 1987, pp. 1136.

[144] Palluel, P., "Backscattered components of electron secondary emission from metals," *CR Acad. Sci*, Vol. 224, 1947, pp. 1492–1494.

[145] Sternglass, E. J., "Backscattering of kilovolt electrons from solids," *Physical Review*, Vol. 95, No. 2, 1954, pp. 345.

[146] Bronstein, I. et al., "Secondary electron emission, Moscow," *Science*, 1969.

[147] Darlington, E. and Cosslett, V., "Backscattering of 0· 5-10 keV electrons from solid targets," *Journal of Physics D: Applied Physics*, Vol. 5, No. 11, 1972, pp. 1969.

[148] Verma, R., "The backscattering of low-energy electrons from carbon," *Journal of Physics D: Applied Physics*, Vol. 10, No. 8, 1977, pp. 1167.

[149] Ruzic, D., Moore, R., Manos, D., and Cohen, S., "Secondary electron yields of carbon-coated and polished stainless steel," *Journal of Vacuum Science and Technology*, Vol. 20, No. 4, 1982, pp. 1313–1316.

[150] Cazaux, J., "Secondary electron emission yield: graphite and some aromatic hydrocarbons," *Journal of Physics D: Applied Physics*, Vol. 38, No. 14, 2005, pp. 2442.

[151] Bruining, H., "Secondary electron emission: Part ii. absorption of secondary electrons," *Physica*, Vol. 5, No. 10, 1938, pp. 901–912.

[152] Oyarzabal, E., Martín-Rojo, A., Ferreira, J., Tafalla, D., and Tabarés, F., "Anomalous secondary electron emission of metallic surfaces exposed to a Glow Discharge plasma," *Journal of Nuclear Materials*, Vol. 438, 2013, pp. S792–S795.

[153] Oyarzabal, E., Martin-Rojo, A., and Tabarés, F., "Electron-induced secondary electron emission coefficient of lithium, tungsten and stainless steel surfaces exposed to low-pressure plasmas," *Journal of Nuclear Materials*, Vol. 452, No. 1, 2014, pp. 37–40.

[154] Petry, R. L., "Secondary electron emission from tungsten, copper and gold," *Physical Review*, Vol. 28, No. 2, 1926, pp. 362.

[155] Bronshtein, I. and Roshchin, V., "Electron Reflection and Secondary Electron Emission from Metallic Surfaces in the Region of Small Primary Energies," *Soviet Physics-Technical Physics*, Vol. 3, No. 11, 1958, pp. 2271–2280.

[156] Inai, K., Ohya, K., Kawamura, G., and Tomita, Y., "Electron Velocity Distribution at a Sheath Edge in the Presence of Secondary Electron Emission From a Metal Surface," *Contributions to Plasma Physics*, Vol. 50, No. 3-5, 2010, pp. 458–463.

[157] Tolias, P., "On electron backscattering from dust grains in fusion plasmas," *Plasma Physics and Controlled Fusion*, Vol. 56, No. 4, 2014, pp. 045003.

[158] Tolias, P., "On secondary electron emission and its semi-empirical description," *Plasma Physics and Controlled Fusion*, Vol. 56, No. 12, 2014, pp. 123002.

[159] Takamura, S., Miyamoto, T., and Ohno, N., "Deepening of floating potential for tungsten target plate on the way to nanostructure formation," *Plasma and Fusion Research*, Vol. 5, 2010, pp. 039–039.

[160] Ye, M., , He, Y., , Hu, S., , Wang, R., , Hu, T., , et al., "Suppression of secondary electron yield by micro-porous array structure," *Journal of applied Physics*, Vol. 113, No. 7, 2013, pp. 074904.

[161] Ye, M., He, Y., Hu, S., Yang, J., Wang, R., Hu, T., Peng, W., and Cui, W., "Investigation into anomalous total secondary electron yield for micro-porous Ag surface under oblique incidence conditions," *Journal of Applied Physics*, Vol. 114, No. 10, 2013, pp. 104905.

[162] Curren, A. N., "Carbon and carbon-coated electrodes for multistage depressed collectors for electron-beam devices A technology review," *IEEE Transactions on Electron Devices*, Vol. 33, No. 11, 1986, pp. 1902–1914.

[163] Curren, A. N., Jensen, K. A., and Roman, R. F., "Secondary electron emission characteristics of molybdenum-masked, ion-textured OFHC copper," Tech. rep., NASA Technical Paper, 1990.

[164] Baglin, V., Bojko, J., Scheuerlein, C., Gröbner, O., Taborelli, M., Henrist, B., and Hilleret, N., "The secondary electron yield of technical materials and its variation with surface treatments," Tech. rep., LHC Project Report, 2000.

[165] Pivi, M., King, F., Kirby, R., Raubenheimer, T., Stupakov, G., and Le Pimpec, F., "Sharp reduction of the secondary electron emission yield from grooved surfaces," *Journal of Applied Physics*, Vol. 104, No. 10, 2008, pp. 104904.

[166] Suetsugu, Y., Fukuma, H., Shibata, K., Pivi, M., Wang, L., et al., "Experimental studies on grooved surfaces to suppress secondary electron emission," *Proc.IPAC10, paper TUPD043*, 2010.

[167] Bundaleski, N., Belhaj, M., Gineste, T., and Teodoro, O., "Calculation of the angular dependence of the total electron yield," *Vacuum*, Vol. 122, 2015, pp. 255–259.

[168] Kurrelmeyer, B. and Hayner, L. J., "Shot effect of secondary electrons from nickel and beryllium," *Physical Review*, Vol. 52, No. 9, 1937, pp. 952.

[169] Rao, S. R., "Total secondary electron emission from polycrystalline nickel," *Proceedings of the Royal Society of London. Series A, Containing Papers of a Mathematical and Physical Character*, Vol. 128, No. 807, 1930, pp. 41–56.

[170] Araki, S. J. and Wirz, R. E., "Collision Modeling for High Velocity Ions in a Quiescent Gas," *42nd AIAA Plasmadynamics and Lasers Conference, Honolulu, Hawaii*, 2011, pp. 1–10.

[171] Araki, S. J., *Multi-Scale Multi-Species Modeling for Plasma Devices*, Ph.D. thesis, University of California, Los Angeles, 2014.

[172] Patino, M., Chu, L., and Wirz, R., "Ion-neutral collision analysis for a well-characterized plasma experiment," *48th AIAA/ASME/SAE/ASEE Joint Propulsion Conference & Exhibit, Atlanta, Georgia*, 2012, p. 4119.

[173] Wirz, R. E., Chu, L., Patino, M., Mao, H.-S., and Araki, S., "Well-characterized plasma experiments for validation of computational models," *32nd International Electric Propulsion Conference, Kurhaus, Wiesbaden, Germany*, 2011, pp. 1–12.

[174] Eggens, C. J., "A computer simulation for the creation of a transient high density plasma by convergent neutral beams," Tech. rep., Lawrence Livermore Laboratory, 1977.

[175] Araki, S. J. and Wirz, R. E., "Modeling of Elastic Collisions between High Energy and Slow Neutral Atoms," Tech. rep., DTIC Document, 2015.

[176] Giuliano, P. N. and Boyd, I. D., "Particle simulation of collision dynamics for ion beam injection into a rarefied gas," *Physics of Plasmas (1994-present)*, Vol. 20, No. 3, 2013, pp. 033505.

[177] Kapper, M. G., *A high-order transport scheme for collisional-radiative and nonequilibrium plasma*, The Ohio State University, 2009.

[178] Dalgarno, A., "The mobilities of ions in their parent gases," *Philosophical Transactions of the Royal Society of London A: Mathematical, Physical and Engineering Sciences*, Vol. 250, No. 982, 1958, pp. 426–439.

[179] Dham, A. K., Meath, W. J., Allnatt, A., Aziz, R. A., and Slaman, M., "XC and HFD-B potential energy curves for Xe-Xe and related physical properties," *Chemical Physics*, Vol. 142, No. 2, 1990, pp. 173–189.

[180] Capece, A., Patino, M., Raitses, Y., and Koel, B., "Secondary electron emission from lithium and lithium compounds," *Applied Physics Letters*, Vol. 109, No. 1, 2016, pp. 011605.

[181] Seah, M. P. and Dench, W., "Quantitative electron spectroscopy of surfaces: a standard data base for electron inelastic mean free paths in solids," *Surface and interface analysis*, Vol. 1, No. 1, 1979, pp. 2–11.

[182] Cimino, R. and Collins, I., "Vacuum chamber surface electronic properties influencing electron cloud phenomena," *Applied surface science*, Vol. 235, No. 1, 2004, pp. 231–235.

[183] Takahashi, T., Tokailin, H., and Sagawa, T., "Angle-resolved ultraviolet photoelectron spectroscopy of the unoccupied band structure of graphite," *Physical Review B*, Vol. 32, No. 12, 1985, pp. 8317.

[184] Patino, M. I., Raitses, Y., Koel, B. E., and Wirz, R. E., "Application of Auger spectroscopy for measurement of secondary electron emission from conducting material for electric propulsion devices," *Proc. 33rd Int. Electric Propulsion Conf.(Washington, DC, USA, 6–10 October 2013)*, 2013, pp. 1–8.

[185] Patino, M., Raitses, Y., Koel, B., and Wirz, R., "Analysis of secondary electron emission for conducting materials using 4-grid LEED/AES optics," *Journal of Physics D: Applied Physics*, Vol. 48, No. 19, 2015, pp. 195204.

[186] Norton, P. and Bindner, P., "Experimental verification of a zero order desorption model: D2 on Ni (110)," *Surface science*, Vol. 169, No. 1, 1986, pp. L259–L265.

[187] McGuire, G., *Auger electron spectroscopy reference manual: a book of standard spectra for identification and interpretation of Auger electron spectroscopy data*, Springer Science & Business Media, 2013.

[188] sensitivity factors taken from AugerScan version 3.3.0.1, A.

[189] SAES Getters USA, I.

[190] Drouin, D., Couture, A. R., Joly, D., Tastet, X., Aimez, V., and Gauvin, R., "CASINO V2. 42A Fast and Easy-to-use Modeling Tool for Scanning Electron Microscopy and Microanalysis Users," *Scanning*, Vol. 29, No. 3, 2007, pp. 92–101.

[191] Saltas, V. and Papageorgopoulos, C., "Adsorption of Li on Ni (110) surfaces at low and room temperature," *Surface science*, Vol. 461, No. 1, 2000, pp. 219–230.

[192] Sullenberger, R., *Uptake and retention of residual vacuum gases in lithium and lithium films*, Ph.D. thesis, M. Sc. thesis, Princeton University, 2012.

[193] Engbæk, J., Nielsen, G., Nielsen, J. H., and Chorkendorff, I., "Growth and decomposition of lithium and lithium hydride on nickel," *Surface science*, Vol. 600, No. 7, 2006, pp. 1468–1474.

[194] Spencer, J. N., Bodner, G. M., and Rickard, L. H., *Chemistry: structure and dynamics*, John Wiley & Sons, 2010.

[195] Wyckoff, R. W. G. and Wyckoff, R. W., *Crystal structures*, Vol. 2, Interscience New York, 1960.

[196] Bottomley, D., Lüpke, G., Bloch, J., Van Driel, H., and Timsit, R., "On the detection of elemental Li on Al-Li alloy surfaces using Auger electron spectroscopy," *Applied surface science*, Vol. 62, No. 1-2, 1992, pp. 97–99.

[197] Palmberg, P. W., *Handbook of Auger Electron Spectroscopy: A Reference Book of Standard Data...*, Physival Electronics Industries, 1972.

[198] Baldwin, M. and Doerner, R., "Formation of helium induced nanostructure fuzzon various tungsten grades," *Journal of Nuclear Materials*, Vol. 404, No. 3, 2010, pp. 165–173.

[199] Hoffmann, R. C., *Electron-induced electron yields of uncharged insulating materials*, Ph.D. thesis, Utah State University, 2010.

[200] Viswanathan, V., Thygesen, K. S., Hummelshøj, J., Nørskov, J. K., Girishkumar, G., McCloskey, B., and Luntz, A., "Electrical conductivity in Li2O2 and its role in determining capacity limitations in non-aqueous Li-O2 batteries," *The Journal of chemical physics*, Vol. 135, No. 21, 2011, pp. 214704.

[201] Radin, M. D. and Siegel, D. J., "Charge transport in lithium peroxide: relevance for rechargeable metal–air batteries," *Energy & Environmental Science*, Vol. 6, No. 8, 2013, pp. 2370–2379.

[202] Parker, S. and Rhead, G., “Oxidation of lithium monolayers on silver (111): A study by AES, work function and secondary emission changes,” *Surface science*, Vol. 167, No. 2-3, 1986, pp. 271–284.

[203] Hoenigman, J. and Keil, R., “An XPS study of the adsorption of oxygen and water vapor on clean lithium films,” *Applications of surface science*, Vol. 18, No. 1-2, 1984, pp. 207–222.

[204] Patino, M., Raitses, Y., and Wirz, R., “Secondary electron emission from plasma-generated nanostructured tungsten fuzz,” *Applied Physics Letters*, Vol. 109, No. 20, 2016, pp. 201602.

[205] Yang, J., Cui, W., Li, Y., Xie, G., Zhang, N., Wang, R., Hu, T., and Zhang, H., “Investigation of argon ion sputtering on the secondary electron emission from gold samples,” *Applied Surface Science*, Vol. 382, 2016, pp. 88–92.

[206] Gineste, T., Belhaj, M., Teyssedre, G., and Puech, J., “Investigation of the electron emission properties of silver: From exposed to ambient atmosphere Ag surface to ion-cleaned Ag surface,” *Applied Surface Science*, Vol. 359, 2015, pp. 398–404.

[207] Hilleret, N., Scheuerlein, C., and Taborelli, M., “The secondary-electron yield of air-exposed metal surfaces,” *Applied Physics A: Materials Science & Processing*, Vol. 76, No. 7, 2003, pp. 1085–1091.

[208] Krasnov, A., “Molecular pumping properties of the LHC arc beam pipe and effective secondary electron emission from Cu surface with artificial roughness,” *Vacuum*, Vol. 73, No. 2, 2004, pp. 195–199.

[209] Christmann, K., Penka, V., Rehm, R., Chehab, F., and Ertl, G., “Dual path surface reconstruction in the H/Ni (110) system,” *Solid state communications*, Vol. 51, No. 7, 1984, pp. 487–490.

[210] Kuzucan, A., Neupert, H., Taborelli, M., and Störi, H., “Secondary electron yield on cryogenic surfaces as a function of physisorbed gases,” *Journal of Vacuum Science & Technology A: Vacuum, Surfaces, and Films*, Vol. 30, No. 5, 2012, pp. 051401.

[211] Laponsky, A. and Whetten, N. R., “Dependence of Secondary Electron Emission on Crystal Orientation,” *Physical Review Letters*, Vol. 3, No. 11, 1959, pp. 510.

[212] Soshea, R. and Dekker, A., “Fine Structure of Secondary Emission vs Angle of Incidence of the Primary Beam on Titanium Single Crystals,” *Physical Review*, Vol. 121, No. 5, 1961, pp. 1362.

[213] Palmberg, P., “Secondary emission studies on Ge and Na-covered Ge,” *Journal of Applied Physics*, Vol. 38, No. 5, 1967, pp. 2137–2147.

[214] Komar, A., Korobochko, Y. S., Grachev, B., and Mineev, V., "Mechanism of the Origin of the Fine Structure of the Angular Dependence of the Secondary-Electron Emission Coefficient of Single Crystals," *Sov Phys Solid State*, Vol. 10, No. 5, 1968.

[215] Minnebaev, K., Khaidarov, A., Ivanenko, I., Minnebaev, D., and Yurasova, V., "Features of angular dependence of secondary electron emission from metal single crystals," *Nuclear Instruments and Methods in Physics Research Section B: Beam Interactions with Materials and Atoms*, 2017.

[216] Taub, H., Stern, R., and Dvoryankin, V., "Temperature Dependence of Mean Free Path in Secondary Electron Emission," *physica status solidi (b)*, Vol. 33, No. 2, 1969, pp. 573–577.

[217] De Lara, J., Pérez, F., Alfonseca, M., Galán, L., Montero, I., Román, E., and Garcia-Baquero, D. R., "Multipactor prediction for on-board spacecraft RF equipment with the MEST software tool," *IEEE Transactions on Plasma Science*, Vol. 34, No. 2, 2006, pp. 476–484.

[218] Swanson, C. and Kaganovich, I. D., "Modeling of reduced effective secondary electron emission yield from a velvet surface," *Journal of Applied Physics*, Vol. 120, No. 21, 2016, pp. 213302.

[219] Fiflis, P. R., *Interaction of plasmas with lithium and tungsten fusion plasma facing components*, Ph.D. thesis, University of Illinois at Urbana-Champaign, 2016.

[220] Tanyeli, İ., Marot, L., Mathys, D., van de Sanden, M. C., and De Temmerman, G., "Surface modifications induced by high fluxes of low energy helium ions," *Scientific reports*, Vol. 5, 2015.

[221] Massey, H. and Smith, R., "The passage of positive ions through gases," *Proceedings of the Royal Society of London. Series A, Containing Papers of a Mathematical and Physical Character*, Vol. 142, No. 846, 1933, pp. 142–172.

[222] Massey, H. S. W., Burhop, E., and Gilbody, H., *Electronic and Ionic Impact Phenomena. Vol. 4: Recombination and Fast Collisions of Heavy Particles*, Oxford, 1974.

[223] Dillon Jr, J., Sheridan, W., Edwards, H., and Ghosh, S., "Charge Transfer Reactions in Monatomic and Diatomic Gases," *The Journal of Chemical Physics*, Vol. 23, No. 5, 1955, pp. 776–779.

[224] Ghosh, S. and Sheridan, W., "Experimental Determinations of Charge Transfer Cross Sections and Secondary Electron Emission by Ion Bombardment," *The Journal of Chemical Physics*, Vol. 26, No. 3, 1957, pp. 480–485.

[225] Hasted, J. and Hussain, M., "Electron capture by multiply charged ions," *Proceedings of the Physical Society*, Vol. 83, No. 6, 1964, pp. 911.

[226] Okuno, K., Koizumi, T., and Kaneko, Y., "Symmetric resonance double charge transfer in Kr+++ Kr and Xe+++ Xe systems," *Physical Review Letters*, Vol. 40, No. 26, 1978, pp. 1708.

[227] Johnsen, R. and Biondi, M. A., "Thermal-energy charge transfer, quenching, and association reactions of doubly charged ions in the rare gases," *Physical Review A*, Vol. 20, No. 1, 1979, pp. 87.

[228] Koizumi, T., Okuno, K., Kobayashi, N., and Kaneko, Y., "Drift Tube Study of Symmetric Resonance Single-and Double-Charge Transfer in Kr++ Kr, Xe++ Xe, Kr+++ Kr, and Xe+++ Xe Systems," *Journal of the Physical Society of Japan*, Vol. 51, No. 8, 1982, pp. 2650–2656.

[229] Drake, G. W., *Springer handbook of atomic, molecular, and optical physics*, Springer Science & Business Media, 2006.

[230] Johnson, L. K., *Absolute Differential Cross Sections for Small-angle Neutral-neutral and Ion-neutral Elastic Scattering at KeV Energies*, Ph.D. thesis, Rice University, 1987.

[231] Sakabe, S. and Izawa, Y., "Cross sections for resonant charge transfer between atoms and their positive ions: collision velocity? 1 au," *Atomic Data and Nuclear Data Tables*, Vol. 49, No. 2, 1991, pp. 257–314.

[232] Mahadevan, P. and Magnuson, G., "Low-Energy (1-to 100-eV) Charge-Transfer Cross-Section Measurements for Noble-Gas-Ion Collisions with Gases," *Physical Review*, Vol. 171, No. 1, 1968, pp. 103.

[233] Helm, H., "The cross section for symmetric charge exchange of He+ in He at energies between 0.3 and 8 eV," *Journal of Physics B: Atomic and Molecular Physics*, Vol. 10, No. 18, 1977, pp. 3683.

[234] Rao, M., Van Brunt, R. J., and Olthoff, J. K., "Resonant charge exchange and the transport of ions at high electric-field to gas-density ratios (E/N) in argon, neon, and helium," *Physical Review E*, Vol. 54, No. 5, 1996, pp. 5641.

[235] Cramer, W. and Simons, J., "Elastic and Inelastic Scattering of Low-Velocity He+ Ions in Helium," *The Journal of Chemical Physics*, Vol. 26, No. 5, 1957, pp. 1272–1275.

[236] Hayden, H. C. and Utterback, N. G., "Ionization of helium, neon, and nitrogen by helium atoms," *Physical Review*, Vol. 135, No. 6A, 1964, pp. A1575.

[237] Belyaev, V., Brezhnev, B., and Erastov, E., "Resonance Charge Exchange of Low Energy Carbon and Nitrogen Ions," *Zh. Eksp. Teor. Fiz., 54: 1720-5 (June 1968).*, 1968.

[238] de Heer, F., van Eck, J., and Kistemaker, J., "Electron capture into an excited state by H and He," *Sixth International Conference on Ionization Phenomena in Gases, Serma, Paris*, 1963, p. 73.

[239] et al, K. B. I., "Resonance charge exchange of ions of inert gases in the energy interval of 200 to 4000 eV," *Zh Tekh Fiz (in Russian)*, Vol. 45, No. 3, 1975, pp. 586–592.

[240] Galli, A., Giardini-Guidoni, A., and Volpi, G., "Charge exchange in noble gases," *Il Nuovo Cimento (1955-1965)*, Vol. 26, No. 5, 1962, pp. 845–854.

[241] Kobayashi, N., "Concentration effect of the reactant gas in the injected-ion drift tube mass spectrometer," *Journal of the Mass Spectrometry Society of Japan*, Vol. 20, No. 2, 1972, pp. 123–129.

[242] Kaneko, Y., Kobayashi, N., and Kanomata, I., "Low Energy Ion-Neutral Reactions. I. 22Ne++ 20Ne, and Ar++ N2," *Journal of the Physical Society of Japan*, Vol. 27, No. 4, 1969, pp. 992–998.

[243] Martinez, R. I. and Dheandhanoo, S., "Instrument-independent CAD spectral databases: absolute cross-section measurements in QQQ instruments," *J. Res. Nat. Bur. Stand.*, Vol. 92, 1987, pp. 229–237.

[244] Cramer, W., "Elastic and Inelastic Scattering of Low-Velocity Ions: He+ in Ne, Ne+ in He, and Ne+ in Ne," *The Journal of Chemical Physics*, Vol. 28, No. 4, 1958, pp. 688–690.

[245] Von Wolf, F., "Über die Gültigkeitsgrenzen des Resonanzprinzips der Umladung," *Annalen der Physik (in German)*, Vol. 5, No. 30, 1937, pp. 313–332.

[246] Pullins, S. H., Dressler, R. A., Torrents, R., and Gerlich, D., "Guided-ion beam measurements of Ar++ Ar symmetric charge-transfer cross sections at ion energies ranging from 0.2 to 300 eV," *Zeitschrift für Physikalische Chemie International journal of research in physical chemistry and chemical physics*, Vol. 214, No. 9/2000, 2000, pp. 1279.

[247] von Köding, H. and Nibbering, N. M., "A fourier transform ion cyclotron resonance study of two-and one-electron capture reactions between doubly charged rare gas ions and rare gas atoms," *International journal of mass spectrometry*, Vol. 185, 1999, pp. 281–289.

[248] Hishinuma, N. and Sasaki, T., "Relative Cross Section of a 2P1/2 Ion to a 2P3/2 Ion in Kr+-Kr and Xe+-Xe Charge Transfer Reactions," *Journal of the Physical Society of Japan*, Vol. 30, No. 6, 1971, pp. 1767–1767.

[249] Nichols, B. J. and Witteborn, F. C., "Measurements of resonant charge exchange cross sections in nitrogen and argon between 0.5 and 17 eV," Tech. rep., NASA Technical Report, 1966.

[250] Phelps, A., "The application of scattering cross sections to ion flux models in discharge sheaths," *Journal of applied physics*, Vol. 76, No. 2, 1994, pp. 747–753.

[251] Rostagni, A., "Ricekche sui raggi positivi e neutrali," *Il Nuovo Cimento (1924-1942)*, Vol. 12, No. 3, 1935, pp. 134–153.

[252] Hishinuma, N., "Relative Charge Transfer Efficiencies of 2 P 3/2 and 2 P 1/2 Rare-Gas Ions in Their Own Gases," *Journal of the Physical Society of Japan*, Vol. 32, No. 1, 1972, pp. 227–234.

[253] Kimura, M. and Watanabe, T., "Charge Transfer Cross Sections for Krˆ+-Kr and for Xeˆ+-Xe and the Effects of the Initial J-State in the Ions," *Journal of the Physical Society of Japan*, Vol. 31, No. 5, 1971, pp. 1600.

[254] Karmohapatro, S., "Charge Exchange between Krypton Ions and Atoms," *The Journal of Chemical Physics*, Vol. 35, No. 4, 1961, pp. 1524–1525.

[255] von Köding, H., Pinkse, F. A., and Nibbering, N. M., "Rate coefficients of single and double electron transfer from Xe to Xe2+ at low collision energies as determined by use of Fourier transform ion cyclotron resonance mass spectrometry," *Physica Scripta*, Vol. 1995, No. T59, 1995, pp. 418.

[256] E. Johnson, R., "Charge Transfer and Fine Structure Transitions in Kr+ (2Pj)+ Kr and Xe+ (2Pj)+ Xe Collisions," *Journal of the Physical Society of Japan*, Vol. 32, No. 6, 1972, pp. 1612–1614.

[257] Firsov, O. B., "Resonant recharging of ions in slow collisions," 1951.

[258] Fetisov, I. and FIRSOV, B., "Resonance Charge Exchange of Doubly Charged Ions in Slow Collisions," *Soviet Physics JETP*, Vol. 37, No. 10, 1960.

[259] Sommerville, J. D., King, L. B., Chiu, Y.-H., and Dressler, R. A., "Ion-Collision Emission Excitation Cross Sections for Xenon Electric Thruster Plasmas," *Journal of Propulsion and Power*, Vol. 24, No. 4, 2008, pp. 880–888.

[260] Phelps, A. and Jelenković, B., "Excitation and breakdown of Ar at very high ratios of electric field to gas density," *Physical Review A*, Vol. 38, No. 6, 1988, pp. 2975.

[261] Johnson, S. G., "NIST Standard Reference Database Journal of Physical and Chemical Reference Data Reprints," *Energy*, Vol. 41, 2012.

[262] Hagstrum, H. D., "Instrumentation and experimental procedure for studies of electron ejection by ions and ionization by electron impact," *Review of Scientific Instruments*, Vol. 24, No. 12, 1953, pp. 1122–1142.

[263] Okhrimovskyy, A., Bogaerts, A., and Gijbels, R., "Electron anisotropic scattering in gases: A formula for Monte Carlo simulations," *Physical Review E*, Vol. 65, No. 3, 2002, pp. 037402.

[264] de Lara, J., Perez, F., Alfonseca, M., Galan, L., and Raboso, D., "Multipactor electron simulation tool (MEST)," *Power Modulator Symposium, 2004 and 2004 High-Voltage Workshop. Conference Record of the Twenty-Sixth International*, IEEE, 2004, pp. 547–550.

[265] Furman, M. A. and Lambertson, G. R., "The electron-cloud instability in the arcs of the PEP-II positron ring," *Lawrence Berkeley National Laboratory*, 1998.

[266] Furman, M. and Pivi, M., "Probabilistic model for the simulation of secondary electron emission," *Physical Review Special Topics-Accelerators and Beams*, Vol. 5, No. 12, 2002, pp. 124404.

[267] Katz, I., Parks, D., Mandell, M., Harvey, J., Brownell Jr, D., Wang, S., and Rotenberg, M., "A three dimensional dynamic study of electrostatic charging in materials," Tech. rep., NASA Technical Report NR-135256, 1977.

[268] Hunger, H.-J. and Küchler, L., "Measurements of the electron backscattering coefficient for quantitative EPMA in the energy range of 4 to 40 keV," *physica status solidi (a)*, Vol. 56, No. 1, 1979.

[269] Cazaux, J., "Electron back-scattering coefficient below 5 keV: Analytical expressions and surface-barrier effects," *Journal of Applied Physics*, Vol. 112, No. 8, 2012, pp. 084905.

[270] Everhart, T., "Simple theory concerning the reflection of electrons from solids," *Journal of Applied Physics*, Vol. 31, No. 8, 1960, pp. 1483–1490.

[271] Barut, A., "The Mechanism of Secondary Electron Emission," *Physical Review*, Vol. 93, No. 5, 1954, pp. 981.

[272] Darlington, E., "Backscattering of 10-100 keV electrons from thick targets," *Journal of Physics D: Applied Physics*, Vol. 8, No. 1, 1975, pp. 85.

[273] Fitting, H.-J. and Technow, R., "Electron backscattering at various angles of incidence," *physica status solidi (a)*, Vol. 76, No. 2, 1983.

[274] Fitting, H.-J., Schreiber, E., and Glavatskikh, I., "Monte Carlo modeling of electron scattering in nonconductive specimens," *Microscopy and Microanalysis*, Vol. 10, No. 06, 2004, pp. 764–770.

[275] Staub, P.-F., "Bulk target backscattering coefficient and energy distribution of 0.5-100 keV electrons: an empirical and synthetic study," *Journal of Physics D: Applied Physics*, Vol. 27, No. 7, 1994, pp. 1533.

[276] Fitting, H., “The energy loss of transmitted and backscattered electrons,” *Journal of Physics D: Applied Physics*, Vol. 8, No. 13, 1975, pp. 1480.

[277] Love, G., Cox, M., and Scott, V., “A versatile atomic number correction for electron-probe microanalysis,” *Journal of Physics D: Applied Physics*, Vol. 11, No. 1, 1978, pp. 7.